/USAAVLABS SYMPOSIUM PROCEEDINGS

AERODYNAMIC PROBLEMS
ASSOCIATED WITH
V/STOL AIRCRAFT

VOLUME I

PROPELLER AND ROTOR AERODYNAMICS

**22-24 June 1966**

Statler-Hilton Hotel

Buffalo, New York

DISCLAIMER NOTICE
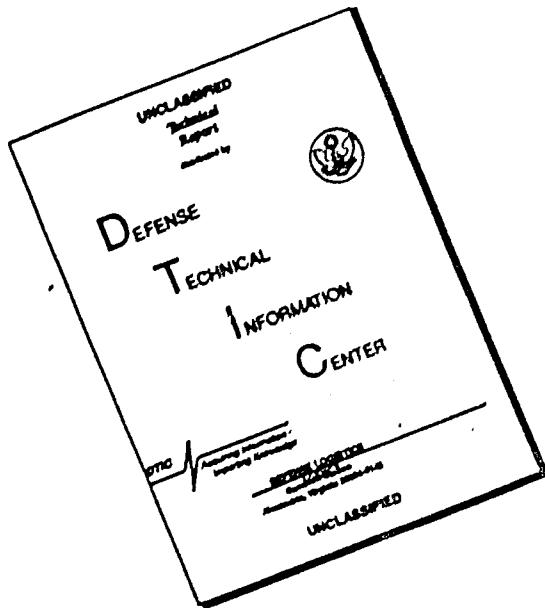
THIS DOCUMENT IS BEST
QUALITY AVAILABLE. THE COPY
FURNISHED TO DTIC CONTAINED
A SIGNIFICANT NUMBER OF
PAGES WHICH DO NOT
REPRODUCE LEGIBLY.

CAL/USAAVLABS

SYMPOSIUM PROCEEDINGS

AERODYNAMIC PROBLEMS
ASSOCIATED WITH
V/STOL AIRCRAFT

Published in Four Volumes as Follows:

Volume I   Propeller and Rotor Aerodynamics

Volume II   Propulsion and Interference Aerodynamics

Volume III   Aerodynamic Research on Boundary Layers

Volume IV   Panels on Recommended V/STOL Aerodynamic Research,
             Panel Summaries, Featured Speakers, and Technical
             Paper Discussions

This is VOLUME I and contains those technical papers presented

Wednesday, 22 June 1966
Statler-Hilton Hotel
Buffalo, New York

D D C
SEP 7 1967
C

FOREWORD

The rapid advances made in helicopter and V/STOL aircraft development in the past few years have spotlighted areas in which significant aerodynamic problems have been encountered, and in some cases the problems still exist. Fortunately, a technological maturity has now been attained in the industry, making possible investigations through knowledgeable scientific approaches that have produced an enlightened understanding of the problems and, in many cases, have led to practical solutions. The next generation of flight vehicles, currently in the design and development stages, are offering challenges to the aerodynamicist and engineer, and it is evident that future vehicle developments will demand an ever-increasing rate of technological advance in the knowledge and understanding of aerodynamic phenomena.

Several years have passed since a technical specialists' meeting was held to direct attention specifically to the low-speed aerodynamic problem areas of helicopters and V/STOL vehicles. Therefore, in the interest of disseminating up-to-date information, the cosponsors of this symposium, the U.S. Army Aviation Materiel Laboratories (USAAVLABS) and Cornell Aeronautical Laboratory, Inc. (CAL), believe such a meeting among technical specialists in the field would be timely. It is hoped that this symposium will, through the presentation of selected technical papers, establish the state of the art of aerodynamic analysis in the basic problem areas and spotlight those critical areas where research is urgently needed. The ultimate objective is to identify those advances required in the state of the art that can assure the availability of the analytical tools needed to develop and analyze the next generation of helicopters and V/STOL aircraft.

In keeping with these objectives, five technical sessions, each dealing with specific basic areas of aerodynamic analysis associated with V/STOL aircraft, have been formed. In addition, a panel session has also been scheduled in which outstanding members of industry and government from three countries will present their recommendations for areas of research that need to be pursued if the state of the art is to advance at the required rate.

It is believed that the formal presentation of the selected papers and the panel presentations and recommendations will stimulate constructive discussions among the specialists in attendance. While a significant amount of time has been allotted during the sessions for this to be accommodated, it is hoped the sessions will, in addition, stimulate discussions and serious thought between the attendees and the technical members of the various organizations who were unable to attend. In order to foster this latter objective, the informal discussions (questions and answers, etc.) will be recorded, printed, and mailed to each attendee for inclusion in his copy of the proceedings.

The proceedings of the symposium have been bound in four volumes -- a separate volume for the technical sessions of each day, and one volume for the panel sessions. We are indebted to the authors for preparing their manuscripts in a form that could be directly reproduced. This material was published as provided by the authors and was neither checked nor edited by CAL or USAAVLABS.

The cosponsors of the symposium are grateful to the many people who contributed to its success. In particular, our thanks go to Colonel Harry L. Bush, Commanding Officer of the U.S. Army Aviation Materiel Laboratories, and Mr. Ira G. Ross, President of Cornell Aeronautical Laboratory, Inc., who opened the sessions; to Mr. Charles W. Harper, our keynote speaker; to Major General William Bunker, Deputy Commanding General, U.S. Army Materiel Command, for his address at the symposium banquet; to the five session chairmen --

Arthur Jackson, Hamilton Standard

Franklyn J. Davenport, Vertol Division of The Boeing Company

John W. White, U.S. Army Aviation Materiel Laboratories

Irven H. Culver, Lockheed-California Company

Sean C. Roberts, Mississippi State University

and to the two panel chairmen --

Larry M. Hewin, Technical Director, USAAVLABS

Harold A. Cheilek, Vice President - Technical Director, CAL

and, most especially, of course, to the authors and panel members without whom there could not have been this symposium on low-speed aerodynamic problems.

SYMPOSIUM TECHNICAL CHAIRMAN

Richard P. White, Jr., CAL
John E. Yeates, USAAVLABS

CONTENTS
VOLUME I
PROPELLER AND ROTOR AERODYNAMICS

---

[*]Speech transcribed

TECHNICAL SESSION I

PROPELLER AERODYNAMICS

Wednesday Morning
22 June 1966

SESSION CHAIRMAN

A. Jackson
Hamilton Standard

A THEORY FOR STATIC PROPELLER PERFORMANCE[*]

by

J. C. ERICKSON, JR. & D. E. ORDWAY

Therm Advanced Research, Inc.
Ithaca, N.Y., U.S.A.

Abstract

The successful design of a propeller type V/STOL aircraft requires
the precise evaluation and associated optimization of the propeller
performance at the static condition. A general theory for perform-
ance calculations has been formulated based on a continuous vortex
representation along the lines of the classical lifting-line model.

The trailing vortex sheets in the propeller wake must deform in
order to remain force free. In contrast to the cruise problem,
this deformation is appreciable just behind the propeller, and its
determination and representation constitute the heart of the static
problem.

A computer program has been developed to calculate both the inflow
at the propeller and the induced velocity at any field point for an
arbitrary description of the trailing vortex sheets. To approximate
the force-free condition imposed on the wake, an initial wake hy-
pothesis derived from generalized actuator disk theory was first
used. The resulting contraction of the trajectories of the elements
of the trailing vortex sheets was reasonable, but other comparisons
with both detailed and gross measurements for two typical propellers
were unsatisfactory and a refined hypothesis was derived.

The refined wake hypothesis provides a reasonable representation of
the "pitch" of the elements of the deformed trailing vortex sheets
as well as of the contraction. Based on this hypothesis, compari-
sons of the thrust coefficient and figure of merit at one power
coefficient of a third propeller show excellent agreement with test
data.

Introduction

The need for peak propeller performance with V/STOL aircraft is greater than with conventional aircraft as the propellers must generate a total lift equal to the gross weight of the aircraft. Since the payload of these vehicles is 20% to 30% of the gross weight, a small improvement in the lift or hover performance of the propellers results in a large improvement in payload capacity.

The design of high-performance propellers for V/STOL aircraft has been hindered by the lack of a suitable theory for the determination of performance at the hover operating condition. The principal difficulty in the static case is locating the elements of the trailing vortex sheets, i.e. these elements must deform such that they are force free. In general, there is an axial elongation of the sheets, together with a radial contraction and a tangential distortion. The edges of the sheets are also locally unstable and tend to roll up as for a finite wing. While these deformations are not of primary significance in forward flight, they are the heart of the static problem. Without a free stream, not only do the deformations occur much closer to the propeller and so exert more influence, but they are also much larger. In fact, the axial elongation which constitutes only a perturbation of the pitch of the regular helical sheets in forward flight now determines the total variation of the "pitch".

In our initial studies of the static thrust problem we used a simple wake model in which the essential deformation was discontinuous[1-4]. Although the results themselves were not satisfactory, they did indicate that continuous deformation of the vortex sheets was necessary for an adequate model. Such a "Continuous Deformation Model" is developed in detail in Ref. 5, which was co-authored with H. V. Borst and R. M. Ladden of Curtiss-Wright. Here we have condensed this work and tried to present the principal features.

Basic Equations

We consider a propeller rotating at a constant angular speed Ω in an inviscid fluid otherwise at rest at infinity. The blade thickness-to-chord and chord-to-radius ratios are assumed to be reasonably small. We can then represent the blades by radial bound vortex lines, together with a force-free system of trailing vortex sheets, i.e. the classical lifting line formulation.

A propeller-fixed cylindrical coordinate system (x,r,θ) is chosen with the axis of rotation as the x-axis, see Fig. 1 . In this system the flow is steady and the N blades are located in the plane $x = 0$ such that

$$\theta_p = 2\pi(p-1)/N \qquad p = 1, 2, \ldots , N \qquad (1)$$

2
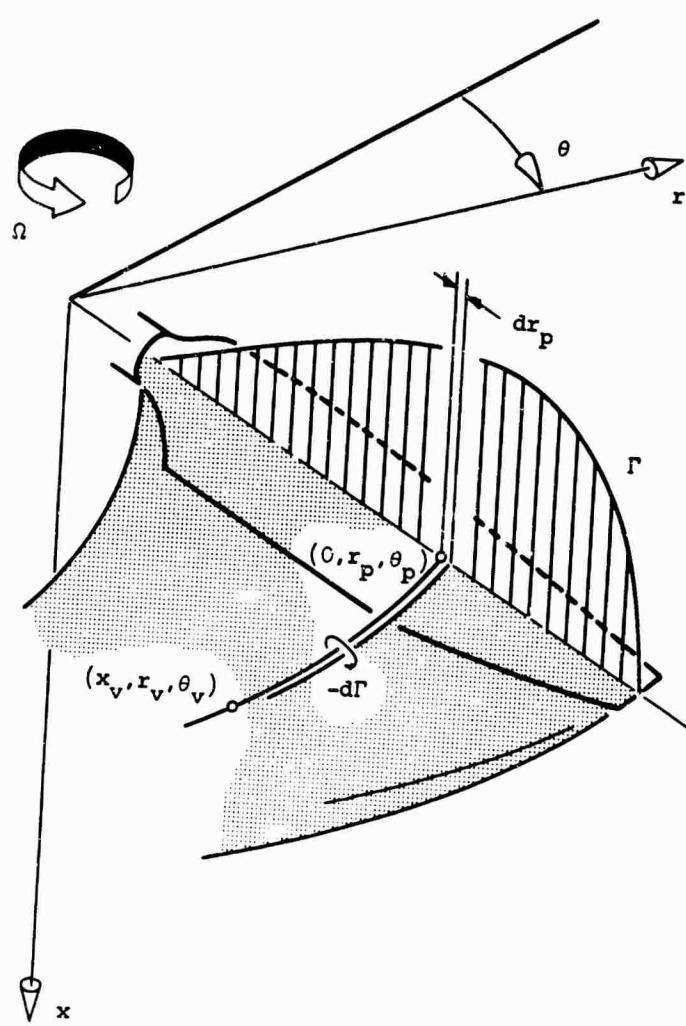
Figure 1. Propeller Coordinates and Vortex
Representation.

3

i.e., the $p = 1$ blade coincides with $\theta = 0$.

The induced velocity field is determined by integration of the Biot-Savart law over all the vortex elements and may be expressed in the form

$$u = \sum_{p=1}^{N} \int_{R_h}^{R_p} \left[\Gamma(r_p)\, \mathcal{U}_B - \frac{d\Gamma(r_p)}{dr_p}\, \mathcal{U}_T \right] dr_p \tag{2}$$

$$v = \sum_{p=1}^{N} \int_{R_h}^{R_p} \left[\Gamma(r_p)\, \mathcal{V}_B - \frac{d\Gamma(r_p)}{dr_p}\, \mathcal{V}_T \right] dr_p \tag{3}$$

$$w = \sum_{p=1}^{N} \int_{R_h}^{R_p} \left[\Gamma(r_p)\, \mathcal{W}_B - \frac{d\Gamma(r_p)}{dr_p}\, \mathcal{W}_T \right] dr_p \tag{4}$$

where u, v, w are respectively the axial, radial and tangential components of the velocity induced at a field point (x, r, θ) and are taken positive in the positive x-, r- and θ-directions; R_h is the radius of the propeller hub; R_p is the radius of the propeller tip; Γ is the strength of the bound blade circulation at $(0, r_p, \theta_p)$; $-d\Gamma$ is the strength of the vortex sheet element trailing from $(0, r_p, \theta_p)$; r_p is the radial variable of integration along the pth blade; $\mathcal{U}_B, \mathcal{V}_B, \mathcal{W}_B$ are respectively the influence functions for the axial, radial and tangential components of the velocity induced at (x, r, θ) by a bound radial vortex element of unit strength and unit length at $(0, r_p, \theta_p)$; and $\mathcal{U}_T, \mathcal{V}_T, \mathcal{W}_T$ are respectively the influence functions for the axial, radial and tangential components of the velocity induced at (x, r, θ) by an arbitrarily deformed vortex sheet element of unit strength and semi-infinite length trailing from $(0, r_p, \theta_p)$. The influence functions can be derived from first principles[6] or obtained from previous results[7] and are summarized in Table 1 . In the trailing functions, (x_v, r_v, θ_v) are the corresponding axial, radial and angular coordinates of any point along the vortex sheet element; u_v, v_v, w_v are the values of u, v, w at (x_v, r_v, θ_v) ; and t is a time parameter described below.

The contribution to the induced velocity from the bound vortices is easy to calculate and is identically zero, in particular, when the field point coincides with the lifting line. The contribution to the induced velocity from the trailing vortex sheets, on the other hand, is much harder. Not only do the associated influence functions require an integration over the semi-infinite length of the elements, but what is worse, their locations or "trajectories" are not fixed. Rather, they must drift force free by aligning themselves with the streamlines of the flow, which in general differential form[6] are

4

TABLE 1

SUMMARY OF INFLUENCE FUNCTIONS

$$\mathcal{U}_B = -r\sin(\theta_p-\theta)/4\pi D_B^3$$

$$D_B \equiv [r_p^2 + r^2 - 2r_p r\cos(\theta_p-\theta) + x^2]^{\frac{1}{2}}$$

$$\mathcal{V}_B = x\sin(\theta_p-\theta)/4\pi D_B^3$$

$$D_T \equiv [r_v^2 + r^2 - 2r_v r\cos(\theta_v-\theta) + (x_v-x)^2]^{\frac{1}{2}}$$

$$\mathcal{W}_B = -x\cos(\theta_p-\theta)/4\pi D_B^3$$

$$\mathcal{U}_T = \int_0^\infty \frac{-v_v r\sin(\theta_v-\theta) + (\Omega r_v+w_v)[r_v-r\cos(\theta_v-\theta)]}{4\pi D_T^3}\, dt$$

$$\mathcal{V}_T = \int_0^\infty \frac{u_v r_v\sin(\theta_v-\theta) - v_v(x_v-x)\sin(\theta_v-\theta) - (\Omega r_v+w_v)(x_v-x)\cos(\theta_v-\theta)}{4\pi D_T^3}\, dt$$

$$\mathcal{W}_T = \int_0^\infty \frac{-u_v[r_v\cos(\theta_v-\theta)-r] + v_v(x_v-x)\cos(\theta_v-\theta) - (\Omega r_v+w_v)(x_v-x)\sin(\theta_v-\theta)}{4\pi D_T^3}\, dt$$

5

$$\frac{dx}{u} = \frac{dr}{v} = \frac{d\theta}{\Omega+(w/r)} \qquad (5)$$

These equations can be integrated in terms of the parametric time t that it takes a fluid particle to move along this trajectory, giving

$$x_v = \int_0^t u_v \, d\tau \qquad (6)$$

$$r_v = r_p + \int_0^t v_v \, d\tau \qquad (7)$$

$$\theta_v = \theta_p + \Omega t + \int_0^t (w_v/r_v) \, d\tau \qquad (8)$$

For convenience, Eqs. (2) to (4), together with the auxiliary relations of Eqs. (6) to (8), may be expressed as

$$u = \mathcal{O}_u(\Gamma, -d\Gamma/dr; \ u,v,w) \qquad (9)$$

$$v = \mathcal{O}_v(\Gamma, -d\Gamma/dr; \ u,v,w) \qquad (10)$$

$$w = \mathcal{O}_w(\Gamma, -d\Gamma/dr; \ u,v,w) \qquad (11)$$

where $\mathcal{O}_u, \mathcal{O}_v, \mathcal{O}_w$ are respectively the Biot-Savart operators for the axial, radial and tangential induced velocity components. Another equation is re-quired to relate the circulation strength and velocity field through the pro-peller geometry. The force and velocity diagram for a typical section of the blade at the radial station $(0,r_p,\theta_p)$ is shown in Fig. 2, where W_p is the total local velocity seen by the blade section; u_p,v_p,w_p are respectively the local axial, radial and tangential inflow, i.e. those components of the in-duced velocity at $(0,r_p,\theta_p)$; α is the local blade angle of attack; β is the local blade pitch setting; ϕ_p is the angle between Ωr_p and W_p ; γ is the tangent angle of the sectional lift-drag polar; and dD and dL are re-spectively the elemental profile drag and lift on the blade section. From the definition of the sectional lift coefficient in terms of the density ρ and the local blade chord b , namely

$$c_L \equiv 2(dL/dr_p)/\rho W_p^2 \, b \qquad (12)$$

the Kutta-Joukowski formula can be written as

6

$$\Gamma \approx b \, W_p \, C_L / 2 \qquad (13)$$

where the lift coefficient is assumed known[8,9] as a function of α for a given section at approximately the local Mach and Reynolds numbers. Eqs. (9), (10), (11) and (13) are our complete set of equations.
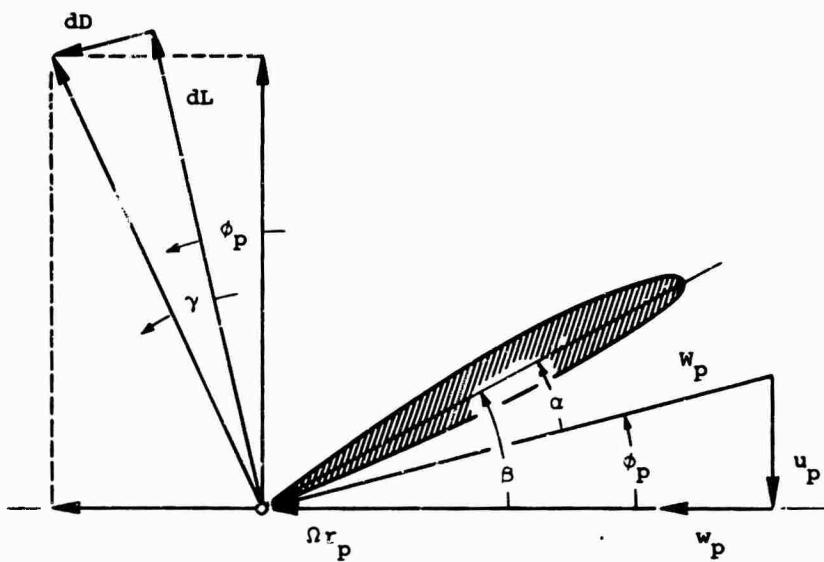
Figure 2. Velocity and Force Diagram at Typical Section.

Once the inflow and circulation have been found, the prediction of the overall performance can be computed. In particular, if we resolve the resultant of dL and dD as indicated by the dotted lines in Fig. 2 and integrate, the total thrust T and power P in nondimensional form are

$$c_T = \frac{\pi^2 N}{8} \int_{R_h / R_p}^{1} c_L \, \frac{\cos(\phi_p + \gamma)}{\cos \gamma} \left(\frac{W_p}{\Omega R_p} \right)^2 \frac{b}{R_p} \, d\left(\frac{r_p}{R_p} \right) \qquad (14)$$

$$c_P = \frac{\pi^3 N}{8} \int_{R_h / R_p}^{1} c_L \, \frac{\sin(\phi_p + \gamma)}{\cos \gamma} \left(\frac{W_p}{\Omega R_p} \right)^2 \frac{b}{R_p} \frac{r_p}{R_p} \, d\left(\frac{r_p}{R_p} \right) \qquad (15)$$

where the thrust and power coefficients of the propeller are defined by

7

$$c_T \equiv \pi^2 T / 4 \rho \Omega^2 R_p^{\ 4} = T / \rho n^2 D_p^{\ 4} \tag{16}$$

$$c_P \equiv \pi^3 P / 4 \rho \Omega^3 R_p^{\ 5} = P / \rho n^3 D_p^{\ 5} \tag{17}$$

respectively, with $\Omega = 2\pi n$ and $R_p = D_p/2$. From the thrust and power coefficients we can calculate the figure of merit F/M , given in percent, by

$$F/M \equiv 100 \sqrt{2c_T^{\ 3} / \pi c_p^{\ 2}} = 79.8 \ c_T^{\ 3/2} / c_p \tag{18}$$

As we have implied by the form of Eqs. (16) and (17), the characteristic length is R_p , the characteristic velocity ΩR_p and the characteristic density ρ . If the equations are nondimensionalized with respect to these quantities, complete similiarity exists with the exception of the sectional lift and drag data which in general must include the effects of Mach number and Reynolds number, as noted earlier.

Outline of Solution

The set of equations described above can only be solved by numerical techniques and iteration is the approach which we have chosen.

First, we rewrite Eqs. (9) to (11) in a different, but equivalent, form, namely

$$u = u - K_u[u - \mathcal{O}_u(\Gamma, \ \dots \ )] \tag{19}$$

$$v = v - K_v[v - \mathcal{O}_v(\Gamma, \ \dots \ )] \tag{20}$$

$$w = w - K_w[w - \mathcal{O}_w(\Gamma, \ \dots \ )] \tag{21}$$

where K_u, K_v, K_w are respectively the iteration factors for the axial, radial and tangential components of the induced velocity field. They are chosen as necessary to achieve convergence and may be constant or depend on any of the variables of the problem.

Iteration begins, then, by finding a zeroth, or initial, approximation to the inflow and so the blade circulation through Eq. (13), the Kutta-Joukowski formula. The first approximation to the inflow follows by operating with the Biot-Savart operators on the zeroth approximation to the blade circulation and some guess at the induced velocity field in the propeller wake. These results,

8

along with the iteration factors and the zeroth approximations to the inflow
and the wake velocity field, are in turn substituted into the right-hand sides
of Eqs. (19) to (21) to give the first approximations to the inflow and the
wake velocity field. The iteration continues by operating as before on the
first approximation to determine a second, and so forth. Once convergence
within a prescribed accuracy is reached, the propeller performance can be cal-
culated.

Rigorously, the iteration approach necessitates, at each step of the iter-
ation, calculation of the induced velocity field at a sufficient number of
points to define accurately the local streamlines in the propeller wake. Un-
fortunately, the number of calculations required is excessive. As a result,
we looked for some way which would reduce the number of calculations but still
satisfy the force-free condition of the wake, at least in an approximate sense.
Inasmuch as the development of a satisfactory approximation proceeded through-
out the investigation, we will defer the details until later.

Computer Program and Numerical Analysis

In order to carry out the iterative solution which we have outlined, a
general computer program was developed to evaluate the induced velocity field.
Once the inflow at the propeller was established, the resulting predictions of
the overall performance were found by means of a modification of the integra-
tion method of the existing C-W strip analysis[9].

The computer program was written in FORTRAN 63 for the CDC 1604 computer.
To achieve flexibility, most of the principal operations were relegated to
subroutines. The numerical analysis which these subroutines implement is given
below and consists of representation of the bound blade circulation distribu-
tion and the computation of the velocity components induced by the bound blade
vortices and trailing vortex sheets.

The blade circulation distribution Γ is generally tabulated numerically
at several radial stations, but for certain integrations we need Γ in analyt-
ic form. A suitable representation[5] is a Glauert-type series

$$\Gamma = \Omega R_p^2 \sum_{\ell=1}^{\mathscr{L}'} G_\ell \sin \ell \vartheta_p \tag{22}$$

$$r_p \equiv \tfrac{1}{2}(R_p + R_h) - \tfrac{1}{2}(R_p - R_h) \cos \vartheta_p \tag{23}$$

where G_ℓ is the ℓth nondimensional Glauert coefficient; and ϑ_p is the
Glauert variable which runs from 0 to π between the hub and tip. There are
various ways that the Glauert coefficients can be evaluated. We used the

9

method of least squares, which minimizes the error at the specified data points. The program provides for the numerical values of Γ to be given at up to 30 points, with $\mathscr{L}$ as high as 20 . Usually $\mathscr{L}$ = 15 was adequate. For a fairly smooth circulation, the worst error at any point was on the order of 1%, and for an irregular shape, about twice as great.

The computation of the contribution of the bound blade vortices to the induced velocity is relatively simple and proceeds as follows. Values of the influence functions are calculated at the radial stations for which Γ is tabulated. These values are multiplied by the corresponding values of Γ to give a set of values for the integrands. Values of the integrand not contained in this set are found as necessary by 3-point Lagrangian interpolation. The integration itself then is carried out to a prescribed accuracy over the radial variable by a generalized Gaussian scheme[5] devised by A. L. Kaskel at TAR. The accuracy used was ± 0.00005 of the tip rotational speed which required the weighting of the integrand at about 30 to 50 points.

As pointed out earlier, the computation of the velocity induced by the trailing vortex sheets is much more complicated, principally due to the wake deformation. Since most of the deformation occurs just behind the propeller, however, integration of Eqs. (6) to (8) is necessary for only a distance of a blade radius or so. Further downstream the trajectories may be approximated as regular helices with suitable pitch. To carry out the trajectory integrations, a prescribed velocity field along the trailing vortex sheets has to be stored in the computer as input data. Though the real flow field is not axisymmetric, we can in effect imagine that it is[5] and store the velocity field at a number of values of x and r . A 3-point Lagrangian interpolation, first in r and then in x , is carried out for other values in between. At each of 15 radial stations, we took 20 axial stations between the propeller plane, or slightly upstream when necessary, and some distance downstream. With the velocity field stored, the trajectory can be evaluated in a step-by-step marching scheme using a 2-term constant slope method[5]. Simultaneously, it is convenient to perform the integration over t for evaluation of the trailing influence functions, see Table 1. The integrands are calculated at each new location in the march and integrated by Simpson's rule. Assessment of this scheme was made by calculation of an example for which the trajectory was known exactly. Agreement was excellent. In addition, a number of tests on actual trajectories were made with different values of the marching time increment Δt . It was found that the size of Δt was more critical for the integration of the influence functions to a desired accuracy than for the trajectory itself. We selected $\Omega \Delta t = 0.008$ for the first 58 steps and $\Omega \Delta t = 0.104$ for the remaining steps, about 100 to 200, until the time is reached at which all of the trajectories have become helical. At this time, the march is stopped and the contributions of the helical portions to the influence functions are found from the calculation of their θ-average. These θ-average contributions can be extracted from

10

the results of theory of the Generalized Actuator Disk[10] and involve simply the evaluation of some well-defined functions. The details are given in Ref. 5.

When the calculation of the influence functions is complete, we proceed to the integrations of the second terms of Eqs. (2) to (4). Unfortunately, the singularities of the integrand complicate the picture. The square-root behavior inherent in Eq. (22) makes the strength of the elements of the trailing vortex sheets infinite at the hub and the tip, but this is no problem if we carry out the integrations in terms of the Glauert variable. A real difficulty is the existence of singularities which arise in the influence functions when the field point coincides with an element of the trailing vortex system. In particular, at the lifting line itself the singularities are not integrable for a nonzero value of the radial inflow. We handled this difficulty by making two artificial, regular helical steps in the marching scheme before the trailing elements deform in the desired fashion. Since Δt is taken very small, the displacement from the lifting line is infinitesimal compared to the blade chord and is unimportant. Two types of singularities[11], Cauchy and logarithmic, are left. To integrate over these singularities, we sum the influence functions over all the blades and break the results into "singular" and "regular" parts. If we define

$$
S_u \equiv \frac{\Omega r + w}{4\pi [u^2 + (\Omega r + w)^2]^{\frac{1}{2}}} \frac{1}{r_p - r} - \frac{(\Omega r + w)^3}{8\pi r [u^2 + (\Omega r + w)^2]^{\frac{3}{2}}} \ln \left| \frac{r_p - r}{R_p} \right| \tag{24}
$$

$$
S_v \equiv 0 \tag{25}
$$

$$
S_w \equiv - \frac{u}{\Omega r + w} S_u \tag{26}
$$

where u and w are the inflow at r from the previous approximation, these singular parts can be integrated analytically in the usual principal value sense and the regular parts can be integrated by the generalized Gaussian scheme mentioned previously. If the induced velocity off the blades and trailing vortex sheets is desired, the contribution from the trailing vortex sheets has no singular part, and so integration proceeds exactly as for the regular part. The computer program can accommodate up to 108 elements for the trailing vortex sheet from any blade. Generally, we made our runs with 45 to 60 elements, between 20 and 35 of which were taken in the immediate neighborhood of the singularities to obtain adequate definition of the regular parts. The accuracy specified for the Gaussian integration was again ± 0.00005 of the tip rotational speed and required the weighting of the integrand at 40 to 200 points.

The program was checked out by re-computing two cases from our earlier

11

studies[1-4] in which the elements of the trailing vortex sheets were assumed to be undeformed regular helices of both finite and infinite length. Excellent agreement was found in the intermediate steps as well as in the values of the inflow. A further check was made later when the program was applied to the computation of the induced velocity at a series of field points for two marine propellers. The trailing vortex sheets were again assumed to be composed of undeformed regular helices of infinite length. Our values agreed[12] with corresponding values calculated using the computer program developed by J. E. Kerwin[13].

Development of Wake Model and Results

As an initial wake hypothesis or approximation to the force-free condition of the wake, we assumed that the velocity components along the trailing vortex sheets at a constant radius varied in the same way, regardless of the blade circulation distribution and condition of operation. To find these variations, we normalized the corresponding θ-average velocity components from pp. 329 and 333 of Ref. 10 with respect to their values at the propeller plane, and with slight modifications, truncated the results at one and one-half radii downstream. Thus, the wake could be calculated completely in terms of the induced velocity at the blades.

Initial computations for the three-bladed C-W 3(109654) propeller[5] at $\Omega R_p = 1002$ fps and $\beta(0.7R_p) = 11.3°$ diverged with iteration factors of 1 , but factors of 1/2 gave a definitely convergent trend through three successive approximations. The predicted shape of the envelopes of the trajectories of the elements of the trailing vortex sheets were also physically reasonable in comparison with Canadair, Ltd. and C-W flow visualization results. However, comparison of the third approximation to the axial inflow with C-W measurements indicated that the theoretical values were on the order of 65% of the measured values over the mid-blade. The corresponding performance predictions were, for a given C_p , roughly 8% above the measured C_n , 6% above the measured $\beta(0.7R_p)$ and 12% above the measured F/M .

In order to test the initial wake hypothesis more thoroughly, we proceeded to computations for the three-bladed C-W 3(109652) propeller[5] at $\Omega R_p = 785$ fps and $\beta(0.7R_p) = 10.0°, 14.0°, 16.0°$. Three successive approximations to the inflow were computed using iteration factors of 1/2 and the convergence was sufficient to justify comparison of the predictions with tests. Although the trajectory envelopes were again reasonable, comparison of the axial inflow for the 14.0° setting still showed that the theoretical values were about 75% of the C-W measured values over the mid-blade. Furthermore, the performance predictions, see Fig. 3, were unfavorable, the predictions being worst at the lowest pitch setting. What was most disturbing, not only was the shape of the F/M curve incorrect, see Fig. 3, but also the predicted variation of the

12
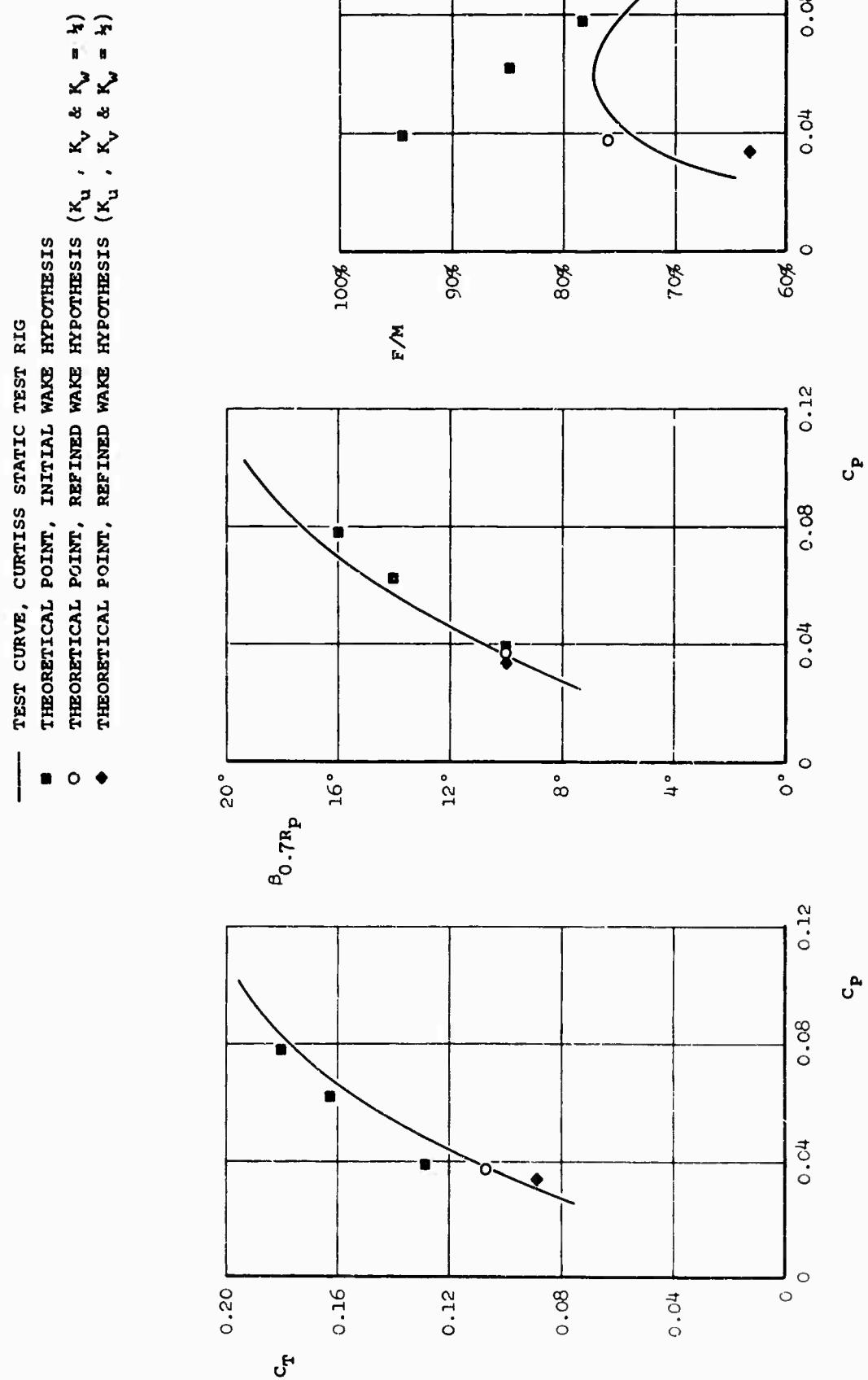
Figure 3. Comparison of Predicted and Measured Performance.

13

velocity components along the trailing vortex sheets did not agree with C-W wake measurements.

The major conclusion from the results for these two propellers was that the initial wake hypothesis was inadequate and required refinement. In particular, although the envelopes of the trajectories of the trailing vortex sheet elements were good, the effective "pitch" of the elements was not correct. A secondary conclusion was that iteration factors of 1/4 would have been better than 1/2 .

We based our refined wake hypothesis on the initial hypothesis, but with changes made specifically to overcome the deficiencies revealed in the comparisons with tests. This refined wake hypothesis or approximation to the force-free condition of the wake was identical to the initial hypothesis inboard of the 0.5 radial station. However, outboard, the variation of the axial induced velocity component from Ref. 10 was applied along streamlines rather than along constant radii. The variation of the radial induced velocity component was then fixed by assuming that both the initial and refined wake hypotheses should give the same trajectory envelopes. For the tangential component the refined hypothesis was assumed identical with the initial hypothesis, since w is small compared to Ωr anyway.

As an initial test of the refined wake hypothesis, we chose to re-compute the third approximation to the 3(109652) propeller at the 10.0° setting. In Fig. 4 the third approximations to the inflow components are plotted for the initial and refined wake hypotheses. The large differences are clarified by Fig. 5 which shows the projections for the respective trajectories of the tip element of one vortex sheet. For the refined hypothesis, we see that the effective "pitch" is much lower, and so, the axial and radial inflow much larger. The velocity variation along the trailing vortex sheets is found to be qualitatively correct as well, and the performance predictions included in Fig. 3 for iteration factors of both 1/4 and 1/2 are encouraging. Study indicates that the refinement would also improve the performance prediction at the higher pitch settings.

To continue testing the refined wake hypothesis, we performed computations for the three-bladed C-W 3(13168A10P3) propeller[5] at $\Omega R_p = 750$ fps and $\beta(0.7R_p) = 14.0°$. Three successive approximations to the inflow were computed using iteration factors of 1/4 . The axial inflow changed smoothly from step to step. Inboard near the hub and outboard of the 0.8 radial station the iteration converged. Over the mid-blade the convergence trend, distinctly different from our previous iterations, was inconclusive as far as the iteration was carried out. Still, the trajectory envelopes were good and comparison of the third approximation to the axial inflow with C-W measured values showed reasonable agreement in overall magnitude, but some difference in shape. Comparisons of the performance predictions with the test data are excellent. The predictions generally improved with each step in the iteration, moving monotonically

14
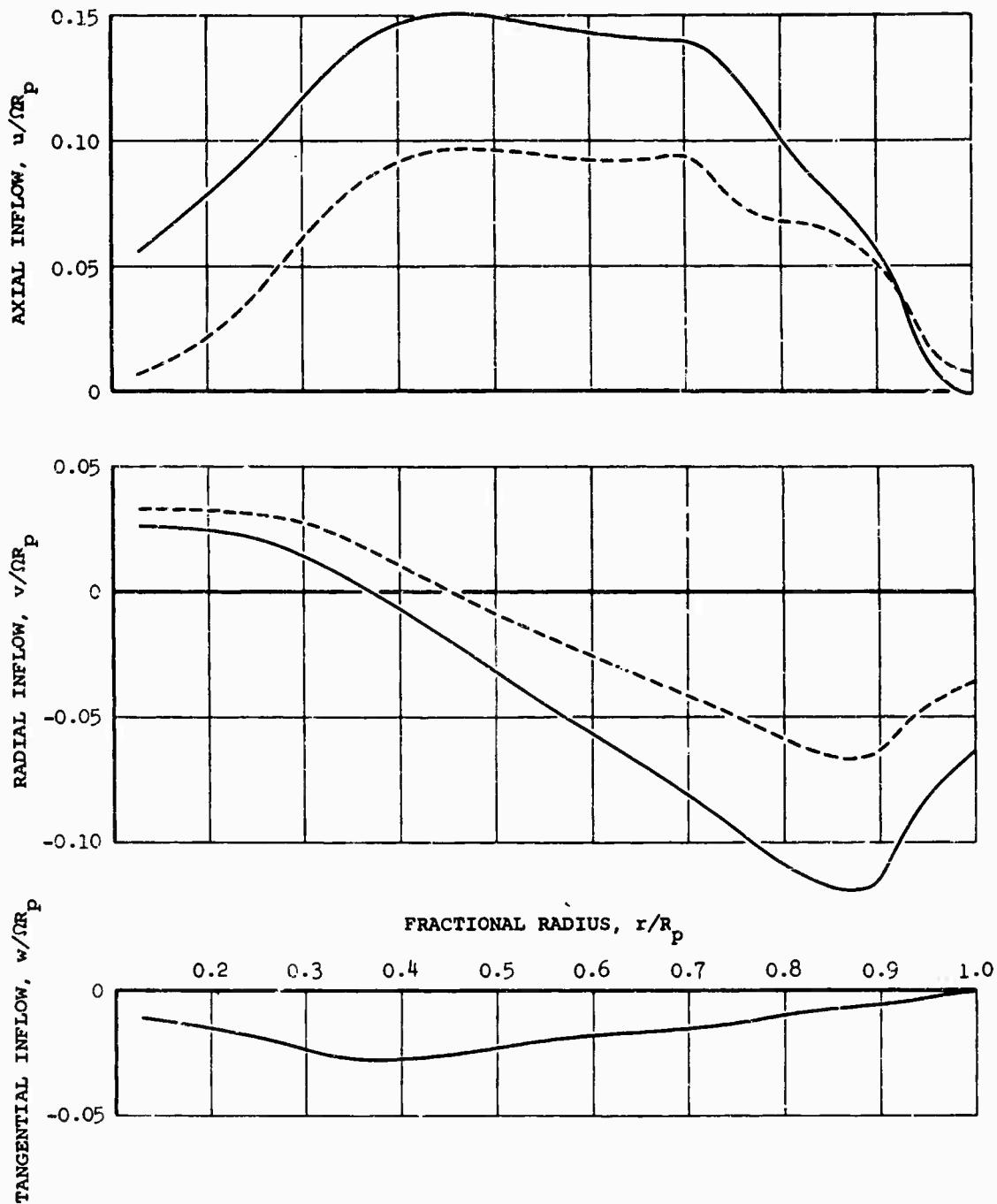
Figure 4. Inflow Components for Initial (--) and
Refined (——) Wake Hypotheses,
3(109652) Propeller, $\beta_{0.7R_p}$ = 10.0° .
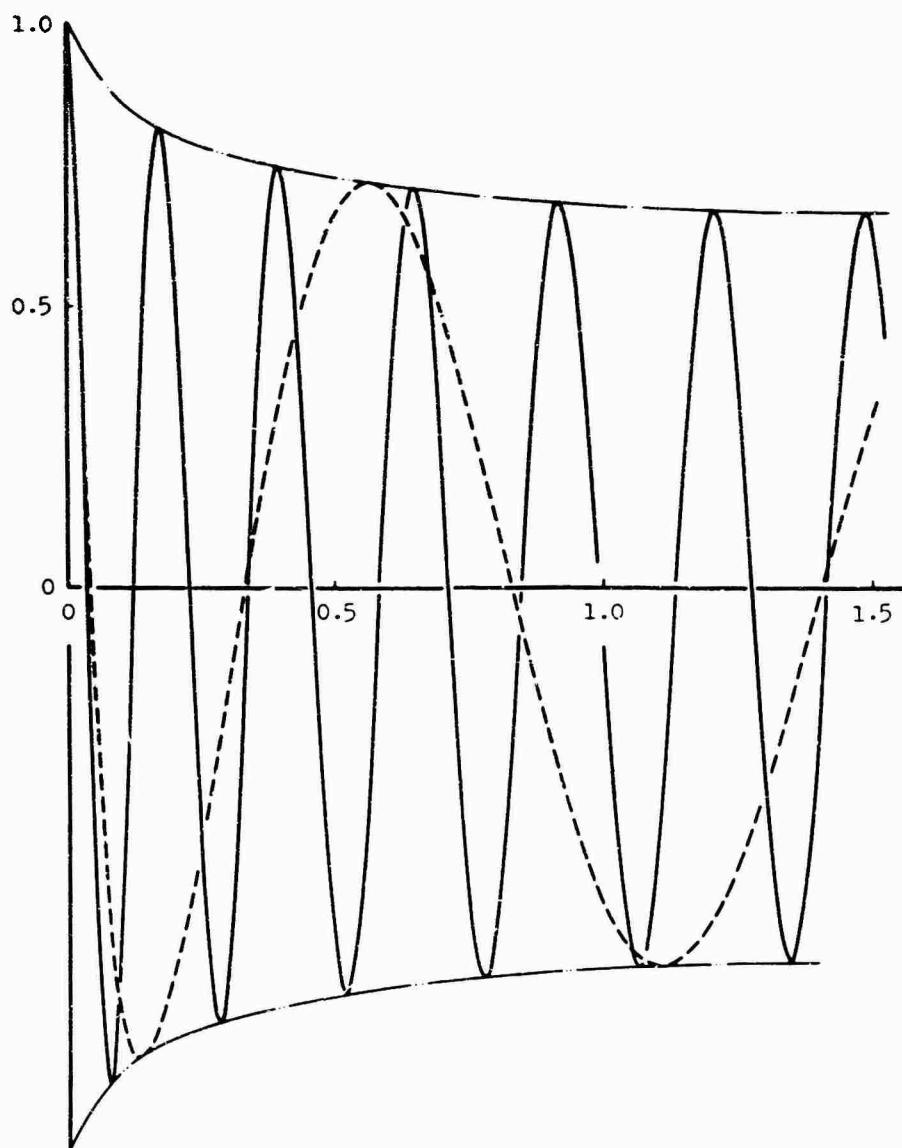
Figure 5. Trajectory Projection of Vortex Sheet
Element from Tip. Initial (--) and
Refined (—) Wake Hypotheses,
3(109652) Propeller, $\beta_{0.7R_p} = 10.0°$.

16

from the zeroth approximation to the third approximation. For the third approximation the performance predictions were, for a given C_p , roughly 1% above the measured C_T , 2% below the measured $\beta 0.7R_p)$ and 2% above the measured F/M .

TABLE 2

SUMMARY OF PERFORMANCE COMPARISONS

Propeller	C_p	Theory			Curtiss Test		
		C_T	$\beta_{0.7R_p}$	F/M	C_T	$\beta_{0.7R_p}$	F/M
3(1C9654)[*]	0.0477	0.141	11.3°	88.5%	0.131	10.7°	79.2%
3(1C9652)[**]	0.0370	0.107	10.0°	75.5%	0.105	10.2°	73.6%
3(13168A1CP3)[***]	0.0576	0.140	14.0°	72.6%	0.138	14.3°	71.3%

[*]   - Third Approximation, Initial Wake Hypothesis

[**] - First Approximation, Refined Wake Hypothesis

[***] - Third Approximation, Refined Wake Hypothesis

In Table 2 we have summarized the performance comparisons to date for all three propellers.

Conclusions

From the results obtained in this study, we are able to draw the following conclusions:

A model based on continuous deformation of the wake is necessary to calculate the inflow, and so the performance, of a V/STOL propeller at the static condition. Both the envelopes of the trajectories of the elements of the trailing vortex sheets and the "pitch" of these elements must be predicted accurately.

An initial wake hypothesis, or approximation to the force-free condition of the wake, gives a reasonable prediction of the trajectory envelopes, but an inadequate prediction of the "pitch". However, a refined wake hypothesis

appears to give an adequate prediction of both the envelopes and the "pitch".

While the performance predictions for one propeller using the refined wake hypothesis are excellent, further approximations in the iteration procedure, as well as predictions at other pitch settings and for other propellers, are required. Comparison should also be made between the wake velocities used in the refined wake hypothesis and those found both by actual calculations and test measurements.

Acknowledgements

References

1. Ordway, D. E., and Erickson, J. C., Jr., *A New Approach to the Static Thrust Problem, Phase I, Formulation and Preliminary Assessment of Mathematical Model*, THERM, Incorporated, TAR-TR 631, March 1963.

2. Erickson, J. C., Jr., and Ordway, D. E., *A New Approach to the Static Thrust Problem, Phase II, Calculation of Thrust and Torque, Model X-100 Propeller*, $\beta_{0.7R_p} = 10.0°$, THERM, Incorporated, TAR-TR 632, May 1963.

3. Erickson, J. C., Jr., and Ordway, D. E., *A New Approach to the Static Thrust Problem, Phase III, Further Inflow Calculations with Extensions to Partially Negative Γ Distributions*, THERM, Incorporated, TAR-TR 635, August 1963.

4. Erickson, J. C., Jr., and Ordway, D. E., *A New Approach to the Static Thrust Problem, Phase IV, Further Development of Performance Calculation Method*, THERM, Incorporated, TAR-TR 638, December 1963.

5. Erickson, J. C., Jr., Ladden, R. M., Borst, H. V., and Ordway, D. E., *A Theory for VTOL Propeller Operation in a Static Condition*, U. S. Army Aviation Materiel Laboratories, Technical Report 65-69, October 1965; AD623527.

6. Sears, W. R., *Theoretical Aerodynamics, Part 1: Introduction to Theoretical Hydrodynamics*, 1957 Edition, Ithaca, New York, 1957.

7. Ordway, D. E., Sluyter, M. M., and Sonnerup, B. U. O., *Three-Dimensional Theory of Ducted Propellers*, THERM, Incorporated, TAR-TR 602, August 1960.

8. Enos, L. H., and Borst, H. V., *Propeller Performance Analysis Aerodynamic Characteristics, NACA 16 Series Airfoils*, Report No. C-2000, Curtiss-Wright Corp., Propeller Div., Caldwell, N. J., December 2, 1948.

9. Foss, R. L., *Strip Analysis Method for Evaluating Static Thrust*, Report No. C-2402, Curtiss-Wright Corp., Propeller Div., Caldwell, N. J., November 19, 1952.

10. Hough, G. R., and Ordway, D. E., *The Generalized Actuator Disk*, Developments in Theoretical and Applied Mechanics, Volume II, Proceedings of the Second Southeastern Conference on Theoretical and Applied Mechanics, Pergamon Press, 1965, pp. 317-336.

11. Ordway, D. E., and Greenberg, M. D., *General Harmonic Solutions for the Ducted Propeller*, THERM, Incorporated, TAR-TR 613, August 1961.

12. McCarthy, J. H., Denny, S. B., and Kuo, C., *Comparison of Theoretical Values of Propeller-Induced Vibratory Pressures with Values Measured in a Water Tunnel and on Full-Scale and Model Ships*, Paper presented at "Workshop on Fluctuating Propeller Forces", David Taylor Model Basin, 21 and 22 April 1966.

13. Kerwin, J. E., and Leopold, R., *A Design Theory for Subcavitating Propellers*, Transactions of the Society of Naval Architects and Marine Engineers, Vol. 72, 1964, pp. 294-335.

NOTES

PROPELLER TESTING AT ZERO VELOCITY

by

H. V. BORST   R. M. LADDEN

Curtiss-Wright Corporation
Wood-Ridge, New Jersey,   USA

SUMMARY

The hover performance of the propeller installed on current V/STOL
aircraft has been below expectation because it has not been possible to design
an optimum blade due to the lack of an accurate propeller theory at zero air-
speed. It is necessary to have an accurate theory for predicting performance
so that a series of blades can be evaluated at the hover condition to find
the configuration for peak efficiency. When developing a theory for calcu-
lating performance, a good experimental base is required so that the accuracy
of the theories can be checked.

A review of the available test facilities indicated a new test rig
was required for testing full scale propellers. As a result, a new test rig
was built and put in operation. Special equipment was also obtained for
measuring the conditions in the wake of propellers operating at hover in order
that data would be provided for the development of an adequate theory. The
results of tests of several propellers with varying geometry are presented
along with the available wake survey data.

INTRODUCTION

The level of performance achieved by propellers operating at zero
velocity is of relatively little importance with conventional aircraft, as
the take-off distance is determined mainly by the level of thrust at approxi-
mately 75% of the take-off velocity. With the use of propellers on VTOL

aircraft to obtain direct lift, the level of performance obtained directly influences payload range characteristics of the VTOl aircraft. For instance, an improvement of 1% in propeller performance can result in an increase of as much as 3 to 5% in the payload of the aircraft. Thus, it is imperative that the characteristics of the propeller be optimized so that best configuration and performance is obtained.

Because propellers have been in use for many years, it was believed that the desired optimization could be easily obtained. Unfortunately, the propellers on all V/STOL aircraft have operated at levels of thrust below the optimum level that could be expected. As a result, the performance of these aircraft is disappointing and it is, therefore, necessary to find methods of improving the propellers to obtain the desired performance.

At the conventional forward flight conditions, considerable testing has been accomplished on both model and full scale propellers. The testing was done for a wide range of propeller rotational speed, forward velocity, blade and power loading, and blade configurations. Special two dimensional airfoil data were also obtained, covering a wide range of geometry variables, as well as a wide range of Mach number and angle of attack. As a result of this testing, an adequate base was established that made it possible to confirm theoretical methods of calculating the flight performance of propellers. The vortex theory of propellers developed by Theodorsen and Goldstein, [1 and 2] proved to have a satisfactory accuracy for correcting the two dimensional airfoil data; thus allowing the overall performance of propellers to be determined by calculation. Because the performance of propellers could be accurately determined from two dimensional airfoil data by analyzing each section along the blade, it became possible to design an optimum propeller for any given flight condition.[3] Tests of such designs have confirmed the calculations and, as a result, all modern propellers have been designed with this technique.

When the available data on propellers operating at the hover condition were examined it became apparent that a satisfactory experimental base,

2

similar to that available at the flight conditions, did not exist. This was especially true for propellers operating at loadings for peak hover perform- ance, for such conditions were generally at lower power conditions than was of interest with conventional propellers. Since the theory of propeilers de- veloped for the forward speed flight conditions breaks down at the hover con- dition, it was necessary to establish an experimental base for checking new theoretical methods, and provide an understanding of the flow conditions for developing such a theory. Only with adequate theoretical procedure can the performance be accurately calculated at the hover condition, for the experi- mental cut and try methods are expensive and not practical.

Once accurate theoretical methods have been developed for calculating the performance of propellers at the static condition, it will be possible to optimize the blade to obtain peak hover performance for any given diameter, blade number, RPM and power by using a procedure[3] similar to that developed for flight. This ability to optimize a design for hover as well as for the flight condition will make it possible to select the best overall blade characteristics for the entire range of flight conditions, and in doing so, will obtain the optimum overall propeller design. The key for improved pro- pellers for VTOL aircraft is to develop an accurate theory of propellers for the hover operating condition, and this can only be done if an adequate ex- perimental base is available. The work done so far in developing the required data is presented in this paper.

SYMBOLS

AF   blade activity factor, $\dfrac{100,000}{16} \displaystyle\int_{.2}^{1.0} \left(\dfrac{b}{d}\right)\left(\dfrac{r}{R}\right)^3 d\left(\dfrac{r}{R}\right)$

b   blade width ft.

C_{L_i} design section lift coefficient

C_p power coefficient $\dfrac{P}{\rho n^3 D^5}$

C_T thrust coefficient $\dfrac{T}{\rho n^2 D^4}$

D   propeller diameter, ft.

h   blade section maximum thickness, ft.

n   propeller rotational speed, rps

R   propeller radius, ft.

r   propeller radius, ft. at a station

T   thrust, lb.

ρ air density, slugs/cu. ft.

TEST EQUIPMENT

The equipment necessary for determining the propeller performance at the static condition is made up of a power source, suitably mounted, and the necessary instrumentation for measuring torque, thrust, rotational speed, and ambient air conditions. The power source must be capable of supplying torque above the design value of the propeller at a range of rotational speeds. The full scale and model test rigs available for conducting measurement at the static condition are discussed in this section, along with a discussion of the special equipment needed for measuring conditions in the wake.

Wright Field Whirl Rigs

The four whirl rigs at the Wright-Patterson Air Force Base are available to measure the performance of propellers at the static condition, and to run structural proof tests. Static thrust propeller calibration run on the Wright Field rigs has been accepted as the standard throughout the military services and the industry. Four rigs are available for running propellers and measuring thrust, torque and RPM. Their characteristics are:

Rig No.	Max. HP	Fig.	Remarks
1	10,000	-	7' Extension Shaft Available
2	3,500	-	3' Propeller Clearance
3	3,500	1	3' Propeller Clearance
4	30,000	2	15' Extension Shaft Available

4

The rigs have more than adequate power for testing any propeller envisioned in the future, especially those suitable for VTOL aircraft which must operate near peak efficiency.

Since the Wright Field test rigs were also designed to prove the structural integrity of the propellers, it was necessary to build a massive structure as shown in Figures 1 and 2 to take the loads generated in case of propeller failure. Because of this large mass which supports the motors, the measured propeller performance has often been questioned with regard to the effects of wake blockage. This blockage was thought to give a higher reading of thrust compared to that which would be measured in free air.

NACA Test Rig

In conjunction with the NASA 16 foot high speed wind tunnel, a test stand was built to use the 6000 HP wind tunnel propeller dynamometer as a power source to measure the thrust of propellers at the zero velocity condition.[4] The dynamometer had a small overall diameter and was mounted on the stand so as to duplicate free air conditions as nearly as possible. The area about the propeller was protected by walls so that the effects of external winds were effectively eliminated. Unfortunately, the need for accurate propeller performance data did not exist during the time the NACA static thrust rig was operational. Therefore, limited testing was accomplished with this rig, and what was accomplished, was done with propellers designed mainly for the wind tunnel test. When the need for high performance propellers became apparent, the NACA rig was no longer operational and the time and money required for putting the rig back in operating condition was considered to be excessive.

Model Test Rigs

Several test rigs were designed and built for measuring the performance of propellers at the static condition. The information gained was to fill the gap in propeller hover performance data. Canadair built a rig designed to eliminate blockage, and the rig is suitable for testing propellers

5

up to approximately 8 feet diameter.[5] This rig is powered by an automobile engine and some valuable data have been obtained including some excellent flow visualization pictures.

The dynamometer used to run 30" diameter model propellers in a wind tunnel was also set up to run these propellers at the static condition. The propellers from the X-19 and X-100 wind tunnel models in 18" diameter were also run as a model test rig. This model wind tunnel dynamometer was run outdoors under zero wind conditions, and was powered by small diameter variable frequency motors mounted so that the blockage aft of the propellers tested was effectively eliminated.

Curtiss-Wright Test Rig

To obtain further information on the flow conditions around the propeller, and to obtain full scale data with approximately zero blockage, a test rig was designed to measure static thrust. As shown in Figure 3, this rig was designed to eliminate blockage and be capable of measuring the performance of full scale propellers up to approximately 18 feet diameter. The rig is powered with an R3350 reciprocating engine of approximately 2500 HP and drives the propeller with an extended shaft which places the disk of the propeller approximately 18 feet ahead of the engine face.

Upstream of the engine the extension shaft is broken to include a Baldwin-Lima-Hamilton A-160 Torque Cell, Figure 4. Between this cell and the propeller disk, the shaft is again broken to contain a metal diaphragm. The purpose of the diaphragm is to preload the tapered roller bearings so as to eliminate unwanted deflections of the bearings as well as any thermal growth of the shaft. This isolates the thrust load at the strain gaged four-leg thrust ring which is located just aft of the propeller. The gauge installation is designed to be insensitive to changes of temperature caused by frictional energy.

6

Thrust, torque, propeller RPM, and wind velocity signals are read out on four channels of a DYMEC Digital Data Acquisition System. Thrust and torque signals taken from the thrust ring and the torque cell are scanned and printed on tape. Readout accuracy is on the order of 0.1 percent. The propeller RPM is measured with a magnetic pickup directly on the propeller shaft and is also printed out. Because of the effect of wind on the performance of a fixed pitch propeller operating at the static condition, wind velocity, as measured with a cup anemometer, was also monitored. The wind velocity was measured away from the wake produced by the test propeller, but close enough to sample the general ambient air conditions. Experience indicated that useful data was not obtained when the wind velocity exceeded 3 MPH with propellers operating at a fixed blade angle.

When the propeller is operating at a fixed blade angle, as was the case in these tests, any change in ambient wind conditions will change the angle of attack; and will also change the thrust and power conditions observed from the desired zero velocity conditions. Small changes in ambient velocity up to approximately 20 feet per second have little influence on the actual dynamic pressure seen by the blade, for the rotational speed is high compared with this level of wind velocity. If the propellers were tested with a constant speed control so that the blade angles were adjusted to compensate for changes of wind velocity, the effects of wind changes could be minimized. With a conventional type of propeller control incorporating the features of an integral and proportional control term, the change in RPM could be reduced by a factor of 5. This would extend the allowable spread in wind conditions at which testing could be accomplished, and it is recommended if extensive testing is to be done.

Although large changes in propeller performance are experienced, due to the effects of wind when testing on the static thrust stand with propellers operating at constant blade angle, these changes are not encountered in flight. Tests of the X-19 airplane have indicated that the integral plus proportional control used to maintain RPM, is also used to maintain thrust

7

and torque within close limits. This allows the aircraft to be flown in high ambient wind condition without difficulty.

The DYMEC system's output is in volts, making it necessary to calibrate the system. Although the strain gauges used to measure thrust are temperature compensated, the thrust ring is calibrated immedi.   ' before and after each run by use of a deadweight. The weight used is of t ; same order of magnitude as the thrust measured. Experience with the torque cell indicated that periodic calibrations were sufficient. These calibrations were done with levers and weights and required about one half day to complete.

Propellers Tested

Conventional propellers, as well as propellers designed for VTOL aircraft, were tested in their original configurations. They were further tested with modifications on the Curtiss-Wright test rig to provide basic performance data at the static condition. These propellers were also tested on other rigs to determine the effects of blockage and propeller size on the measured performance. The blades tested had a wide variety of characteristics in order to give a range for analysis. Table 1 shows the important characteristics of the propellers tested.

Wake Survey Instrumentation

The instrumentation used for determining conditions within the wake is the Lintronic Model 40W Linear Constant Temperature Hot-Film Anemometer. It is similar in principle to the hot-wire anemometer. In this case, a thin preheated platinum element, which is extremely sensitive to temperature differentials caused by variations in airflow, is fused to a Pyrex glass wedge. The hot-film anemometer is rugged and maintains stability in physical characteristics for extended periods of time, yielding good signal to noise ratio and very high frequency response. Most important, it has been designed to yield a linear variation of velocity with electrical signal so that a quick calibration at one point is sufficient. A complete description can be found in the operating manual.[6]

8

To measure the conditions in the wake, a test probe containing the hot-film wedge is mounted on a boom that can be positioned at any distance aft of the disk, and at any station along the blade radius as shown in Figure 9. By remote control, the probe can be rotated about its tip, and can also be rotated about its axis of symmetry. This enables the element of the probe to be positioned perpendicular to the resultant velocity vector, in much the same way a total pressure tap opening must be aligned to the flow to get a meaningful result.

The test procedure is as follows: The orientation of the probe is adjusted until maximum signal voltage is obtained. Then the space coordinates, in this case three angles, are recorded together with the highly damped probe voltage, to read an average value. An oscillograph records the unsteady portion of the velocity field. This procedure of maximizing the average velocity component, simplifies the test procedure, and considerably lessens the time required. It is not necessary to seek a maximum unsteady velocity, since measurements have indicated that the unsteady portion of the velocity is less than 10 percent of the resultant. Tests have also indicated that the average to peak velocity ratio does not vary with small excursions of the probe alignment.

METHOD OF DATA PRESENTATION

A propeller is generally run at a constant blade angle on the static test rig, and thrust and horsepower are measured as a function of rotational speed. These data are reduced to standard propeller coefficients C_T and C_p, and thus correct the data to standard day conditions. Since the efficiency of a propeller operating at zero flight speed is zero at hover, another definition is required to assess the relative merits of the various propeller configurations. As in the case of helicopters, the term "Figure of Merit" is used, as it is considered a good measure of the relative performance of propellers. The Figure of Merit is actually a measure of the adiabatic efficiency of the process of converting shaft power into thrust. In appendix A, the

9

Figure of Merit is derived in terms of standard propeller coefficients and is

$$FM = .707 \frac{C_T^{3/2}}{C_P}$$

When comparing the performance of propellers, the Figure of Merit is plotted as a function of power coefficient. Power is used rather than thrust coefficient as it is the input and determines the point where maximum efficiency is desired.

RESULTS

An evaluation of the existing test results indicated a new rig was needed to test propellers for V/STOL aircraft at the static condition. The data obtained with this rig are presented along with detailed flow measurements of the conditions in the wake.

Blockage Effects

The effects of the blockage produced by the body supporting the propeller shaft on the Wright Field 30,000 horsepower dynamometer was found by tests with the NAA static test rig.[4] The tests were conducted with a 10 foot diameter, three blade propeller on a half scale model of the 30,000 HP rig. This corresponds to a 20 foot diameter propeller on the full scale rig. Tests were made duplicating the case of the propeller operating close to the support and on an extended shaft. The results of these tests are shown in Figure 10, and they indicate that the Figure of Merit is approximately three percent higher than would be obtained in free air with the blockage produced on this rig. The use of an extended shaft to place the disk ahead of the test stand had only a small effect in reducing the blockage effects.

As the blockage effects should be proportional to the relative frontal area of the propeller and the afterbody, it could be expected that even higher changes would be obtained when propellers less than 20 feet are tested. Unfortunately, there are no data available to support this conclusion.

10

Testing of identical propellers at the Wright Field rigs, and on the Curtiss-Wright test rigs further supported the results obtained on the NAA rig. Figure 11 shows an apparent increase in Figure of Merit of the same order of magnitude as was measured on the simulated NAA rig.

Size Effect

To determine the effects of size or Reynolds number, propellers with blades identical except for size were tested and Figures of Merit were plotted in Figures 12 and 13. For the propeller with 109652 blade, the Figure of Merit increases from 12 to 14 points (when operating near peak efficiency) as the diameter is increased for 2' 6" to 15'0". Comparisons of performance with 1'6", 5'0", and 13'0" diameter propellers with identical blades show smaller scale effects, the maximum being 4 to 5 points in Figure of Merit, shown in Figure 13. This propeller, with 13168A10P3, is not operating as efficiently as the previous propeller configuration with 109652 blades, and this may influence the results.

From the above tests it is apparent that Reynolds number and size are important parameters influencing performance at the static or hover condition. The Reynolds number influences the profile drag losses produced by the blades. If the induced losses were known, correction due to Reynolds number could be generated from data such as shown in Figures 12 and 13. However, these losses cannot be calculated as yet, and the model propeller data is currently worthless for predicting performance of the full scale propeller.

Blade Planform

The effects of changes in planform on the overall performance at the static condition were obtained from tests of the 10188A2P2, the 13168A10P3 and 136148A2P3 blades. These blades are nearly identical except for planform as a result of changes in tip width. Figure 8 shows the 10188A2P2 and 13168A10P3 could effectively be built by cutting off the tip of the 136148A2P3 blade.

11

The performance comparison at a tip speed of 650 feet per second, Figure 14, indicates that loading changes due to changes in tip shape can have a large effect on overall performance. Note too, that the peak performance is obtained at lower values of power with the blades which have the lower activity factor or smallest tip width.

Blade Angle Distribution

The effects of a reduction in blade angle at the tip of a propeller, which had tested at a high level of Figure of Merit at the static condition, were determined by retwisting the 109652 blade as shown in Figure 5. The blade twist was reduced as previous tests with other blades had indicated a reduction in performance by an increase in blade angle or loading at the tip. The performance of propeller with the retwisted blades, Figure 15, showed a loss of 1.5 points of peak Figure of Merit over the original. The two propellers have approximately the same performance at loading above that for peak efficiency, indicating that the performance at peak efficiency is very sensitive to blade loading.

Blade Number

Three and four blade propellers were run using 109652 blades to determine the effects of changing blade number, Figure 16. Peak efficiency of the four blade propeller occurs at a power coefficient approximately 50 percent higher than that of the three blade propeller. This indicates a better power absorption characteristic with the four blade propeller. Further, the peak Figure of Merit of the four blade propeller is at least a half a point above that produced by three blades. This small increase in Figure of Merit was less than would be expected (based on propeller characteristics at forward velocity flight condition).

Detailed Wake Data

In addition to the requirement of gross performance measurements, detailed information is needed to establish the position and strength of the

propeller wake. With this information it is possible to both set up the initial position of the shed vortices, and to check the methods of calculating the inflow.

Accurate propeller wake surveys are difficult to obtain since the direction of the flow velocity vector must be found. Also, instrumentation capable of measuring rapid variations of velocity with time, must be available, as the flow is rapidly varying in space fixed coordinates. This requires a very short response time.

Using the hot-film wake survey equipment as described previously, measurements were made aft of three blade propellers with 109652 and 13168A10P3 blades. The data were taken 10 inches aft of the propeller using 109652 blades when operating at a tip speed of 785 fps and a power coefficient of 0.0605, Figure 17. This operating condition corresponds to the propeller operating at nearly peak efficiency. The wake survey data for the propeller using 13168A10P3 blades was obtained 13 inches aft of the disk as indicated in Figures 18 and 19. The operating conditions of this propeller correspond to a power coefficient of 0.0412, and to tip speeds of 550 and 750 fps. Because of the large differences in blade characteristics, the data covers a wide difference in blade loading.

The variations of the axial velocity, with blade span obtained for both propellers, show a rapid decrease as the tip is approached. The propeller with 109652 blades appears to maintain load further out on the blade than the propeller with highly tapered 13168A10P3 blades. The radial velocity, which is of same order as the tangential component, results in a large contraction of the wake. This contraction is of major importance in developing a theory for predicting performance. Due to the contraction of the wake, the axial velocity well inside the projected area of the disk is zero. Thus the axial, tangential, and radial velocities at the given fractional radius are for that position aft of the propeller, and do not correspond to conditions at that radius at the disk.

13

The variation of velocity aft of the propeller given in Figures 17, 18 and 19 are average values. Since the survey equipment is stationary and the blades are moving, the flow is pulsing. An indication of the magnitude of the average velocity to peak values is shown in Figure 20 for both the 109652 and 13168A10P3 blades. Note that the average velocity inboard is very near the peak, whereas the average velocity is 0.7 to 0.8 of the peak value.

CONCLUSIONS AND RECOMMENDATIONS

1. Blockage can have a large influence on the measured performance of propellers at the hover condition.

2. Size and Reynolds number are important parameters influencing performance of propellers at the hover condition. Model propeller data do not correspond to that measured on the full scale propeller.

3. On a whirl test stand where influences of wind can be encountered, the tests should be conducted at a constant RPM rather than constant blade angle. In any other case, the tests must be run under conditions of nearly dead calm air.

4. The contraction behind propellers is large immediately aft of propellers operating at zero velocity.

5. Four blade propellers show little improved Figure of Merit, but they do show a large improvement in power absorption ability.

6. Theoretical studies should be continued to develop accurate methods for calculating performance at the static condition.

7. Additional testing should be done on a rig with low or zero blockage to establish more data for checking theoretical performance calculation.

14

REFERENCES

1. Theodorsen, T., Theory of Propellers, McGraw-Hill, New York, New York, 1948.

2. Goldstein, S., "On the Vortex Theory of Screw Propellers," Proc. Roy. Soc. 1929.

3. Glover, L., "Applications of the Calculus of Variations to the Determination of the Optimum Propeller C-2342A Data", December 2, 1954.

4. Salters, Leland B., Jr., and Norton, Harry T., Jr., "An Investigation of the Effects of the WADC 30,000 Horsepower Whirl Rig Upon the Static Characteristics of a Propeller", NACA RM SL52F20.

5. Phillips, F. C., "The Canadian CL-84 V/STOL Tilt-Wing Prototype", Proceedings of 1st National V/STOL Symposium.

6. Anon., "Operating Manual for Linear Constant-Temperature Hot-Film Anemometer Model 40W", Lintronic Laboratories, Ithaca, N. Y., 1963.

TABLE I

PROPELLERS TESTED

Propeller Type	Dia.	No. of Blades	Blade Design	Activity Factor	Int. Des. C_L	(b/D).75	(h/b).75	Blade Characteristic Fig. No.
Conventional	15' 0"	3	109652	115	.500	.079	.045	5
Conventional	15' 0"	4	109652	115	.500	.079	.045	5
Conventional	15' 0"	3	109652M	115	.500	.079	.045	5
Conventional	2' 6"	3	109652	115	.500	.079	.045	5
VTOL	10' 0"	3	10188A2P2	188	.068	.144	.094	6
VTOL	13' 0"	3	13168A10P3	168	.057	.131	.094	7
VTOL	5' 0"	3	13168A10P3	168	.057	.131	.094	7
VTOL	1' 6"	3	13168A10P3	168	.057	.094	.094	7
VTOL	13' 6"	3	136148A2P3	148	.048	.117	.091	8

16
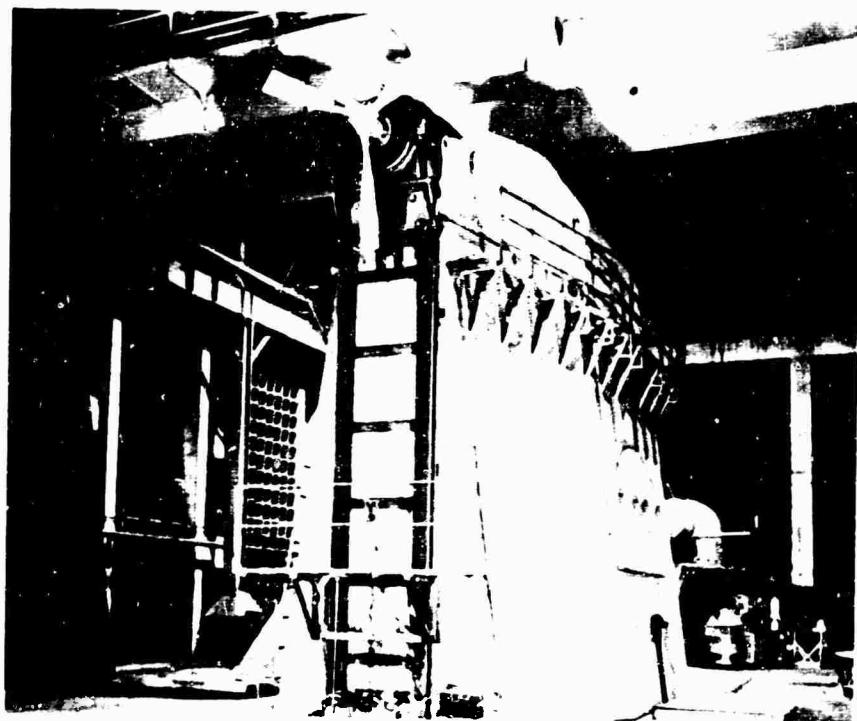
FIGURE 1 WRIGHT FIELD WHIRL RIG 3
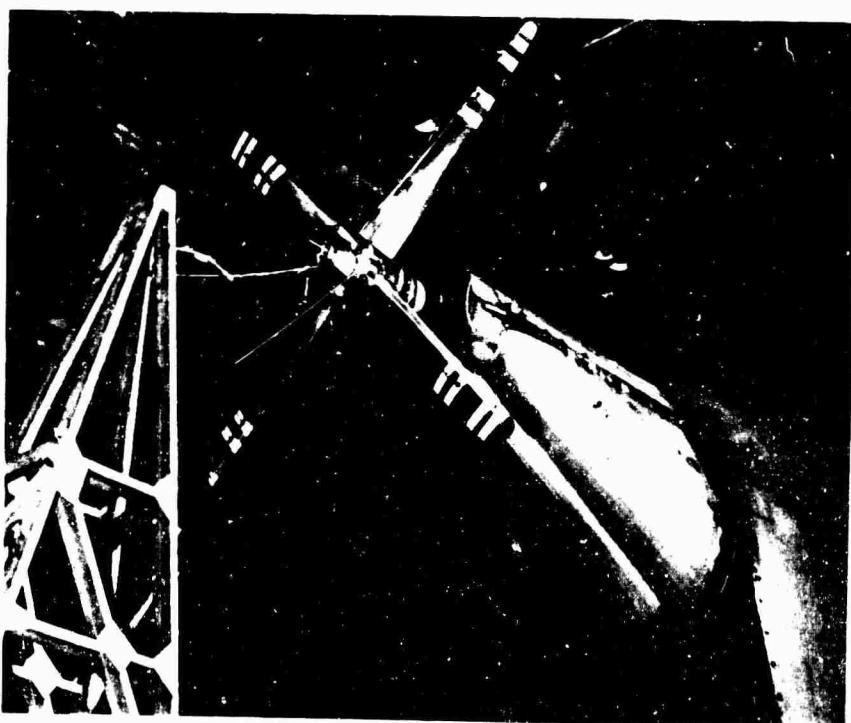
FIGURE 2 WRIGHT FIELD WHIRL RIG 4

17
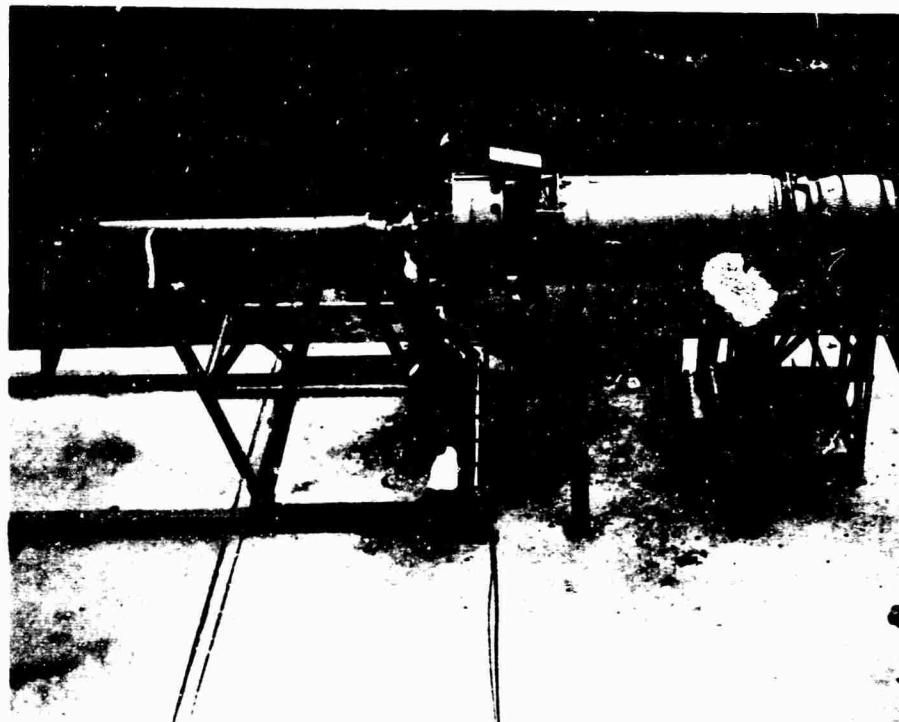
FIGURE 3   CURTISS-WRIGHT STATIC THRUST RIG
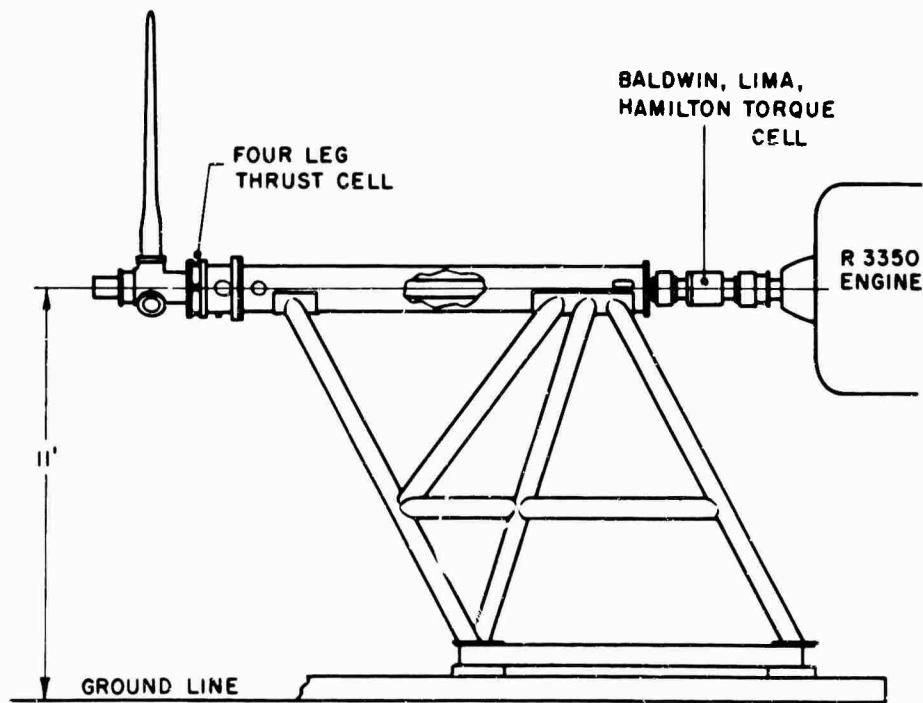
FIGURE 4   CURTISS-WRIGHT STATIC PROPELLER THRUST RIG

INCHES

0   10   20   30   40   50   60   70   80   90

DEVELOPED PLANFORM

L.E.

BLADE CHARACTERISTICS

109652 DESIGN
DIA. = 15'0"   115 AF   .500 IC_{L_i}

$\beta°$

$b"$

C_{L_i}

RETWIST

h/b

FRACTIONAL RADIUS - r/R
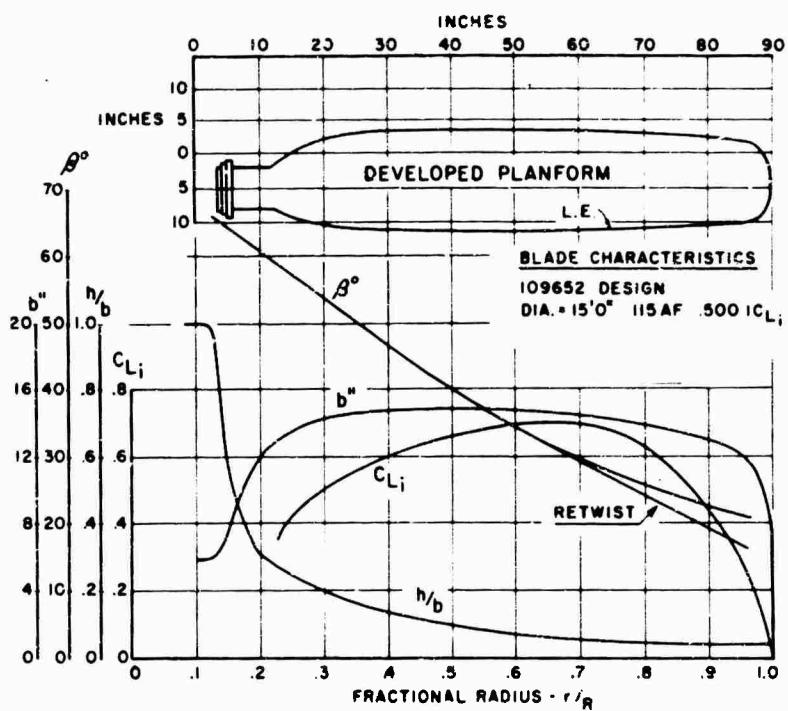
FIGURE 5   NACA 65 - SERIES SECTIONS

10188 A 2P2

DIA. = 10'0"   AF = 189 IC_{L_i} = .068

b - ft.

β

h/b

C_{L_i}

FRACTIONAL RADIUS - X = r/R
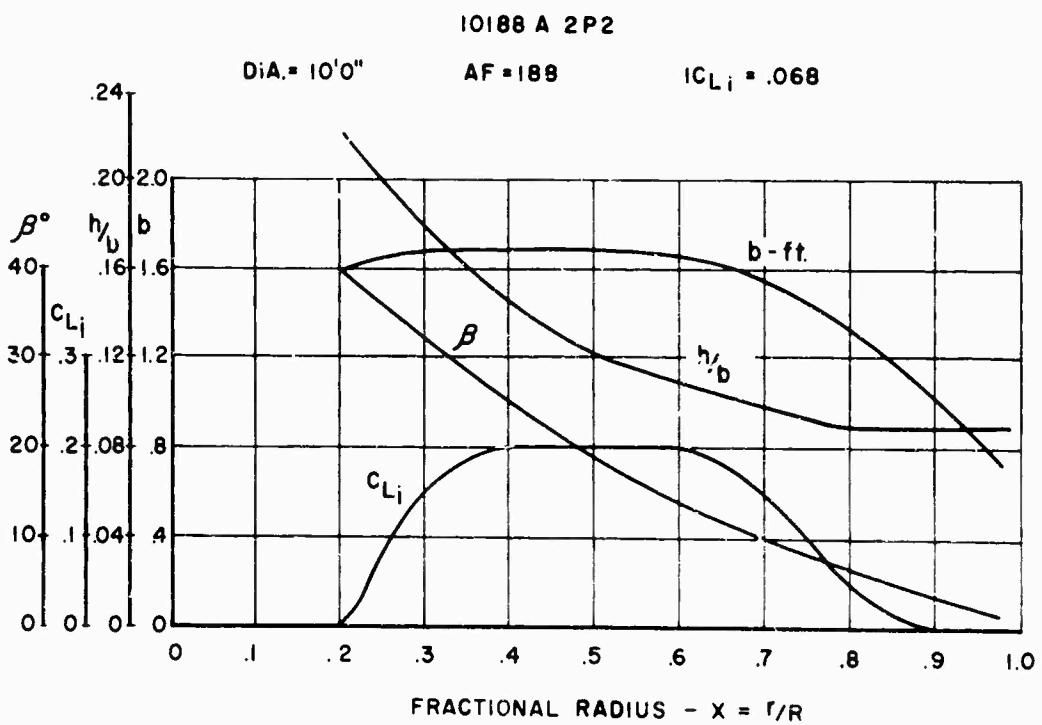
FIGURE 6   BLADE CHARACTERISTICS

19

13168 A 10 P3

DIA = 13' 0"   AF = .68   IC$_{L_i}$ = .057

NACA 64 - SERIES SECTIONS
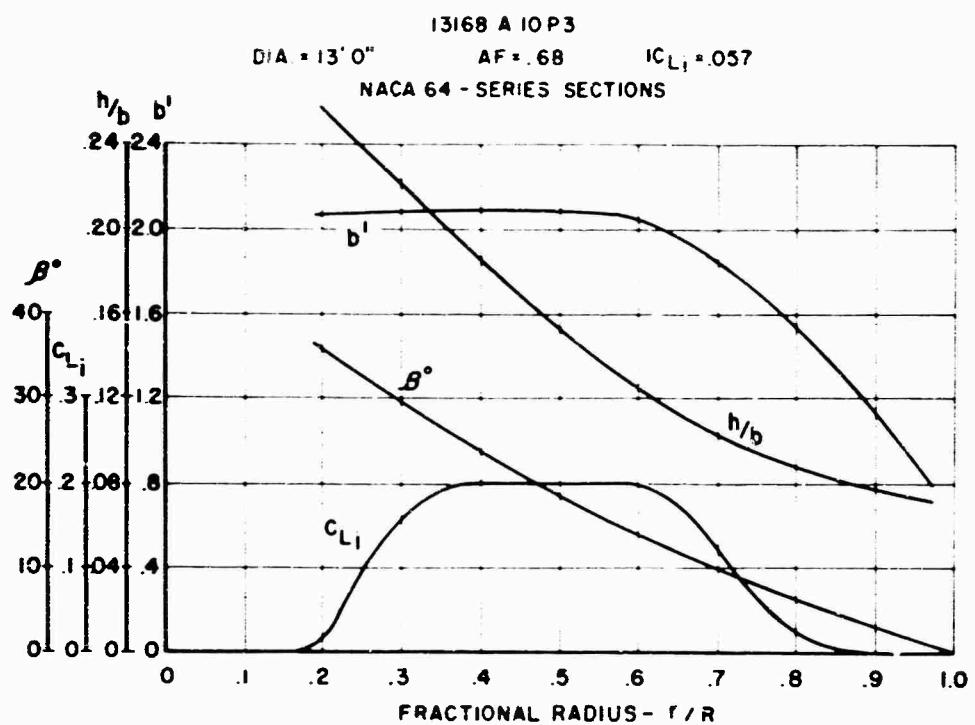
FIGURE 7   BLADE CHARACTERISTICS

3(13168A10P3)

3(10188A2P2)

3(i36148A2P3)

NOTE: SCALED UP TO 12' 6" DIAM.
FOR COMPARATIVE PURPOSES

LEAD EDGE

INCHES
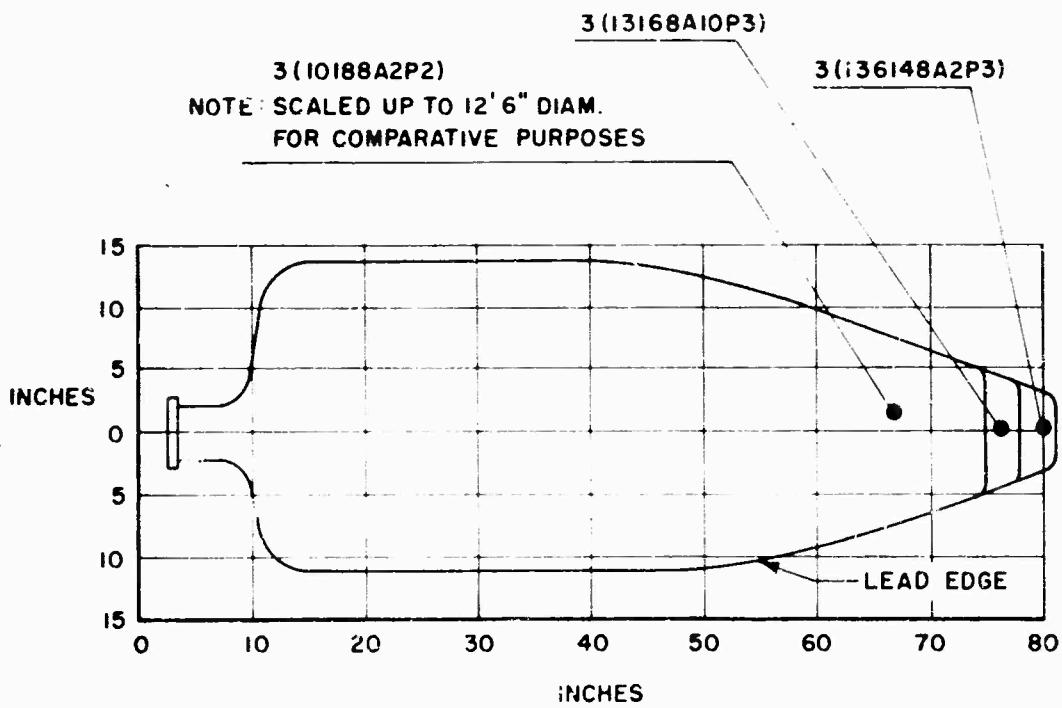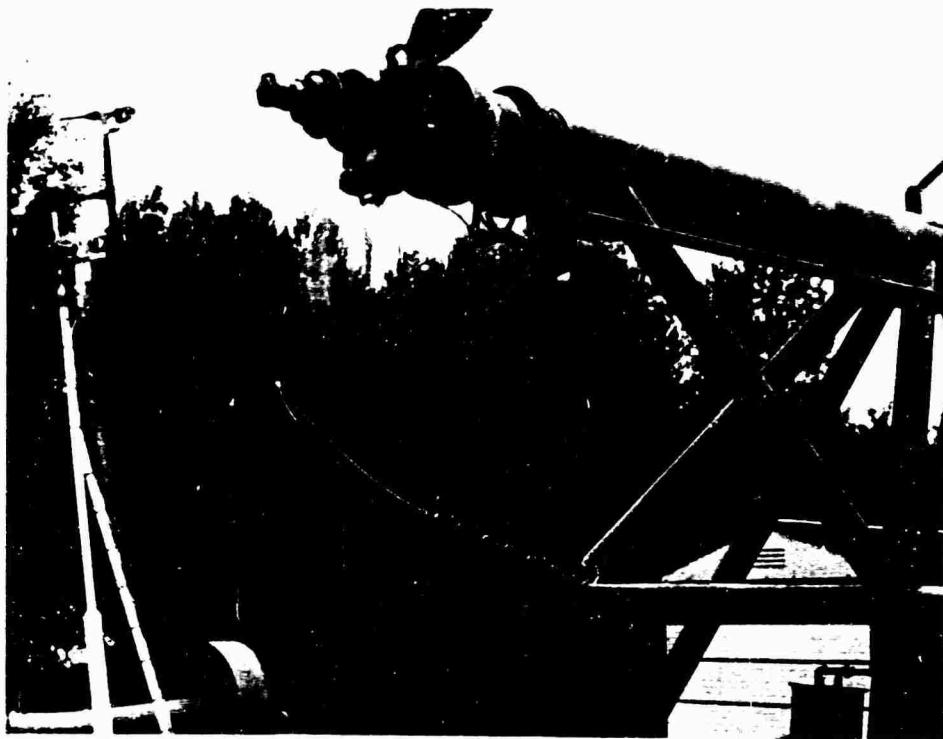
FIGURE 8

FIGURE 9   HOT FILM ANEMOMETER IN POSITION FOR SURVEY
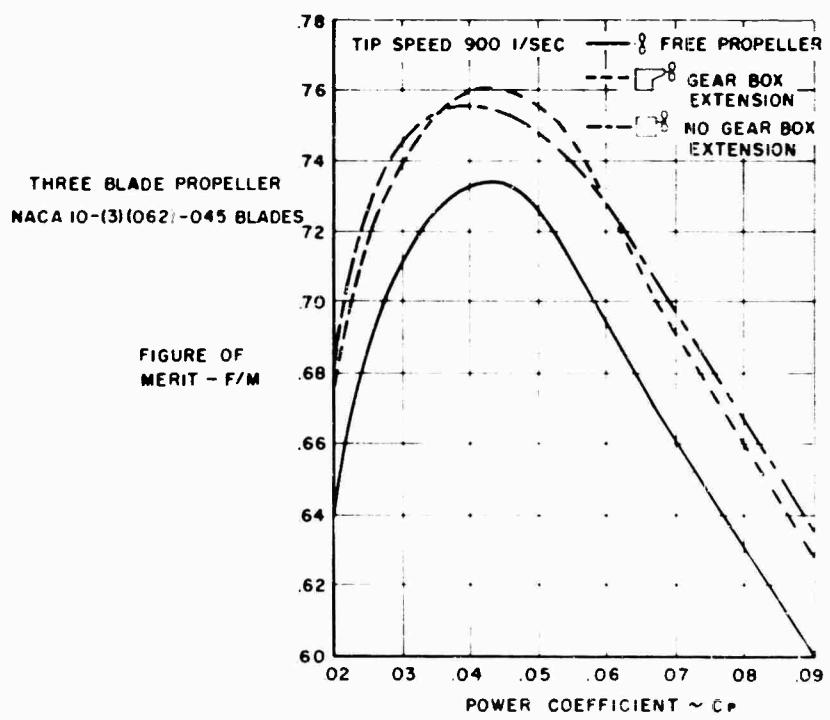
FIGURE 10   EFFECTS OF BLOCKAGE ON MEASURED PERFORMANCE

21
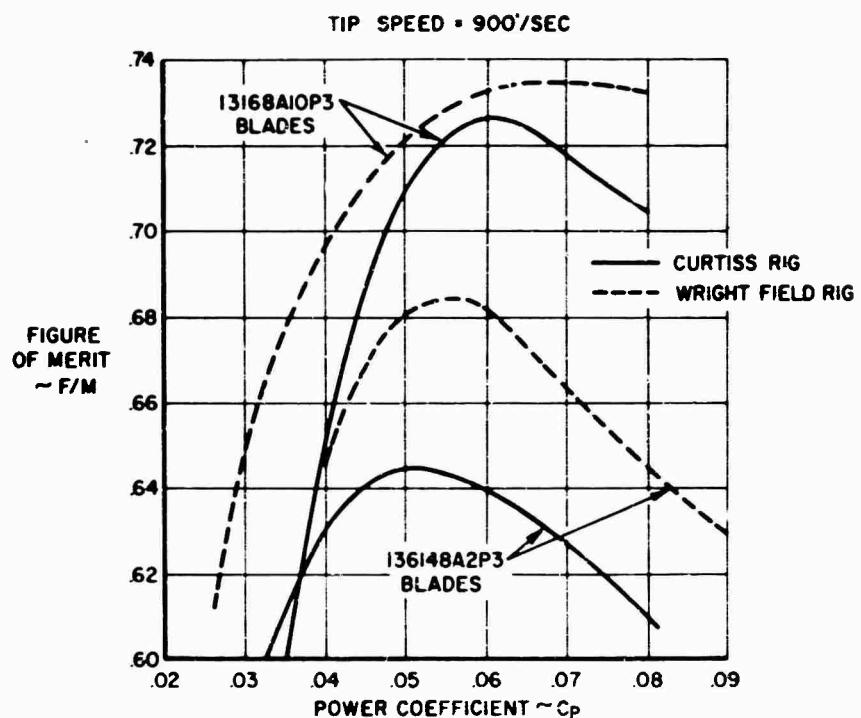
FIGURE 11   COMPARISON OF RIG MEASUREMENTS
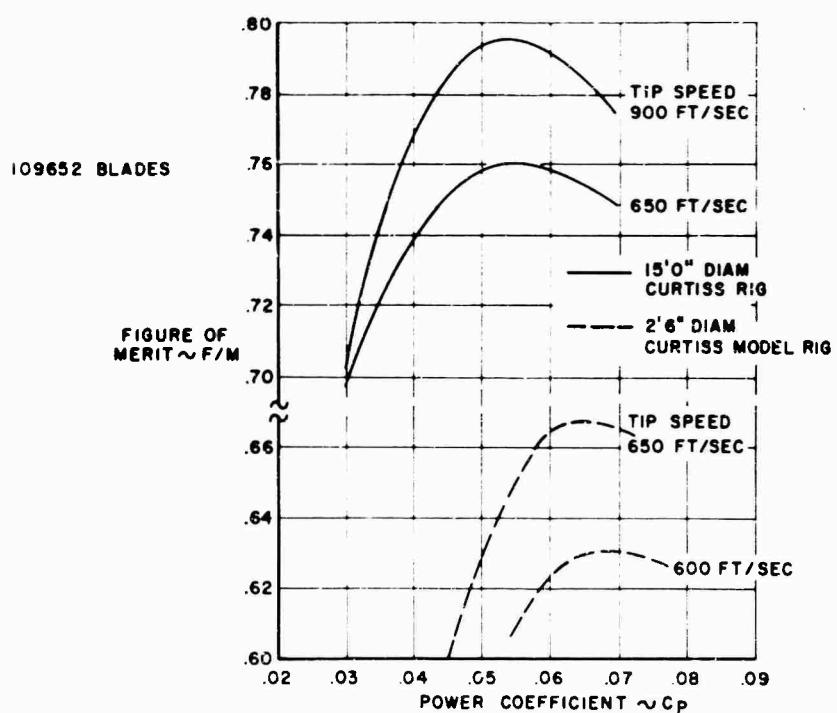
FIGURE 12   EFFECTS OF PROPELLER SIZE

THREE BLADE PROPELLERS
:3I68AIOP3

TIP SPEED FT/SEC

819
819

500

13'0" DIAM CURTISS RIG
5'0" DIAM CANADAIR RIG
1'6" DIAM CURTISS MODEL RIG

FIGURE OF MERIT ~ F/M

POWER COEFFICIENT ~ Cp
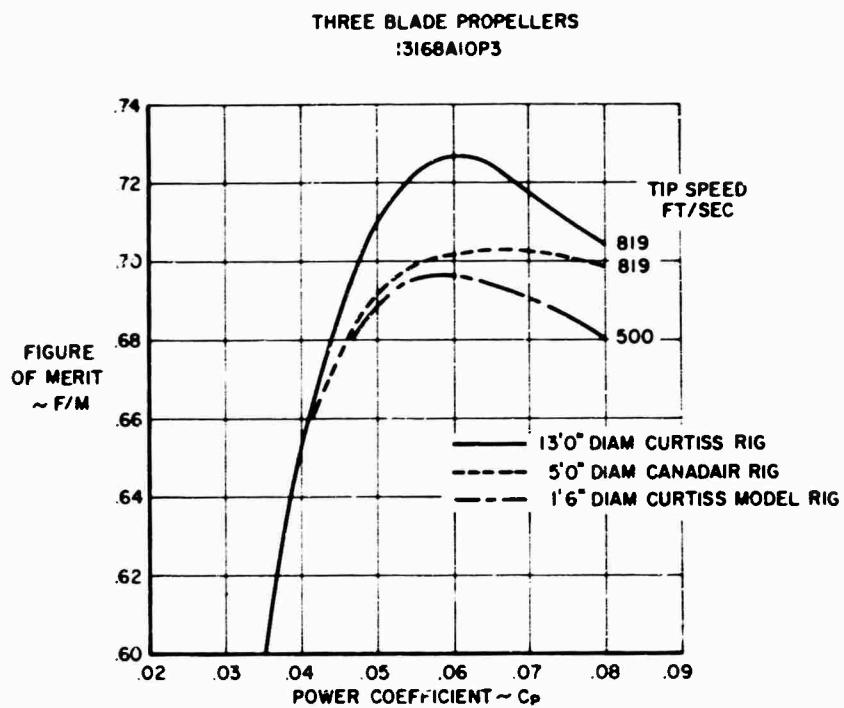
FIGURE 13   EFFECT OF PROPELLER SIZE

THREE BLADE PROPELLERS
TIP SPEED = 650FT/SEC

FIGURE OF MERIT~F/M

3(13168 A 10 P3)
3(10188A 2 P2)
3(136148 A2P3)

POWER COEFFICIENT ~ Cp
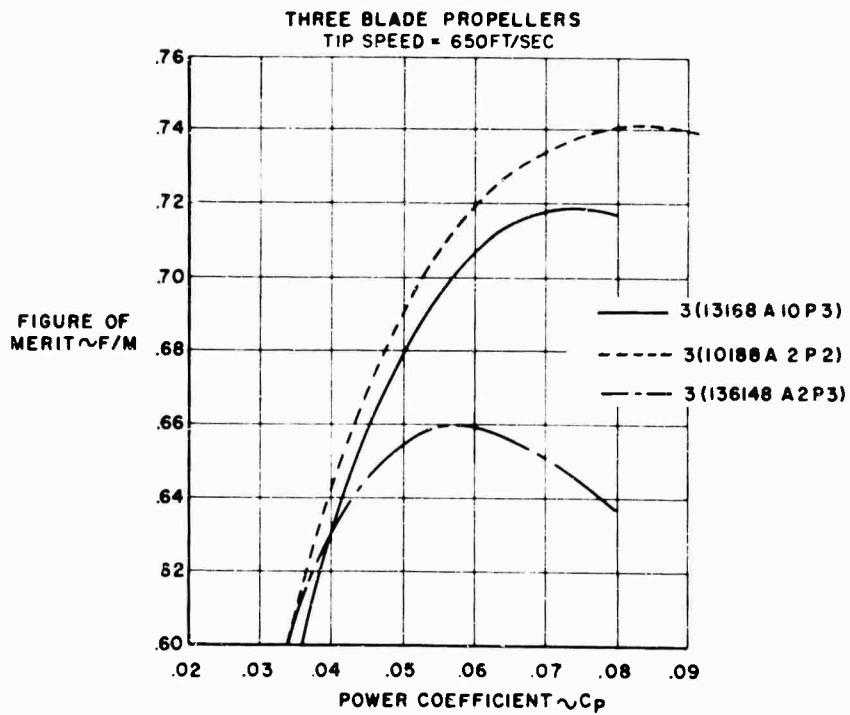
FIGURE 14   EFFECTS OF BLADE PLANFORM

23
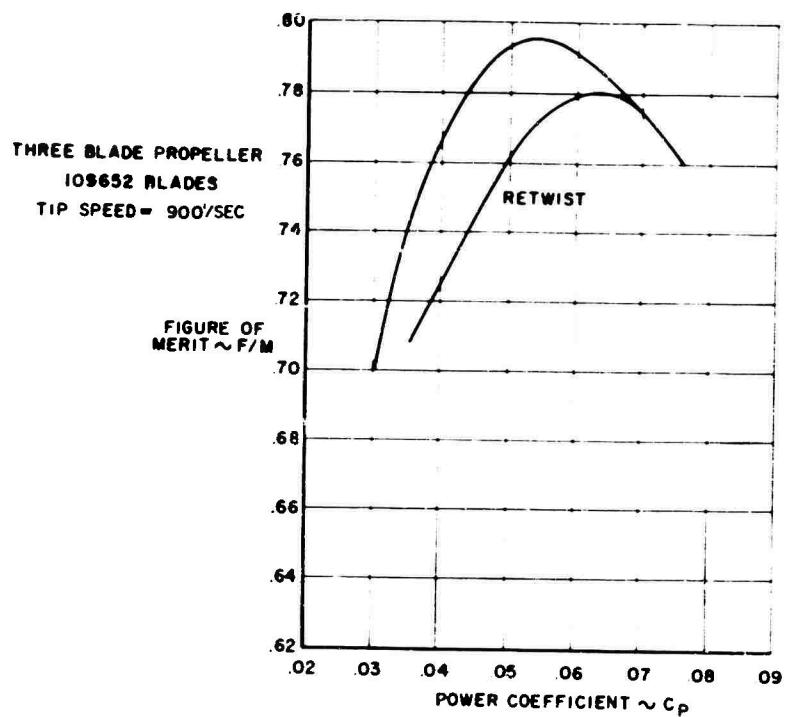
FIGURE 15 EFFECTS OF TWIST
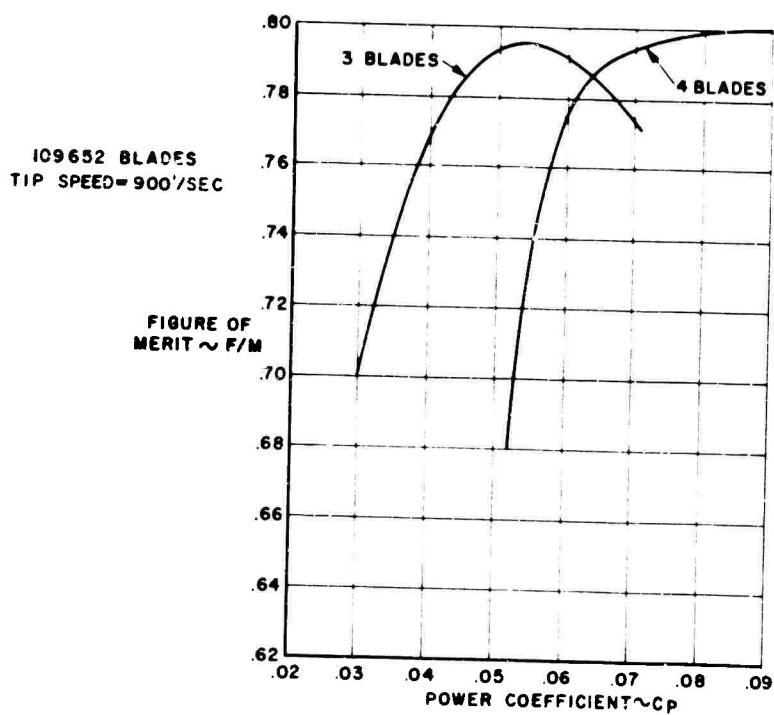
FIGURE 16 EFFECTS OF BLADE NUMBER

24

THREE BLADE PROPELLER
109652 BLADES
DATA MEASURED 10" AFT OF DISK
T=4870LBS HP=865 N=1000RPM C_P=.0605
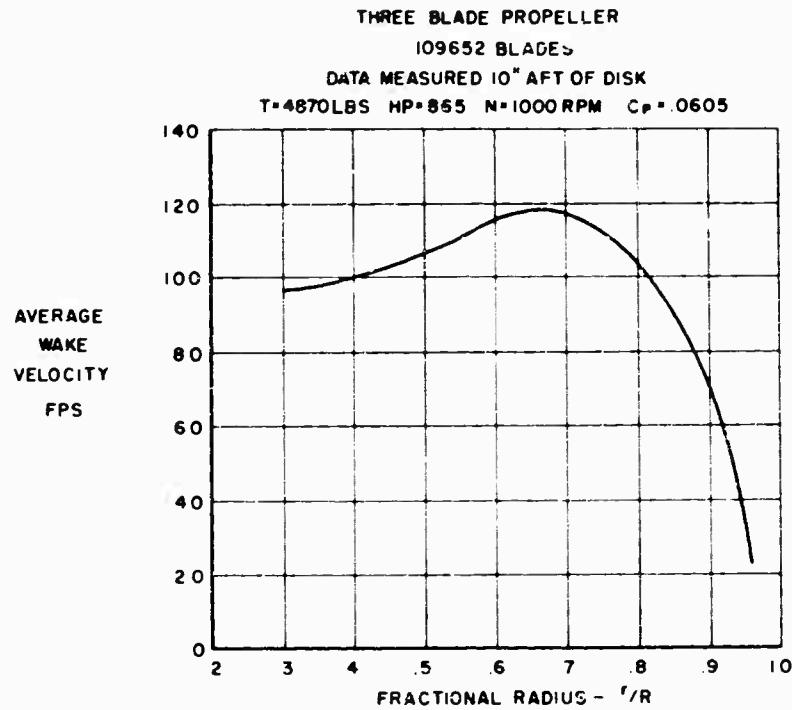
FIGURE 17   AXIAL WAKE VELOCITY TEST DATA

THREE BLADE PROPELLER
13168 A10P3 BLADES
DATA MEASURED 13" AFT OF DISK

T=2500 LBS   HP=400
N=1100 RPM

○ AXIAL
△ TANGENTIAL
□ RADIAL

C_P=.0412
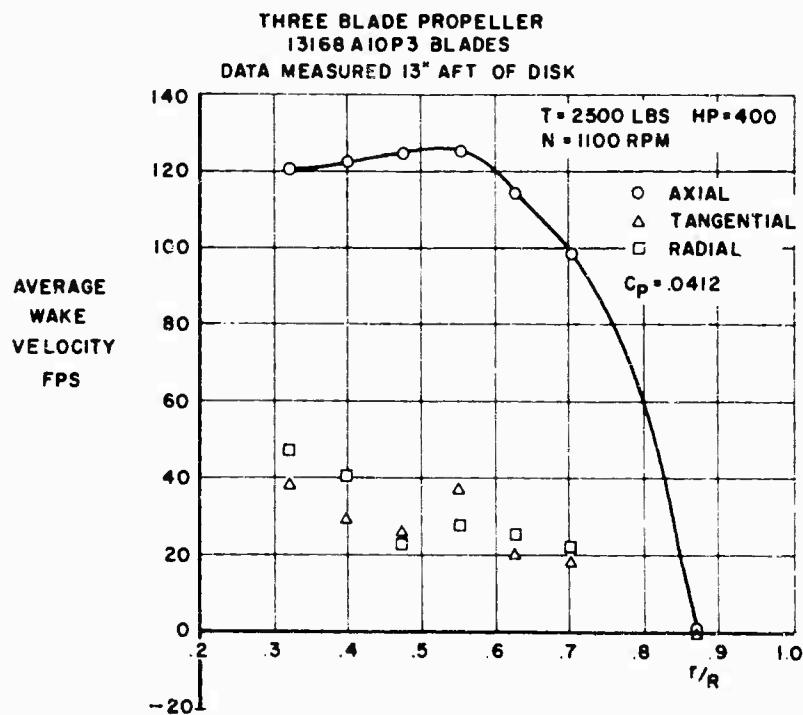
FIGURE 18   AXIAL WAKE VELOCITY TEST DATA

25

THREE BLADE PROPELLERS

13168 A!0 P 3 BLADES

DATA MEASURED 13" AFT OF DISK

T = 940   HP = 150   N = 800 RPM
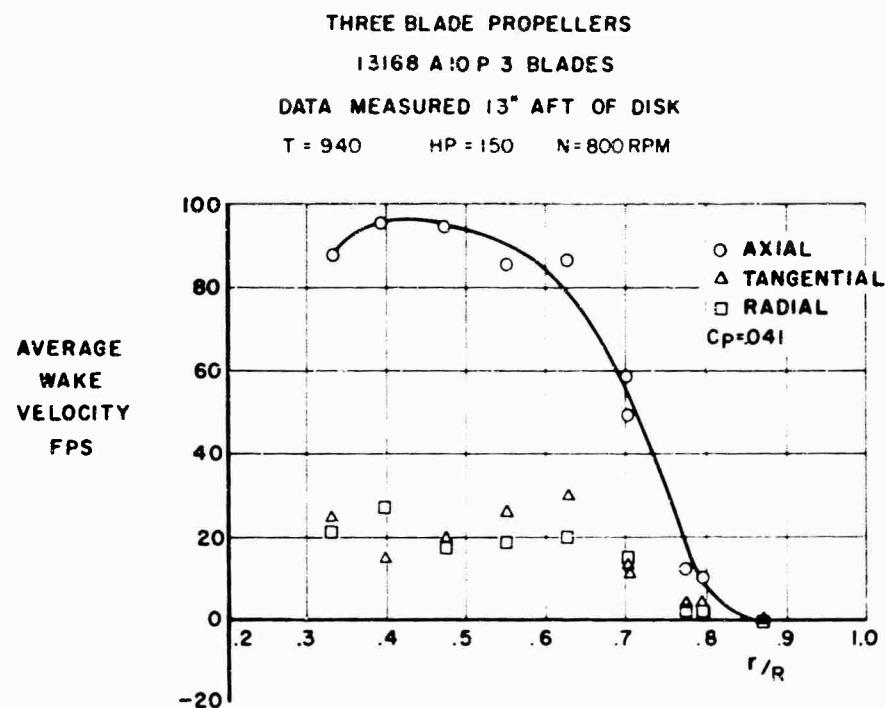
FIGURE 19   AXIAL WAKE VELOCITY TEST DATA
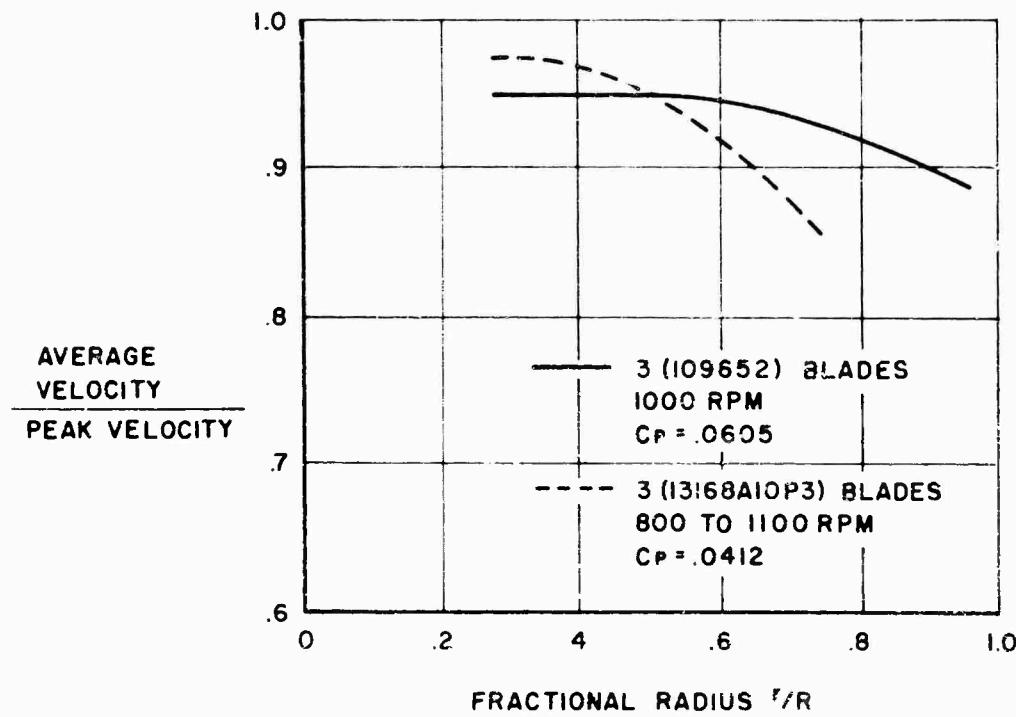

FIGURE 20   RATIO OF AVERAGE TO PEAK VELOCITIES IN WAKE

26

APPENDIX A

DERIVATION OF PROPELLER

FIGURE OF MERIT

1. $FM = \dfrac{HP_{OUT}}{HP_{IN}} = \dfrac{1/2\, m\, V w^2}{550\, HP}$

2. $T = m\, Vw$

3. $\boxed{FM = \dfrac{T}{HP}\dfrac{Vw}{1100}}$

4. $m = \rho\, A_P\, V_P = \rho\left[\dfrac{\pi}{4}\, D_P^2\right] V_P = \rho\left[\dfrac{\pi}{4}\, D_P^2\right]\dfrac{Vw}{2}$

FROM EQUATION (2)

$$Vw = \dfrac{T}{m} = \dfrac{T}{\rho\, A_P\, Vw}\,\dfrac{A_P}{A_w}$$

$$Vw^2 = \dfrac{T}{\rho A_P}\,\dfrac{A_P}{A_w} = \dfrac{T}{A_P}\,\dfrac{D_P^2}{D_w^2\,.002378\,\sigma}$$
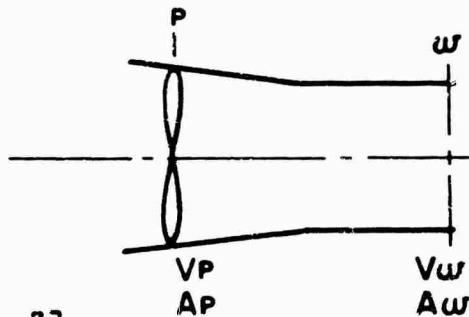
5. $\boxed{Vw = \dfrac{D_P}{D_w}\,20.5\sqrt{\dfrac{T}{A_P}\times\dfrac{1}{\sigma}}}$

SUBSTITUTE (5) INTO (3)

$$FM = \dfrac{T}{HP}\,\dfrac{D_P}{D_w}\,\dfrac{205}{1100}\sqrt{\dfrac{T}{A_P}\times\dfrac{1}{\sigma}}$$

6. $\boxed{FM = \dfrac{T}{HP}\,\dfrac{D_P}{D_w}\,\dfrac{1}{53.64}\sqrt{\dfrac{T}{A_P}\times\dfrac{1}{\sigma}}}$

FIGURE OF MERIT

FOR A PROPELLER $\dfrac{D_P}{D_w} = \sqrt{2}$

7.
$$FM = \frac{T}{HP} \times \frac{1}{38.94} \sqrt{\frac{T}{A_P} \times \frac{1}{\sigma}}$$

FOR A SHROUDED PROPELLER WITH CYLINDRICAL DUCT $\dfrac{D_P}{D_w} = 1$

8.
$$FM = \frac{T}{HP} \times \frac{1}{53.64} \sqrt{\frac{T}{A_P} \times \frac{1}{\sigma}}$$

TO CONVERT TO NON-DIMENSIONAL FORM

WHERE $C_T = T/\rho n^2 D^4$

$\qquad C_P = 550\,HP/\rho n^3 D^5$

SUBSTITUTE INTO EQUATION (8)

$$FM = \frac{\rho n^2 D_P^4 C_T}{\rho n^3 D_P^5 C_P}\frac{550}{536}\frac{D_P}{D_w}\sqrt{\frac{\rho n^2 D_P^2 C_T}{\frac{\pi}{4} D_P}\frac{1}{\sigma}}$$

$$= \frac{550}{53.64}\frac{D_P}{D_w}\frac{C_T}{nD\,C_P} \times C_T^{1/2}\sqrt{.002378\,\frac{4}{\pi}}$$

$$= \frac{550}{53.64}\;0550\;\frac{C_T^{3/2}}{C_P}\frac{D_P}{D_w}$$

$$\boxed{FM = .565\,\frac{D_P}{D_w}\frac{C_T^{3/2}}{C_P}}$$ FOR $\dfrac{D_P}{D_w} = \sqrt{2}$ (10) $\boxed{FM = \dfrac{.798\,C_T^{3/2}}{C_P}}$

28

NOTES

PROPELLER RESEARCH AT CANADAIR LIMITED

by

G. N. Adams

Canadair Limited
Montreal, Canada

INTRODUCTION

So far this morning, you have heard one paper from someone who
thinks about propellers, and one paper from someone who sells propellers;
now you're going to hear a paper from someone who buys them.

As Mr. Jackson said, Canadair's interest in VTOL aircraft goes
back to about 1956. At that time, we did some design studies and concluded
that the type of aircraft which promised the best compromise between VTOL
and STOL performance was the flapped-tilt-wing aircraft using propellers.
So, we went shopping for propellers and visited the various propeller manu-
facturers. We found that, at that time, they seemed to be lacking in relevant
test data for the static thrust condition.

Now, they tried to put together methods of estimating the static
performance of propellers suitable for VTOL aircraft and came up with
some methods that gave some rather peculiar results. One manufacturer
came up with a method which showed that, if you made the activity factor
high enough, you could get a figure of merit higher than one. Another manu-
facturer showed you got the highest figure of merit at a low activity factor.
Still another manufacturer showed that, if you made the tip speed high enough,
you'd get figures of merit well over 0.90. As recently as two years ago, one
manufacturer was promising that he knew how to design a propeller that would
give a figure of merit of 0.87. (It now appears that he had the digits trans-
posed.) Of the manufacturers we contacted about that time, the only one
using conservative data for static thrust estimation was Hartzell.

MODEL TEST RIG

We realized that we were going to have to learn something about propellers ourselves; so, in 1960, we persuaded the Canadian Government to fund a research program at Canadair Limited which has been going on more or less continuously ever since. In order to test model propellers, we built ourselves a propeller test rig which is shown in Figure 1. This is a rather more modest rig than the facility at Wright Field.

This rig was built to accommodate propellers up to 7 feet in diameter, although most of the testing which we have done to date has been with propellers between 4 and 5 feet in diameter. This is due to the fact that our interest shifted to higher disk loadings after the rig was built. One of the things illustrated in Figure 1 (apart from the propeller itself), is a traversing mechanism which enables us to position probes in front of or behind the propeller disk for measuring various quantities of interest in that field; this will be discussed later on. A smoke jet and a stroboscope, which we use for flow visualization work, are shown on the right side of this figure.

Figure 2 illustrates the rig from the rear end; you can see the engine a little more clearly there, as well as the corner of the traversing mechanism. You'll notice that the rig appears to be on wheels -- it is movable, but it is not mobile. Originally, we intended to use the rig outdoors, where we would have a minimum of trouble with interference effects and recirculation, but we found that the rate of data production was so low outdoors (waiting for the wind to die down) that we eventually moved indoors to make the results more reproducible, even though they might not be truly representative of performance in free air. Indoors, we still have problems -- particularly with recirculation.

One thing we have found that may be of use to anybody else setting up such a facility is to avoid symmetry at all costs. If you have your propeller slipstream blasting straight at a wall, the column of air seems to be unstable. It sort of thrashes around, and this changes the recirculation pattern in the room and changes your propeller performance from one moment to the next. It would appear that you should align the rig in the most irrational angle you can think of in the test facility so as to try and arrive at a stable flow condition.

At the back of the rig, we had an enclosed cab for outdoor tests. The operator sat in this cab and controlled the tests. Now, as illustrated in Figure 3, we've shifted to a control station at the side of the rig, where we have the controls to operate the engine, as well as our instrumentation readouts. This has proved to be a much more satisfactory arrangement. This figure again shows the propeller, the smoke jet, and the strobe unit, as well as a water tank. We now run the water through the engine continuously, instead of trying to cool it in the usual way.

I think the equipment we have on the rig is more clearly seen in the schematic diagram of Figure 4. We represented the rig in this figure as we expect it to be soon; not all of the equipment shown is now on the rig, nor has it all been used.

One of the principles which we have gone to recently -- as a result of previous experience -- is the principle of redundancy. The general idea is that every quantity should be measured in two different ways at the same time. This is partly from the point of view of equipment becoming unserviceable and also partly because we want to be able to tell, when we get an apparent change in performance, whether this is due to an actual change in performance or whether it's due to a change in the instrumentation that we are using. If both readouts indicate a change, we assume it's really there.

The propeller, as shown in Figure 4, is 4 to 7 feet in diameter. The propeller centerline is about 8 feet above the floor, which of course is not really high enough but, as in Mr. Borst's case, it is about all that we could afford. The rig is driven by an automobile engine (which is nominally 425 shaft horsepower) through a clutch, a four-speed gear box, and an overrunning clutch to protect the propeller if the engine seizes up. We have a toothed wheel which gives pulsations proportional to rpm; these pulses are displayed on a frequency converter which gives an rpm indication. They are also counted on a digital counter, which gives us a truer answer. The coupling shown allows the shaft to slide longitudinally, as well as isolating it from some of the effects of the bearings not shown upstream. The two necked portions of the shaft are equipped with torsion strain gauges, whose leads come out through a slipring to a readout. Both sets of these gauges read torque.

3

The set of gauges towards the front of the rig carries both torque and thrust and, if there are interaction effects of thrust, these could show up on the torque measurement at this point. The set of gauges on the other side of the thrust bearing should obviate any interaction from thrust; however, they do measure the torque of the thrust bearing. So it's a question of looking at both sets of test results and choosing the lesser evil. So far, we've found that the interaction seems to be negligible. As illustrated, there is a thrust bearing which bears against a hydraulic load cell, and the pressure in the load cell is read out on a pressure gauge, which is our primary measurement of thrust.

The propeller is supported on a heavy shaft which runs in two sets of bearings (illustrated as floating cage ball bearings). These are multiple-row ball bearings in which there is a cage full of holes which is free to float end-wise. Thus, besides allowing rotation, there's a limited amount of end float allowed on the bearings. We are presently using roller bearings for this purpose and depending upon the shaft rotation to allow the shaft to creep through the bearings. We have encountered some trouble with the bearings tending to cock over a bit and shove the shaft through, giving us spurious thrusts at low rpm's.

Immediately behind the propeller, a magnetostrictive transducer is shown; this works on the principle that, when you apply a stress to a permeable material, the permeability changes in the direction of the stress. The transducer has poles arranged in it in such a way as to measure both torque and thrust. This also is a piece of equipment which is not as yet working satisfactorily.

The smoke jet is positioned in various places to put the smoke through the propeller when we're doing our flow visualization. Also shown is a traversing mechanism for a probe. We get various readouts from this, depending on the kind of traversing we're doing at the time. Our measurements are taken from pitot tubes, total head tubes, pressure transducers, hot-wire anemometers, or anything which we think might give us some useful information.

4

PERFORMANCE MEASUREMENTS

One of the chief problems in performance measurements on this rig has been poor repeatability. We find that testing the same propeller at different times of the year seems to give different figures of merit. We have also found a fairly consistent trend where the figure of merit of the propeller decreases with time, in general.

We calibrate the rig frequently -- before and after tests -- but this does not seem to eliminate the poor repeatability problem. We believe that, with the revised instrumentation which we now have and are still installing, we'll be able to get better repeatability. But, again, this remains to be seen.

Although "figure of merit" is a commonly used term, it might be well to define this term as it is used in this paper. But first, let us discuss efficiency. The efficiency of any moving device is defined as the force times the velocity over the power required. But, in the static condition, the velocity of the propeller is zero and, therefore, according to this definition, the efficiency is zero. A propeller works by giving momentum to air, and the most efficient way of producing a thrust by giving momentum to air is to give the air a uniform velocity over the maximum possible area. This is the principle of the actuator disk.

Thus, figure of merit, as used in this paper, is simply defined as the power absorbed by the actuator disk over the actual power used by the propeller producing the same thrust. In other words, the actuator disk would have a figure of merit of one (according to the definition which I am using and which the propeller people usually use). A propeller doesn't actually work like an actuator disk -- as you will see later on from the flow visualization illustrations -- but this does form a useful yardstick for measuring and comparing performance of propellers.

The highest figure of merit which we ever measured on our rig is approximately 0.818, but this is probably incorrect. Looking at the results over a period of years, the highest figure of merit that we would say with any confidence that we have measured is around 0.78.

FLOW MEASUREMENTS

So far, the only flow measurements which we've done have been mean value flow measurements using manometers to measure pressure. In the slip-stream, we've measured the velocity using pitot static tubes. In the inflow region, which is not necessarily on the upstream side of the propeller but is out of the slipstream, we have measured static pressure using a reverse total head tube and assumed that the total pressure was ambient. We usually do our flow measurements at about 800 feet per second tip speed, which is less than the tip speed for maximum performance. This is partly to reduce the noise for the benefit of the people who are working close to the propeller and partly to reduce the stress level at which the propeller is operating when people are walking around it. Our flow visualization work has shown that at least a first-order effect of the pattern of flow behind the propeller is independent of the rpm. If there are any changes, they are certainly a second-order effect.

Figure 5 shows a plot of mean velocity vectors measured around the propeller. The propeller axis is shown on the left-hand side of the figure, while the blade axis is shown in the middle of the figure. Note that the vertical scale is expanded by a factor of roughly three-to-one relative to the horizontal scale, as far as the points at which the velocity vectors are drawn goes. The vectors themselves have been drawn at the true angle. As illustrated, we have meas-ured quite close to the propeller (0.05 radius), and we've done a lot of measure-ments very close to the tip of the propeller. These results are typical of one particular four-bladed propeller which we tested; quantitative results are not presented because we are still in the early stages of testing. The length of the arrows in Figure 5 is an indication of the actual velocity measured at the point. Note that, outboard of approximately 90% radius, we have reverse flow -- flow coming in what you would think of as the upstream direction towards the pro-peller and also coming in from the tip. This flow seems to be coming in to join the tip vortex before being expelled backward.

Figure 6 illustrates mean streamlines which have been based on the vectors as shown in Figure 5, on our flow visualization, and on a certain amount of intuition. The scales are exactly the same as those in Figure 5 and, because of the expanded vertical scale, the contraction appears quite gradual; but, in fact, it is roughly three times as fast as shown here.

Figure 7 shows dynamic pressure contours obtained from the same data. Because they are on the same axis, these contours are somewhat

6

distorted. These are lines of dynamic head, which is measured in inches of water.

Velocity vectors at the propeller can be used to calculate both the angle of attack of individual stations on the propeller and (knowing the blade geometry and characteristics) the lift coefficient at each blade station. From this, you can also calculate an integrated performance of the propeller to compare with the measured values; our early results in this area were very encouraging. We were getting calculated thrusts and torque within a couple percent of the measured value. However, some tests conducted later with more refinements gave results which were not quite so good.

We initially tested a relatively conventional propeller and found that the lift coefficient was very high on the inboard half of the propeller and very low on the outboard half, except for the last five percent of the radius. Outboard of about 0.95, we had very high lift coefficient. This is largely because of the reverse flow that you get near the tip. In actual fact, the torque contribution is negative at the tip. The tip of the propeller is windmilling, even though it may be producing some positive thrust.

The inboard part of a propeller is inherently inefficient because of the geometry of the inflow angle, and as a result, the lift coefficient results in a large component in the torque direction. The inboard part of a blade, then, is chiefly serving as a fairing for the structure which supports the outboard part of the blade. It may also serve to pressurize, to some extent, the air going into the engine inlet. Hopefully, you'll recover enough in this way to recover the drag of the inboard part of the propeller. This applies, of course, only to static conditions. Oddly enough, this propeller, which seemed to have a rather poor C_L distribution, had as good a figure of merit as any we have measured. Another propeller which we tested had a much more satisfactory lift coefficient distribution along the blade, with the exception of the tip, and yet it had a lower figure of merit than this one. The lift-to-drag ratio at the blade stations is not really very important, because the profile power is much less than the induced power in the static condition. I think it is the induced velocity distribution which is most important in setting up propeller performance for static conditions. I also think that, if there are any big gains to be made in static performance, they probably lie in controlling the behavior of the tip vortices.

7

FLOW VISUALIZATION

Canadair has done a great deal of work on flow visualization. Figure 8 shows a test setup in which we are putting smoke through the propeller from three jets at three different radii; continuous illumination was used in this test. The blurring of the smoke streams as they go downstream is due to two reasons: one is simply diffusion of the smoke; the second is that there are periodic changes in the streamline at blade frequency, and we're seeing the blurred average of these in this illumination. Note that the smoke from the outermost jet is entering the propeller from behind. This is characteristic in free air in the static condition. We produce our smoke using heated oil, which we have found gives reasonably satisfactory smoke without being too harmful to people in the test area. We illuminate the smoke from the back, of course, because we get much brighter illumination when looking through it towards the light, rather than looking at it from the opposite side.

A rake with multiple jets (again with continuous illumination) is shown in Figure 9. The results as illustrated are very much as you would expect the flow through a propeller to look.

The results of the rake being positioned lower are illustrated in Figure 10. Here you see the flow entering the tip section of the propeller from behind, although it does appear to enter from a generally forward direction when you are far enough away from the propeller. Actually, the smoke turns forward to enter the propeller and appears to flow radially inward along the blade for some considerable distance. Looking at this illustration, it is obvious that, if you try to do static thrust performance in a wind tunnel, you will encounter a large wall effect.

Figure 11 illustrates the rake positioned behind the propeller and, once again, it is evident that there is a noticeable difference in the direction of the flow -- there's sort of a boundary at the flow going backward as it ought to inboard, and forward outboard, and you can see the tip vortex somewhat distinctly quite far in from the tip of the blade.

8

To observe the occurrences at blade frequency, stroboscopic illumination is required. Figure 12 shows the sort of flow conditions that you see with stroboscopic light synchronized once per revolution. This is taken at a moment just before the blade passes through the vortex from the previous blade. Note the clearly marked cores of the vortices from the blade, as well as the fact that the flow seems to penetrate the disk and actually go forward of the propeller blade. Looking at this angle, this could be an illusion; but, in fact, in the laboratory, you can stand in the propeller plane and see that the flow actually does penetrate the propeller plane. It seems that, as the vortex leaves the trailing edge of the propeller blade and expands as air flows into it, the vortex moves radially inward (essentially in the propeller plane at first) and then turns backward. Looking from the side, this gives a very rapid contraction and, as the vortex grows, it actually penetrates the disk and passes in front of the propeller blades. Figures 13, 14, and 15 show various stages of vortex formation with respect to the propeller.

While we were doing this stroboscopic visualization of the flow (which we thought of ourselves), it seemed so simple that we thought that somebody must have done it before. As we discovered, Jacques Valensi[*] of the University of Marseille did it in 1935. He published an excellent report which describes stroboscopic measurements of flow and contains still photographs which he analyzed and interpreted. He pulsed the smoke and, by measuring the space in between the pulses, he got the velocity in the field; from this data, he was able to compute the diagrams of the flow directions and velocities in the propeller field.

He also presents a very interesting survey of earlier propeller work; it is interesting to see, for example, that a man named Riabouchinsky in Russia measured instantaneous pressure profiles behind a propeller in 1909. So you can see there is really nothing very new about the technique.

The clarity of tip phenomena and of the flow phenomena in general is enhanced at higher blade angles, of course, where you have a stronger

---

[*] "Étude de l'écoulement de l'air autour d'une hélice," Jacques Valensi, Publications Scientifiques et Techniques de Ministere de l'Air, No. 73, Institut de Méchanique des Fluides de l'Universite d'Air-Marseille, 1935.

9

vortex. Also, if you have fewer blades, the vortices are most spread out and are easier to see.

A two-bladed model propeller running at a blade angle of 16° at a three-quarters radius is illustrated in Figure 16. It's much easier to see what's going on, even though it may practically be of less interest. You can see the vortex forming quite distinctly at the trailing edge of the blade in this illustration. Figure 17 shows the same thing 45° earlier -- in other words, before the blade has arrived. Figures 18, 19, 20, and 21 illustrate the flow coming in at 60% radius, an intermediate situation, 40% radius, and approximately 30% radius, respectively. In Figure 18, you can see the very pronounced breaks due to the vortex sheet from the previous blade. At this sheet, you have a sort of discontinuity -- you get a velocity component outboard on the upstream side and inboard on the downstream side. Since these velocity components remain there, the two sections move farther apart as they move downstream, which actually gives a three-dimensional effect. The flow comes along and then does sort of a corkscrew and comes back again -- it sort of whips around the blade quickly.

In Figure 21, it looks as if the flow disappears behind the shaft; actually, it's just that the light is being cut off because the light is coming through from behind. Figure 22 shows a front view in which you can see the three-dimensional aspect of this. There is a lateral shift caused by the vortex sheet. We don't see any particular evidence in our work of the vortex sheets rolling up. As far as we've been able to determine, behind the propeller it doesn't seem to roll up, at least within one radius downstream.

One of the interesting things which we have seen in the flow visualization is the effect of blade mismatching -- in other words, if all four blades of the propeller don't have exactly the same blade angle.

In Figure 23, it is shown that the vortices move downstream at differing velocities and their spacing becomes irregular; they then begin to affect each other -- one will move inboard, another one will move outboard. It is similar to the condition where succeeding smoke rings will pass through previous ones. We've never seen the vortices actually do this -- they try, but they don't seem to be able to get quite around, as shown in Figures 24 & 25.

10

Another problem that we run into in this work is that of inhomo-geneous inflow. Figure 26 illustrates one way in which we approached this problem. We filled the upper half of the room with smoke and then started up the propeller. This figure clearly shows how the smoke was drawn down from the ceiling into the propeller. Now, of course, the laws of convection being what they are, you've got hotter air near the ceiling than you have near the floor. This means that different parts of the propeller are receiving air at different temperatures. How you allow for this in reducing the performance data is a question.

The condition after the smoke has thinned out is shown in Figure 27. Although not clearly shown in this figure, we found that you get a lot of entrainment into the slipstream -- in other words, you have smoke coming down from the ceiling and entering the cylinder of the slipstream down-stream of the propeller, presumably just acting as an ejector. A good bit of the flow that is drawn in does not actually pass through the propeller disk.

FUTURE WORK

Canadair Limited plans to improve performance-measuring equip-ment as indicated earlier. We want to explore in detail the characteristics of figure of merit versus blade angle over a wide range of blade angles -- perhaps from -10 to +25 or +30 degrees at the three-quarter radius point. We think we've seen some peculiar things on one or two of the propellers we have tested, and we wish to explore these in more detail.

We intend to do some instantaneous flow survey work. We have a total pressure transducer which can instantaneously measure total pressures and record them. We're hoping to carry out some work using hot-wire anemometry in association with Therm Advanced Research and McGill University.

Flow photography will continue and will be systematized. We hope to take pictures at specified azimuth angles of the propeller blade and at specific radii. From this, we should be able to get a three-dimensional location of the vortex patterns in both the tip vortex and the vortex sheet. This should be useful to anyone trying to develop a method to predict where these ought to go.

11
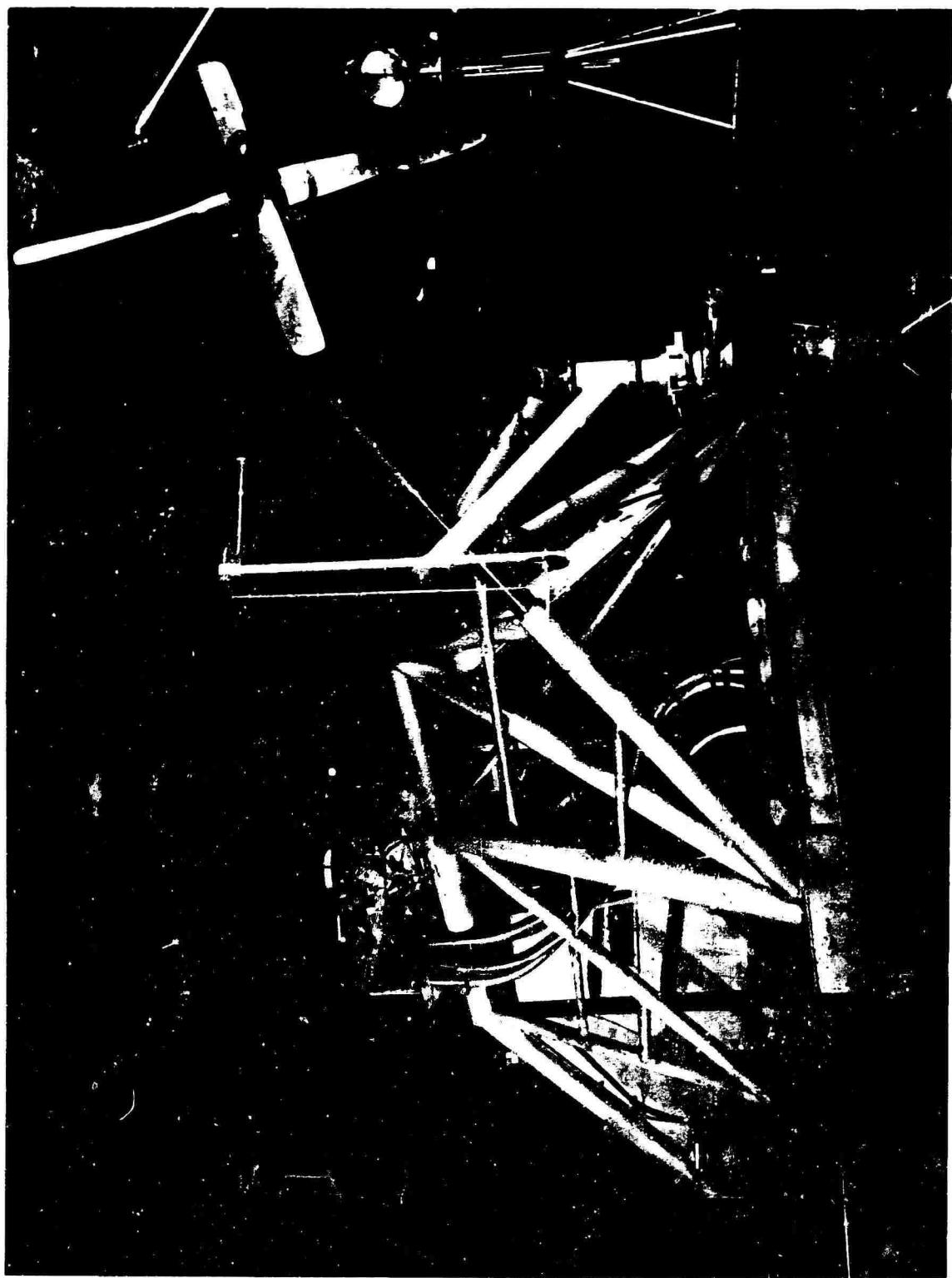
Figure 1 PROPELLER TEST RIG (PROBE TRAVERSING GEAR IN FOREGROUND)

12

Figure 2 PROPELLER TEST RIG

13
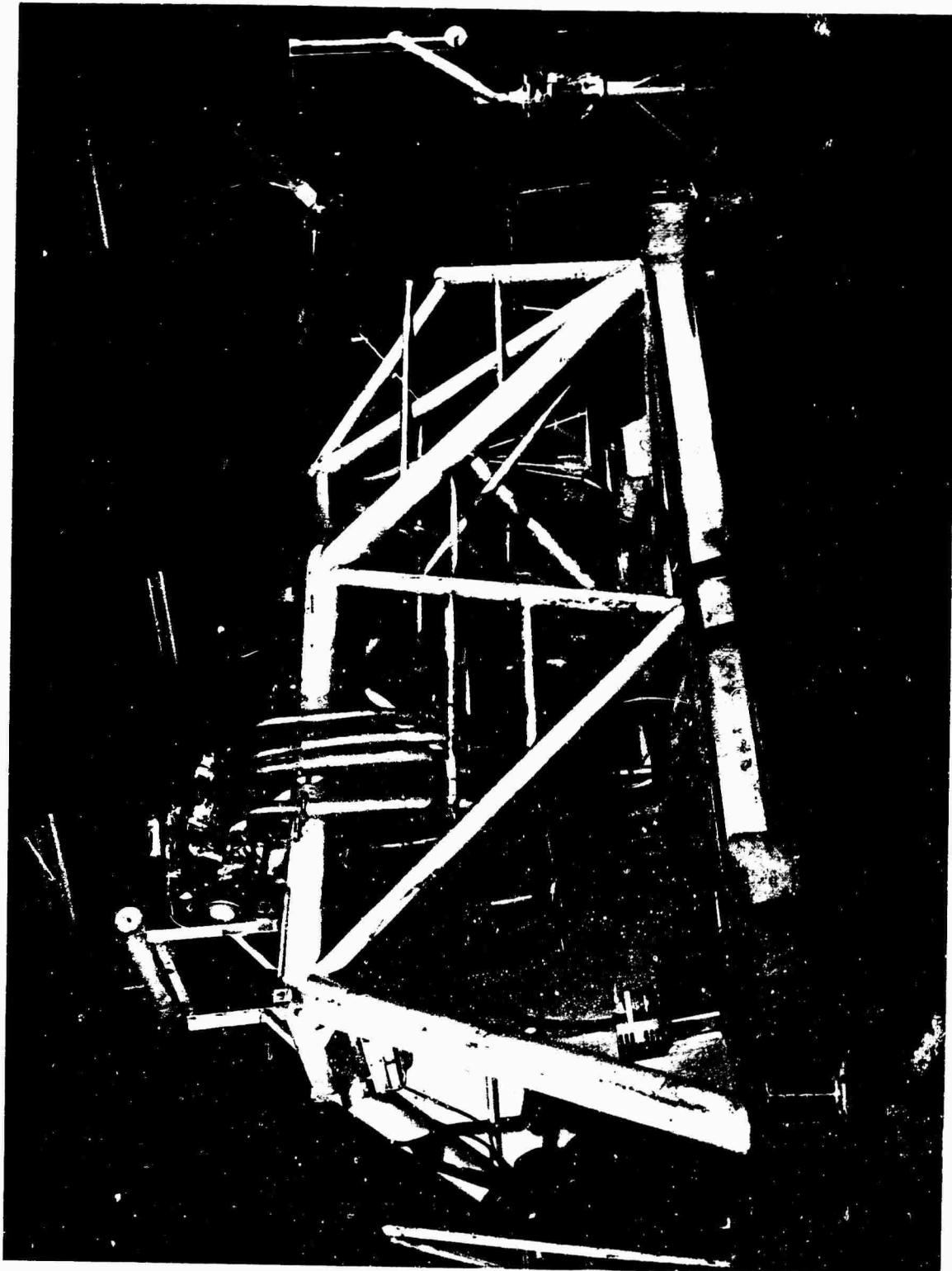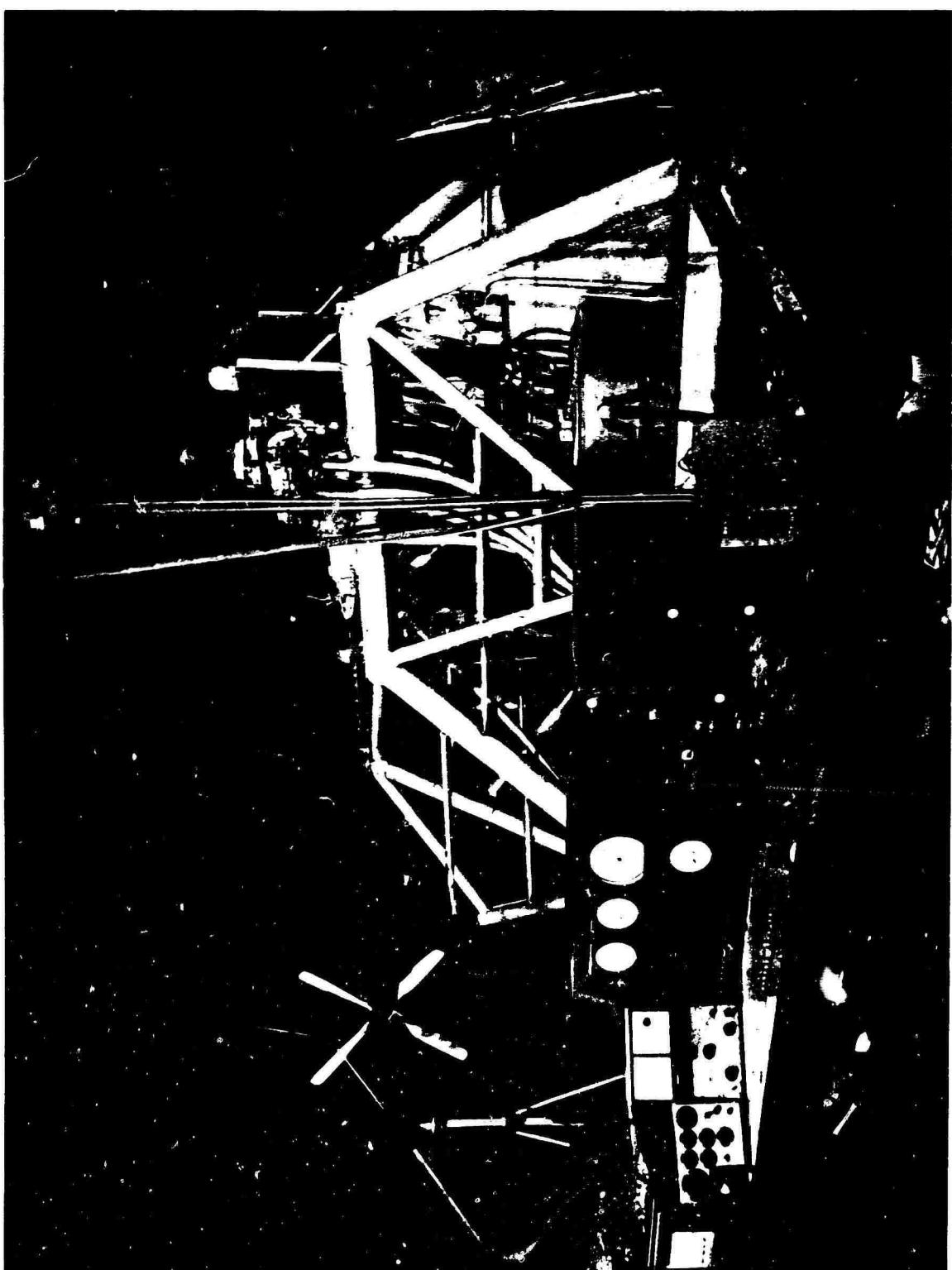
Figure 3 CONTROL AND READ-OUT STATION

Figure 4 SCHEMATIC DIAGRAM OF PROPELLER TEST RIG
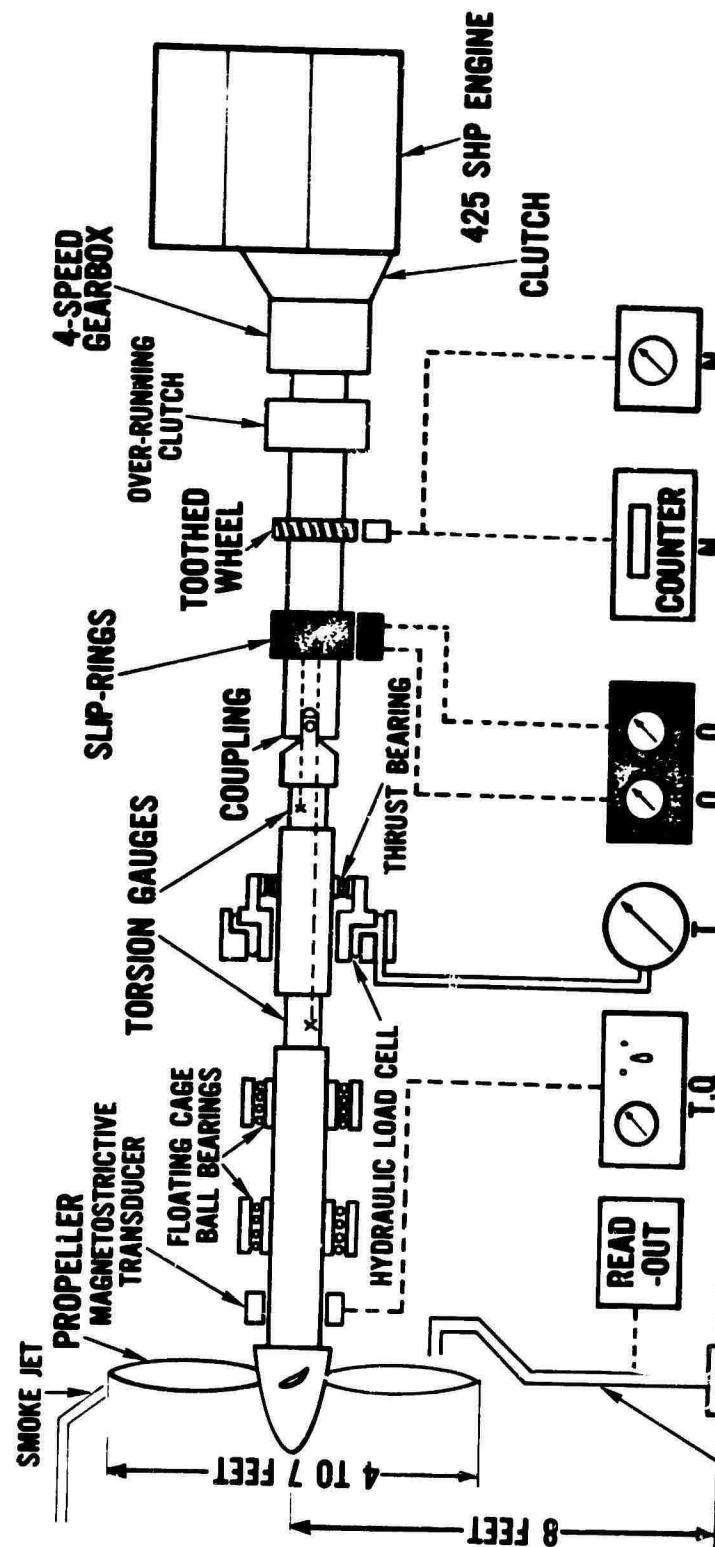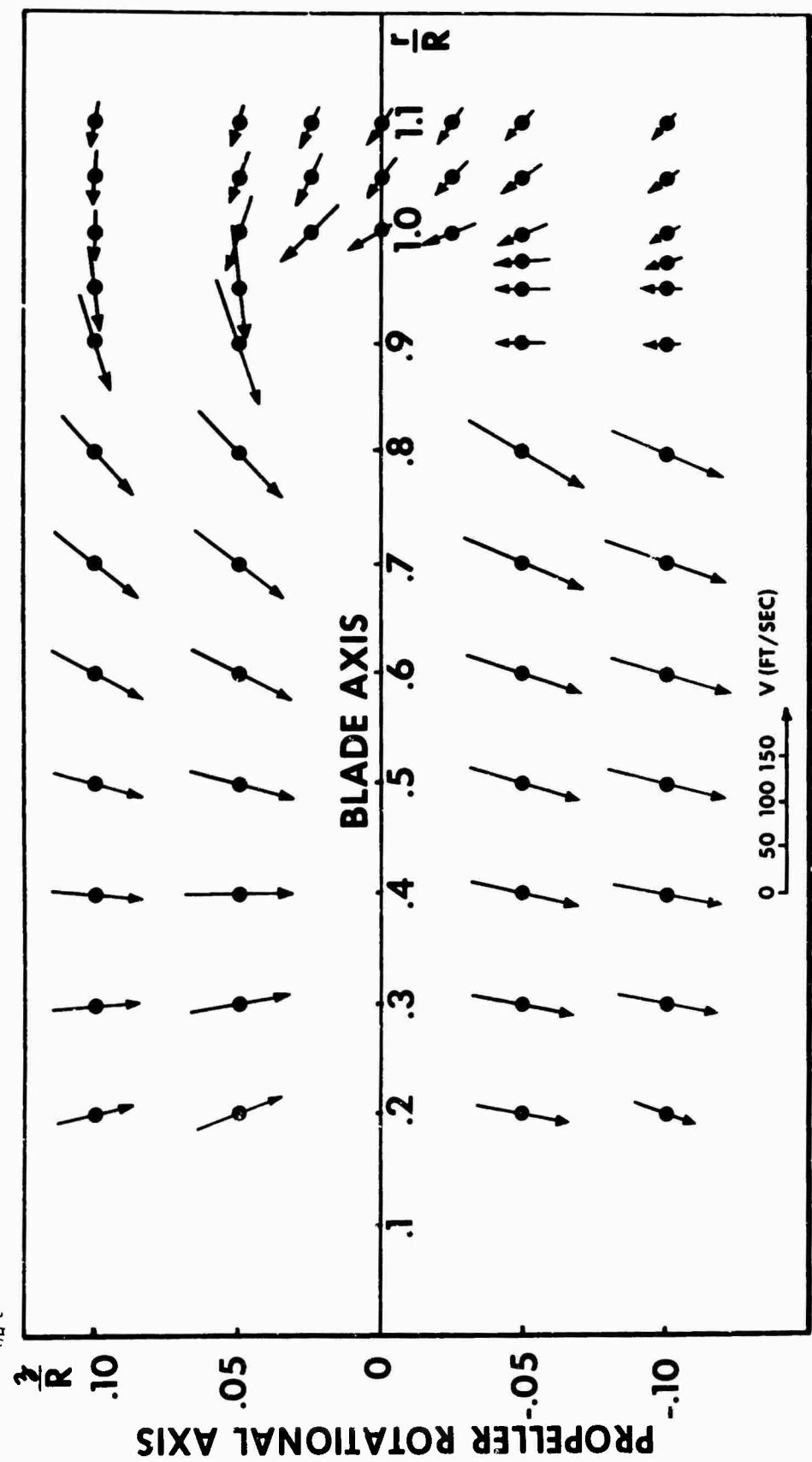
Figure 5 MEAN VELOCITY VECTORS (NOTE EXPANDED VERTICAL SCALE)
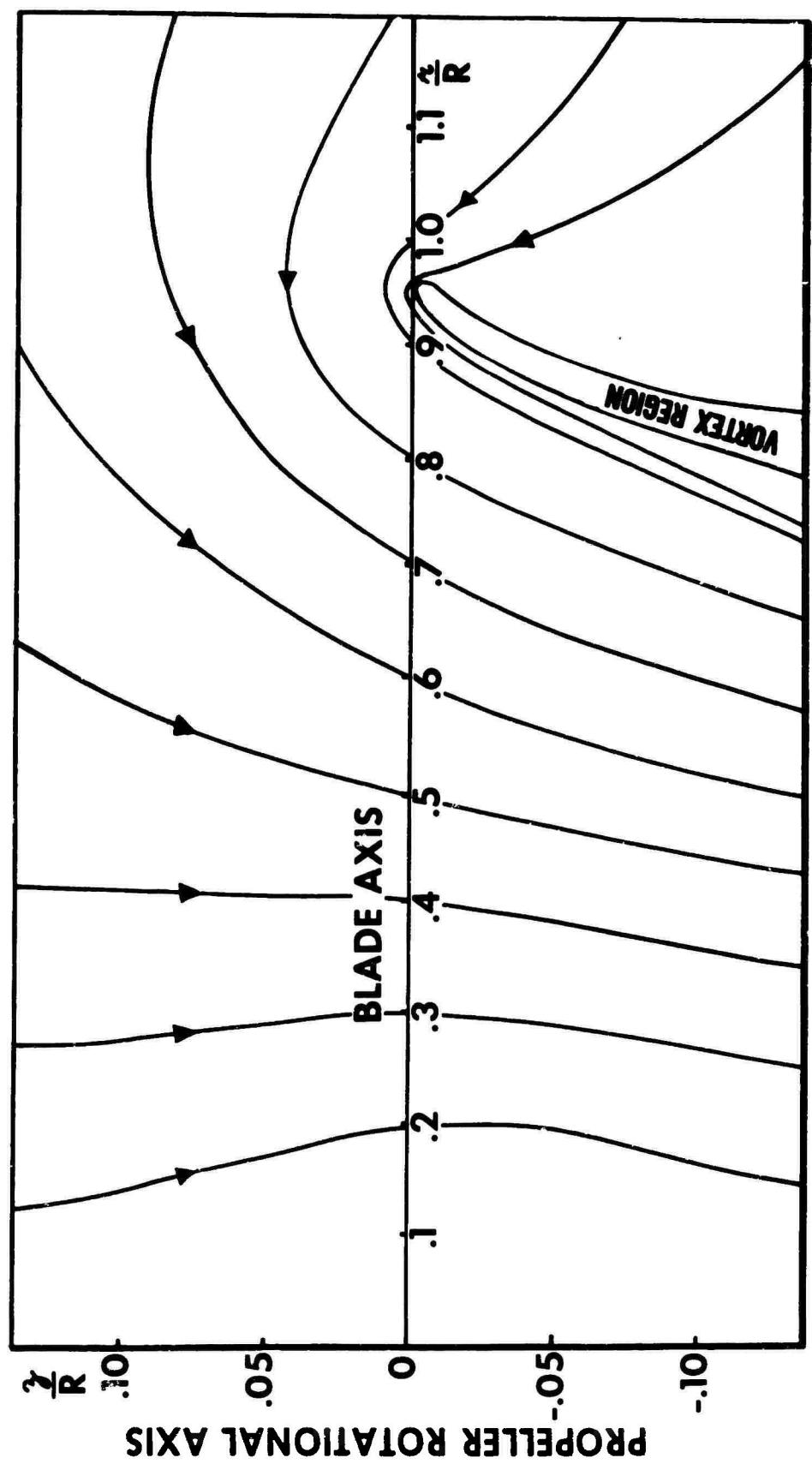
Figure 6 MEAN STREAMLINES
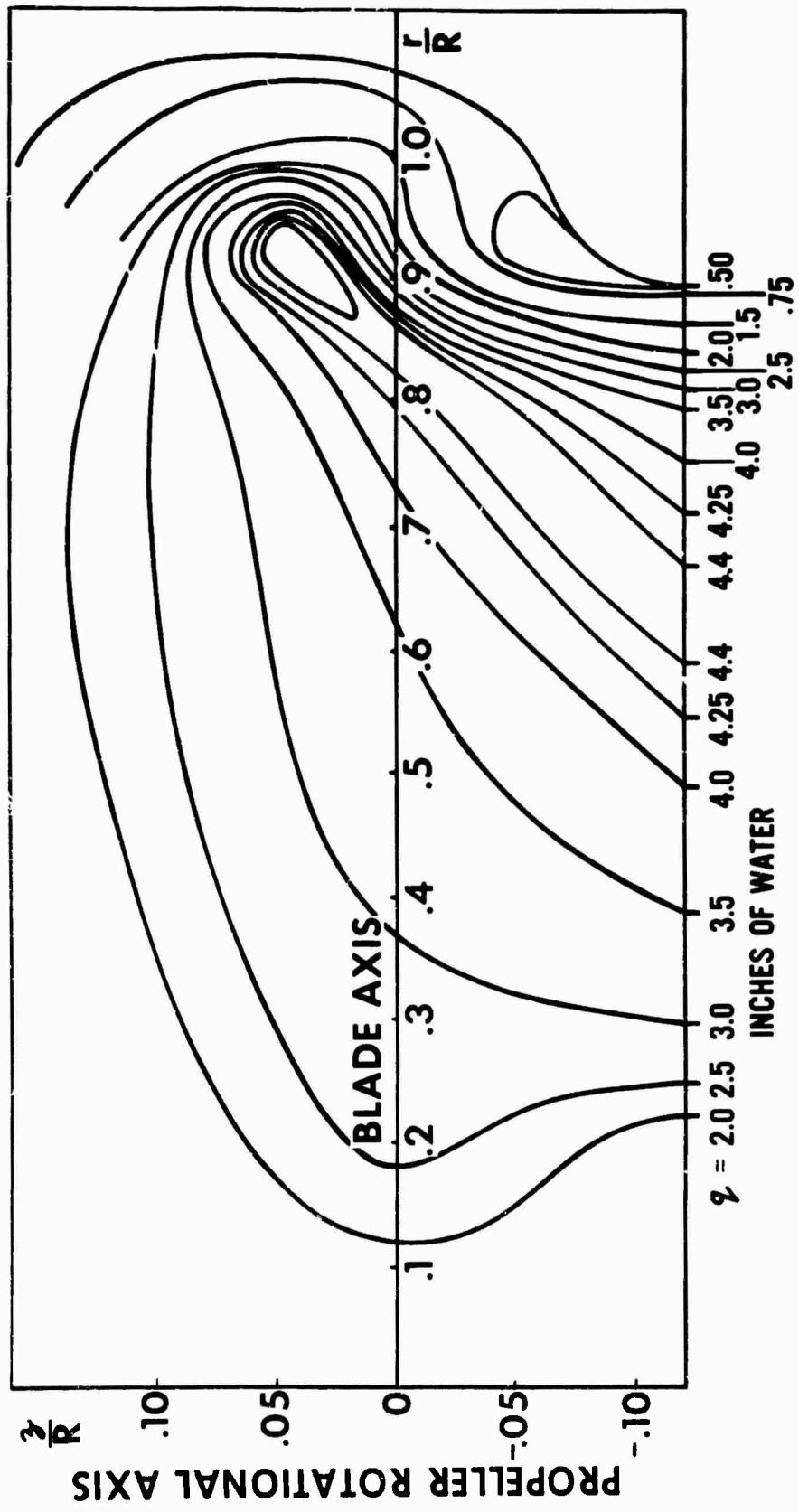
Figure 7 DYNAMIC PRESSURE CONTOURS

18
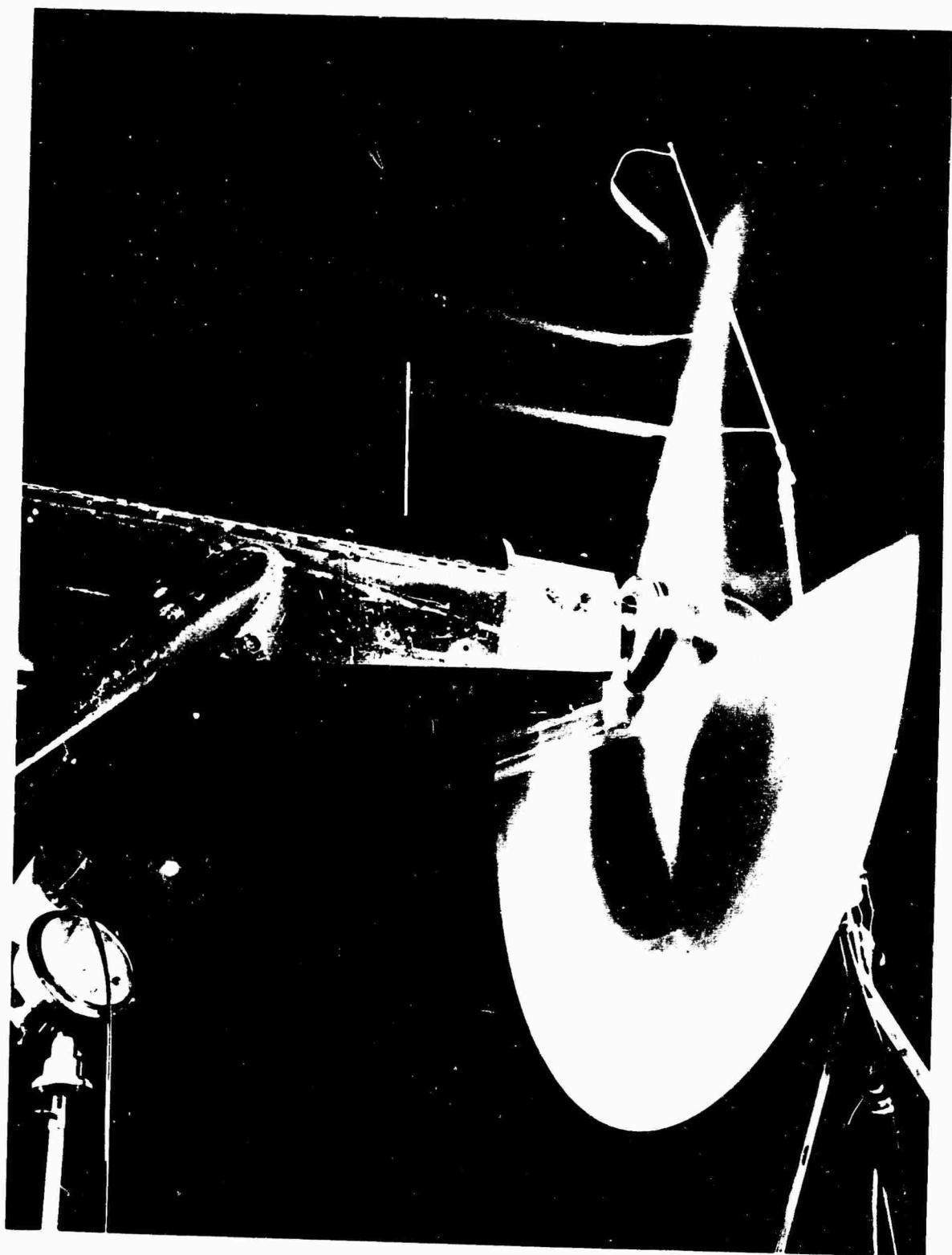
Figure 8   FLOW VISUALIZATION

19
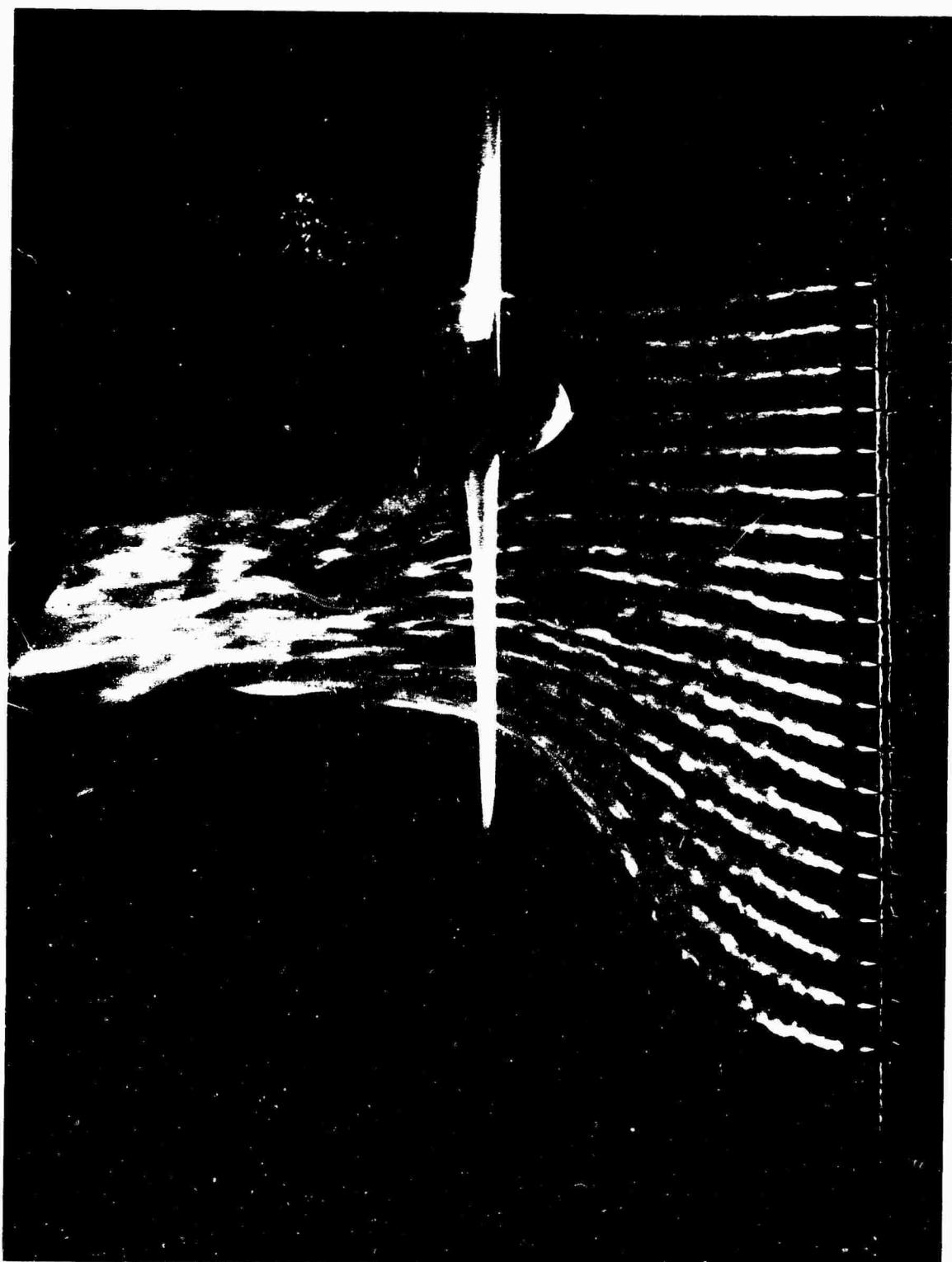
Figure 9 MULTIPLE JETS. CONTINUOUS ILLUMINATION
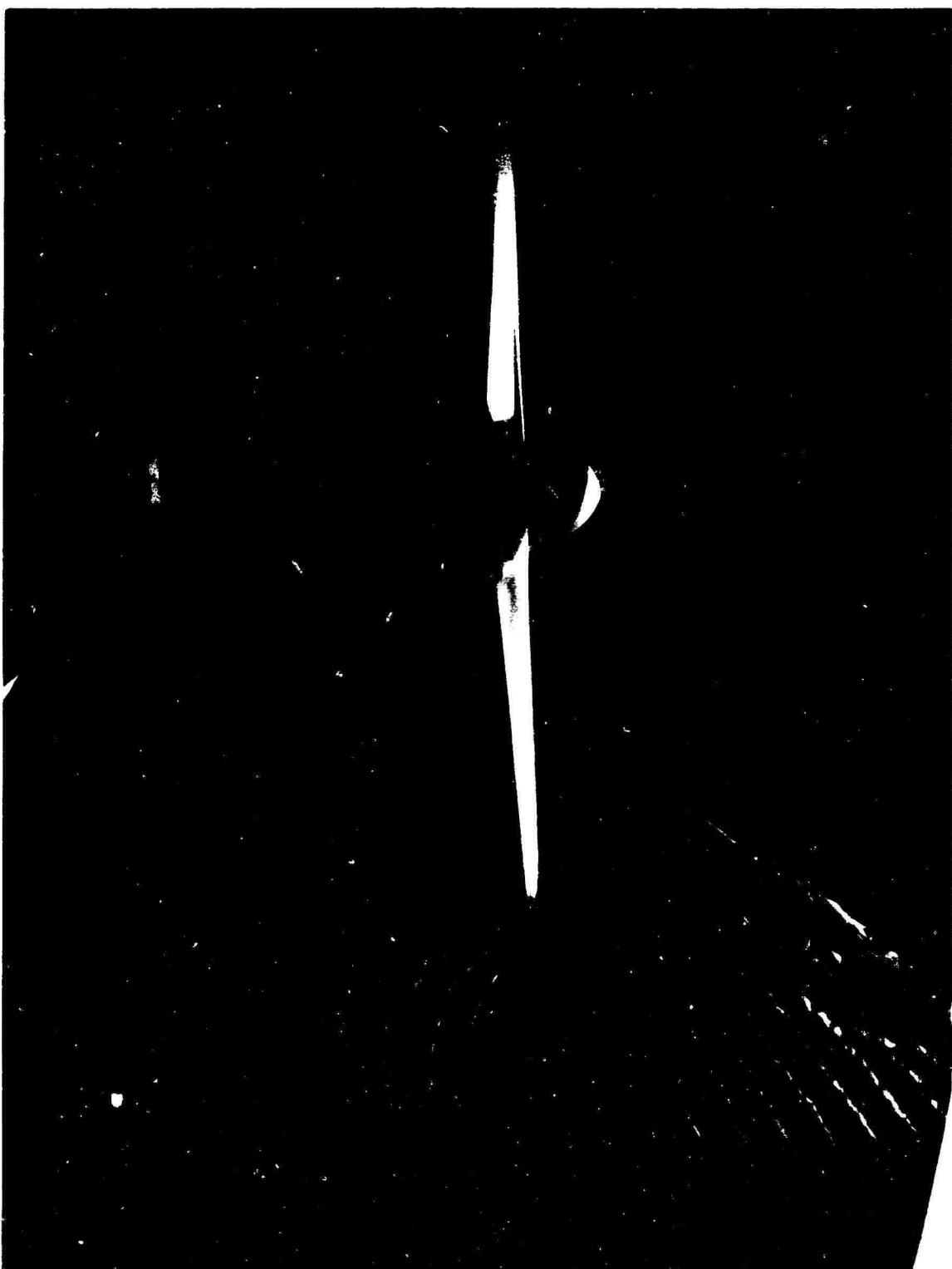
Figure 10 MULTIPLE JETS (NOTE FLOW ENTERS TIP FROM BEHIND)

Figure II   MULTIPLE JETS

22
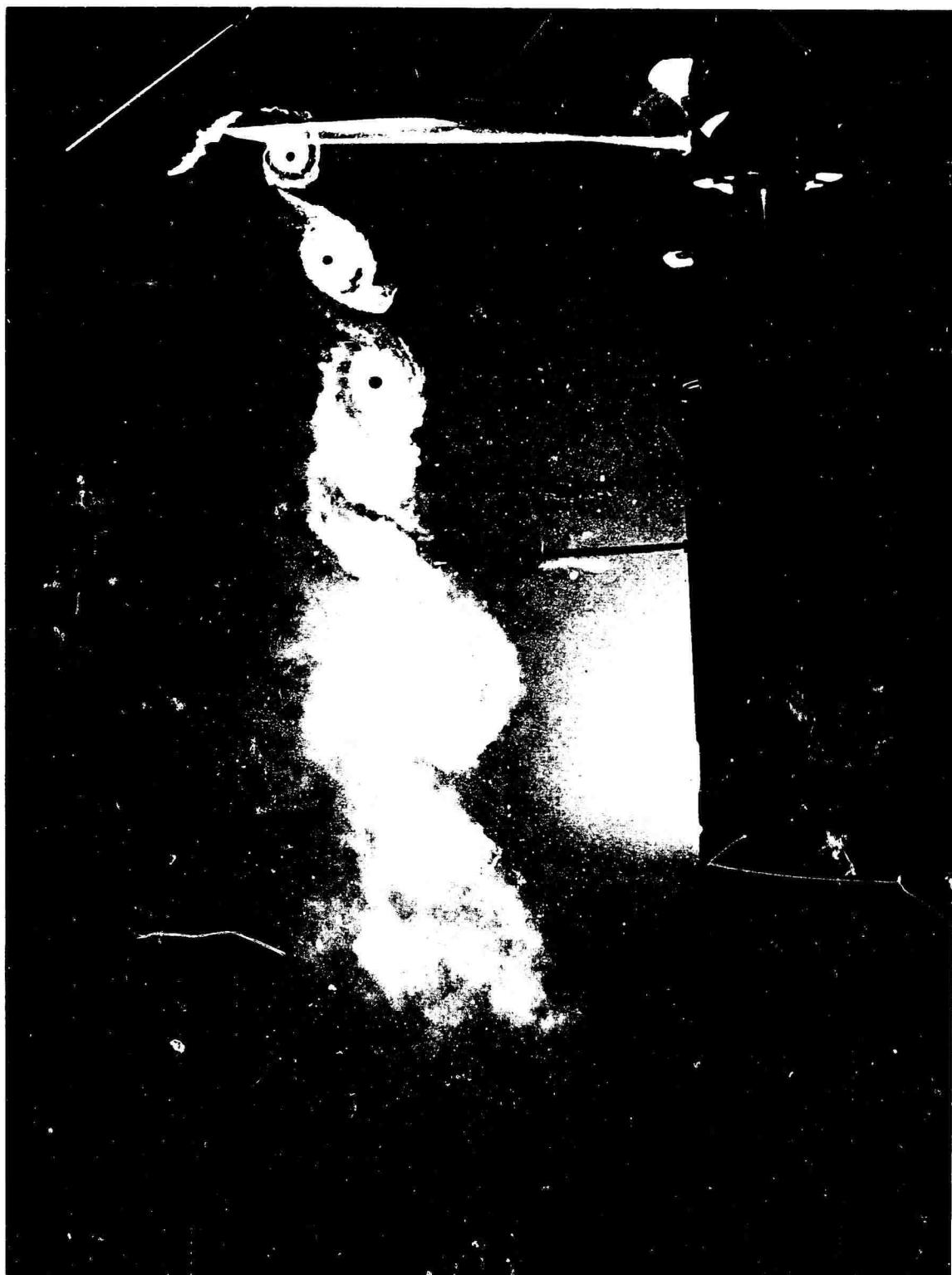
Figure 12 SINGLE JET, STROBOSCOPIC ILLUMINATION. JUST BEFORE ARRIVAL OF BLADE. (NOTE VORTEX CORES)

23
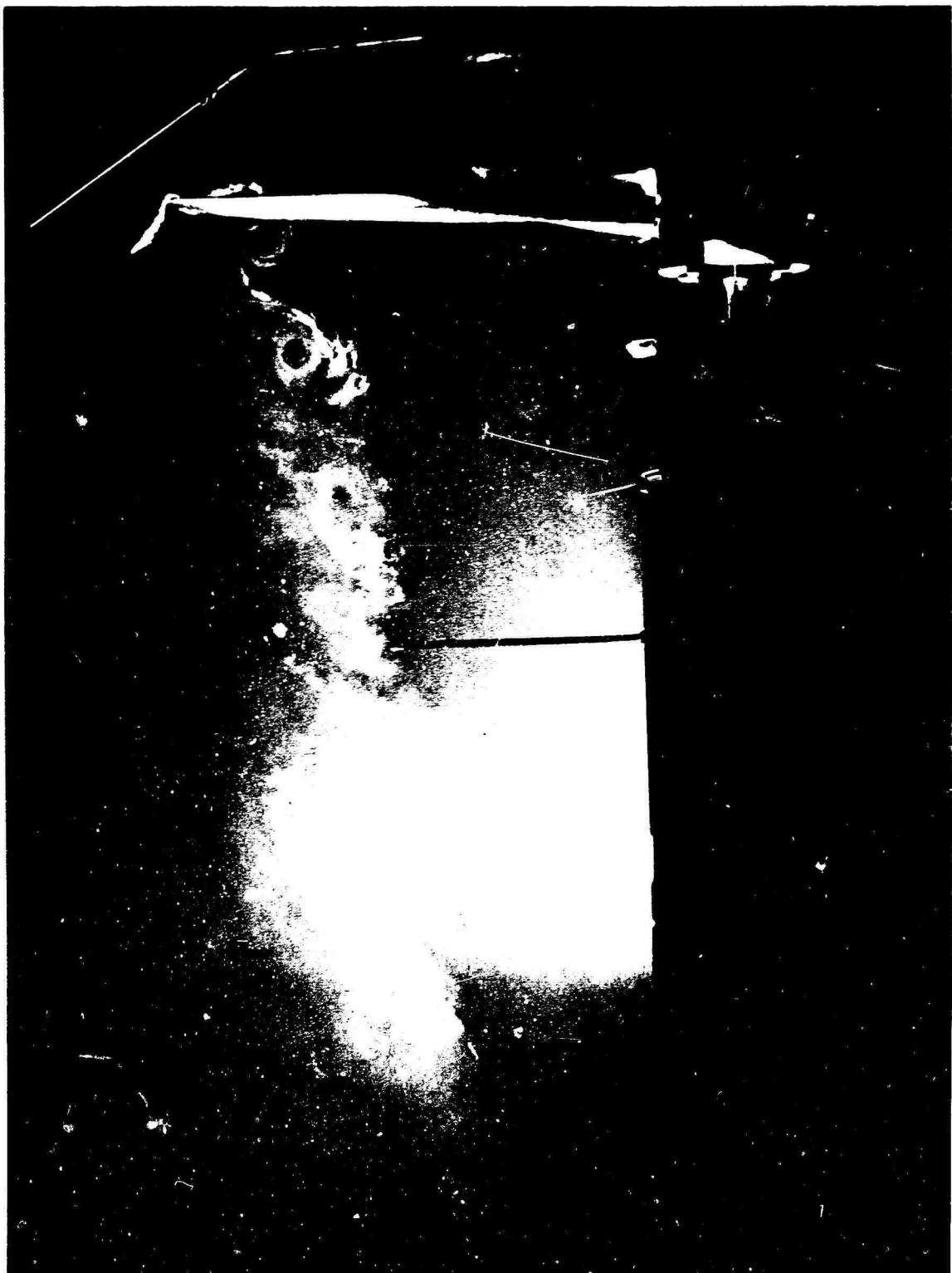
Figure 13 BLADE PASSING

24

Figure 14 JUST AFTER BLADE HAS PASSED

Figure 15 STILL LATER

26
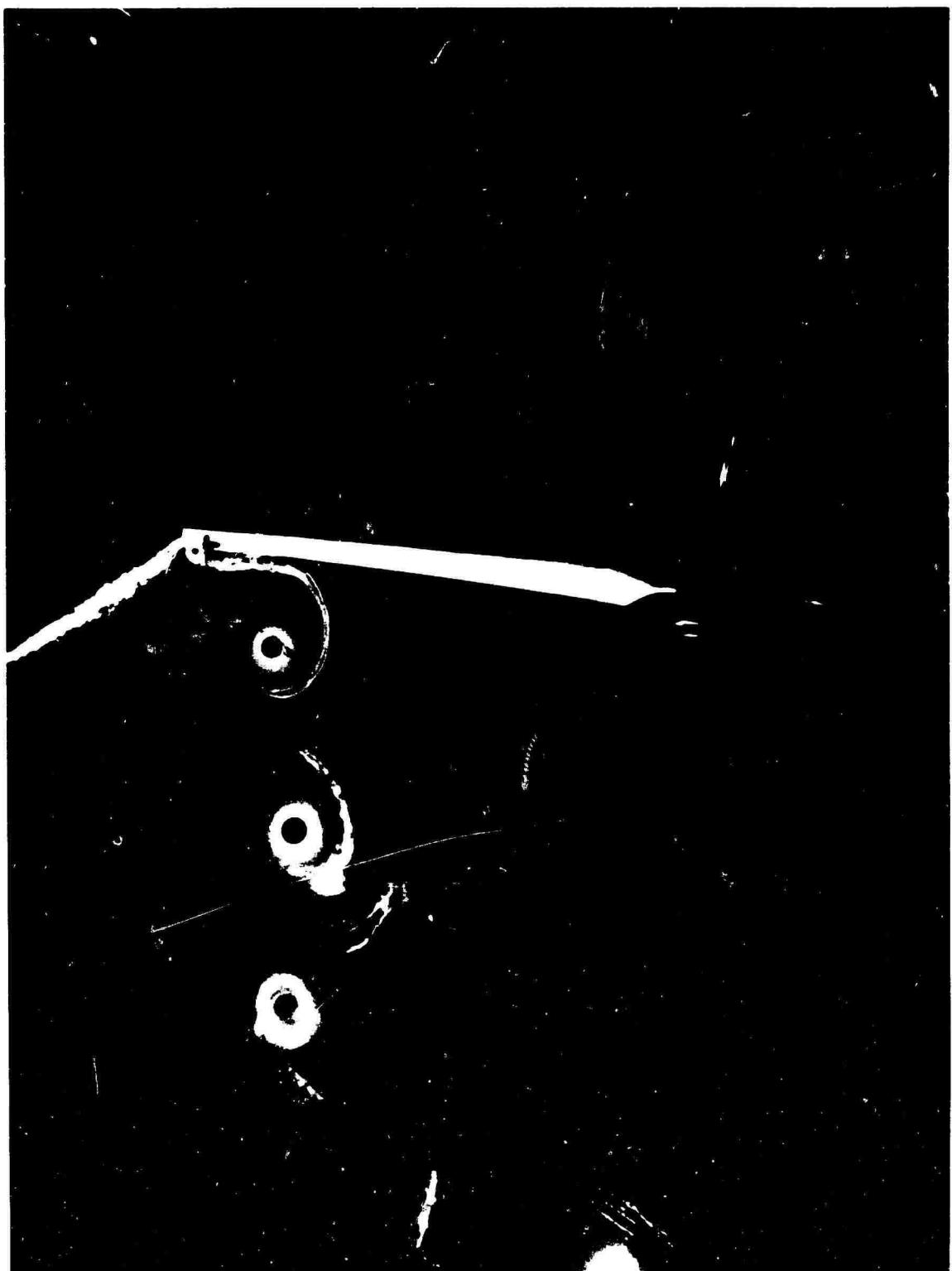
Figure 16 TWO-BLADED PROPELLER, $\beta.75 = 16°$ VORTEX FORMING AT TRAILING EDGE

Figure 17   45 DEGREES BEFORE BLADE ARRIVES

Figure 18 SMOKE ENTERING DISK AT APPROXIMATELY 60% RADIUS (NOTE DISCONTINUITIES DUE TO TRAILING EDGE VORTEX SHEET)

29

Figure 19 INTERMEDIATE SITUATION
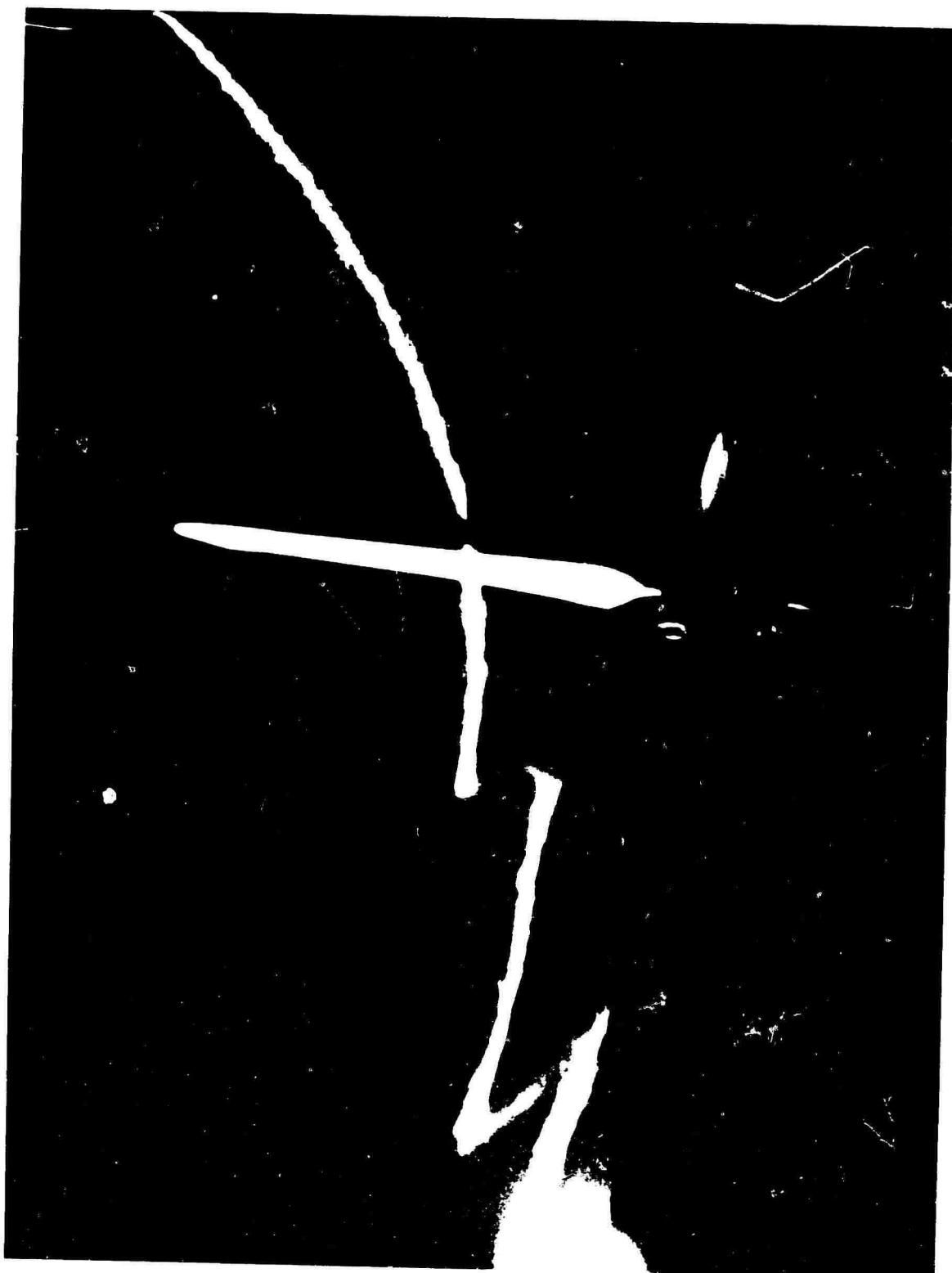
Figure 20 SMOKE AT 40% RADIUS

31
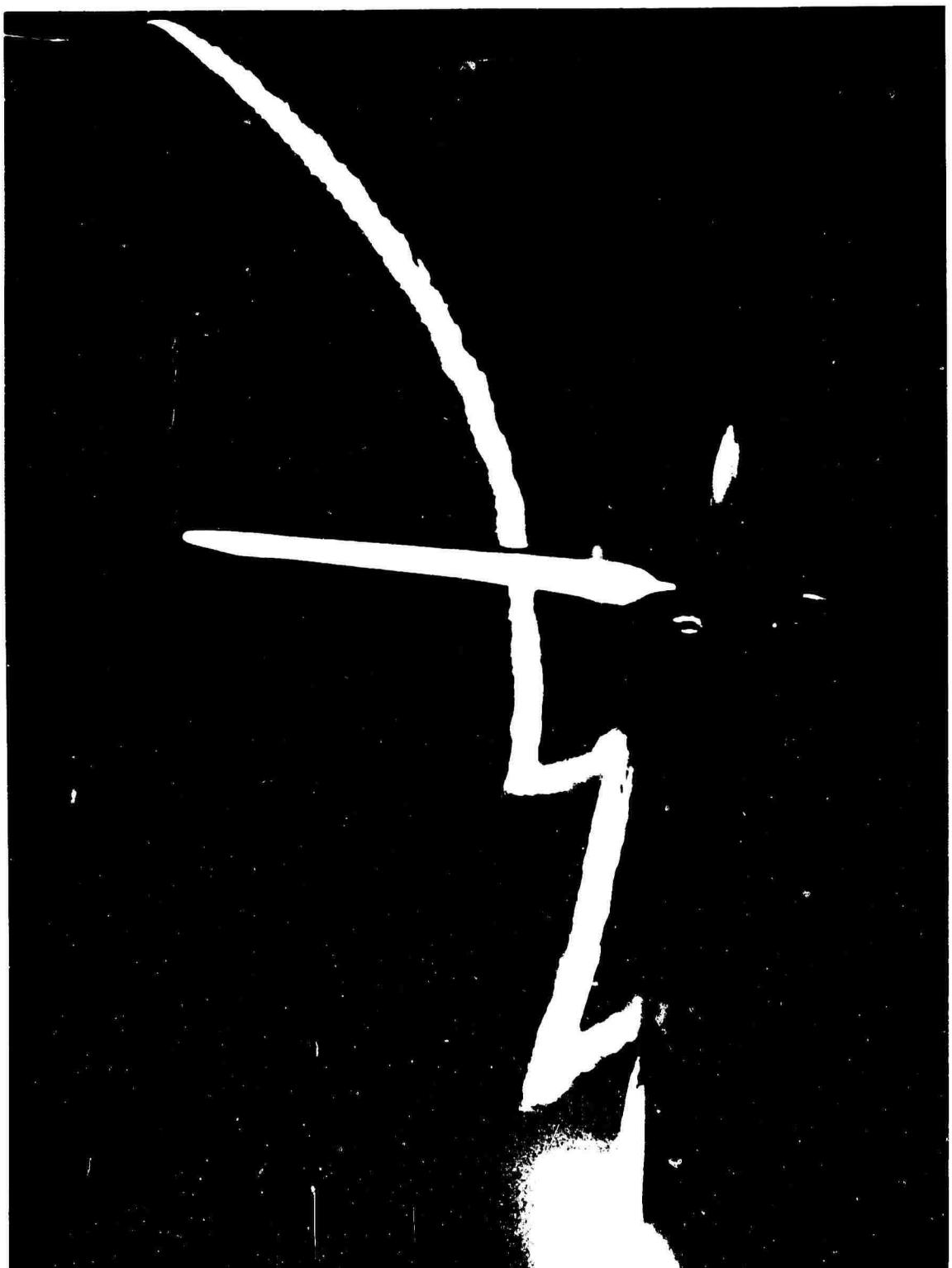
Figure 21 SMOKE AT 30% RADIUS
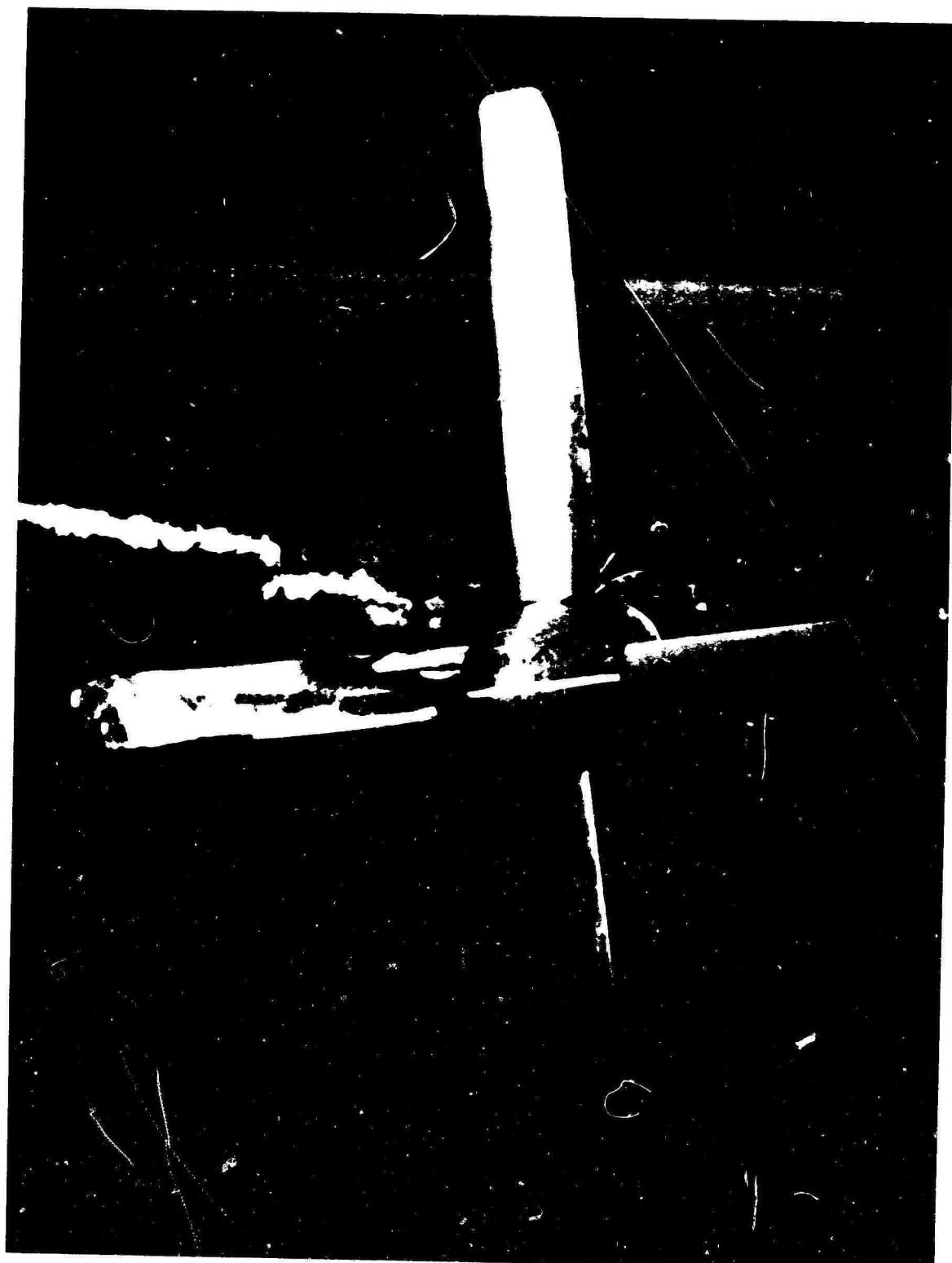
Figure 22 FRONT VIEW, SHOWING TANGENTIAL SHIFT
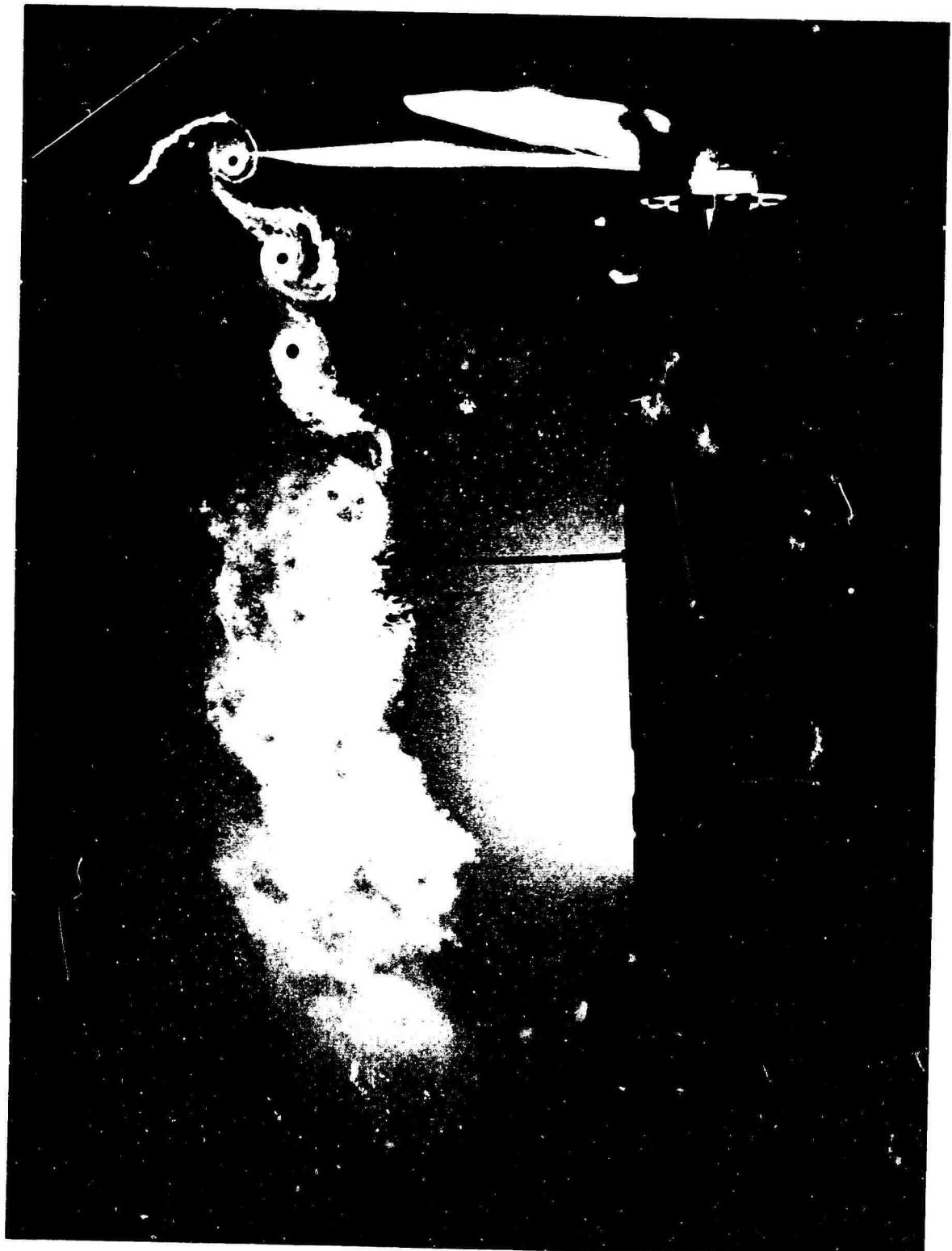
Figure 23   EFFECT OF BLADE ANGLE MIS-MATCHING (4 BLADES)

34
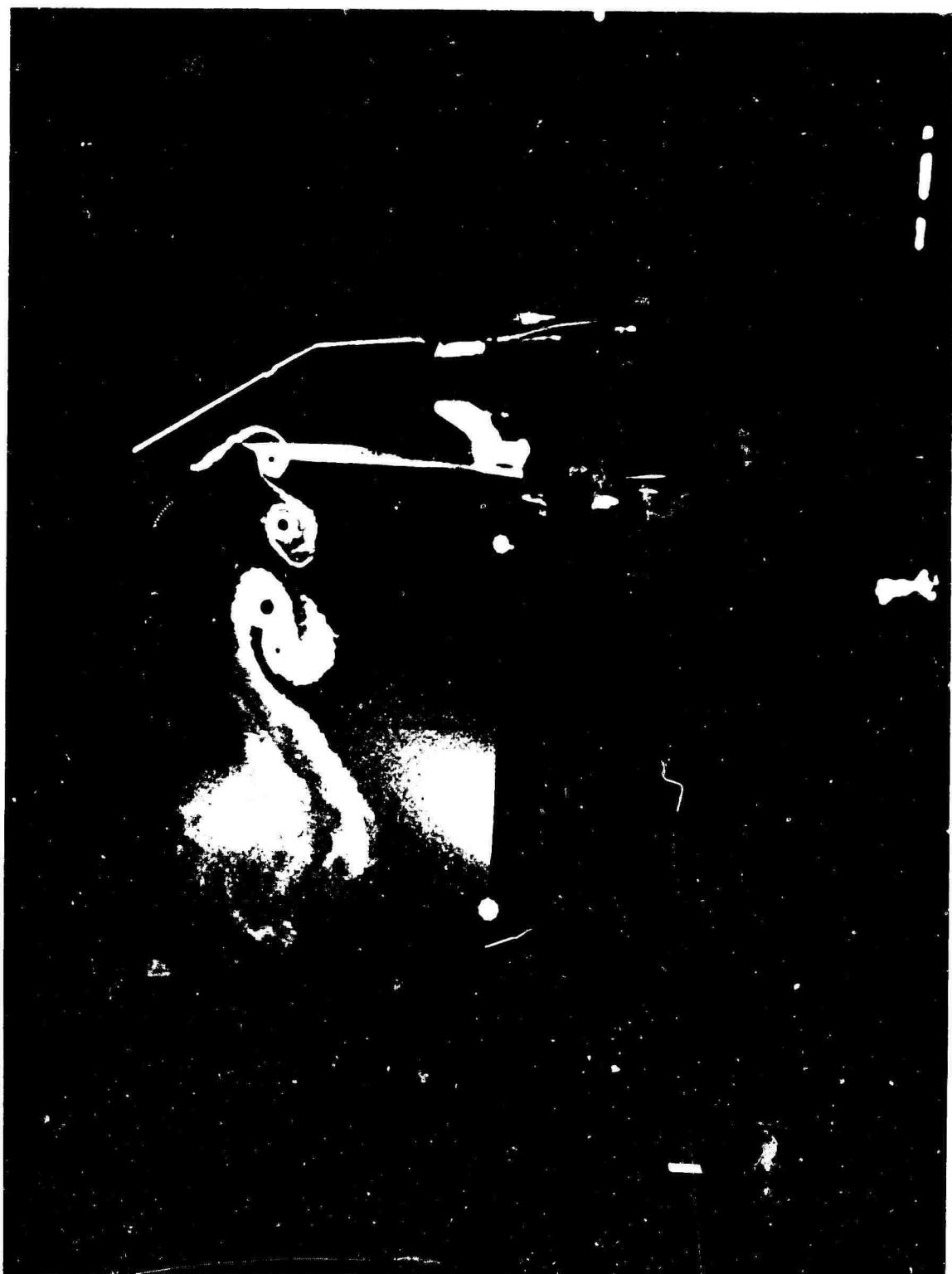
Figure 24 MIS-MATCHING (4 BLADES)

Figure 25 MIS-MATCHING. TiP VORTICES TRYING TO LOOP EACH OTHER (2 BLADES)

Figure 26   ENTRAINMENT FROM THE CEILING

37

Figure 27   ENTRAINMENT

38

PREDICTION OF THE PERFORMANCE AND STRESS CHARACTERISTICS OF VTOL PROPELLERS

by

A.R. Trenka

NOTES

PREDICTION OF THE PERFORMANCE AND STRESS
CHARACTERISTICS OF VTOL PROPELLERS*

by

A. R. Trenka

Cornell Aeronautical Laboratory, Inc.
Buffalo, New York, U.S.A.

SUMMARY

This paper represents the results of efforts to develop an improved method for the prediction of performance and stress characteristics of a single VTOL-type propeller-wing-nacelle combination operating in various flight conditions.

The problem of determining the airloads is treated by representing the propeller blade by a bound vortex of unknown strength and approximating the wake by a mesh of trailing and shed vortex elements.

Engineering beam theory is used to model the elastic behavior of a twisted rotating blade.

An iterative approach is used to solve the aeroelastic equations on a digital computer.

Some results are presented which show the effect on the performance and blade stresses of changing the inclination of the thrust axis with respect to the free stream, changing the wing load with other parameters held fixed, and changing the wake shape.

INTRODUCTION

With the advent of VTOL aircraft, more stringent requirements have been placed on the designer's ability to predict accurately the static thrust and torque characteristics of propellers. The accuracy with which these quantities are predicted may well determine whether the aircraft will fulfill its anticipated role as a VTOL vehicle. Since the entire lifting capability rests on the propellers, a small underestimate of the thrust might greatly reduce the payload.

In addition to the performance prediction problems, oscillatory stresses of unexpectedly large amplitudes have been observed on the propellers of VTOL aircraft during wind-tunnel and full-scale tests. In particular, these stresses have been noted in the transitional range from a hover to an axial flight configuration.

Propeller designers have suddenly found themselves reexamining "tried and true" propeller performance and stress theories and finding them to have, at best, questionable applicability in the hover and transitional flight range. No proven theoretical approach was available for the skewed flight range in which high oscillatory stresses were observed. Furthermore, they found that many of the experimental data upon which previous correlation with theory had been based were not sufficiently accurate to aid in the development of more accurate theories or in the extension of existing ones.

In an effort to provide a theory which would allow accurate prediction of performance and stresses of VTOL-type propellers through their entire flight range, Cornell Aeronautical Laboratory, Inc. (CAL) began the investigation reported, in part, herein. This work was sponsored by the U.S. Army Aviation Materiel Laboratories (USAAVLABS). The basic method developed by CAL and reported in Reference 3 for the prediction of rotary-wing airloads in hovering and forward flight was modified, extended, and applied to the problem of VTOL-type propellers.

2

DEVELOPMENT OF THE THEORETICAL PROGRAM

Statement of the Aeroelastic Problem

Solution of the aeroelastic problem requires a knowledge of the interaction of the aerodynamic, elastic, and inertial forces acting on a wing secion. Once these interactions are known, the loads and motions of the section, and hence the total wing loads and motions, may be determined. The problem is a difficult one for conventional wings. For rotary wings, i.e., propeller blades, the problem is compounded by the nature of the wake shed from the blades, which now takes on the geometry of a distorted heliz; by the rotation-induced elastic coupling between various blade motions; and by the complicated inertia loads which arise when motions occur in a rotating frame.

In addition, there are interference effects from wings and nacelles which lie in the slipstream and which might be quite close to the propeller plane. To define the interaction of these forces, the following aerodynamic and structural models were employed. (The discussion will be limited to steady-state flight.)

Aerodynamic Model

The aerodynamic model accounts for the effects on the blade of (1) a distorted wake, (2) a wing and nacelle lodged in the propeller slipstream, (3) forward flight, and (4) blade deformations under load.

The entire model rests upon periodicity and the ability to predict the wake position with sufficient accuracy.

Representation of the Blade

The blade is represented by a bound vortex of strength, Γ, placed at the blade quarterchord. The Γ of the bound vortex varies both with radius and with time. Since steady-state flight conditions only are being considered, the time variation is periodic of period T'. T' is the time for one rotor revolution; hence, the time variation of Γ is equivalent to the

3

azimuthal variation. Thus, the radial and azimuthal variations of Γ are given by $d\Gamma/dX$ and $d\Gamma/d\psi$ (X is the radial position and ψ is the azimuthal angle). The radial distribution is represented by breaking the bound vortex up into $\overline{NR}$ spanwise segments of constant Γ . The azimuthal variation is similarly accounted for by allowing each radial segment to assume a new value of Γ as it is stepped through $\overline{NA}$ azimuthal stations. Thus, the radial and azimuthal variation of Γ is represented by ($\overline{NR} \times \overline{NA}$) discrete values of Γ . The magnitude of Γ is determined by requiring that the chordwise boundary condition of zero normal velocity at the three-quarterchord of the blade be satisfied.

Representation of the Wake

Because of the variation of Γ with X and ψ , a continuous sheet of vorticity is deposited into the wake. Because of the steady-state flight conditions, the variation of Γ with X and ψ is repeated for each and every blade revolution. The wake is represented in a fashion analogous to the representation of the bound Γ distribution. The continuous wake is modeled by a mesh of "trailing" and "shed" vortex elements, see Figure 1. The "trailing" vortex element is deposited in the wake from the ends of the segmented bound vortex and is equal to the difference between adjacent bound vortex element as the blade moves from one azimuthal position to the next. Its strength is equal to the difference between bound Γ's at successive azimuthal positions. Thus, if a given trailing vortex is followed back into the wake, it is found that its strength varies in a stepwise fashion. It is constant for the interval corresponding to the increment between successive azimuthal positions of the blade. Similarly, consider the shed vortex deposited in the wake at some azimuthal position. It varies in stepwise fashion along its span. The variation corresponds to the spanwise variation of the bound vortex which existed on the blade when the blade was in that azimuthal position.

4
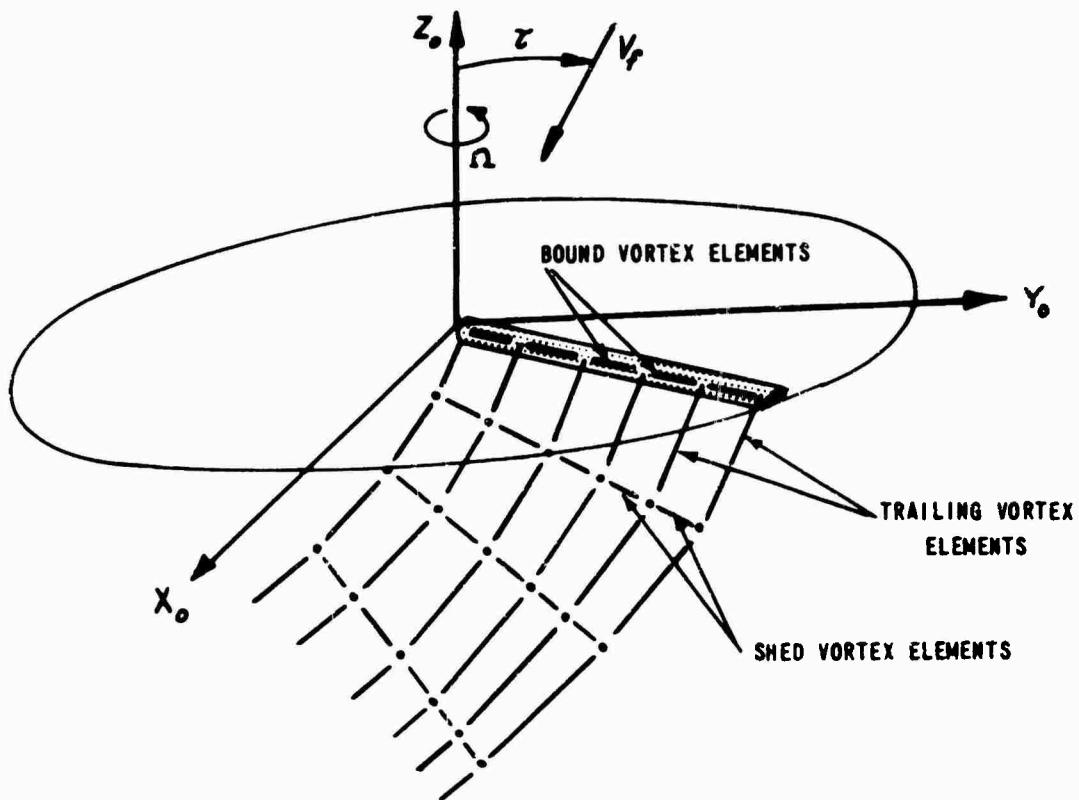
Figure I. PICTORIAL REPRESENTATION OF BLADE WAKE MESH.

Thus, the continuous sheet of vorticity deposited in the wake has been replaced by a mesh of shed and trailing vortex elements whose strengths are proportional to the strength of the bound vortex. This mesh is repeated in a continuous fashion once per revolution of the blade and for each blade in the propeller set.

Now, consider the problem: "How is the wake positioned relative to the blades which generated it?" The wake position is determined by the interplay of such effects as (1) self-induced velocities of the wake, (2) free-stream velocity, and (3) interference velocities from wings, nacelles, fuselages, etc., in and in the proximity of the slipstream. The present method attempts to account for the effects of (1) wake contraction and radial and axial variation of the wake velocity, (2) free-stream velocity, and (3) the perturbing effect of a wing and nacelle completely immersed in the slipstream.

5

The wake contraction and axial and radial velocity variation is estimated for hovering flight by using a system of finite core ring vortices. The theory was developed at CAL under Office of Naval Research sponsorship and is reported in detail in Reference 1. Briefly, the approach replaces the slipstream by an axial system of discrete, finite-core, ring vortices. The system is treated as a starting problem by periodically releasing a new vortex ring in the reference plane while allowing the individual rings to move under mutual influence according to the laws of vortex dynamics. After a sufficient number of rings have been released, a stabilized trajectory is determined down which all successive rings move. The solution was obtained using a digital approach, and the program output yields a time history of the coordinates and velocities of all vortex rings.

This model was applied to the propeller slipstream problem in which the wake is treated as a mesh. The tip-trailing vortex was assumed to move down the surface generated by the stabilized ring vortex trajectory. This was done by requiring that the tip vortex move with the velocities with which the rings move. Thus, at the tip of the blade, the trailing vortex was deposited in the wake with the velocities of the ring at the instant the ring was deposited in the reference plane which now corresponds to the prop plane. This tip vortex, then, was allowed to move for the interval of time corresponding to $1/\overline{NA}$ rotor revolutions. At the end of this period, it would assume new values of velocities corresponding to the velocities which the ring experienced at that position in the wake, and so on down the wake. Since the ring velocity distribution is axially symmetric, tip vortices deposited at various azimuthal stations all move down the wake with the same velocity time history but are displaced in time with respect to one another (see Figure 2).

The result is a tip helix of varying pitch and diameter.

To place the mesh interior to the tip elements, it was assumed that (1) all interior elements move with the same axial velocity as the tip vortex element, and (2) the radial velocity of the interior elements is proportional to the product of the radial position of the element and the radial tip velocity.

6
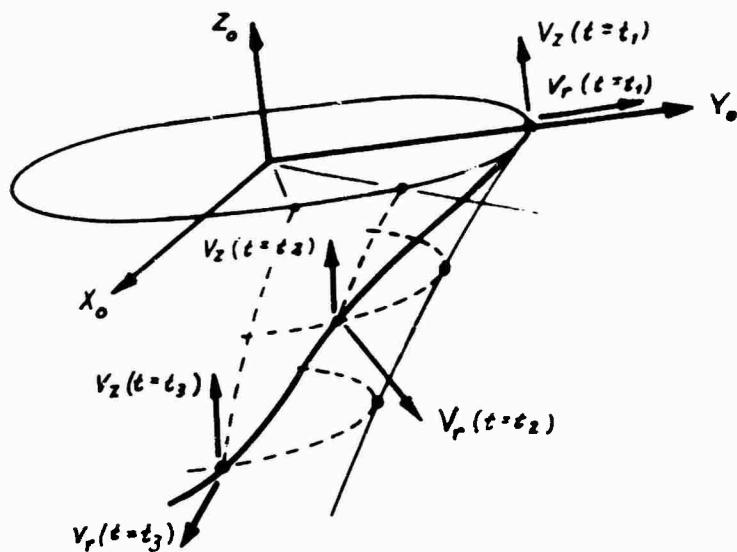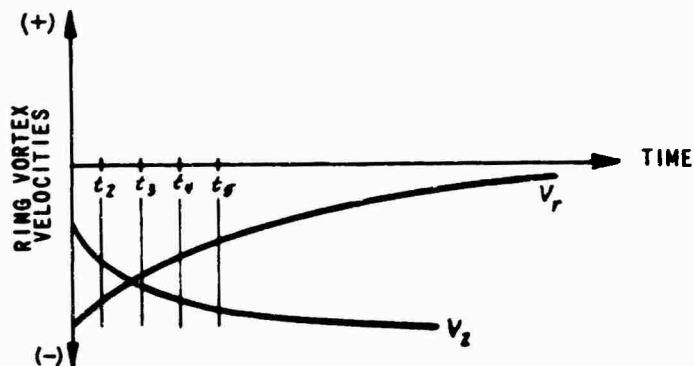
Figure 2. PICTORIAL REPRESENTATION OF TIP VORTEX
MOVING DOWN RING VORTEX TRAJECTORY.

There is no mechanism, at present, to allow for a tangential, or swirl, component of velocity.

This wake model will be referred to as the RVM (ring vortex model).

The wake, as positioned by the RVM, is used as a base from which small perturbations due to the free stream, wing, and nacelle are allowed in the case of low forward speeds. These perturbations are included as incremental velocities at each control point in the wake (as determined from the RVM).

7

Thus, in the hovering condition, a distorted wake is used which includes the effects of contraction, radial and axial velocity variations, and interference effects from wing and nacelle. For the initial stages of transition, i.e., low forward speeds, the freestream is included as an additional perturbation. For higher forward velocities, the model postulated above breaks down, and the wake is treated as a skewed helix of uniform pitch, with none of the effects of contraction or wing and nacelle. However, if a wake shape, i.e., position, is known for a given flight condition, it can be included in the program.

Representation of the Wing and Nacelle

The interference effects of the wing and nacelle can be treated in terms of, first, their direct effect on the angle of attack at the propeller and, second, their effect in distorting the wake. The direct effect is always included when applicable. The second effect is included only in the hovering and low forward speed transition cases.

To model the nacelle, it was assumed that its effects could be adequately approximated by treating it as a Rankine body (source-sink combiation). The Rankine body length was taken equal to the nacelle length and the Rankine body diameter was taken such that its projected frontal area equals that of the nacelle.

The wing was simply treated as a bound vortex placed at the wing quarter chord.

Development of the Mathematical Model of the Propeller and Wake

The equations which will will eventually give the aerodynamic forces required for the aeroelastic problem will now be developed. The equations will be formulated in terms of the strength of the bound vortex Γ. Consider an element of a blade of a propeller in skewed flight with a wing and nacelle immersed in the propeller slipstream (see Figure 3).

8
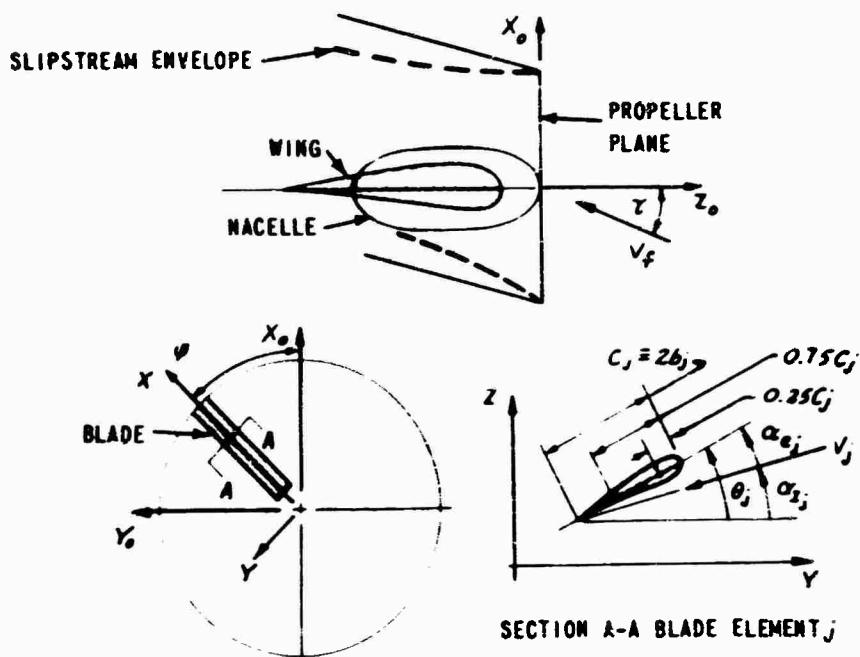
Figure 3. GEOMETRY FOR AERODYNAMIC MODEL OF PROPELLER, WING, AND NACELLE.

The lift per unit length on this j^{th} blade element is

$$\ell_j = \rho V_j \Gamma_j \tag{1}$$

where

ρ = density

V_j = local total velocity

Γ_j = local vortex strength

But ℓ_j can also be written as

$$\ell_j = b_j \rho V_j^2 c_{\ell_j} \tag{2}$$

where

c_{ℓ_j} = section lift coefficient

b_j = local blade semichord

Then from (1) and (2),

$$\Gamma_j = b_j V_j c_{\ell_j} . \tag{3}$$

9

Generally the section lift coefficient, c_{l_j}, is a nonlinear function of the effective angle of attack, α_{e_j}. To allow for the possibility of this nonlinearily, as well as to provide a mechanism by which Reynolds number and Mach number effects can be introduced, the c_{l_j} curve was expanded in a Taylor series about an arbitrary reference angle α_{o_j}; i.e.,

$$c_{l_j} = \left[c_{l_o} + \frac{dc_l}{d\alpha}\bigg|_{\alpha_o} (\alpha_e - \alpha_o) + \frac{1}{2} \frac{d^2 c_l}{d\alpha^2}\bigg|_{\alpha_o} (\alpha_e - \alpha_o)^2 + \cdots \right]_j . \tag{4}$$

It is now required that

$$(\alpha_e - \alpha_o) << 1,$$

and, hence, terms higher than ($\alpha_e - \alpha_o$) may be neglected in Equation (4). Thus, Equation (3) becomes

$$\Gamma_j = b_j V_j \left[c_{l_o} + \frac{dc_l}{d\alpha}\bigg|_{\alpha_o} (\alpha_e - \alpha_o) \right]_j . \tag{5}$$

Equation (5) is regrouped to get

$$\Gamma_j = \Gamma_{o_j} + b_j V_j a_j \alpha_{e_j} \tag{6}$$

where

$$\Gamma_{o_j} = b_j V_j \left[c_{l_o} - \frac{dc_l}{d\alpha}\bigg|_{\alpha_o} \alpha_o \right]_j$$

$$a_j = \frac{dc_l}{d\alpha}\bigg|_{\alpha_{o_j}}$$

The assumption is now made that

$$\sin \alpha_e \approx \alpha_e .$$

This approximation leads to a maximum error in lift of approximately 2% when $\alpha_e = 20^{\circ}$. Since α_e will generally be much less than 20°, it was felt that this assumption would not significantly limit the validity of the theory.

From Figure 3, it is recognized that

$$V_j \alpha_{e_j} \approx V_j \sin \alpha_{e_j} = v_j .$$

10

From lifting-line theory, v_j' can be interpreted as the velocity perpendicular to the airfoil chord at the three quarterchord point. Its sense must be positive up to give increased lift for increased v_j'. Equation (6) now becomes

$$\Gamma_j = \Gamma_{o_j} + b_j a_j v_j' . \tag{7}$$

The perpendicular velocity includes contributions from free stream, wake, nacelle, wing, and blade elastic motions; thus,

$$v_j' = \left[(X\Omega + V_f \sin \tau \sin \psi) \sin \theta - \dot{h} + v^W + v^N + v^I \right]_j \tag{8}$$

where, for the jth blade element,

X_j = radial distance from centerline of rotation to j^{th} blade element

Ω = rotor speed

θ_j = total geometric angle including built-in twist, β_j, and elastic motions, ϕ_j, of the jth blade element

$\dot{h}_j$ = elastic motions perpendicular to the airfoil chord of the jth blade element + $V_f \cos \tau \cos \theta$,

v_j^W = velocity due to wing perpendicular to chord of jth blade element

v_j^N = velocity due to nacelle perpendicular to chord of jth blade element

v_j^I = velocity due to wake perpendicular to chord of jth blade element.

Using the Biot-Savart law applied to the wake mesh, the velocity perpendicular to the airfoil chord induced by the wake can be written as

$$v_j^I = \sum_{i=1}^{\infty} \overline{\sigma}_{ij} \gamma_i \tag{9}$$

where

$\overline{\sigma}_{ij}$ = the geometric portion of the Biot-Savart law for the effect of the ith element at the jth point

γ_i = strength of the ith wake element of vorticity.

11

Recall that the γ's of the wake are proportional to the Γ's of the blade bound vortices at various radial and azimuthal positions. Hence, when Equation (9) is substituted into Equation (8) and the wake terms regrouped, the following is obtained from Equation (7),

$$\left[b_j\, a_j\, \sigma_{jj} - 1 \right] \Gamma_j + b_j\, a_j \sum_{\substack{i=1 \\ i \neq j}}^{\infty} \sigma_{ij}\, \Gamma_i = I_j \tag{10}$$

where

$$I_j = \Gamma_{0_j} + b_j\, a_j \left[(X\Omega + V_f \sin \tau \sin \psi) \sin \theta - \dot{h} + v^{\prime\prime} + v^{\prime\prime} \right]_j .$$

and σ_{ij} results from a regrouping of the $\bar{\sigma}_{ij}$'s .

Equation (10) was written for one blade element at one azimuthal position. Since Γ_j changes with radius and azimuth, similar equations for all values of Γ_j can be written. Since Γ_j is limited to ($\overline{NR} \times \overline{NA}$) values, ($\overline{NR} \times \overline{NA}$) simultaneous algebraic equations in Γ_j result.

In matrix notation,

$$\left[\sigma \right]\left\{ \Gamma \right\} = \left\{ I \right\} \tag{11}$$

where

$\left[\sigma \right]$ is a square ($\overline{NA} \times \overline{NR}$) matrix whose diagonal elements have the form

$$\left[b_j\, a_j\, \sigma_{jj} - 1 \right]$$

and whose off-diagonal elements have the form

$$b_j\, a_j\, \sigma_{ij}$$

$\left\{ \Gamma \right\}$ is a column matrix of the unknown

$\left\{ I \right\}$ is a column matrix of the known quantities

$$-\left[\Gamma_{0_j} + b_j\, a_j \left[(X\Omega + V_f \sin \tau \sin \psi) \sin \theta - \dot{h} + v^{\prime\prime} + v^{\prime\prime} \right]_j \right].$$

At this point let it suffice to say that everything in Equation (11) is known, except the Γ's. Hence, if the matrix Equation (11) can be solved for the Γ's, then sufficient information will be available to generate the required aerodynamic forces in the aeroelastic problem.

12

Structural Model

To determine the inertia and elastic forces required for the aero-elastic problem, a Lagrangian approach was used. Following the development of Reference 2, the kinetic and potential energy of a twisted rolating beam was written. A dissipation term proportional to the elastic displacement and in phase with the elastic velocity was written to account for structural damping forces. The elastic displacements were then expanded in terms of the normal modes of the blades, and the Lagrangian was applied. Since the forcing function of the system, i.e., aerodynamic loads, is periodic with its fundamental frequency being Ω, the steady-state response of the linearized system must be periodic of fundamental frequency Ω. Hence, both the motions and the uniqueness theorem for trigonometric series, corresponding coefficients must be equal. The result is a set of $2M$ (where M is the number of modes retained) simultaneous algebraic equations in the Fourier coefficients (of sine and cosine components) of the motions for each of p harmonics retained. The zeroth harmonic has only M simultaneous equations, since there are no corresponding sine terms in the series.

For the purpose of this study, six degrees of freedom were used-the first four coupled Flapwise-Edgewise bending modes and the first two uncoupled torsion modes.

The following assumptions were made in defining the structural model:

(1) Simple beam theory was applicable.

(2) Airfoil cross sections were symmetrical with respect to the major neutral axis; hence, the center of gravity lay on this axis.

(3) Gravity forces were negligible.

(4) Flight conditions were steady state.

(5) Damping (structural) was proportional to the displacement and in phase with the velocity.

(6) Blade elastic deformations were small.

13

(7)　The blades were effectively cantilevered, and the hub had
infinite impedance.

All the forces required for the aeroelastic problem of a propeller
in transitional steady-state flight have now been defined.　There now remains
the problem of solving the resultant set of simultaneous equations for the
loads and motions.

SOLUTION OF THE AEROELASTIC PROBLEM

Iterative Solution

An iterative approach to the solution was adopted.　First, the Γ -
equations are solved for an assumed set of motions.　The resultant loads
are then used to compute the generalized forces for the equations of struc-
tural deformation of the blade.　The equations of blade deformation are
treated as a forced response problem, and new motions are determined.
Since, in general, the new motions do not agree with the assumed set, the
Γ -equations must be resolved using the new motions.　The process is
repeated until the Γ's and blade elastic motions from the nth iteration agree
with the Γ's and blade elastic motions from the $(n+1)^{th}$, iteration to
within some specified tolerance.　At this point, it is argued that a consistent
set of loads and motions have been obtained, since no change in either occurs
with iteration.　Further, since the problem has a unique solution, this must
be it.

The iterative path between the loads (the Γ -equations) and motions
(the structural equations) is interrupted because of the nonlinear character
of the c_l curve.　Recall, from page　　, Equation (10), that the c_l was
wxpanded in a Taylor series about some known reference angle of attack
α_0.　So long as, from iteration to iteration, $\alpha_0 \approx \alpha_e$, to within some
amount ($\pm \Delta\alpha$, say), the same α_0, a, and c_{l_0} are used in the Γ-equations
in each iterative step.　If $\alpha_0 + \Delta\alpha < \alpha_e$ or $\alpha_0 - \Delta\alpha > \alpha_e$, a new α_0 is deter-
mined, and hence a new a and c_{l_0}, for use in the Γ -equations in the next
iterative step.　This is accomplished by dividing the c_l vs. α curve into a

14
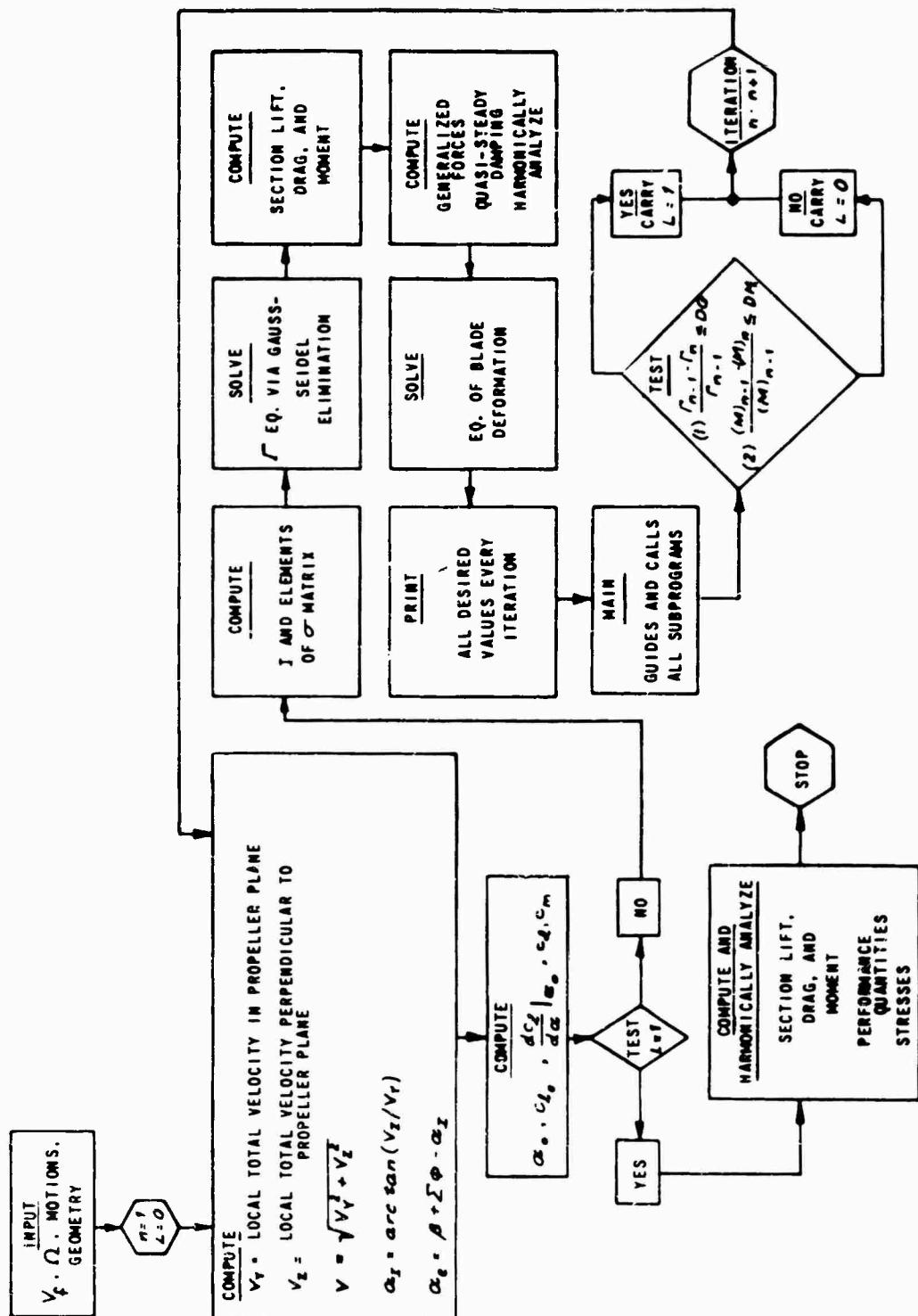
Figure 4. LOGIC DIAGRAM.

15

series of increments in α. At the center of each are evaluated α_o, α, and c_{ℓ_o}. Then, as each new α_e is determined, it is checked to see if it lies in the range corresponding to the α_o used to compute it (i.e., does $\alpha_o - \Delta\alpha \le \alpha_e \le \alpha_o + \Delta\alpha$). If not, it is placed in the proper range, and the iteration is continued. The process is described in logic diagram, Figure 4.

To insure convergence of the iterative scheme employed to solve the equations of motion, it was found that the right-hand side, i.e., the generalized force, should be relatively free from a dependence upon the dependent variables, i.e., the elastic motions. In the present development it is impossible to extract this dependence of the generalized force on the motions. It was proposed to accomplish this artificially by subtracting from both sides of the equations of blade deformation the contribution from the quasi-steady damping. This term was chosen because it is one of the largest motion dependent contributors to the generalized force.

The treatment of this term in the equations of blade deformation differs depending upon whether we consider the right-or the left-hand side of these equations. On the right-hand side, the motions are assumed known from the previous iterative step. On the left-hand side, the deformations are the unknowns to be used in the succeeding iterative step. For example, consider the following representation of the deformation equation at the $(n+1)^{th}$ iteration:

$$m\ddot{X}_{n+1} + k\dot{X}_{n+1} + cX_{n+1} = F_n$$

where F_n is assumed to be a linear function of the elastic motions determined in the nth iteration; i.e.,

$$F_n = c_0 + c_1 \ddot{X}_n + c_2 \dot{X}_n + c_3 X_n.$$

Subtract $c_2 X_{n+1}$ from the left-hand side and $c_2 \dot{X}_n$ from the right-hand side of the equation to obtain

$$m\ddot{X}_{n+1} + \left[k - c_2 \right] X_{n+1} + cX_{n+1} = F_n - c_2 \dot{X}_n.$$

16

When the iterative process has converged,

$$X_n = X_{n+1} \pm \epsilon$$

where:

$\epsilon \le \sigma$ = predetermined allowable error and hence the
solution effected.

Performance and Stresses

Once a converged set of Γ's and motions have been obtained, there
only remains the proper combination of these quantities to obtain the forces
acting on the propeller shaft and the blade stresses. The prop thrust,
torque, normal force, side force, pitching moment, and yawing moment
are then determined (see Figure 5).

Section lift, drag, and torsional moment (ℓ_j, d_j, m_j respec-
tively) are computed at each radial and azimuthal position of the blade
based on the converged loads and motions. These quantities are resolved
into components with respect to the inertial coordinate system (X_o, Y_o,
Z_o). At each azimuthal position, a summation of the spanwise integration
over each blade yields the instantaneous values of the thrust, torque, etc.
This process is repeated for all azimuthal positions. The result is a set
of $\overline{NA}$ values of each of the performance quantities. Hence, with $\overline{NA}$ equally
spaced azimuthal positions, the performance quantities may be represented
by a finite Fourier series of $\overline{NA}$ terms, the zeroth term of which yields the
desired mean values over one revolution:

$$THRUST = T = \frac{1}{\overline{NA}} \sum_{k=1}^{\overline{NA}} \left\{ \sum_{a=1}^{\overline{NC}} \left[\sum_{j=1}^{\overline{NR}} (F_{Z_j}) \Delta X_j \right]_a \right\}_k \tag{12}$$

$$TORQUE = Q = -\frac{1}{\overline{NA}} \sum_{k=1}^{\overline{NA}} \left\{ \sum_{a=1}^{\overline{NC}} \left[\sum_{j=1}^{\overline{NR}} (X_j F_{Y_j}) \Delta X_j \right]_a \right\}_k \tag{13}$$

17
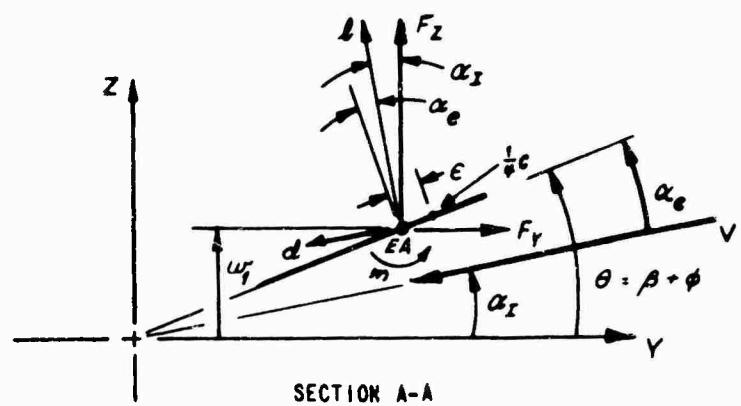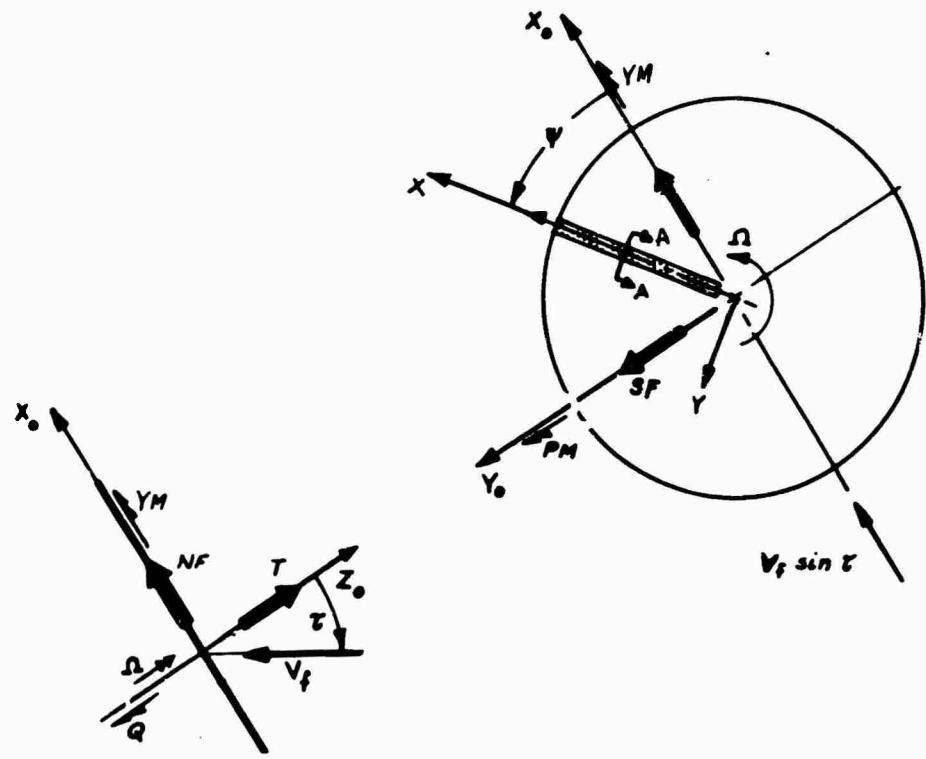
Figure 5. GEOMETRY FOR DETERMINATION OF PERFORMANCE AND STRESSES

$$\text{NORMAL FORCE} = NF = +\frac{1}{\overline{NA}} \sum_{k=1}^{\overline{NA}} \left\{ \sum_{\omega=1}^{\overline{NC}} \left[\sum_{j=1}^{\overline{NR}} (F_{x_j} \cos\psi - F_{Y_j} \sin\psi)\Delta X_j \right]_{\omega} \right\}_k \tag{14}$$

$$\text{SIDE FORCE} = SF = +\frac{1}{\overline{NA}} \sum_{k=1}^{\overline{NA}} \left\{ \sum_{\omega=1}^{\overline{NC}} \left[\sum_{j=1}^{\overline{NR}} (F_{x_j} \sin\psi + F_{Y_j} \cos\psi)\Delta X_j \right]_{\omega} \right\}_k \tag{15}$$

$$\text{PITCHING MOMENT} = PM = +\frac{1}{\overline{NA}} \sum_{k=1}^{\overline{NA}} \left\{ \sum_{\omega=1}^{\overline{NC}} \left[\sum_{j=1}^{\overline{NR}} (F_{Z_j} X_j \cos\psi - m_j \sin\psi)\Delta X_j \right]_{\omega} \right\}_k \tag{16}$$

$$\text{YAWING MOMENT} = YM = \frac{1}{\overline{NA}} \sum_{k=1}^{\overline{NA}} \left\{ \sum_{\omega=1}^{\overline{NC}} \left[\sum_{j=1}^{\overline{NR}} (F_{Z_j} X_j \sin\psi + m_j \cos\psi)\Delta X_j \right]_{\omega} \right\}_k \tag{17}$$

where

k = azimuthal station number

ω = blade number

$\overline{NA}$ = total number of azimuthal stations

$\overline{NC}$ = number of blades;

$F_{x_{j_\omega}} = -\ell_j (dw/dX)_j$ on blade ω

$F_{Y_{j_\omega}} = -\left[\ell \sin\alpha_I + d\cos\alpha_I\right]_j$ on blade ω

$F_{Z_{j_\omega}} = \left[\ell \cos\alpha_I - d\sin\alpha_I\right]_j$ on blade ω

$m_{j_\omega} = \left[2b^2 \rho V^2 c_{m_{c/4}}\right] + \epsilon_j \left[\ell\cos\alpha_e + d\sin\alpha_e\right]_j$ on blade ω

$c_{m_{c/4_j}}$ = section moment coefficient about airfoil quarterchord.

Consistent with the structural model adopted, i.e., simple beam theory, only the longitudinal and shear stresses are developed at any point in the blade cross section. These quantities are also harmonically analyzed.

19

The Digital Program

The entire iterative approach to the solution of the aeroelastic problem has been programmed in FORTRAN IV for use on the IBM 7044 digital computer. The program consists of six main parts.

Part 1

This program positions the wake. The coordinates of the elemental wake vortex end points are computed. These coordinates are computed including the effects of (1) free-stream velocity, (2) wake contraction, (3) wing interference, and (4) nacelle interference in any combination desired. The midpoints of the bound vortex elements are also computed. The program can handle 24 azimuthal stations and 10 radial stations.

Part 2

From the coordinates obtained in Part 1, the effect of the wake vortices of unit strength on the blades is computed, i.e., the $\bar{\sigma}$ of each individual wake element. The proper combinations are made, and the elements which contribute to the $[\sigma]$ matrix of Equation (11) are computed.

Part 3

Part 3 evaluates all the mass and elastic integrals necessary for computing the elements of the structural deformation equations. It also writes the coefficients of the least-square polynomial fit to the two-dimensional airfoil section data used to evaluate α_o, a, c_{ℓ_o}, c_m, and c_d. The mass elastic integrals can be evaluated at a maximum of 30 spanwise stations.

Part 4

From the aerodynamic data of Part 3 and the σ elements of Part 2, the $[\sigma]$ matrix of Equation (11) is formed. The set of simultaneous equations is solved by using the Gauss-Siedel reduction technique (Reference 5). The technique is one of iteration until the set of Γ's from one

20

iteration agrees with the previous set to within some prespecified tolerance. The generalized force is then computed and approximated by an nth order polynomial in X. This results from the fact that the lift is computed at only 10 spanwise stations, while the mass-elastic properties are known at up to 30 stations.

The generalized forces are harmonically analyzed for a fundamental period of one revolution, and the equations of deformation for each harmonic are solved by employing the Gauss elimination process (Reference 5).

Overall convergence tests on Γ's and deformations are made by comparing values obtained in the nth iteration to those obtained in the iteration to those obtained in the $(n+1)^{th}$ iteration.

If the Γ's and deformations are not converged, α_e and α_I are recomputed and the aerodynamic tapes are searched to determine if the same α_o is to be used. Control is returned to Part 3 or continues to Part 5, depending upon the results of the convergence tests.

Part 5

Part 5 computes a time history of the propeller thrust, torque, side and normal forces, pitching and yawing moments, and stresses. These quantities are also harmonically analyzed. The printed output from the program includes the following distributions given as functions of the radial and azimuthal position in the disk: (1) strength of bound vorticity, (2) section lift, drag, and moment, (3) section displacement (total), (4) section effective angle of attack, (5) section induced velocity, and (6) section stresses—longitudinal and shear. Also printed is the azimuthal distribuion of (7) thrust, (8) torque, (9) normal and side forces, and (10) pitching and yawing moments. The harmonic components of (1), (2), (3), (6), (7), (8), (9), and (10) are also printed.

21

DISCUSSION OF RESULTS

The digital program previously outlined was used to obtain theoretical results indicating the effects on the prop performance and blade stresses due to independent variations in the angle which the free stream makes with the thrust axis (τ), wing loads, and wake shape. The study was not an exhaustive one and the results are intended only to indicate trends. The studies were performed for a three-bladed propeller whose blades have the properties shown in Figure 6.

Effects Due to Variations in the Angle Which the Free Stream Makes With The Thrust Axis

Five cases were computed for which the basic parameter varied was τ. However, because both the nacelle and the wing influence were included in these computations the effects due to nacelle and wing varied as τ varied. The strength of the source-sink representing the nacelle decreased as τ decreased. The load carried by the wing also decreased as τ decreased. The free stream, V_f, and prop speed, Ω, were held constant and the angle τ was varied from 20° to 60°. The wake was a fixed pitch skewed helix whose pitch was determined from momentum considerations.

Presented in Figures 7 and 8 are typical performance and blade stress results obtained for the cases analyzed. In Figure 7, the mean values of the thrust, torque, normal force, etc. were used to nondimensionalize the results presented. The oscillatory components are plotted about a zero mean. The results presented are for $\tau = 50$.

The dominant frequency contents of the oscillatory values of the thrust for all cases are 3P (i.e., a frequency equal to 3 times the propeller speed), 6P, 9P, etc. The peak-to-peak magnitude of the 3P component of the thrust is approximately 5% of the mean thrust; the magnitude of the 6P component is approximately 10% of the 3P component. The magnitudes of the 1P, 2P, 4P, 5P, 7P, etc., harmonics are of the order of 1×10^{-8}. Since the only harmonics of the performance quantities which can be

22

theoretically transmitted to the shaft during steady-state flight must be integer multiples of the number of blades, the magnitudes of these latter harmonic components become a measure of the accuracy of the numerical method employed. Torque, normal and side forces, and pitching and yawing moments exhibit the same characteristics as the thrust of dominant 3P, 6P, and 9P harmonics, with all other harmonics negligibly small; however, for the normal and side, forces, and pitching and yawing moments, the phasings of the significant harmonics are such as to cause their time (ψ) histories to appear less sinusoidal.

Figure 8 presents a typical plot of harmonically analyzed blade longitudinal stress versus blade span. Nondimensionalization of the mean longitudinal stress was performed by dividing through by the longitudinal stress at the root of the blade. The harmonics were nondimensionalized in the same manner. These stresses were computed on the camber side of the blade at the 50% chord for all spanwise stations.

From the figure it is seen that all of the harmonics peak at approximately the 60% span. The first harmonic stress component raches approximately 16% of the mean longitudinal stress at this station. Note that magnitudes of the third and fourth harmonics excede that of the second.

Presented in Figure 9 and 10 are plots of the nondimensionalized mean propeller performance versus τ. Figure 11 presents the third and sixth harmonics of prop performance versus τ. Figure 9 shows the variation of the nondimensionalized mean thrust and torque with τ. (The thrust and torque are nondimensionalized by the values of the thrust and torque respectively at $\tau = 40^\circ$.) From the figure it is seen that the curves for both the thrust and the torque increase as τ is increased from 20°. The rate of increase in thrust is larger than the rate of increase in torque.

Figure 10 presents the variation with τ of the nondimensionalized mean side and normal forces and the mean pitching and yawing moments (forces and moments in the prop plane; see Figure 5). The inplane forces have been nondimensionalized by the mean thrust at each τ and the inplane moments have been nondimensionalized by the mean torque at each τ.

23

The inplane forces never excede 8% of the mean thrust load while the inplane moments approach 90% of the mean torque load. Both the inplane forces and moments exhibit a parabolic behavior with increasing τ. The maximum values occur in the range $50^{\circ} \leq \tau \leq 70^{\circ}$. The variations of the third and sixth harmonics of the performance quantities with τ is represented in Figure 11. Each harmonic has been nondimensionalized by its corresponding mean at each τ. While both the third and sixth harmonics of the performance quantities show a strong dependence upon τ, the dependence on τ of the third harmonic is much stronger. The third harmonic for all quantities increased markedly as τ is increased from 20°. The sixth harmonic of all performance quantities increased as τ is increased.

Presented in Figure 12 is the variation with τ of the mean and first four harmonics of the longitudinal stress at the 60% span. The mean stress at each τ was nondimensionalized by the longitudinal stress at the blade root. The harmonics were nondimensionalized by the mean longitudinal stress at each τ.

As τ is increased the mean stress is observed to decrease. This is attributed to the fact that the longitudinal stresses are computed on the camber side of the blade. Hence, as the blade lift load increased with increasing τ the steady bending deflection of the blade increased, tending to relieve the tensile stress due to the centrifugal load on the camber side of the blade. This is observed to be true for all radial stations.

All harmonics of the longitudinal stress show a marked increase as is increased. The first harmonic stress component increased from 10% to 30% of the mean stress as τ went from 20° to 60°. Note that for the τ range presented, the third and fourth harmonics were larger than the second.

To show the effect of changing the wing load, three cases were calculated for three different wing loads while the remaining parameters were held constant. Presented in Figures 13 and 14 are the nondimensionalized mean performance values versus nondimensional wing load. The mean thrust and torque were nondimensionalized by the values of mean thrust and torque for a nominal wing load at $\tau = 40^{\circ}$. The inplane forces and moments

24

were nondimensionalized by the mean thrust and torque respectively at each
assumed value of wing load. The variation of wing load had no effect on the
mean thrust or torque. However, the mean inplane forces and moments
increased in proportion to the increase in wing load. Thus an 8-fold in-
crease in wing load caused a 47% increase in normal force, a 65% increase
in yawing moment, a 79% increase in side force, and a 113% increase in
pitching moment. The variation of the third and sixth harmonics components
of these quantities show a similar pronounced dependence on wing load as
evidenced in Figure 15 (all quantities are nondimensionalized by the corre-
sponding mean value at each wing load). The third and sixth harmonics of
all of the performance quantities, including the thrust and torque, increased
as the wing load increased. For all cases, except the third harmonic of
pitching moment, the harmonics of the performance quantities increased at
a faster rate than the mean values as the wing load increased.

That the mean thrust and torque are not affected by wing load can
be inferred from the following considerations. For the cases investigated,
the maximum lift for all azimuthal stations occurred at approximately 85%
span. Thus a consideration of the occurrences at this station should provide
a key to the behavior of the mean thrust and torque with wing load. Plotted
in Figure 16 is the azimuthal variations of the axial component of the wing-
induced velocity (nondimensionalized by the momentum value of the induced
velocity plus the axial component of the free stream) at $r/R = 0.85$ for the
nominal wing loading. The distribution is the same for all wing loads and
only the magnitude varies. Thus between $\psi = 90^{\circ}$ and $\psi = 270^{\circ}$ an upwash
is induced while over the remainder of the azimuth a downwash occurs
(see Figure 5 for a definition of ψ direction). The value of the maximum
wing-induced upwash and downwash is of the order of 10% of the total axial
component.

As evident from Figure 16, no net upwash or downwash with respect
to azimuth occurred due to the wing; thus no net change in the mean lift was
expected. This is substantiated in Figure 17 which presents the azimuthal
variation of the maximum blade lift for three values of wing load. Since

25

the mean lift remained constant for the wing loads considered, it follows that the mean thrust and probably the torque would remain constant. The nondimensionalizing quantity in Figure 17 was the mean lift.

Note, however, that if the wing were not located on the thrust axis (see Figure 3), as in the case inhand, or were more highly swept, the wing-induced velocities could cause a net change in the mean induced velocity and hence a change in the mean thrust and torque.

That the inplane forces and moments vary directly with wing load is attributed to the fact that these forces and moments are determined (in part, see Equations 14 through 17) from a weighted lift component. The weighting function is the sine or cosine of the azimuthal position of the blade. Thus nonzero harmonics of the lift contribute to the zeroth harmonics of the inplane forces and moments.

The effect of varying the wing load on the blade longitudinal stresses is presented in Figure 18. The mean stress was nondimensionalized by the longitudinal stress at the blade root and the harmonics of the stresses were nondimensionalized by the mean stress at each wing load. While the mean stress remained constant as wing load was increased the harmonics of the stresses increased in amplitude. The first harmonic grew by approximately 70% as wing load increased. Note that the third and fourth harmonics are larger than the second for the entire range of wing load considered.

Two hovering ($\tau = 90^{o}$) cases were computed. One case was intended to simulate the model sitting on the ground; hence, the propeller plane was approximately one rotor diameter above the ground; the other case was computed for the same parameters except with the propeller plane well out of ground effect. It was found that the effect of ground was slightly detrimental. Table 1 below presents the nondimensional thrust and torque values for the two cases.

26

Table 1 THE NONDIMENSIONAL THRUST AND TORQUE FOR A PROP HOVERING IN-AND OUT-OF GROUND EFFECT

	THRUST	TORQUE
HOVERING OUT-OF-GROUND EFFECT	1.000	1.000
HOVERING IN-GROUND EFFECT	0.969	0.995

While the torque remained essentially constant, the thrust decreas-
ed by approximately 3%. due to the effect of ground. Examination of the
RVM in the two cases revealed that for the near wake (i.e., within, say,
a quarter propeller radius) the shape and spacing of the wake were essen-
tially the same. Farther down the wake, however, the shape and spacing
were no longer the same. At approximately one propeller radius, the wake
boundary for the in-ground effect case increased in diameter, while that for
the out-of-ground effect case continued to contract. It is believed that for
the case in hand the small increase in thrust and torque obtained as the height
above ground increased was due to the fact that far wake had contracted more.
That the increase was small is attributed to the fact that the near wakes are
almost identical in the two cases. *

---

* Note that the effect of the ground can be either beneficial or determental,
depending upon (1) the degree of wake distortion, (2) the wake spacing,
and (3) the load distribution on the blade. For example, if the blade
load distribution is such that a major portion of the load is carried on
the most outborad blade section (say from 90% span out), then contrac-
tion does not move inboard of the 90% span. If the contracted wake
moves inboard of the 90% span, the wake effect is such as to increase
the load
An additional contributing factor which was not included in the above
analysis is the influence of the ground image system on the induced
velocity at the rotor plane.

27

A third hovering case was computed employing a fixed pitch, uncontracted helical wake with no nacelle effects on either the wake or the propeller blades. The wake pitch was determined from momentum considerations. Figure 19 depicts the wake picture for the out-of-ground effect RVM wake and the fixed pitch wake model.

A summary of the performance results obtained for the two cases is presented in Table 2.

Table 2 THE NONDIMENSIONAL THRUST AND TORQUE COMPUTED
USING RVM WAKE AND A FIXED PITCH HELIX

	THRUST	TORQUE
RVM HELIX	1.000	1.000
FIXED PITCH HELIX	1.031	1.023

For the case in hand, the effect of using a variable pitch, contracting wake was to reduce the computed thrust and torque by 3.1% and 2.3% respectively from the thrust and torque computed using an uncontracted fixed pitch helix.

CONCLUSIONS

Based on the results obtained in this study, the following general conclusions were drawn.

It has been shown during the course of this study that the approach employed to define and formulate the aeroelastic problem associated with VTOL-type propellers operating in all flight ranges from hovering (in-and out-of-ground effect) through transition and into axial flight is a feasible one. Furthermore, the digital program developed to implement solution of the resultant aeroelastic equations converges to a unique solution in a reasonable length of time (approximately 0.75 hour on the IBM 7044).

The effect of increasing ζ is to cause an increase in the mean and oscillatory values of the predicted thrust and torque. The thrust increases at a faster rate than the torque.

The mean inplane forces and moments exhibit a parabolic behavior with increasing ζ. The oscillatory portion of the inplane forces and moments increase as ζ increases.

The mean longitudinal stress on the camber side of the blade decrease as ζ is increased while the oscillatory components increase.

Changing wing load has no effect on the mean thrust, torque, or longitudinal stress. The mean inplane forces and moments increased proportionally as the wing load increased. The oscillatory components of all of the performance quantities and the blade stresses increased as the wing load increased.

The effect of ground proximity was to decrease the predicted thrust and torque of a propeller in the hover mode.

An accurate method of predicting the wake geometry is necessary if propeller performance predictions are required to have an accuracy of better than $\pm 3\%$.

29

REFERENCES

1. Brady, W. G., and Crimi, P., Representation of Propeller Wakes by Systems of Finite Core Vortices, Cornell Aeronautical Laboratory, Inc., Buffalo, New York, CAL Report No. BB-1665-S-2, February 1965.

2. Houboult, J. C., and Brooks, G. W., Differential Equations of Motion for Combined Flapwise Bending, Chordwise Bending, and Torsion of Twisted Nonuniform Rotor Blades, National Advisory Committee for Aeronautics, Langley Field, Virginia, NACA TN 3905, February 1957.

3. Piziali, R. A., and DuWaldt, F. A., Cornell Aeronautical Laboratory, Inc., A Method for Computing Rotary Wing Air Load Distributions in Forward Flight, U.S. Army Transportation Research Command, Ft. Eustis, Virginia, TCREC TR 62-44, November 1962

4. Roark, R. J., Formulas for Stress and Strain, McGraw-Hill Book Company, Inc., New York and London, 1953.

5. Sokolnikoff, I. S., and Redheffer, R. M., Mathematics of Physics and Modern Engineering, McGraw-Hill Book Company, Inc., New York, 1958.

6. Trenka, A. R., Cornell Aeronautical Laboratory, Inc., Development of a Method for Predicting the Performance and Stresses of VTOL-Type Propellers, U.S. Army Aviation Materiel Laboratories, Ft. Eustis, Virginia, USAAVLABS TR 66-26, May 1966, (To be published)

LIST OF SYMBOLS

a_j local slope of lift curve for airfoil section $(dc_\ell/d\alpha)$

b_j local blade semichord, ft

C_j local blade chord, ft

c_{d_j} section drag coefficient

c_{ℓ_j} local section lift coefficient

$c_{\ell_{o_j}}$ local section lift coefficient corresponding to α_{o_j}

$c_{m_{c/4_j}}$ local section moment coefficient about quarterchord

d_j local drag per unit span, lb/ft

h_j local elastic motions perpendicular to airfoil chord $+ V_f \cos \tau$, ft/sec

I_j quasi-steady part of $\Gamma_j + \Gamma_{o_j}$, ft^2/sec

ℓ_j local lift per unit span, lb/ft

M number of vibration modes

m_j local moment per unit span, ft-lb/ft

$\overline{NA}$ number of azimuthal stations

$\overline{NC}$ number of blades

NF normal force, lb

$\overline{NR}$ number of radial stations

PM pitching moment, ft-lb

p number of harmonics

Q torque, ft-lb

SF side force, lb

T' time for one rotor revolution, sec

T thrust, lb

V_j local total velocity at a blade section, ft/sec

V_f free-stream velocity, ft/sec

v_j local total velocity perpendicular to the airfoil chord, ft/sec

v_j^I local velocity perpendicular to airfoil chord due to wake, ft/sec

v_j^N local velocity perpendicular to airfoil chord due to nacelle, ft/sec

v_j^W local velocity perpendicular to airfoil chord due to wing, ft/sec

w_l local elastic displacement of the elastic axis perpendicular to the prop plane, ft

31

X_j radial distance to j^{th} element, ft

$\left.\begin{array}{l} X_o \\ Y_o \\ Z_o \end{array}\right\}$ nonrotating coordinates fixed at prop hub

$\left.\begin{array}{l} X \\ Y \\ Z \end{array}\right\}$ rotating coordinates aligned with the blade

YM yawing moment, ft-lb

α_{e_j} local effective angle of attack, radians

α_{I_j} angle local total velocity makes with the prop plane, radians

α_{o_j} local reference angle of attack, radians

α_w angle of attack of wing, degrees

β_j local built-in twist, radians

Γ_j local bound vortex strength, ft^2/sec

Γ_{o_j} local bound vortex strength corresponding to α_{o_j} , ft^2/sec

Γ_w strength of wing bound vortex

ϵ_j local distance from elastic axis to quarterchord, ft

θ_j local total geometric angle ($= \beta_j + \theta_j$) of a blade section, radians

ρ density of air, $slugs/ft^3$

$\overline{\sigma}_{ij}$ geometric portion of Biot-Savart law for the effect of the ith vortex element at the jth point, 1/ft

τ angle free-stream velocity makes with thrust axis, degrees

ϕ_j local torsional displacement, radians

ψ azimuthal position of the blade, degrees

Ω rotor speed, radians/sec
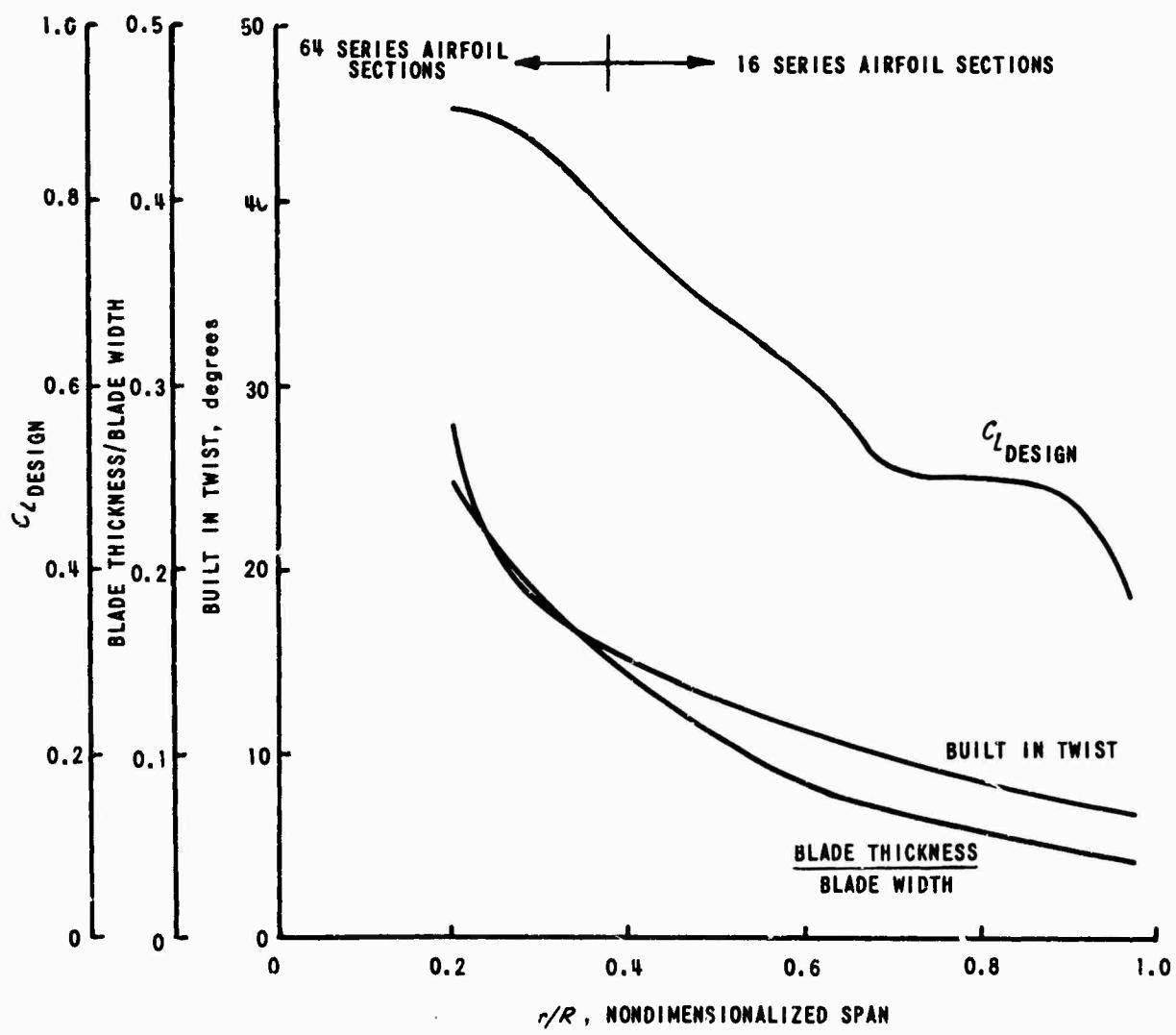
Figure 6   PROPELLER BLADE CHARACTERISTICS

33
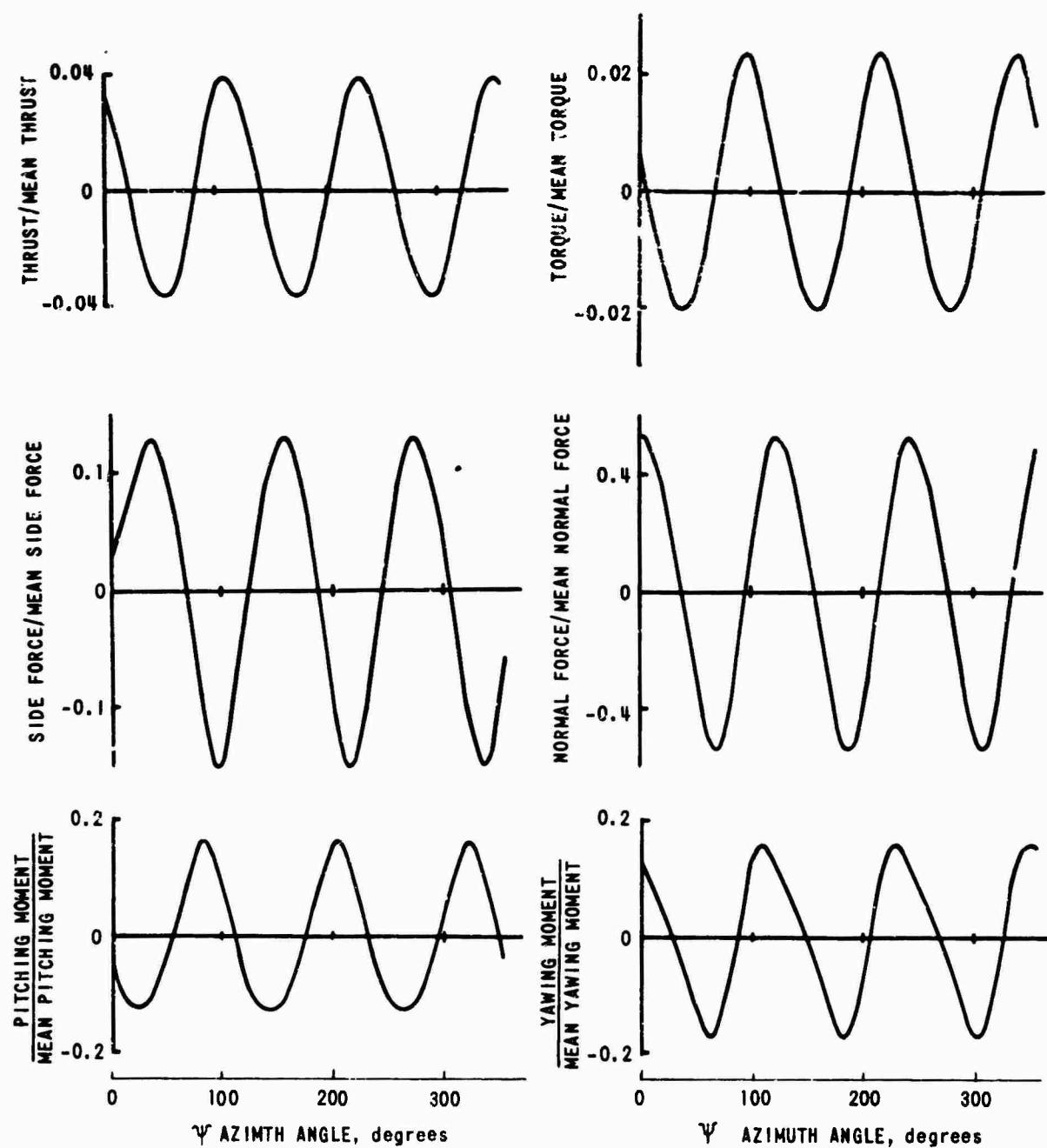
Figure 7   NONDIMENSIONALIZED INSTANTANEOUS VALUES OF THE
PERFORMANCE QUANTITIES VS. AZIMUTHAL POSITION FOR $\tau = 50°$

34
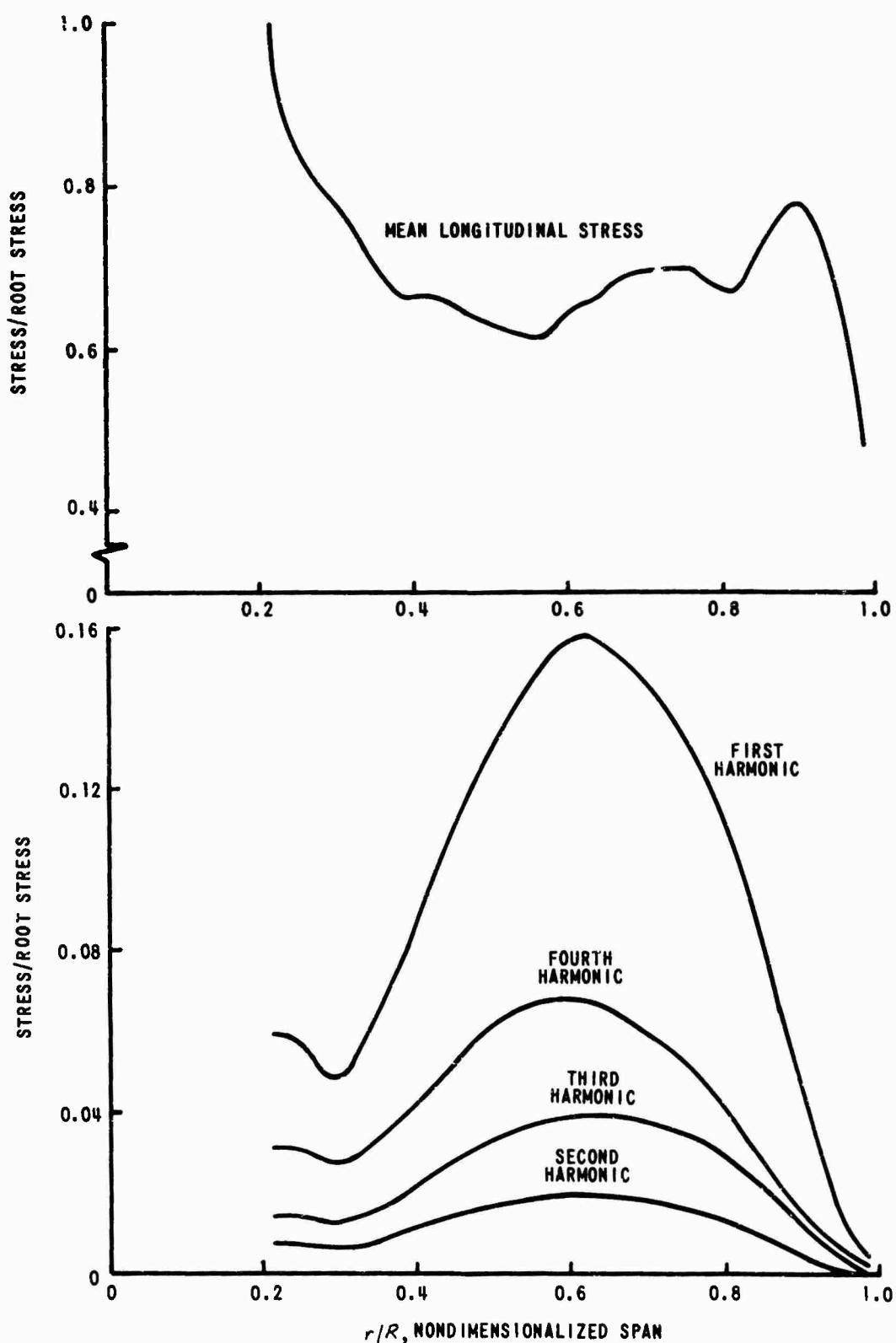
Figure 8 NONDIMENSIONALIZED LONGITUDINAL STRESS
VS. NONDIMENSIONALIZED SPAN FOR τ = 50°

35
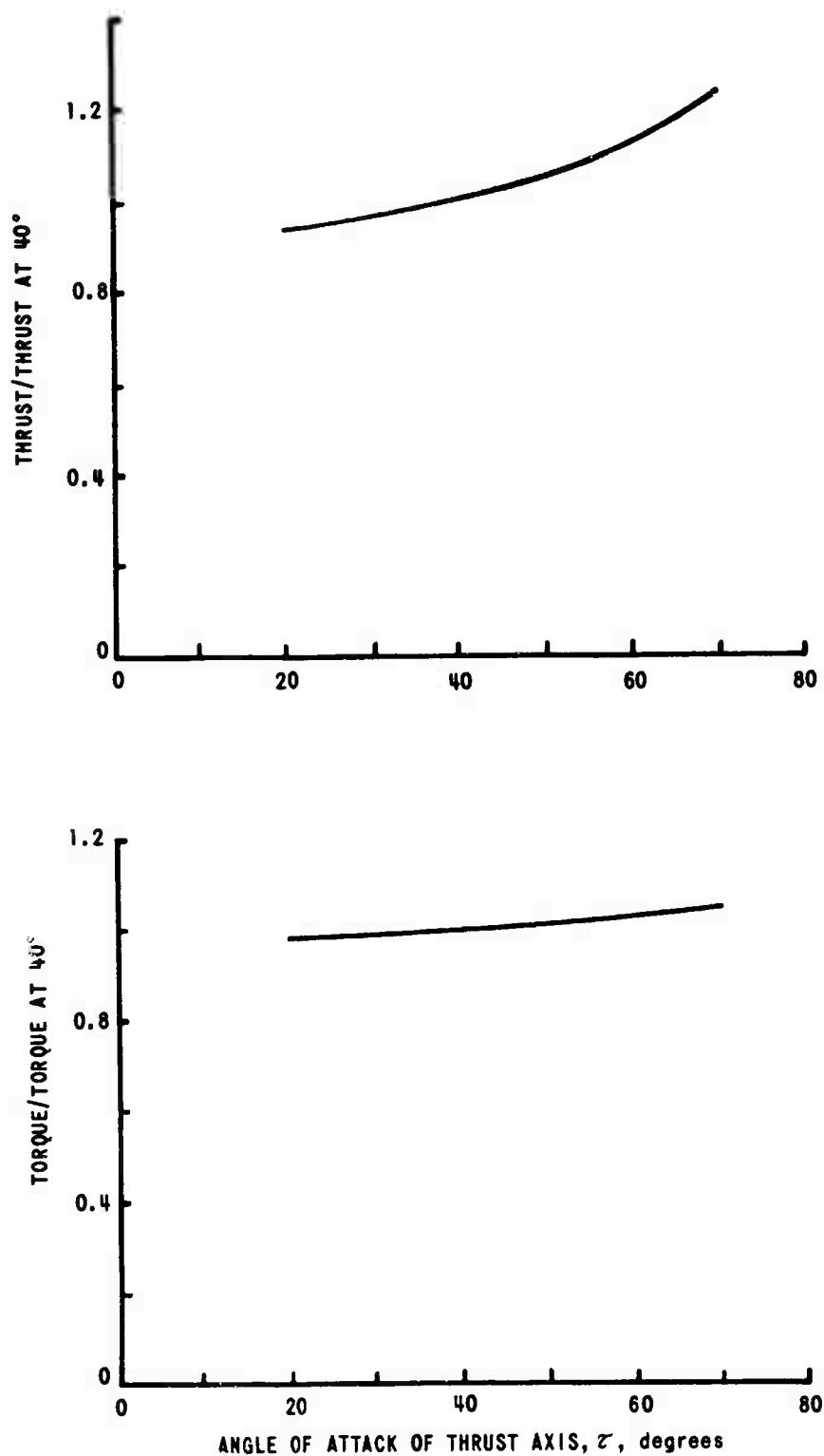
Figure 9 NONDIMENSIONALIZED MEAN THRUST AND
   TORQUE VS. ANGLE OF ATTACK OF THRUST AXIS
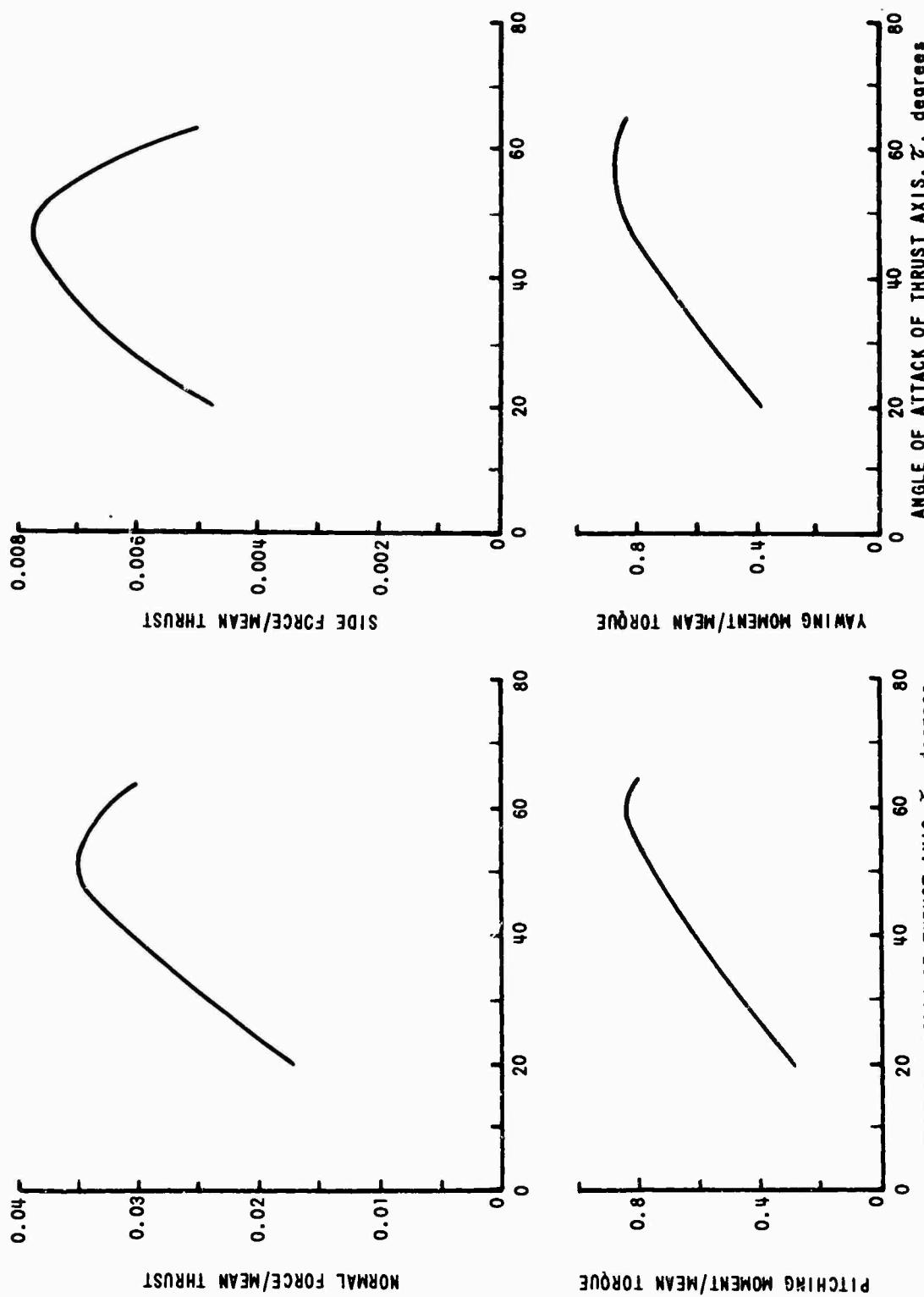
Figure 10 NONDIMENSIONALIZED MEAN THEORETICAL NORMAL FORCE, PITCHING MOMENT,
SIDE FORCE, AND YAWING MOMENT VS. ANGLE OF ATTACK OF THRUST AXIS

37
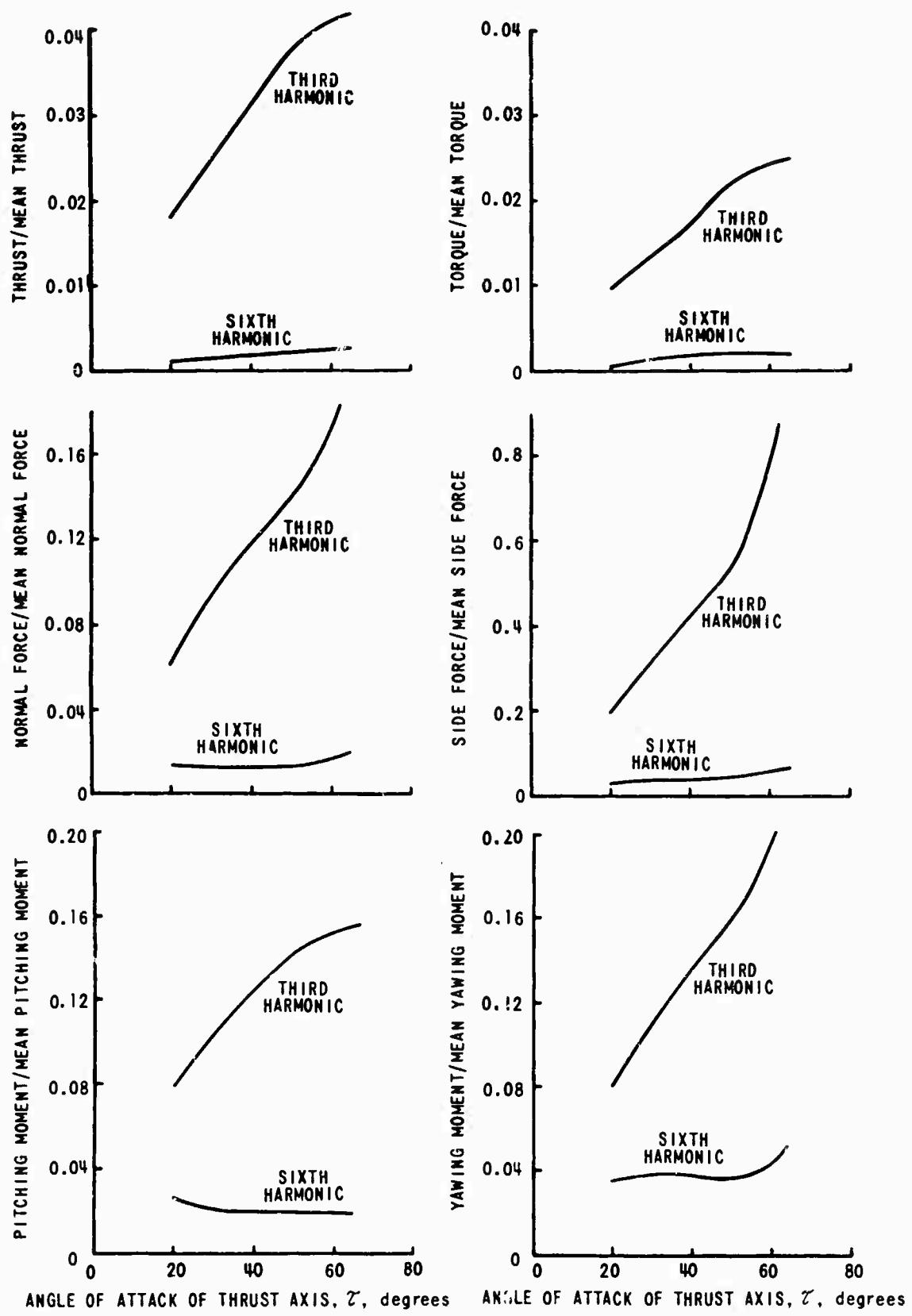
Figure 11   NONDIMENSIONALIZED THIRD AND SIXTH HARMONICS OF THE PERFORMANCE
QUANTITIES VS. ANGLE OF ATTACK OF THRUST AXIS, τ, DEGREES

38
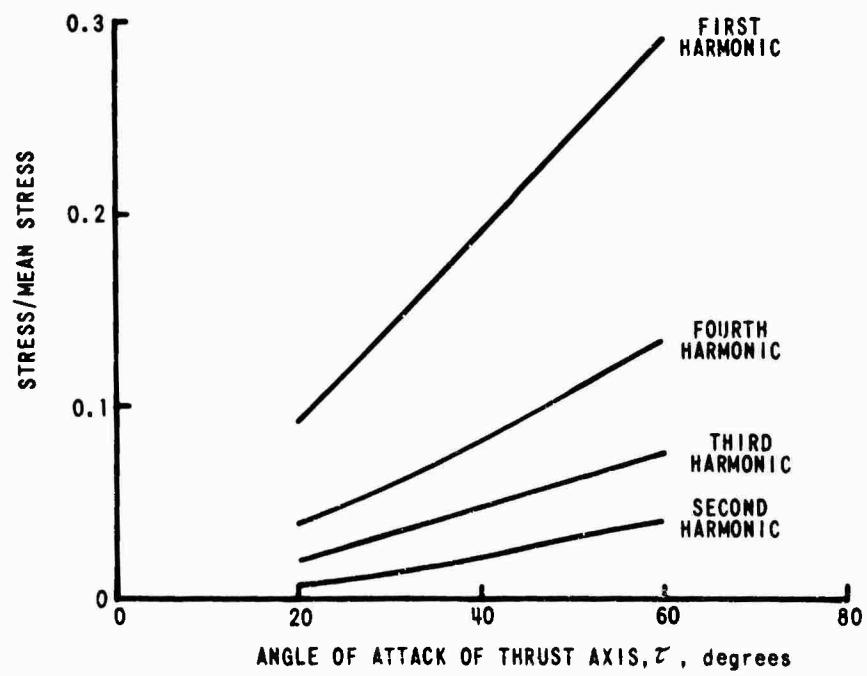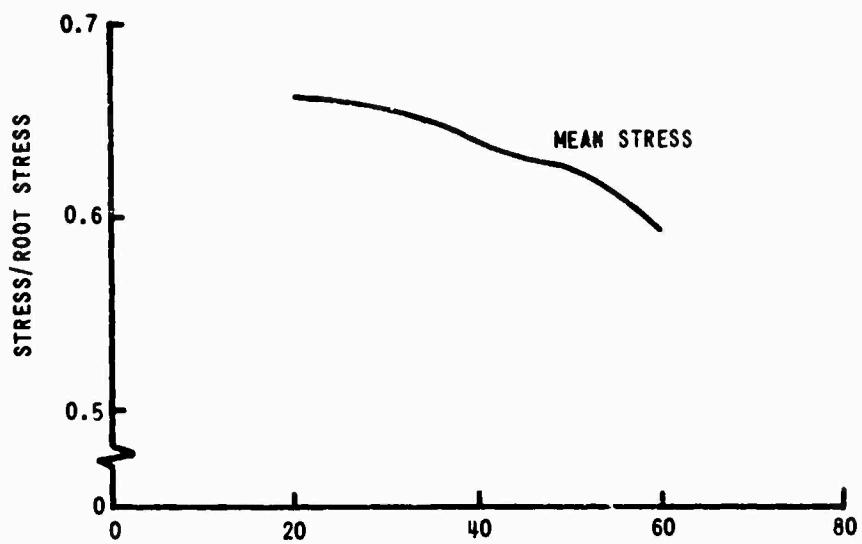
Figure 12 NONDIMENSIONALIZED LONGITUDINAL STRESS VS.
ANGLE OF ATTACK OF THRUST AXIS FOR $r/R \approx 0.60$
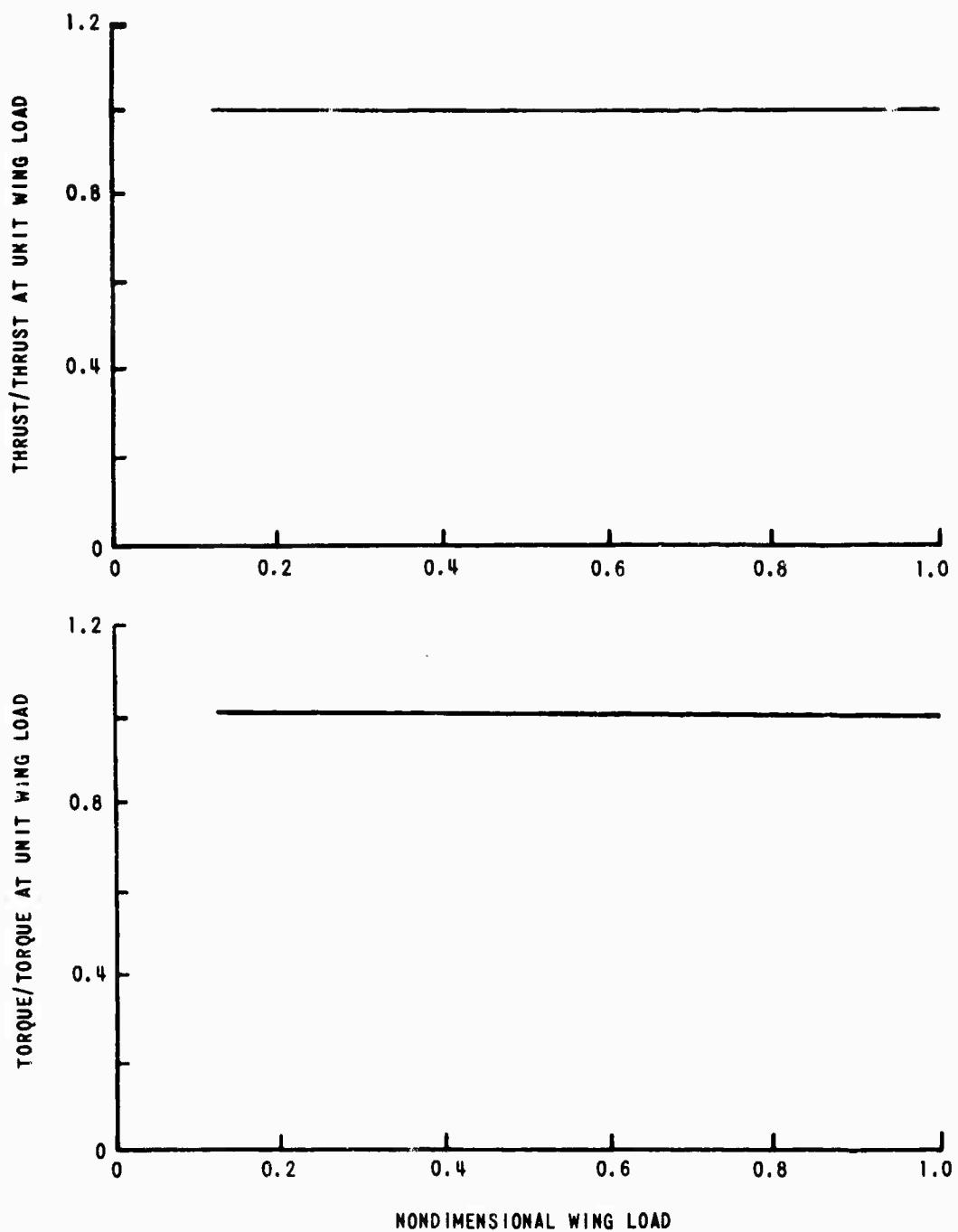
Figure 13 NONDIMENSIONALIZED MEAN THRUST AND TORQUE
VS. WING LOAD, $\tau = 40°$

40
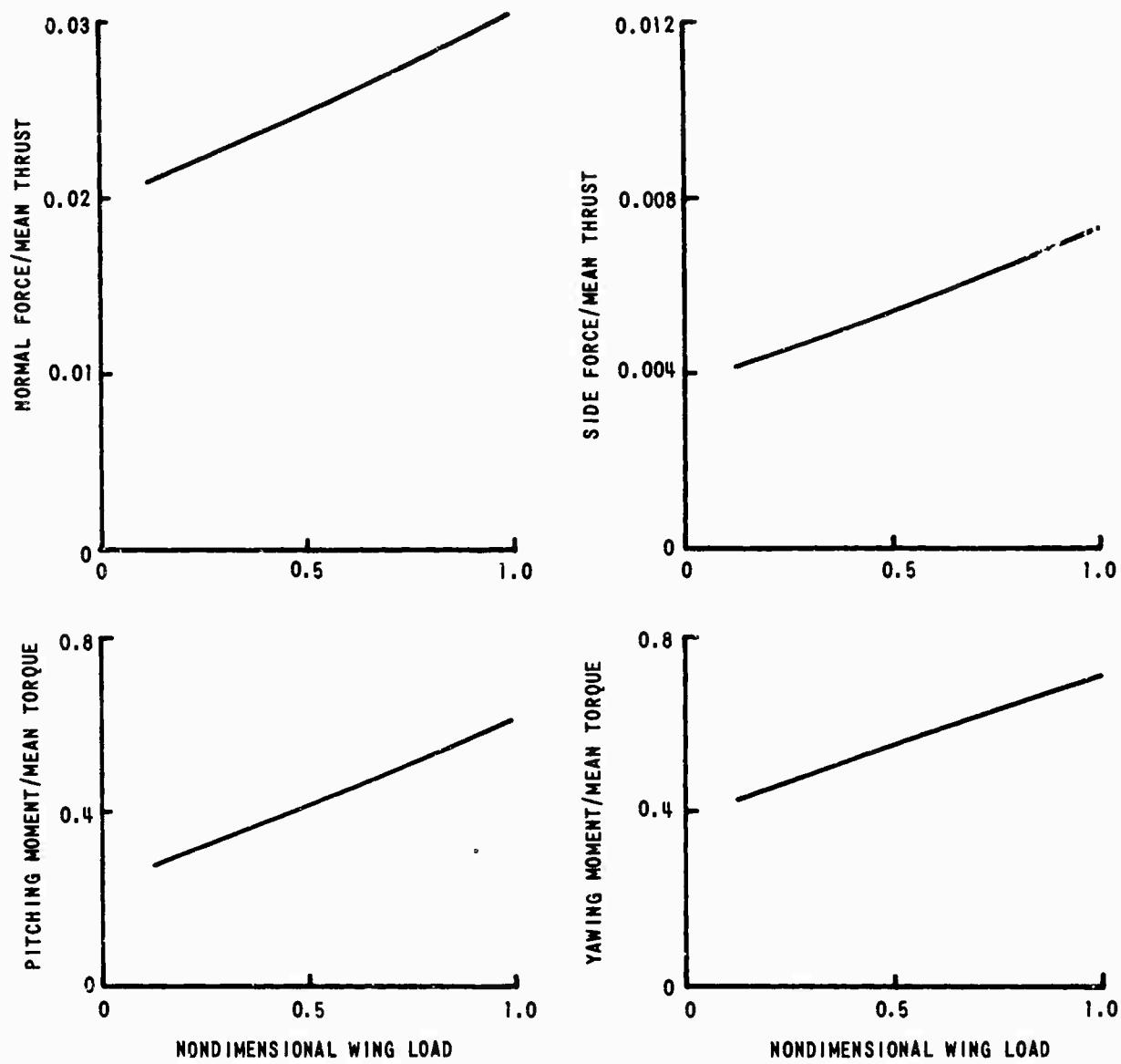
Figure 14 NONDIMENSIONALIZED MEAN NORMAL FORCE, SIDE FORCE, PITCHING
MOMENT AND YAWING MOMENT VS. WING LOAD FOR $\tau = 40°$

41
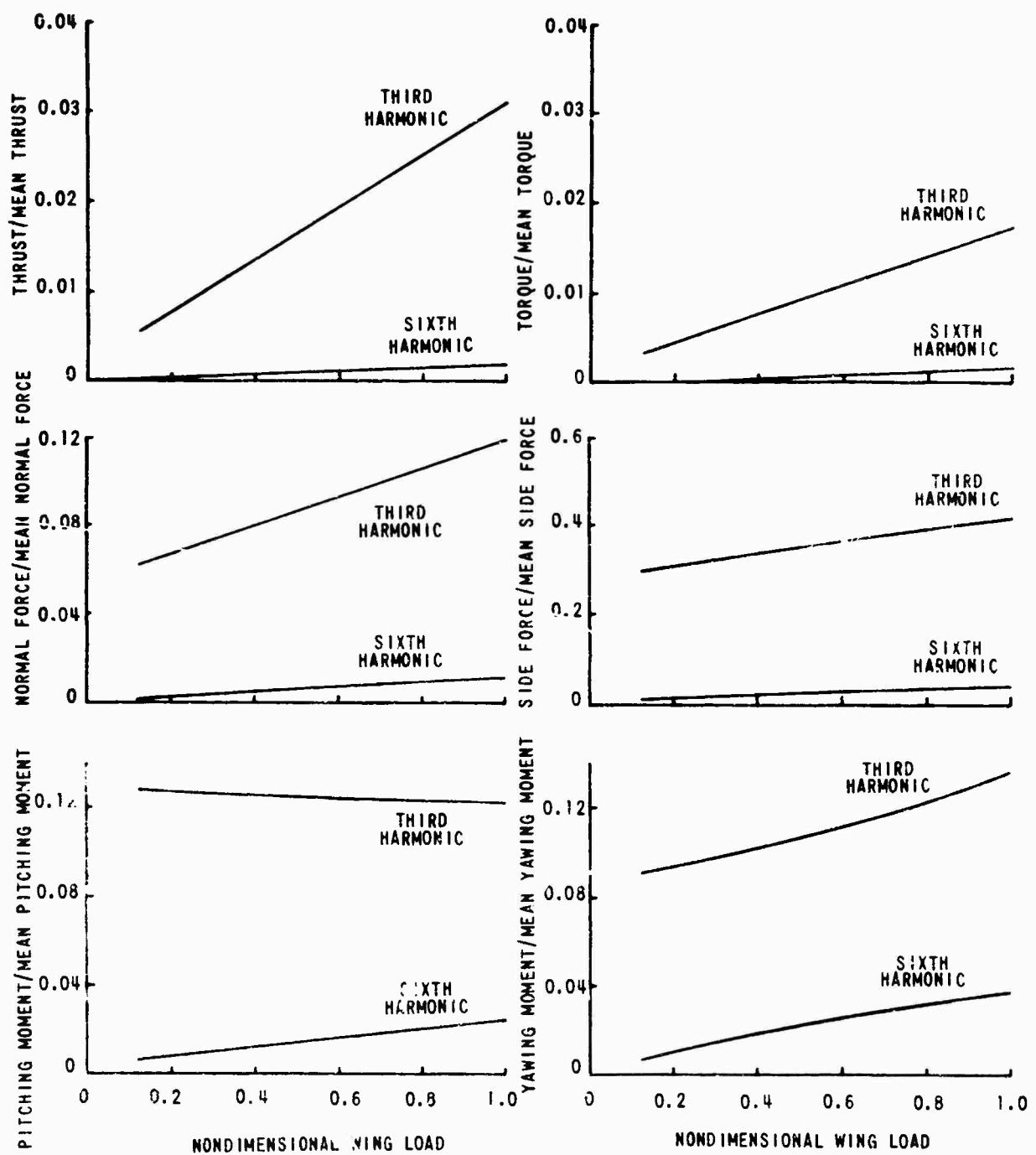
Figure 15 NONDIMENSIONALIZED THIRD AND SIXTH HARMONICS OF THE PERFORMANCE
QUANTITIES VS. WING LOAD. $\tau = 40°$

42
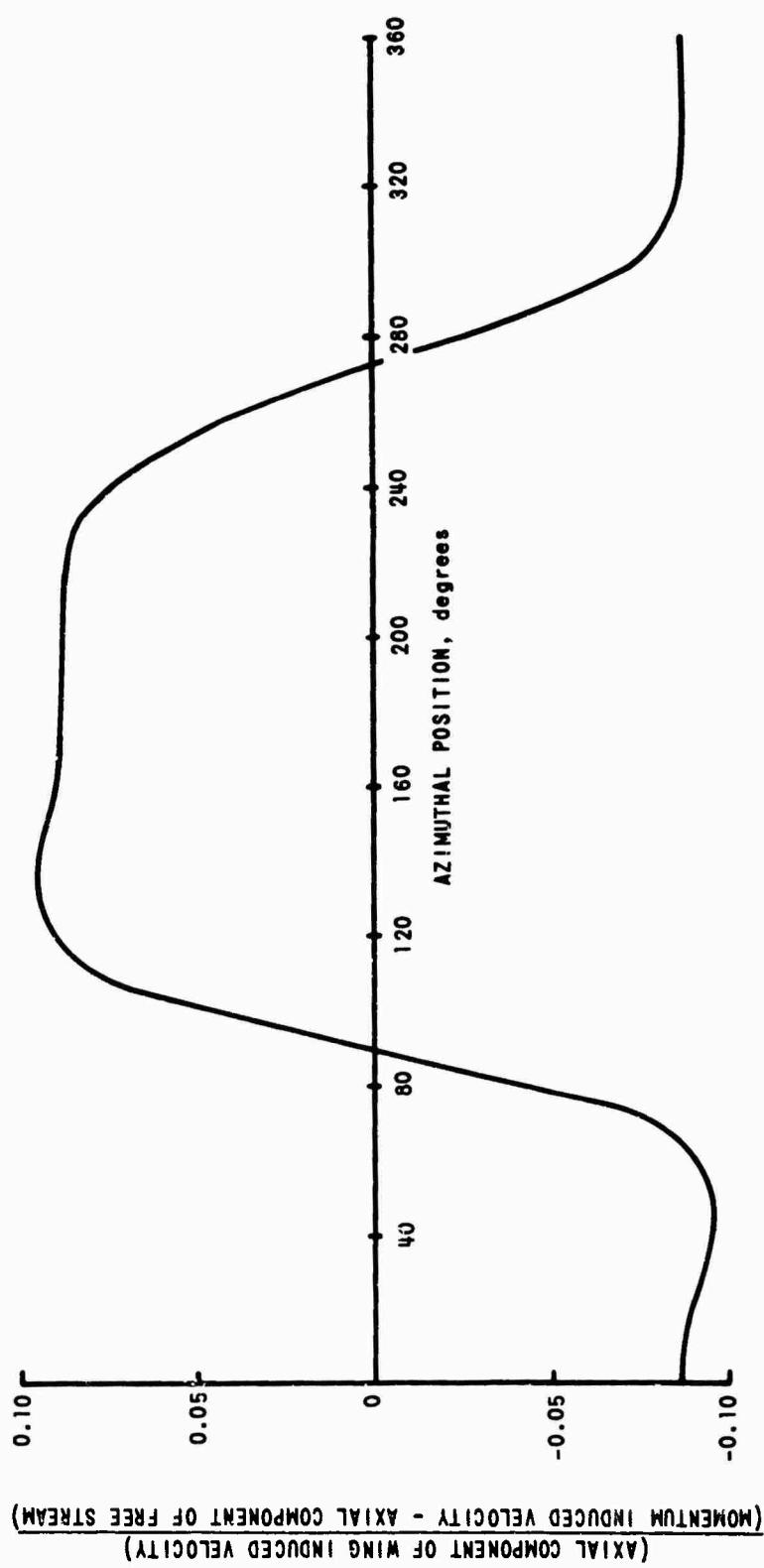
Figure 16 THE AZIMUTHAL VARIATION OF THE NONDIMENSIONALIZED AXIAL COMPONENT OF WING INDUCED VELOCITY AT $r/R \cong 0.85$
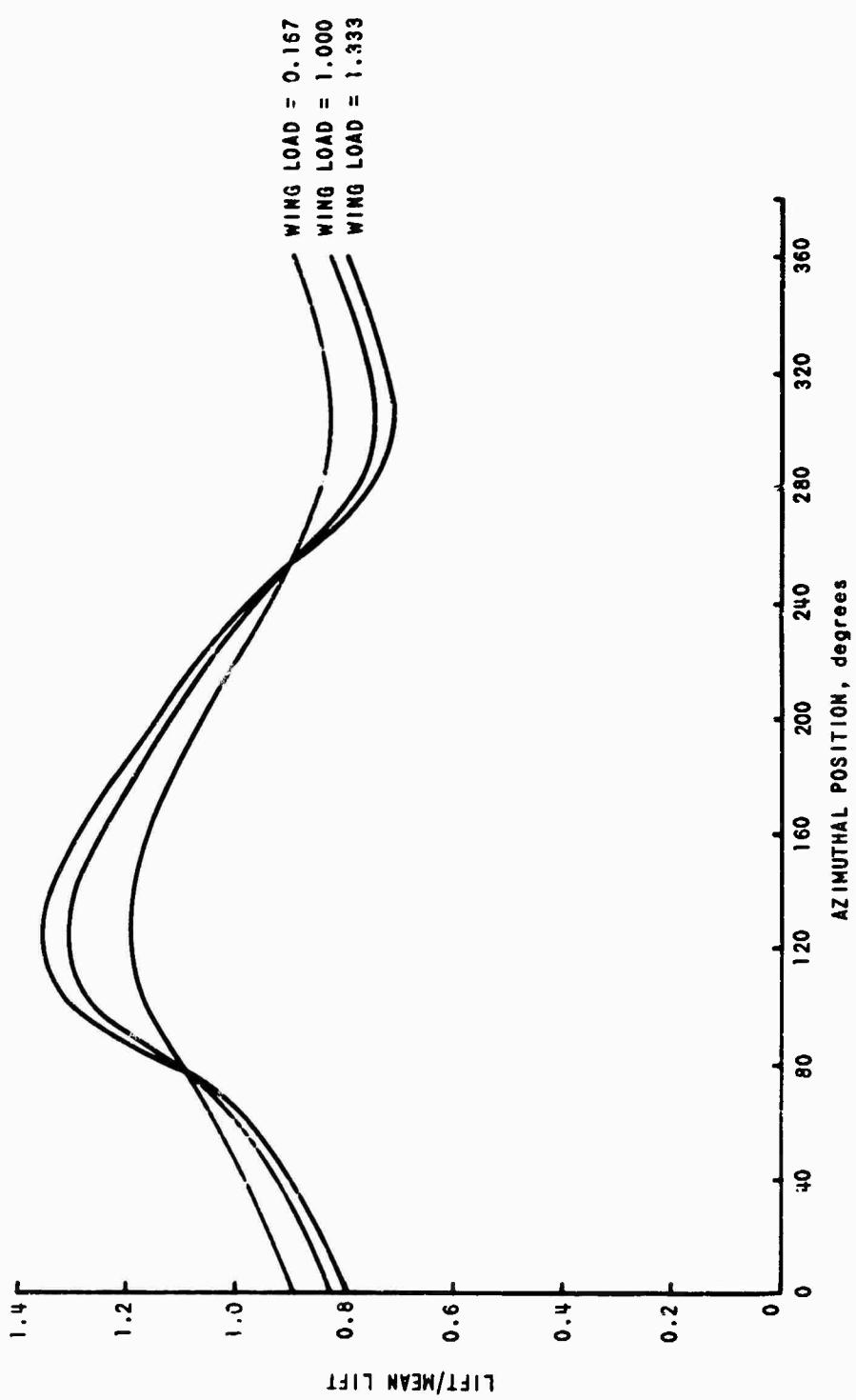
Figure 17 AZIMUTHAL VARIATION OF NONDIMENSIONALIZED MAXIMUM
LIFT FOR SEVERAL VALUES OF WING LOAD

44
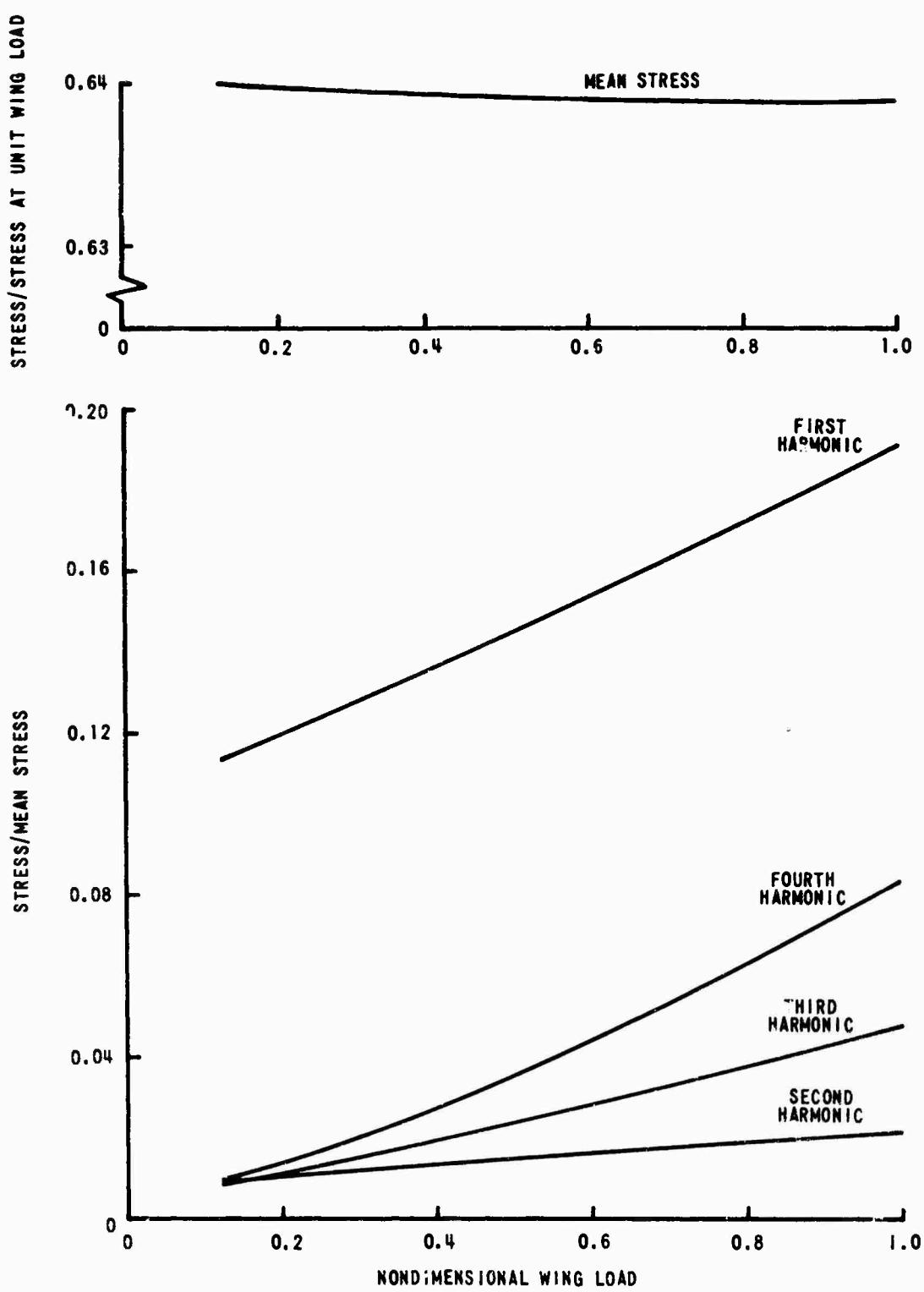
Figure 18 NONDIMENSIONALIZED LONGITUDINAL STRESS VS. WING LOAD
FOR $r/R \approx 0.60$ AT $\tau = 40°$

45

TIP VORTEX

ROOT VORTEX

NACELLE

PATH DOWN WHICH
UNCONTRACTED TIP
VORTEX MOVES

PATH DOWN WHICH
CONTRACTED ROOT
VORTEX MOVES

PATH DOWN WHICH
CONTRACTED TIP
VORTEX MOVES

PATH DOWN WHICH
UNCONTRACTED ROOT
VORTEX MOVES
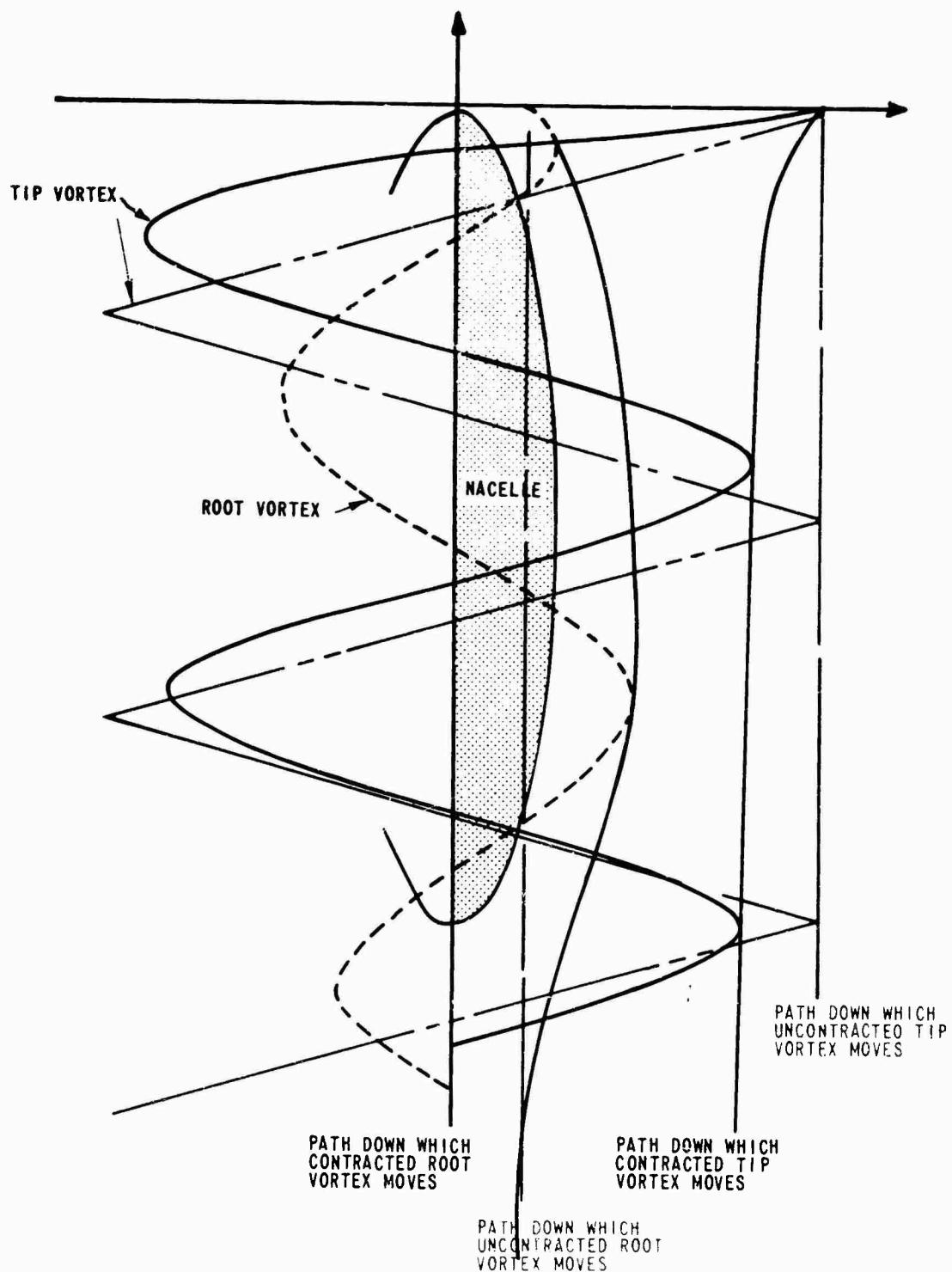
Figure 19 PICTORIAL OF CONTRACTED AND UNCONTRACTED WAKE MODELS

TECHNICAL SESSION II

ROTOR AERODYNAMICS

Wednesday Afternoon
22 June 1966

SESSION CHAIRMAN

F.J. Davenport
Vertol Division
The Boeing Company

NOTES

PERFORMANCE POTENTIAL OF ROTOR BLADE
INBOARD AERODYNAMIC DEVICES

M.I. Young   Jaan Liiva

Conventional rotor aerodynamic efficiency has been shown to become unacceptable for advance ratios greater than five tenths. This deterioration of efficiency is the result of the flow conditions which develop in the inner part of the rotor disk. Wind tunnel test results are presented for a model rotor having an inner segment moving separately from the outer part of the blade. These results show that substantially larger lift and propulsive forces and aerodynamic efficiencies can be realized when this segment has a pitch schedule selected to be consistent with the flow conditions of the inboard part of the rotor.

Several alternatives for achieving comparable performance gains with other aerodynamic devices are discussed.

PERFORMANCE POTENTIAL OF ROTOR BLADE
INBOARD AERODYNAMIC DEVICES*

by

MAURICE YOUNG and JAAN LIIVA

The Boeing Company, Vertol Division
Morton, Pennsylvania, USA

INTRODUCTION

The helicopter rotor has the unique capability of providing both the lift and the propulsive forces required for equilibrating the helicopter along its flight path. This aspect of rotor aerodynamics is perhaps too familiar. One result of this is that the underlying aspects of its aerodynamic efficiency in converting power into both lift and propulsion have, until recent years, received insufficient attention. This resulted in an unduly pessimistic view of the performance potential of the helicopter rotor at tip speed ratios of the order of five-tenths or greater, or, equivalently at flight path speeds greater than 200 knots. Most importantly, this view became a "self-affirming hypothesis". This pessimism fostered a great deal of compound-helicopter research, while objective efforts to illuminate the true limitations of rotor aerodynamic performance and programs to explore means of extending or improving rotor performance tended to be neglected. This paper reports on the results of one

program of theoretical and experimental rotor research aimed at identifying and minimizing the power losses associated with the inner portion of the helicopter rotor, with emphasis on operation as a lifting and propulsive device at tip speed ratios greater than five-tenths. The experimental results are shown to support the theoretical prediction of excellent rotor aerodynamic performance potential for tip speed ratios as large as six tenths, if means are provided for controlling the drag of the inner portion of the rotor in such high speed – high tip speed ratio flight conditions.

Theoretical Considerations
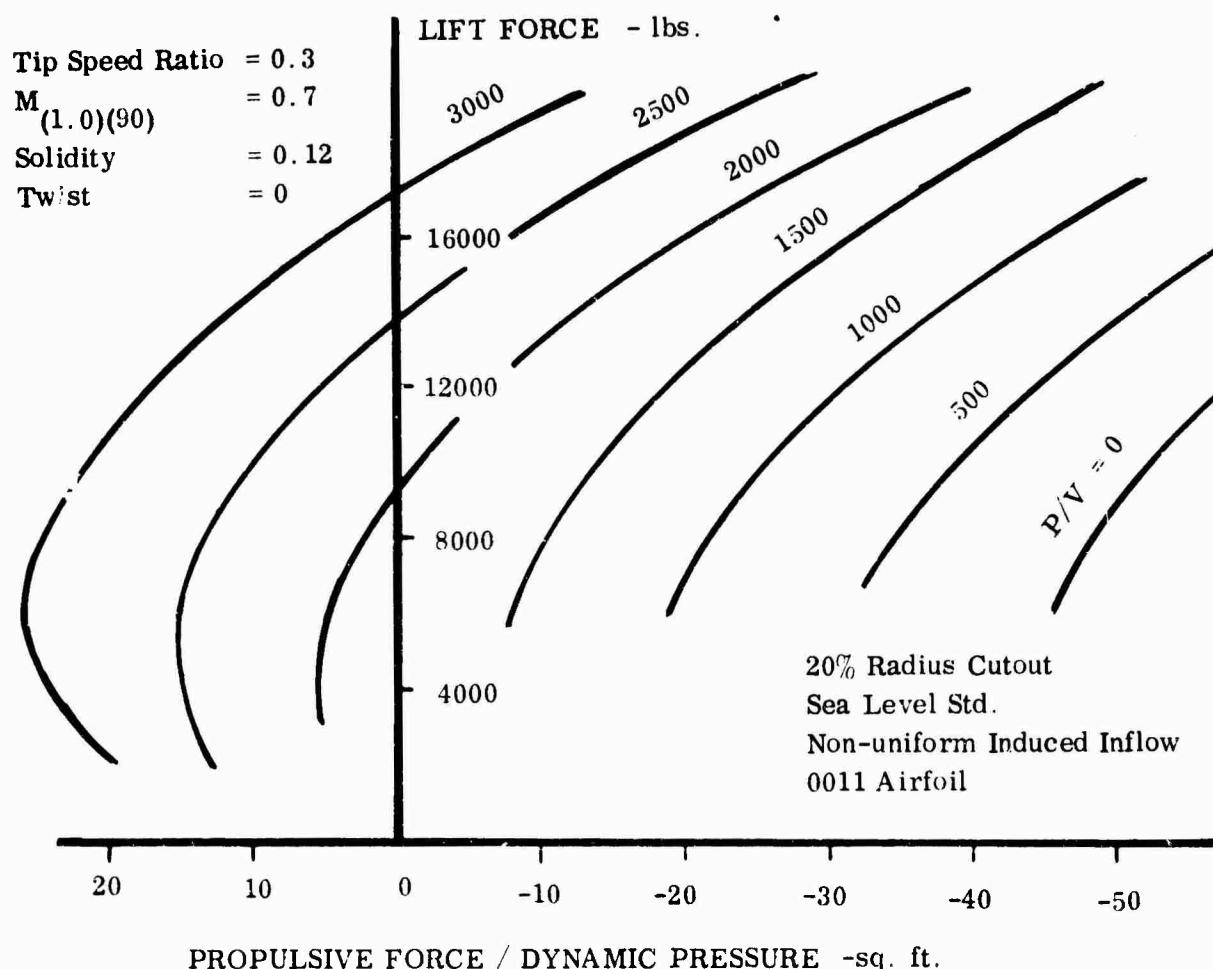
Figure 1. ROTOR POLAR DIAGRAM

The dual function and aerodynamic efficiency aspects of the rotor as a lifting and propulsive device are readily grasped by utilizing a polar diagram suggested by Schairer[2]. Figure 1 is typical of such diagrams. Lift (L) and Propulsive Force (X) are mapped at a given flight condition for various fixed levels of power. The graph designated "P/V equals zero" corresponds to an autorotative state. This is seen to result in a net rotor drag force. Progressive application of power is also seen to result in the rotor first overcoming its own drag, and ultimately producing an excess of propulsive force for equilibrating a parasite drag. By analogy with a wing, we may define a rotor lift to "effective drag" ratio. This is obtained by, in effect, subtracting the useful work per unit time or "thrust power" from the total rotor power. That is

$$\frac{L}{D}_{effective} = \left[\frac{P}{VL} - \frac{X}{L} \right]^{-1}$$

If this operation is carried out on the data of Figure 1, we obtain Figure 2 which permits the assessment of rotor aerodynamic lifting efficiency. The tangent from the origin is seen to define the magnitude of lift at which the maximum rotor lift-to-effective drag ratio occurs.

The rotor propulsive efficiency can be defined by observing in Figure 1 that the spacing of the constant power lines is not uniform, and that for each desired magnitude of lift, there is a well defined variation of the rotors ability to convert additional power into additional propulsive force. For example, at a fixed magnitude of Lift (L) = 7500 lbs., we crossplot propulsive force (X) versus P/V to obtain Figure 3.

Taking the autorotative state (P/V = 0) as a reference, a line of 45° slope would represent 100% propulsive efficiency. It is seen that at the moderate tip speed ratio of three-tenths, the rotor propulsive efficiency is virtually 100% until considerable blade stalling occurs.

3
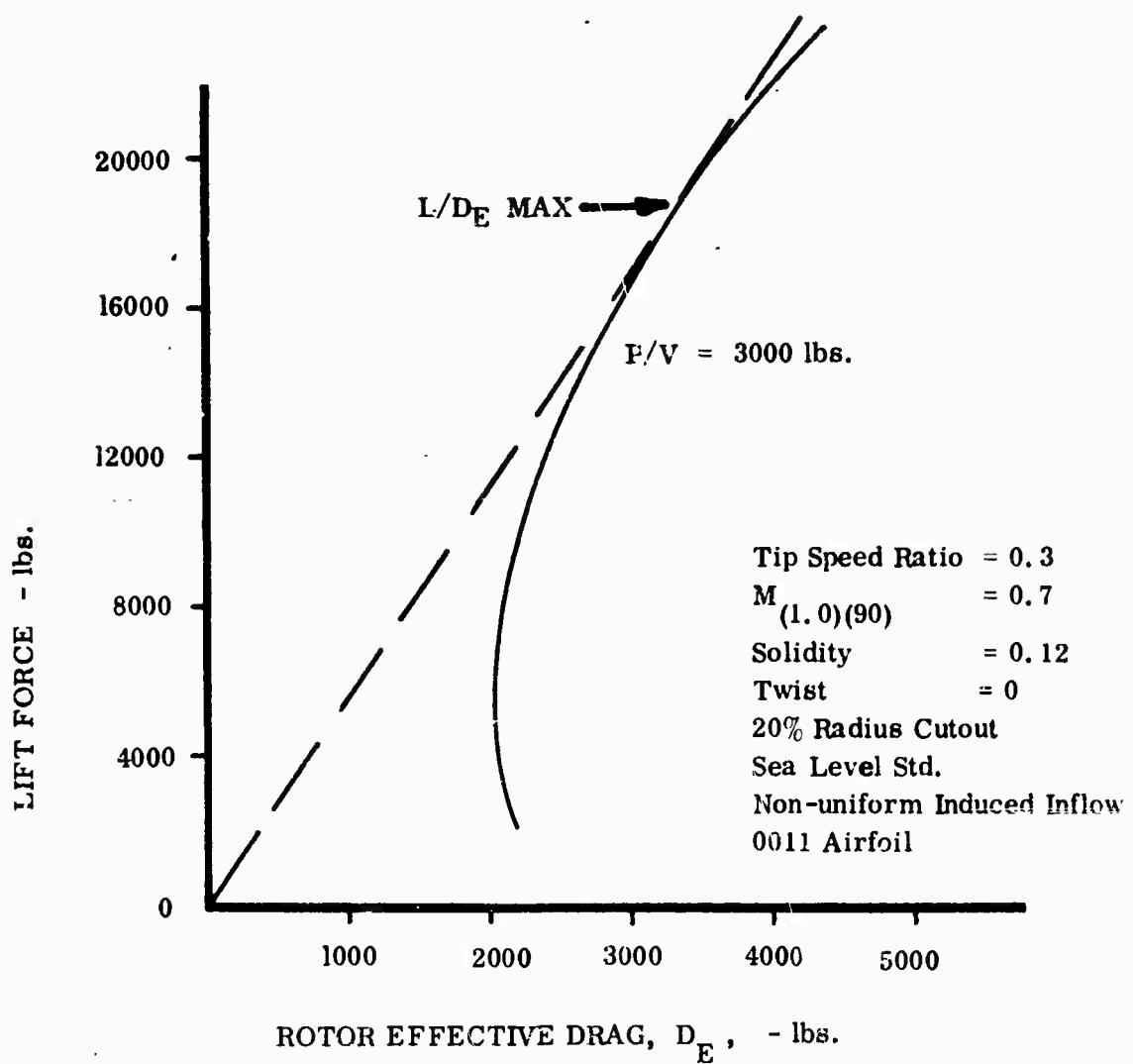
Figure 2. ROTOR LIFT vs ROTOR EFFECTIVE DRAG

4
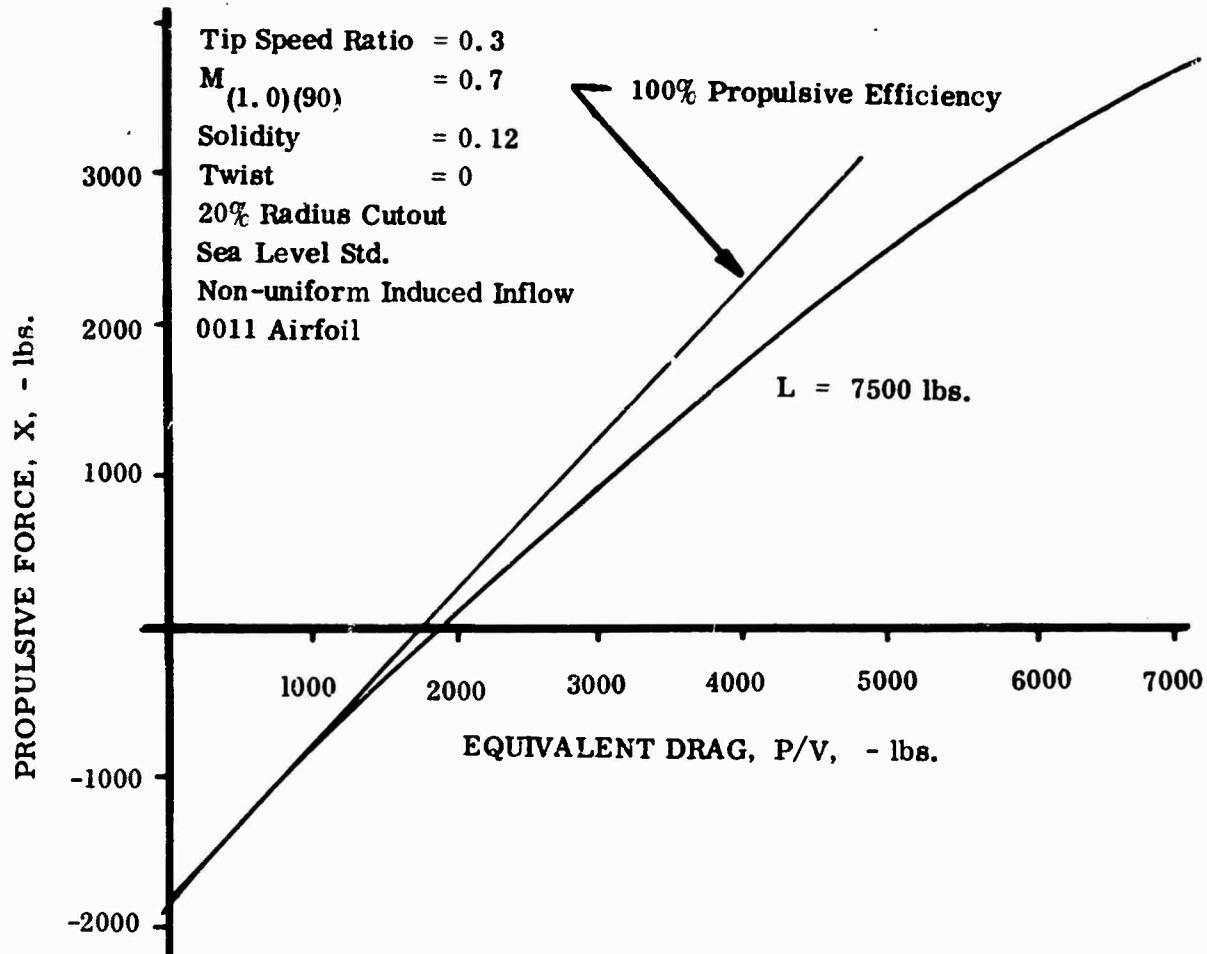
Figure 3. TYPICAL PROPULSIVE EFFICIENCY DIAGRAM

If we consider the propulsion characteristics of this illustrative rotor system at the same magnitude of lift, but over the range of tip speed ratios from three-tenths to six-tenths, a marked deterioration in propulsive efficiency can be noted. Figure 4 shows a marked decrease in propulsive efficiency with increasing tip speed ratio, with a relatively small decrease in the lift-to-effective drag ratio of the rotor (e. g. measured in autorotation when $P/V = 0$). This aspect of conventional rotor performance has provided much of the impetus for the proposed use of

5
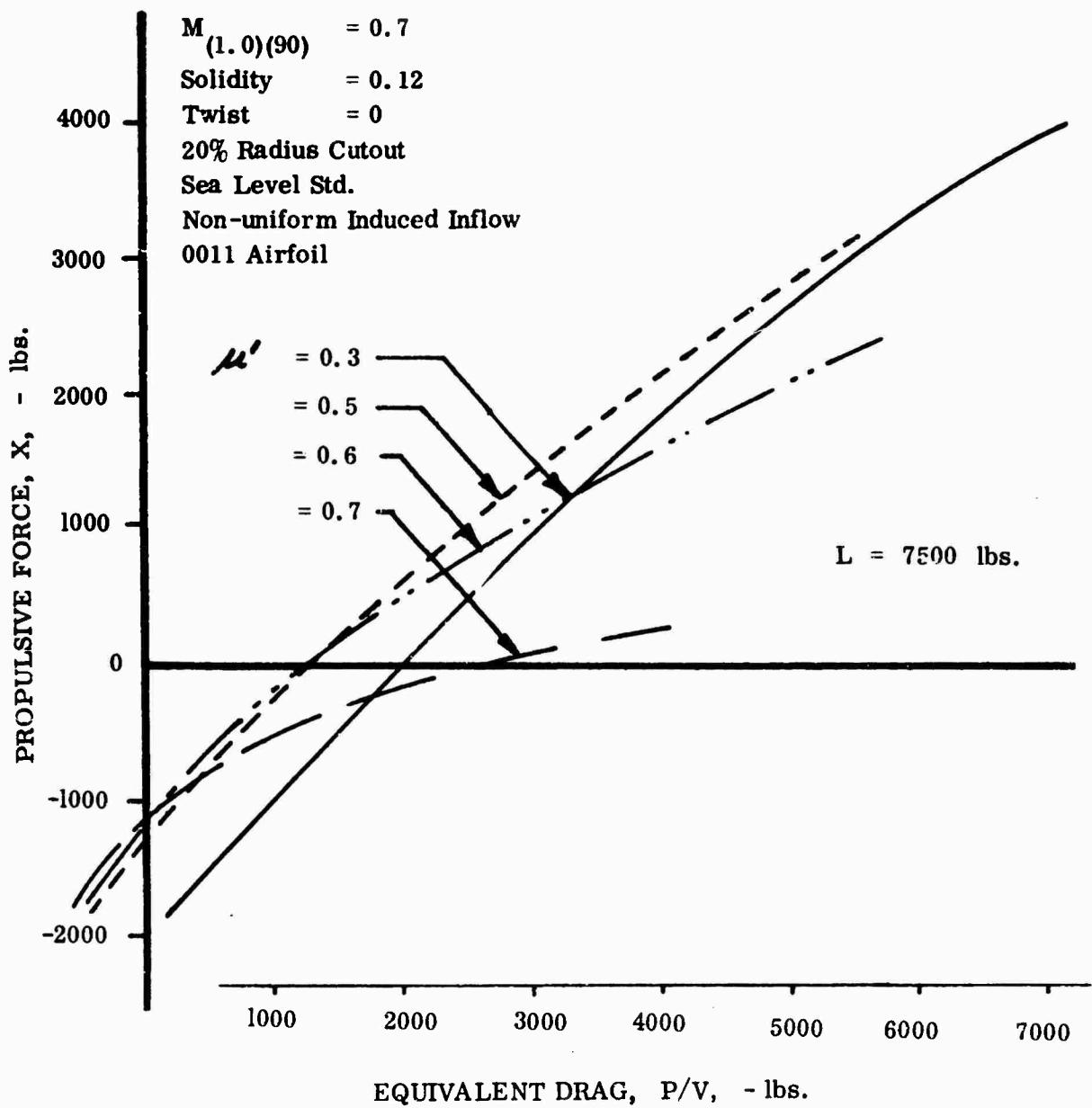
Figure 4. EFFECT OF TIP SPEED RATIO ON PROPULSIVE EFFICIENCY

6

auxiliary propulsion, and the variety of other compound helicopter configurations.

The first important insights into the cause of this marked deterioration of propulsive efficiency were obtained by Gessow and Gustafson of NASA[3] which demonstrated the adverse effects of the drag of the inboard portions of the rotor blade, and by Harris[4] who showed that blade stalling, per se, was not of itself a fundamental cause if rotor solidity were to be increased at tip speed ratios of the order of five-tenths or greater, then the desired increase in propulsive capability would be completely offset by the accompanying increase in the inherent rotor drag at such large tip speed ratios.

Figure 5 illustrates the overriding importance of the drag of the inboard portion of the rotor blade by comparing the propulsive capability of the illustrative rotor of Figure 4 to an idealized rotor which progressively eliminates this region in direct proportion to tip speed ratio (up to five-tenths). It is seen from Figure 5 that idealized "root cutout" (i.e. no spar drag) effectively eliminates the deterioration in propulsive efficiency from which the conventional rotor suffers.

The concept of a separately moveable inner blade segment having a pitch schedule specifically adapted to the flow conditions of the inner portion of the rotor suggested itself as a means of approaching the idealized rotor performance potential, as shown in Figure 5. Such a system appeared to be well suited to a straight-forward comparison, both experimentally, and theoretically, thereby providing a means of verifying the implied aerodynamic principle: minimize the inner rotor blade drag on the retreating side of the rotor disc and maximize the lift on the advancing side for high propulsive efficiency at tip speed ratios greater than five to six-tenths.

MODEL CONCEPT AND DESIGN

Theoretical consideration began with an inboard twistable segment. The inboard portion of the rotor blade was programmed to operate at its optimum angle of attack (maximum section lift to drag ratio) at every point on the advancing side;

7

in the reversed flow region the segment pitch was programmed to provide minimum drag. The inboard segment thereby provides an increase in lift and propulsive force on the advancing side, without a significant change in flapping. By pitching the blade nose-down in the reversed flow region (a minimum drag attitude), the download normally associated with this region is also minimized. Continued theoretical consideration indicated that for tip speed ratios of the order of five to six-tenths, a simple, rigid inboard segment, extending to 50 percent of blade radius provided a good compromise between design complexity and potential performance gains.
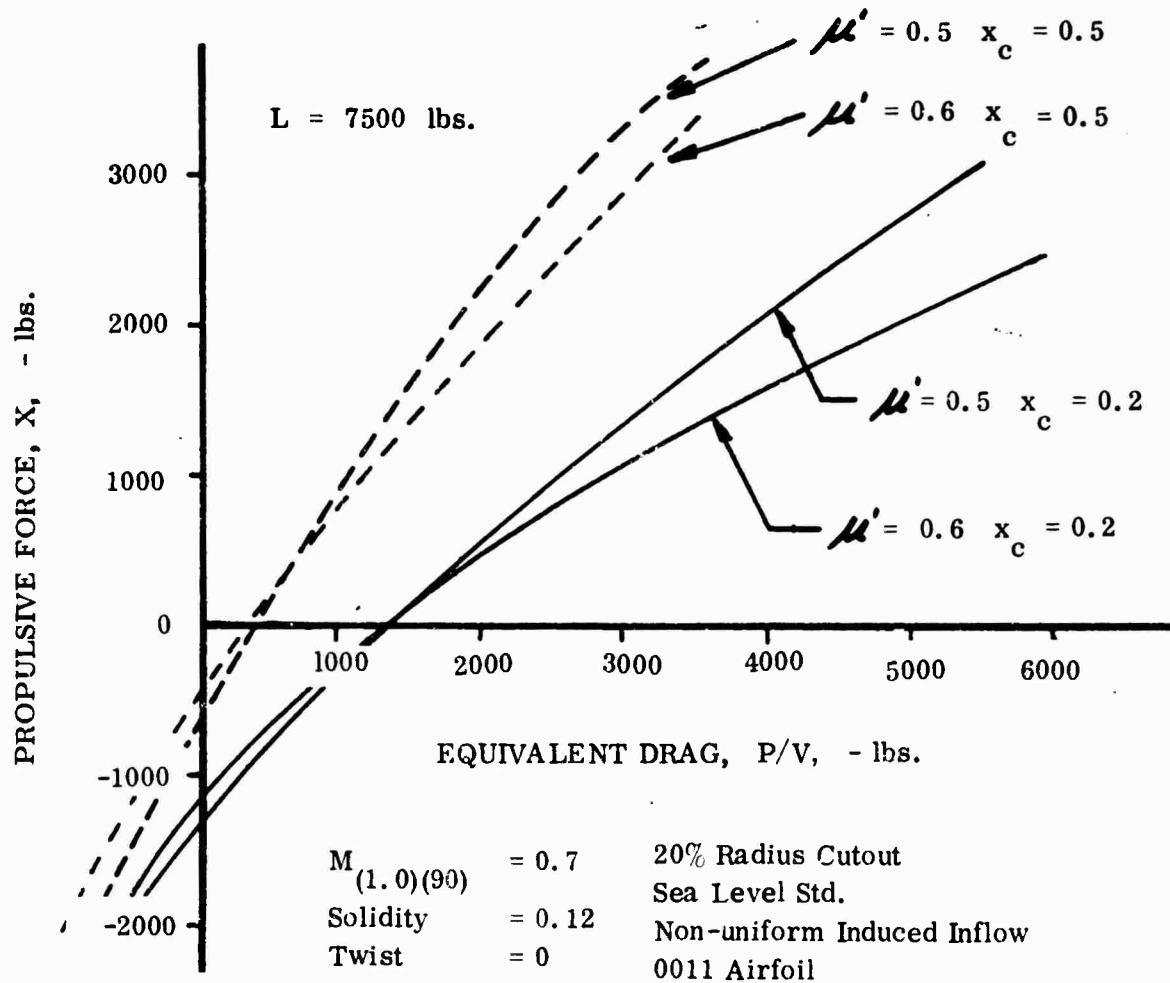

Figure 5. EFFECT OF CUTOUT ON PROPULSIVE EFFICIENCY

8

The pitch schedule shown in Figure 6 was developed analytically for flight at a tip speed ratio of six-tenths. It was designed to provide a rotor propulsive capability to overcome a drag to lift ratio for the vehicle in excess of .00125. (This is equivalent to 10 sq. ft. of parasite drag area at a gross weight of 8,000 lbs.).
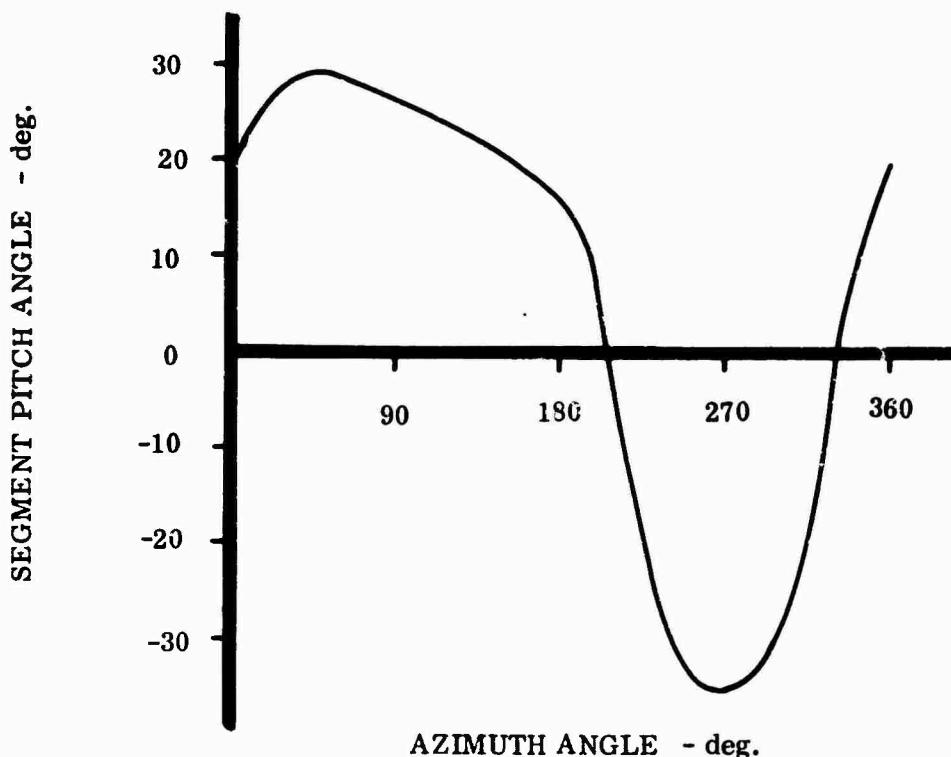

Figure 6. INBOARD SEGMENT PITCH SCHEDULE FOR
BASIC SEGMENTED ROTOR

The theoretical calculations revealed that the optimum schedules of pitch change for an inner segment are essentially pulsatile rather than sinusoidal. In effect, the blade is operated with moderate twist over most of the rotational cycle, and rapidly "untwisted" in the portion of the rotational cycle entailing a significant region of reversed flow. The theoretical performance prediction for the influence of a rotor having an inner blade segment with a specifically programmed schedule of

9

pitch change is shown in Figure 7. It is seen that the idealized rotor propulsive capability with large "root cutout" and no spar drag is predicted to be approachable by a rotor with an inner segment.

Figure 7. SEGMENTED ROTOR - IDEALIZED ROTOR COMPARISON

10


Tip Speed Ratio = 0.6
$M_{(1.0)(90)}$ = 0.7
Solidity = 0.12
Twist = 0
Sea Level Std.
0011 Airfoil
Non-uniform Induced Inflow

"Ideal" Cutout Rotor, $x_c = 0.5$

Basic Segmented Rotor, $x_c = 0.2$

L = 7500 lbs.

PROPULSIVE FORCE, X, - lbs.

EQUIVALENT DRAG, P/V, - lbs.

Figure 7. SEGMENTED ROTOR - IDEALIZED ROTOR COMPARISON

10
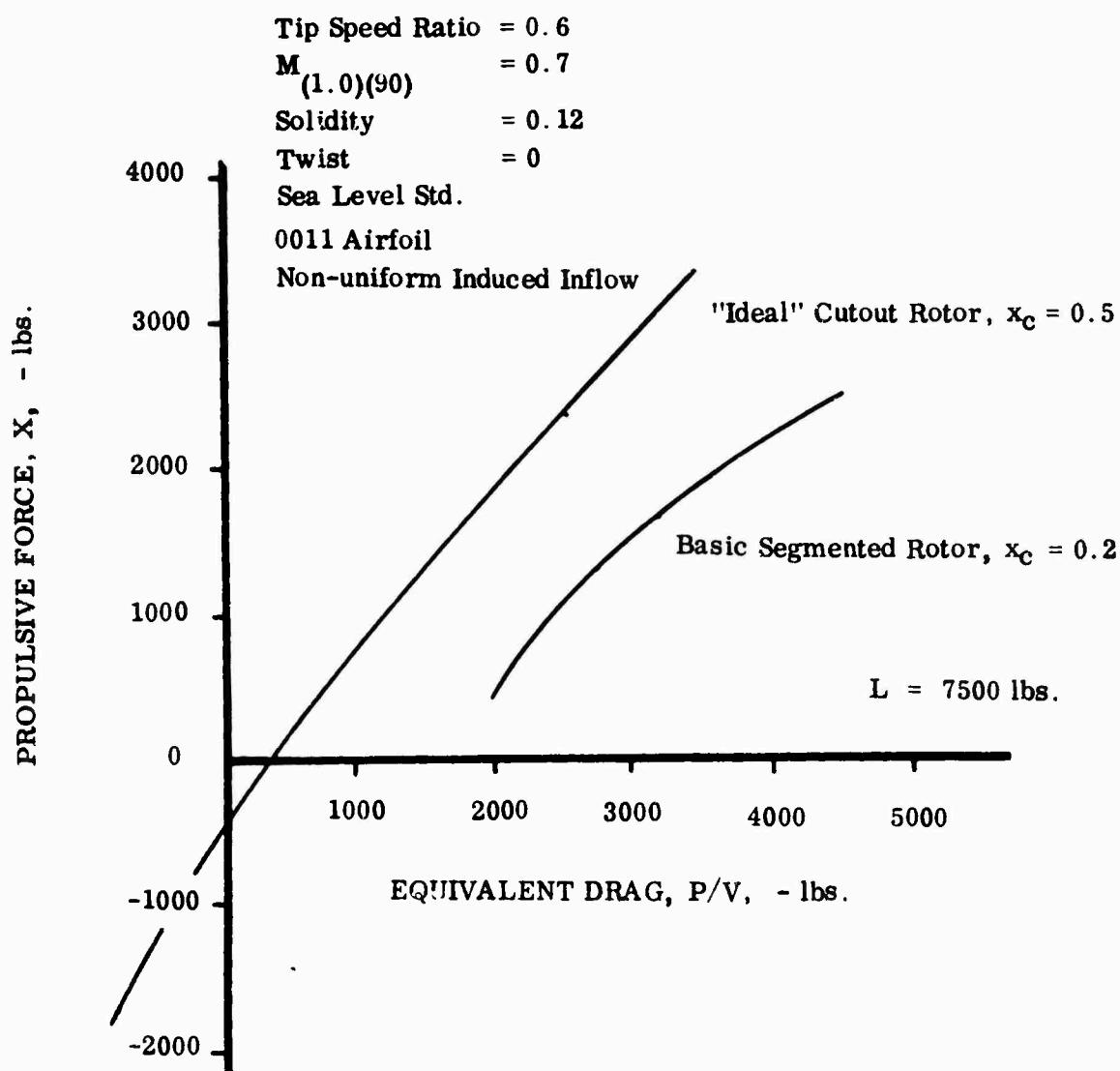
6W 546

Figure 8. MODEL SEGMENTED BLADE CONSTRUCTION DETAILS
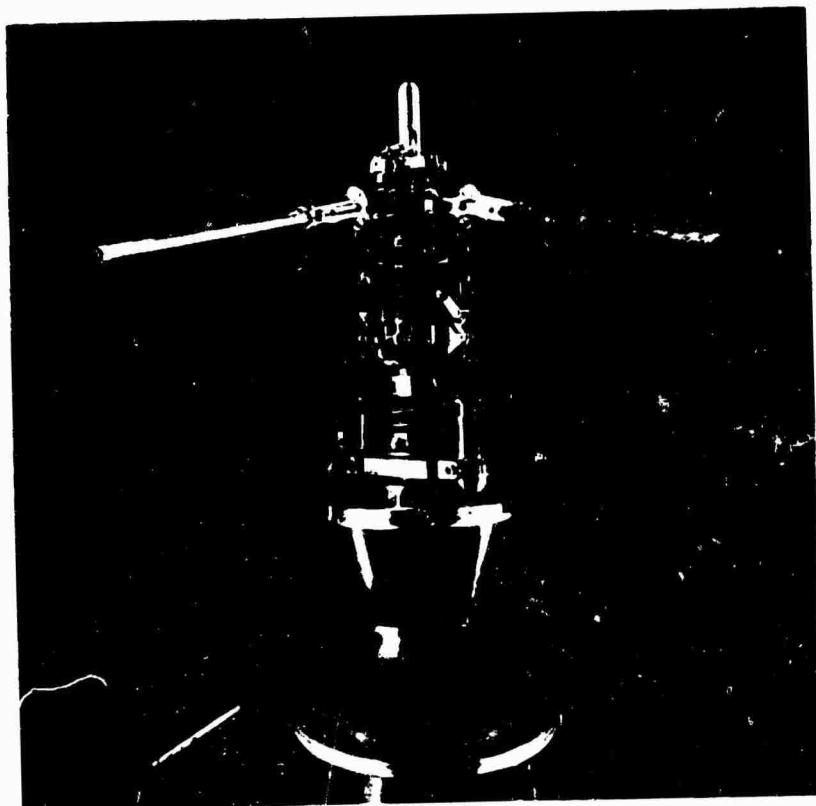
Figure 9. MODEL SEGMENTED ROTOR
HUB INSTALLATION

11
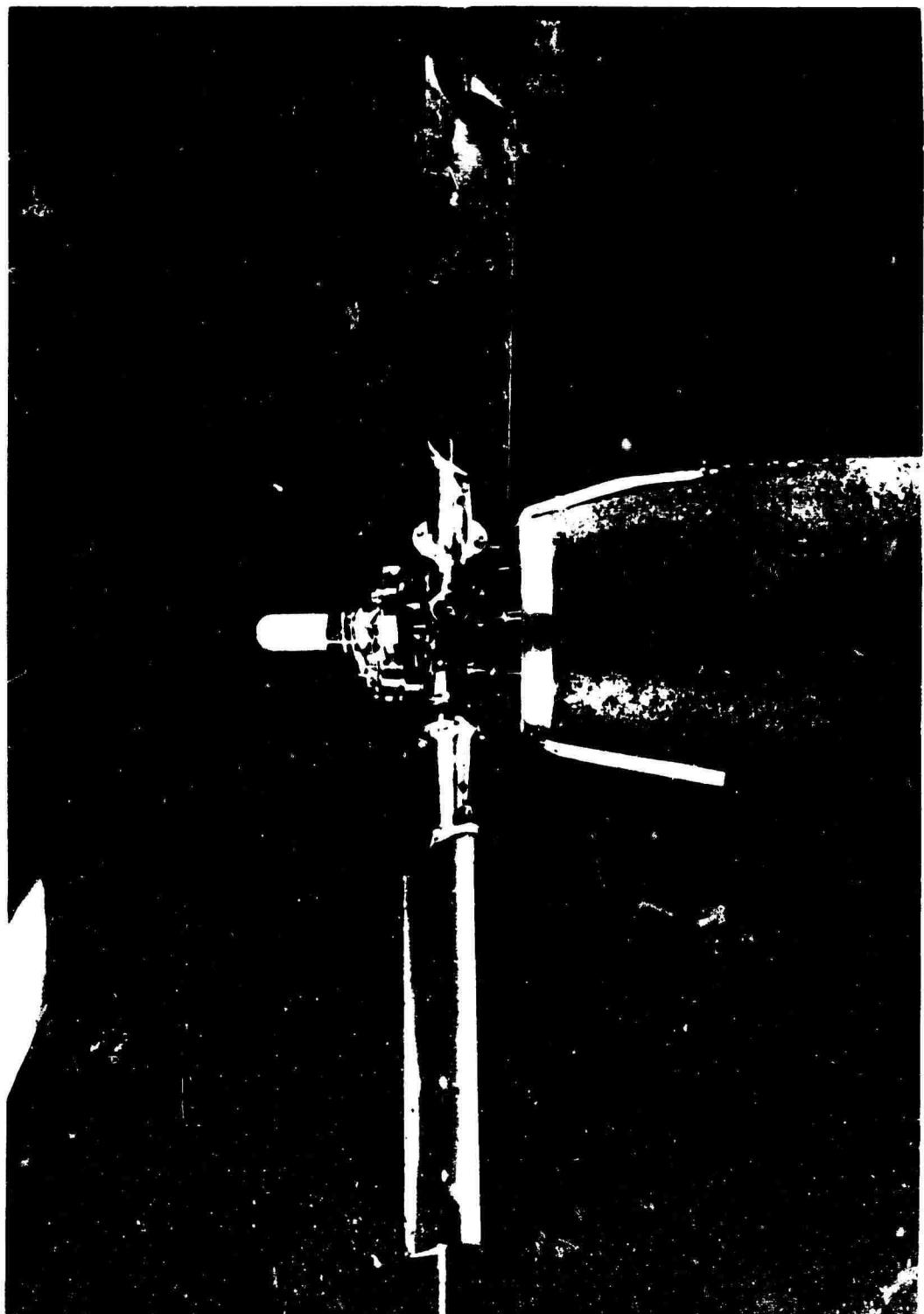
Figure 10. MODEL SEGMENTED ROTOR WIND TUNNEL INSTALLATION

The specific characteristics of the model segmented rotor are given in Table 1. Blade and segment construction are shown in Figure 8. The blade is fully articulated at the root and two pitch change mechanisms are provided by utilizing a conventional swash plate control for the outboard segment and a cam with a specific schedule for the inboard segment. By removing the inner segment, the system can be operated as a conventional rotor. The hub assembly is shown in Figure 9.

EXPERIMENTAL RESULTS

The tests were conducted at the University of Maryland in the Glenn L. Martin Institute of Technology Low Speed 8 Ft. x 11 Ft. Wind Tunnel. The model rotor is shown installed in the tunnel in Figure 10. All test data were recorded in digital form and corrections for tunnel boundary effects were made in the "off-line" data processing.

Data were taken with the segmented rotor, and for comparison the test conditions were repeated with the inner segment locked to the outer to provide comparative conventional rotor data. Figure 11 indicates that the segmented rotor produces more propulsive force than a conventional rotor. Most of this increase in propulsive force was found to result from increased efi. :r..y on the advancing side. This is shown by Figure 12 where the propulsive capability of the basic segmented rotor is compared with one having an alternate cam schedule that eliminates the nose-down pulse in the reversed flow region.

Figure 13 is a summary presentation of the propulsive efficiencies of a conventional rotor, the basic segmented rotor, and the segmented rotor with the alternate, simplified pitch schedule. It shows that the basic segmented rotor has a significantly higher efficiency over the entire range of propulsive forces at a tip speed ratio of six-tenths.

Changes to the azimuthal phasing and magnitudes of the inboard segment pitch schedule were also investigated experimentally. These changes did not result in further gains in either performance or propulsive force.

13

Tip Speed Ratio = 0.6
$M_{(1.0)(90)}$ = 0.36
Solidity = 0.119
Twist = 0
19% Radius Cutout
Hub Tares Are Not Removed

$C_T{}'/\sigma$

$P/qd2V\sigma = 0.185$

0.151

0.151

0.118

0.118

0.084

0.084

.12

.10

.08

.06

.04

.02

Conventional

Limit of Conventional Rotor
Propulsive Force Producing
Capability

Segmented

.06   .04   .02   0   -.02   -.04   -.06

$X/qd^2\sigma$
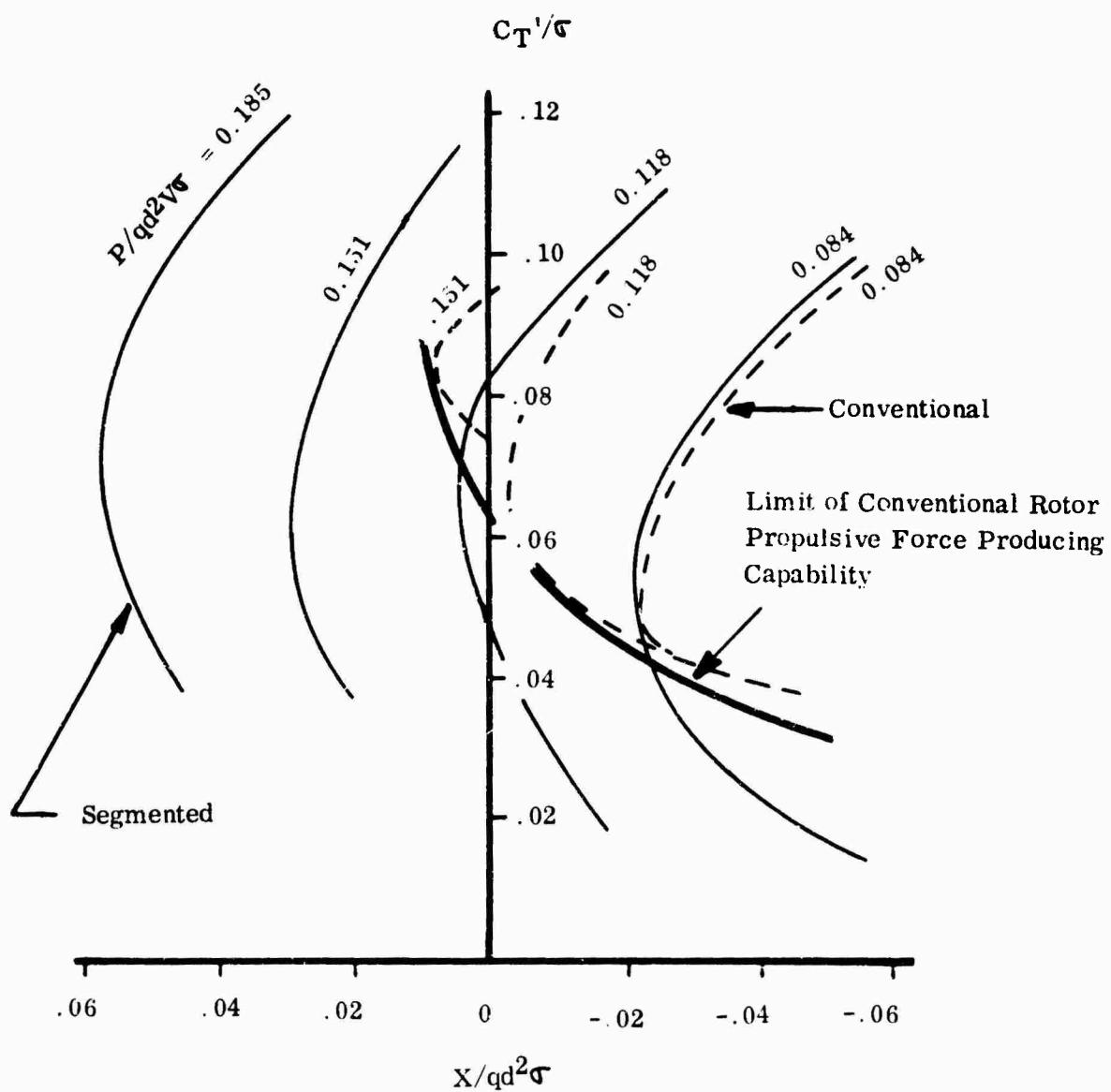
Figure 11.   SEGMENTED ROTOR - CONVENTIONAL ROTOR
EXPERIMENTAL COMPARISON

14
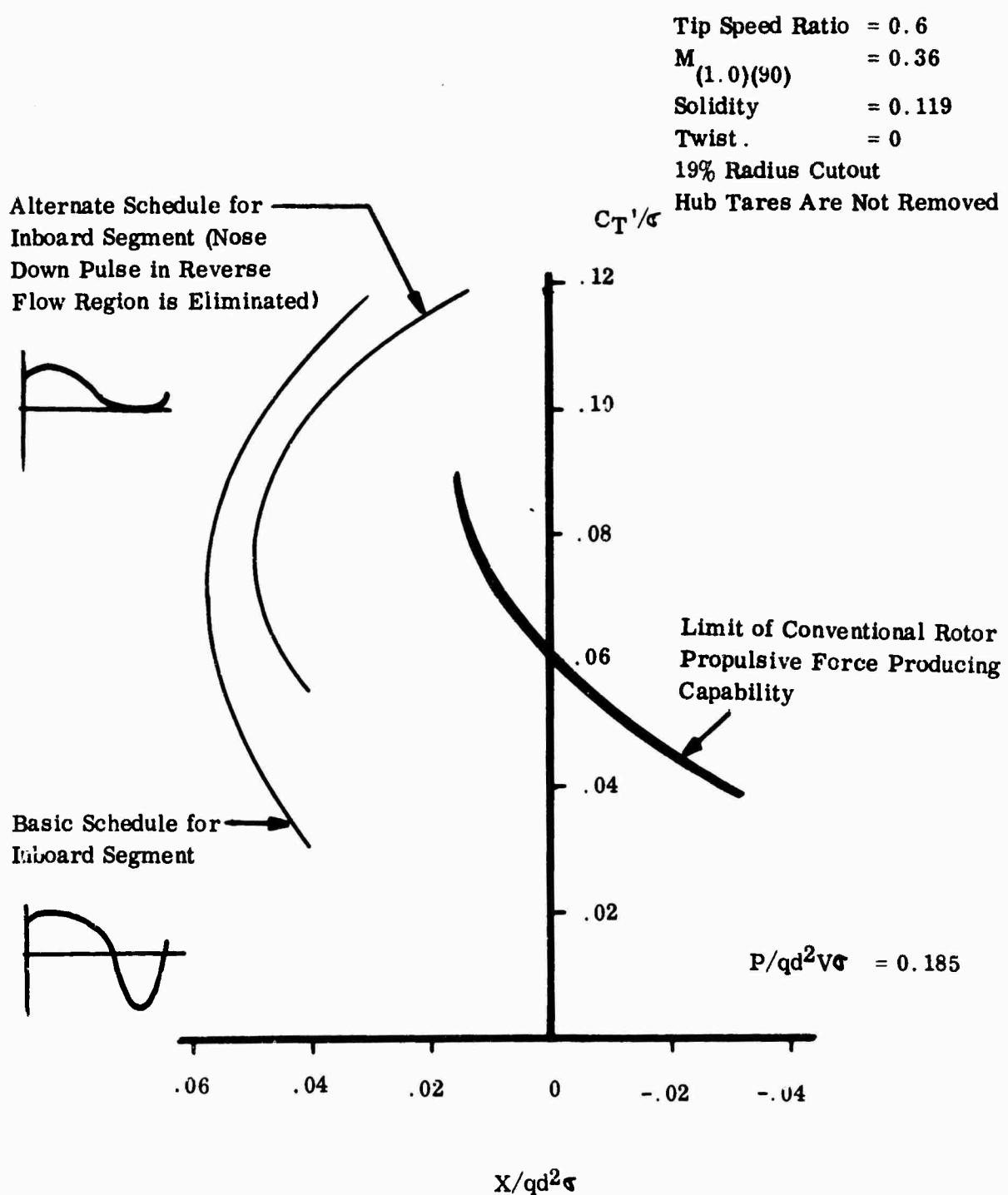
Figure 12. BASIC PITCH SCHEDULE - ALTERNATE PITCH
SCHEDULE EXPERIMENTAL COMPARISON

The experimental data in Figure 11 indicates that the segmented rotor is capable of lifting and propelling an 18,000 lb. helicopter with an equivalent drag area of 18 ft^2 for a tip speed ratio of six tenths and an advancing tip Mach number of 0.94 (assuming a blade design subject to no significant compressibility losses) without auxiliary wings and propulsion. (Calculation details are given in Appendix 1.)

Tip Speed Ratio = 0.6
$M_{(1.0)(90)}$ = 0.36
Solidity = 0.119
Twist = 0
19% Radius Cutout
Hub Tares Are Not Removed

Basic Pitch Schedule Rotor

Alternate Pitch Schedule Rotor

Conventional Rotor
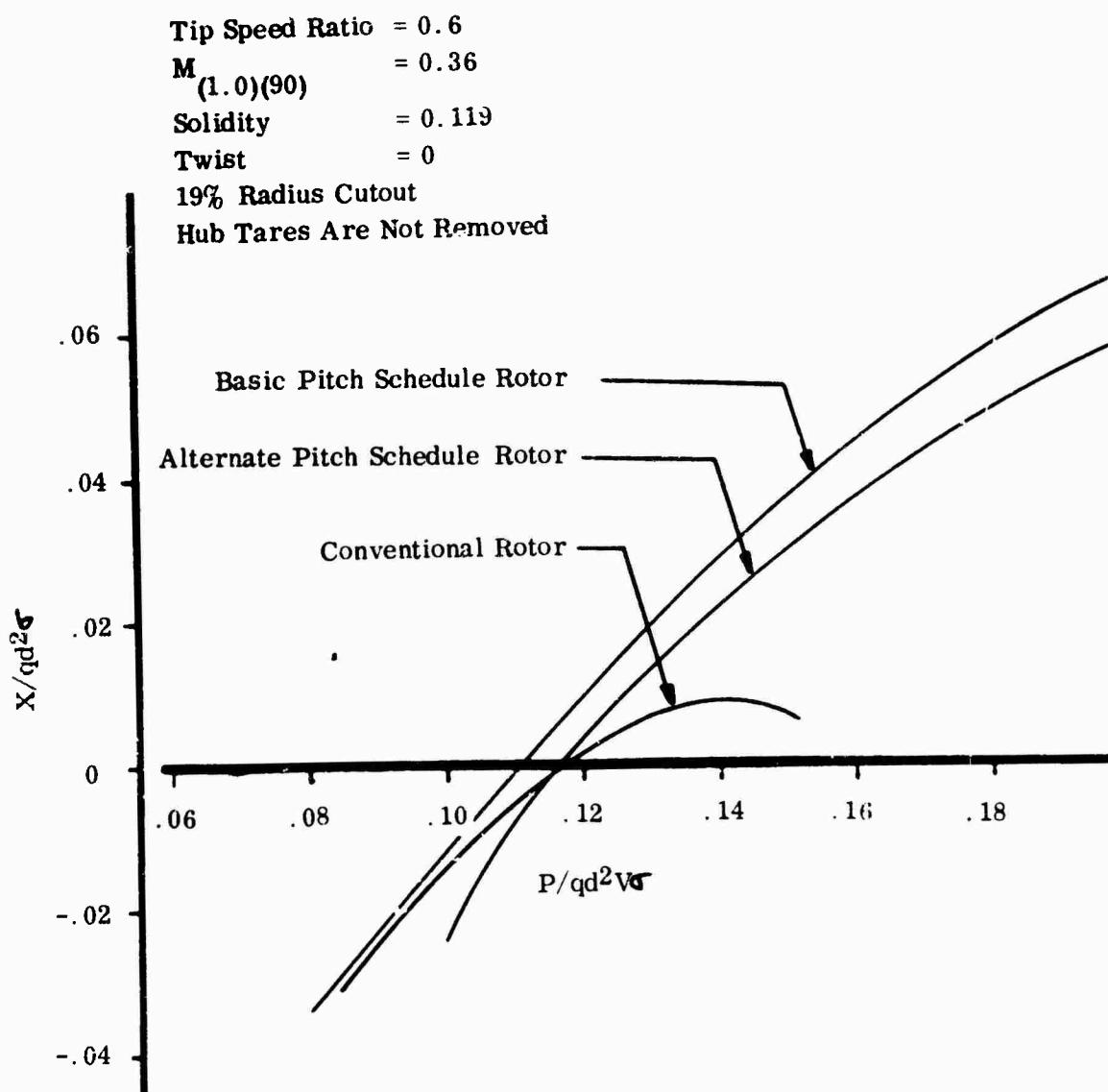
Figure 13. CONVENTIONAL ROTOR - SEGMENTED ROTORS PROPULSIVE EFFICIENCY COMPARISON

16

ALTERNATE AERODYNAMICS APPROACHES TO
ROTOR INBOARD AREA EFFICIENCY

Recognizing the complexity of a purely mechanical approach to implement-
ing the aerodynamic principle, two alternate approaches are considered. The first of
these schemes employs tangential blowing applied to a round shank; the second is an
elliptic shank with a jet flap at the leading and trailing edges.

All of the theoretical calculations were performed with The Boeing Com-
pany's Vertol Division Computer Program for "Rotor Airloads and Performance Anal-
ysis with Wake-Induced Inflow"[5]. In this program the differential equation for flap-
ping is solved by a step by step method. A realistic inflow distribution is computed
internally from the trailing wake structure using a modification of the method outlined
in Reference 6. The airfoil section characteristics used in the strip theory method
for airloads computation reflect the effects of compressibility and angle of attack over
the full range normally encountered on a helicopter. These airfoil characteristics are
derived from wind tunnel tests of airfoil sections. A typical correlation with test data
is shown in Figure 14 for the conventional rotor and in Figure 15 for the segmented
rotor.

Circular Shank with Tangential Blowing

Lockwood [7] has shown that lift can be generated and that drag can be
reduced by applying tangential blowing to a circular cylinder. The data in his report
(Figure 16) were converted to section characteristics as functions of angle of attack
and blowing coefficient. These data were used to evaluate the effect of blowing on a
rotor shank. By recognizing that the relative angles of attack that a rotor shank
experiences are between 10 to 20 degrees on the advancing side and about 210 degrees
on the retreating side, the shank configuration shown in Figure 17 was designed with
two blowing slots. By cycling the valve to provide blowing in opposite directions for
the advancing side and the reversed flow region, lift can be generated in both of these
regions.

Tip Speed Ratio $= 0.6$
$M_{(1.0)(90)}$ $= 0.36$
Solidity $= 0.119$
Hub Tares Are Removed
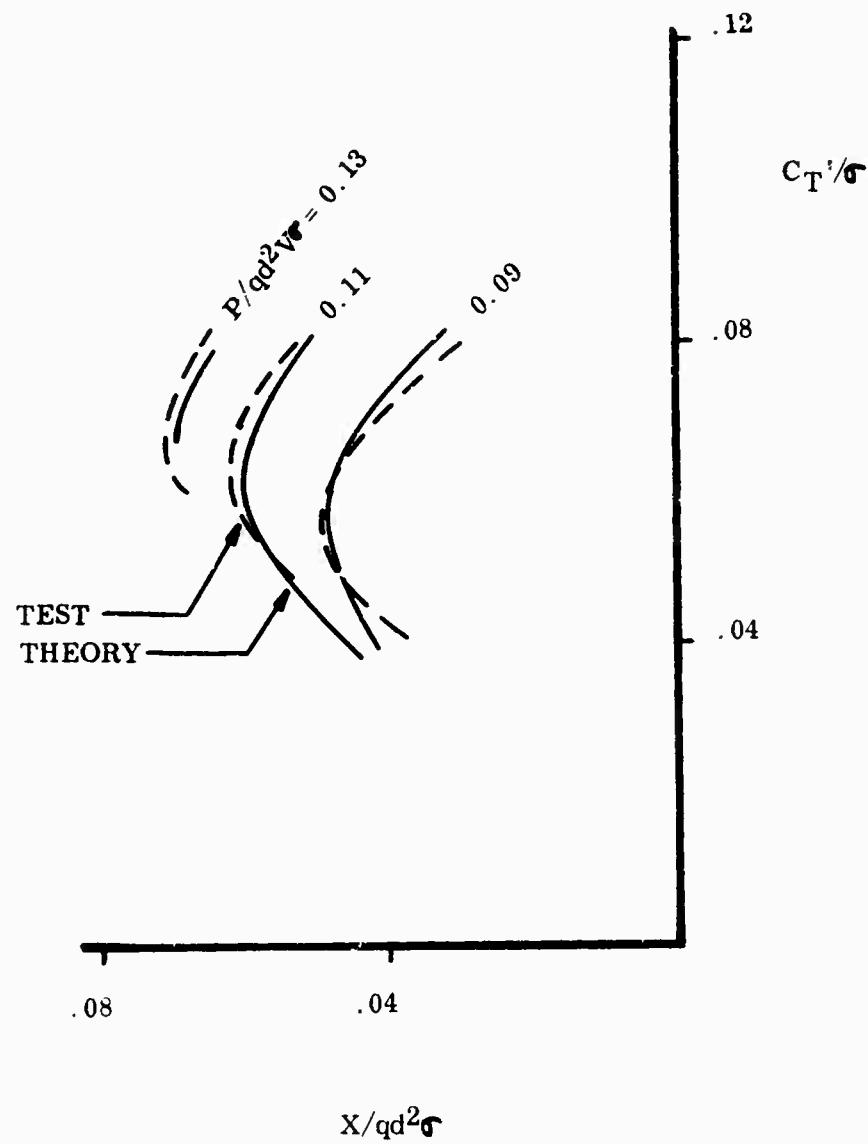
Figure 14. CONVENTIONAL ROTOR CORRELATION

18

Tip Speed Ratio $= 0.6$

$M_{(1.0)(90)} = 0.36$

Solidity $= 0.119$
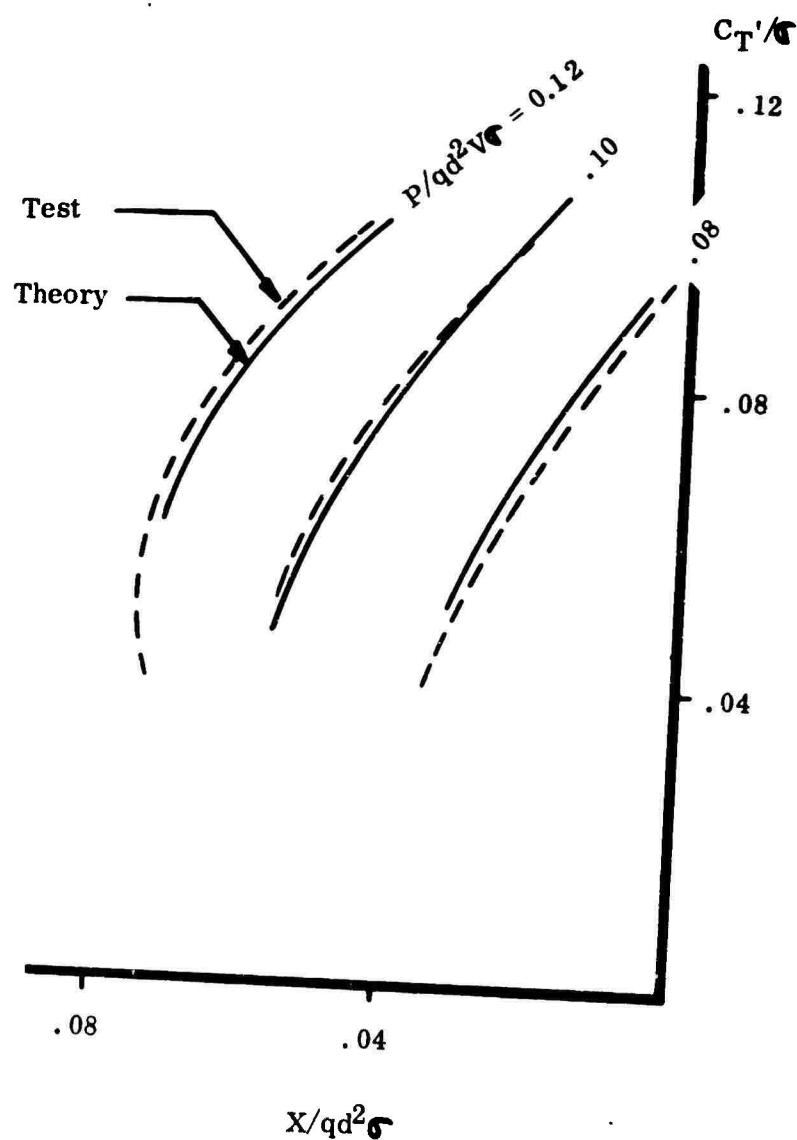

Figure 15. SEGMENTED ROTOR CORRELATION

19
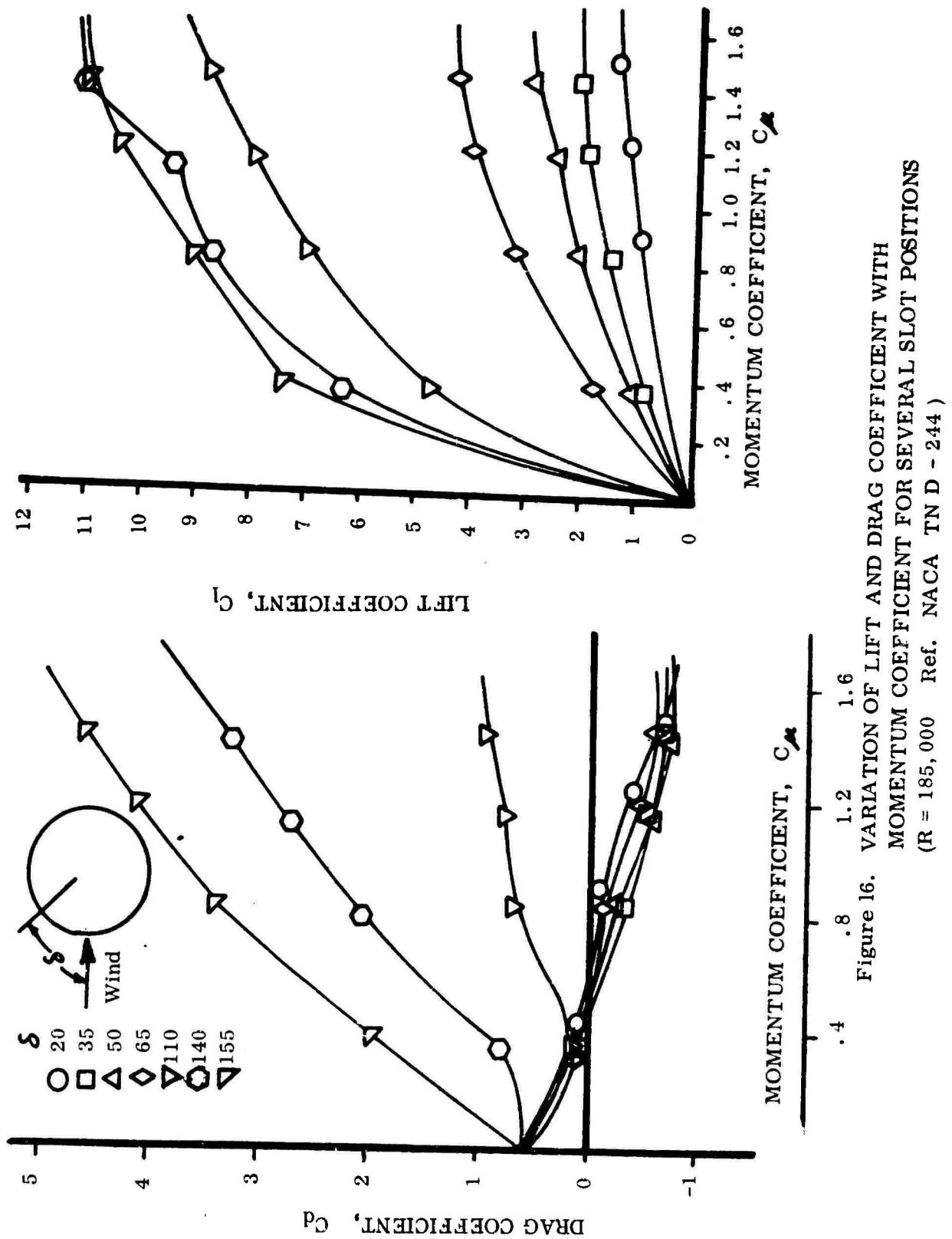
Figure 16. VARIATION OF LIFT AND DRAG COEFFICENT WITH MOMENTUM COEFFICIENT FOR SEVERAL SLOT POSITIONS (R = 185,000   Ref. NACA TN D – 244)
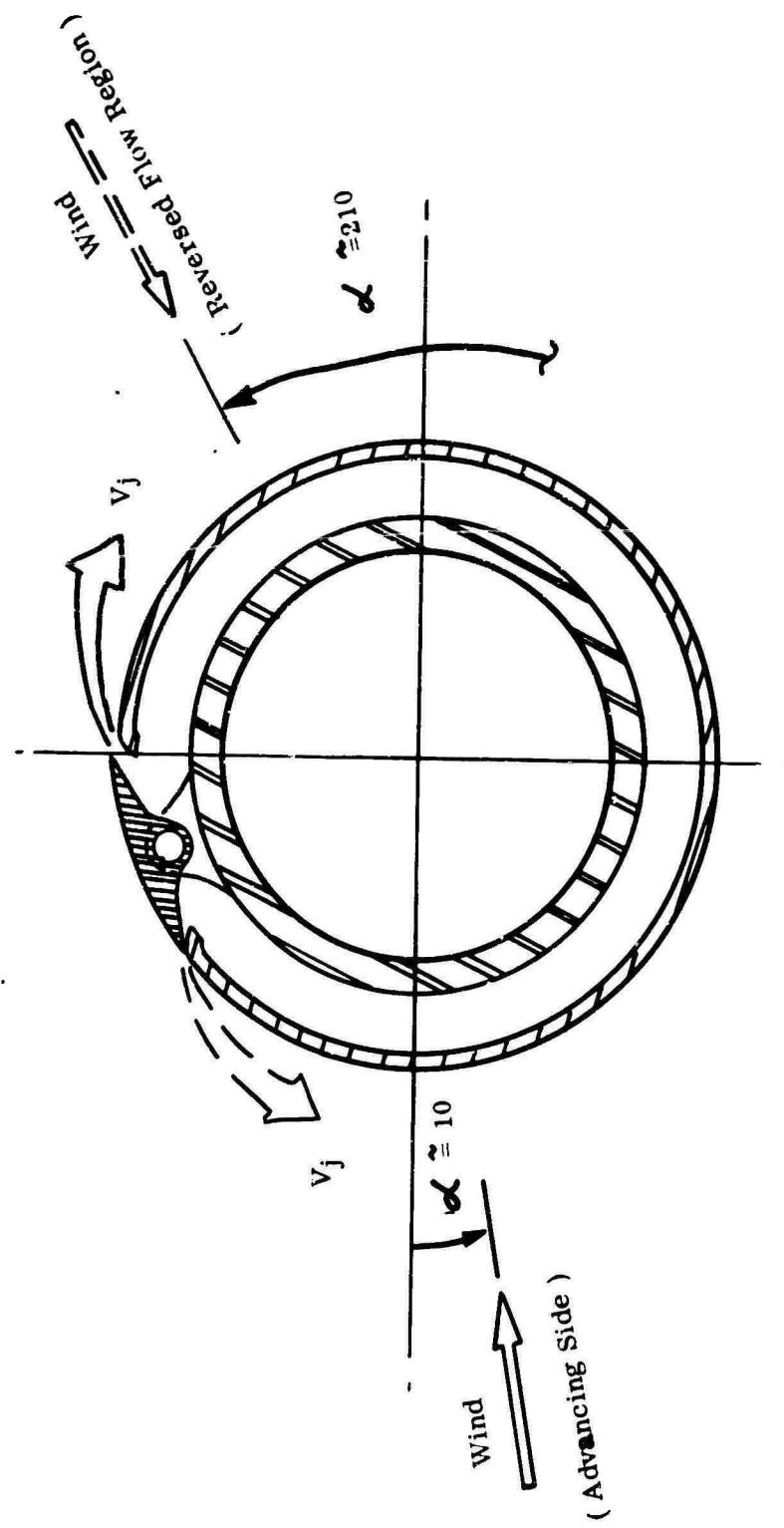
Figure 17. TYPICAL CONFIGURATION FOR CIRCULAR SHANK WITH TANGENTIAL BLOWING

21

Performance and propulsive force capability of the rotor blade with blowing shanks are compared with the segmented rotor in Figure 18 for constant lift. The total power required for the blowing shank rotor is greater than that for the segmented rotor, when the power required for blowing is accounted for. The propulsive force producing capability, however, is comparable to or better than that of the segmented rotor. The difference in power between the two systems can be reduced by optimizing the design of the blowing shank.
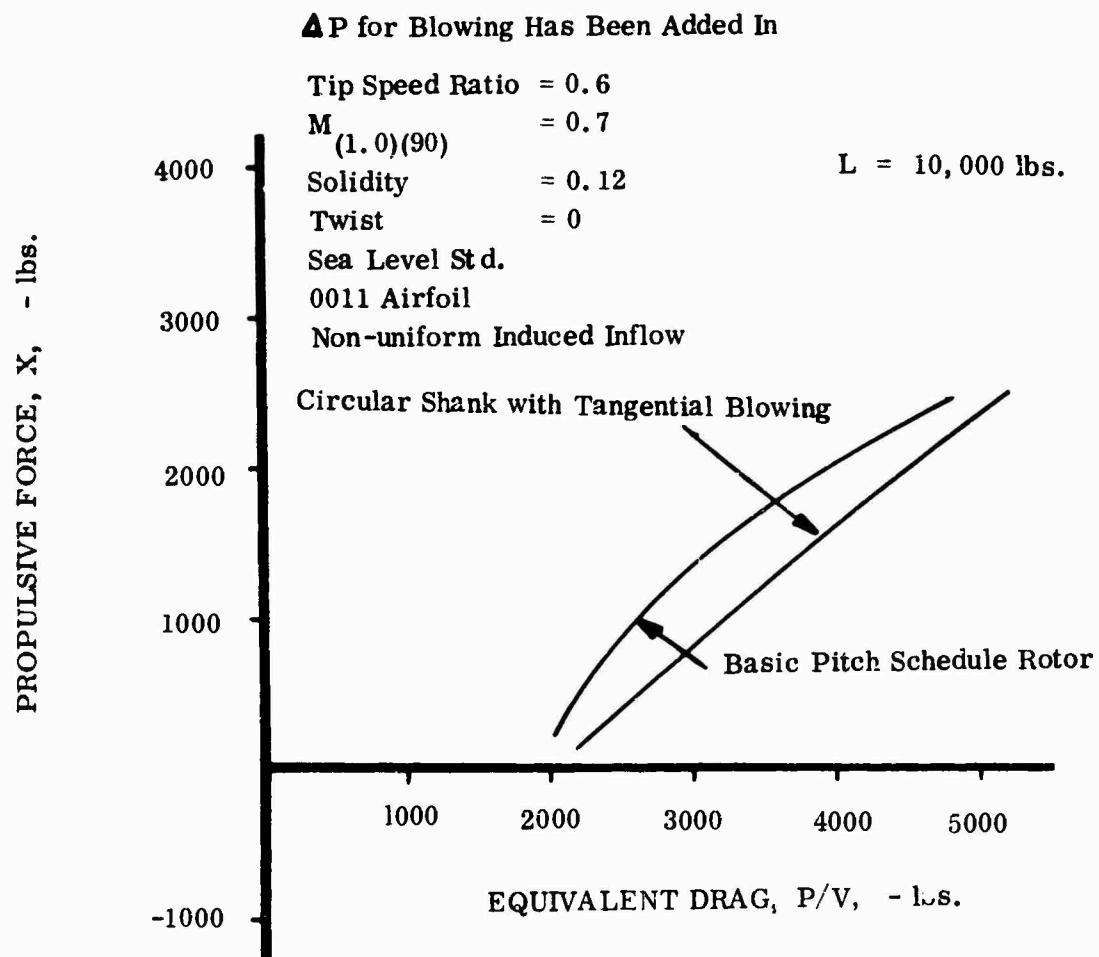

Figure 18. SEGMENTED ROTOR - CIRCULAR SHANK WITH TANGENTIAL BLOWING ROTOR COMPARISON OF PROPULSIVE EFFICIENCY

22
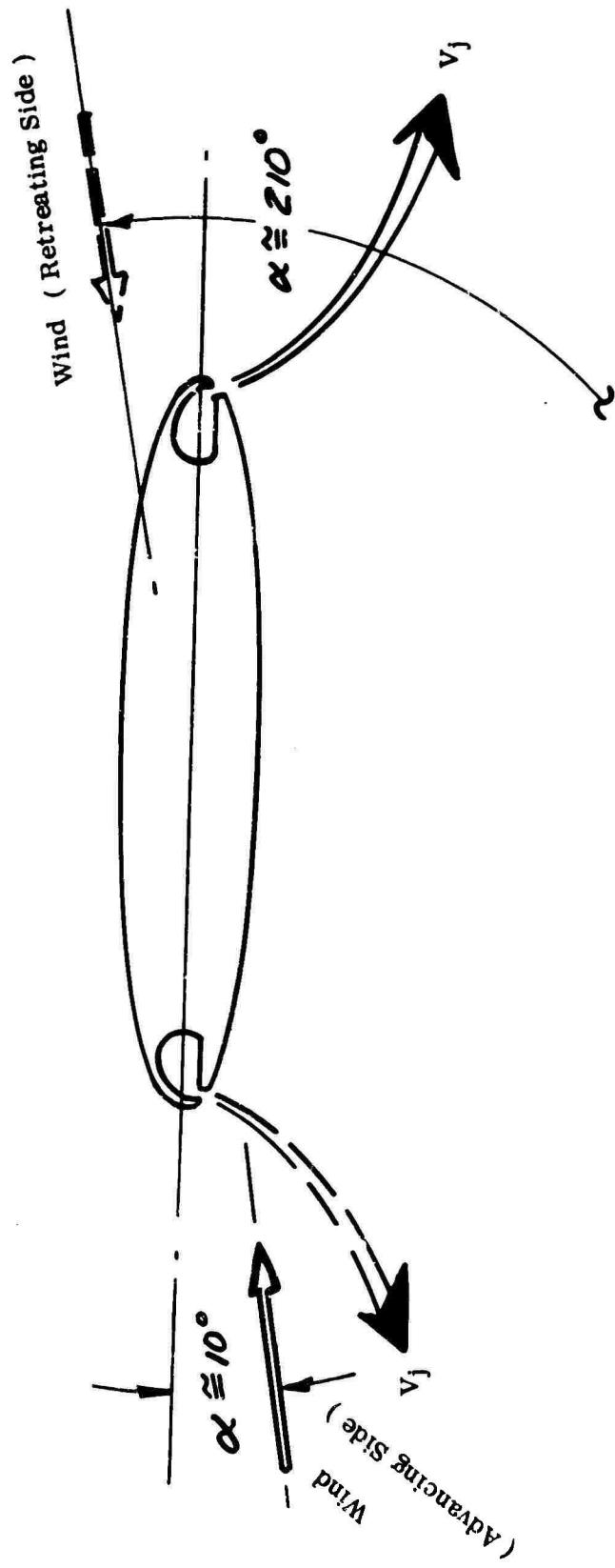
Figure 19. TYPICAL CONFIGURATION FOR ELLIPTIC
SHANK WITH JET FLAP

23

Elliptic Jet-Flap Shank

We can decrease the basic drag of the shank by a factor of four by using an elliptic section rather than a circular section. High lifts can be generated on the advancing side inboard region by applying a jet-flap to the elliptic shank's trailing edge (8, 9). The download normally encountered in the reversed flow region, where the angle of attack is approximately 210 degrees can be reduced or eliminated completely by blowing from the nose of the shank in that region.

A typical arrangement for an elliptic shank with a jet-flap at the leading and trailing edges is shown in Figure 19.

The data from Reference 10 have been used in the Rotor Airloads and Performance Analysis to compute propulsive capability and performance for a rotor with an elliptic shank. The segmented rotor is compared with the jet-flap elliptic shank rotor in Figure 20.
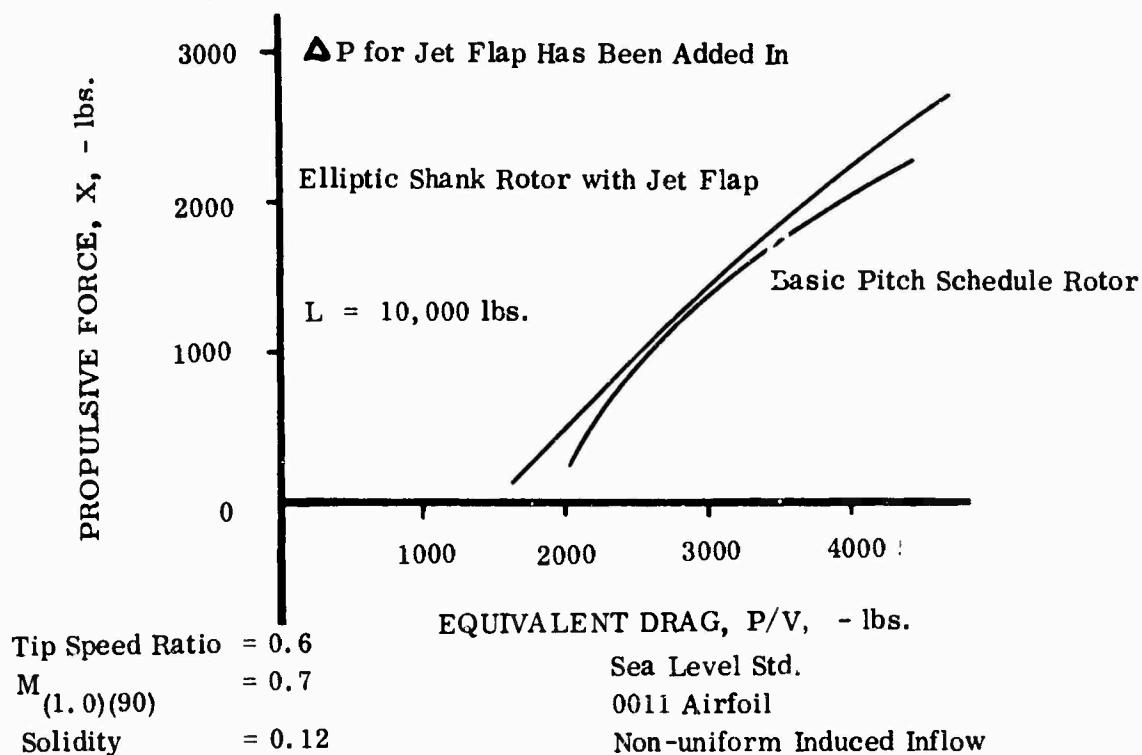

Figure 20. SEGMENTED ROTOR -- ELLIPTIC SHANK ROTOR WITH JET FLAP COMPARISON OF PROPULSIVE EFFICIENCY

24

The propulsive force producing capability and the performance of the rotor with the jet-flap elliptic shanks is comparable to that of the segm ited rotor. There is a marked improvement in power required for the elliptic shank rotor when compared with the circular shank with tangential blowing. The performance of the elliptic shank airfoil can be further improved by optimizing the design for a given flight condition.

CONCLUSIONS

1. A conventional helicopter rotor loses most of its propulsive capability at tip speeds ratios above five or six-tenths.

2. The loss in propulsive efficiency is due to the inefficient operating environment of the rotor blade inboard area at high tip speed ratios.

3. By controlling the angle of attack of the inboard area of the rotor blade independently from the outer, such as the segmented rotor scheme, the propulsive capability of a rotor can be increased for tip speed ratios above six-tenths.

4. The effect of inboard area aerodynamic devices, such as segmented blades, can be predicted analytically.

5. Cylindrical and elliptic rotor shanks with jet-flap type blowing can provide a rotor propulsive effectiveness comparable to that of the segmented rotor.

REFERENCES

1. Ekquist, D.G., Design and Wind Tunnel Test of a Model Helicopter Rotor having an Independently Movable Inboard Blade Panel USAAVLABS Technical Report 65-63. October 1965

2. Schairer, G.S., Looking Ahead in V/STOL, Joint Meeting IAS-RAES, London 1961

3. Gessow, A., and Gustafson, F.G., Effect of Blade Cutout on Power Required by Helicopters Operating at High Tip-Speed Ratios NASA TN D-382, September 1960

4. Harris, F.D., An Analytical Study of Rotor Performance at High Forward Speeds Paper presented before the American Helicopter Society Seventeenth Annual Forum, Washington, D.C., 1961

5. Sewell, R.I., Rotor Airloads and Performance Analysis with Wake-Induced Inflow Boeing Document D8-0312, March 1965

6. Davenport, F.J., A Method for Computation of the Induced Velocity Field of a Rotor in Forward Flight, Suitable for Application to Tandem Rotor Configurations Journal of the American Helicopter Society, Volume 9, No. 3, July 1964

7. Lockwood, J.E., Lift Generation on a Circular Cylinder by Tangential Blowing from Surface Slots NASA TND-244, May 1960

8. Davidson, I.M., The Jet Flap, Journal of the Royal Aeronautical Society, January 1956

9. Spence, D.A., The Lift Coefficient of a Thin, Jet-Flapped Wing. Proceedings of the Royal Society (A), Volume 238, Pages 46-68

10. Davenport, F.J., *Potential Flow Lift and Pitching Moment of Jet Flapped Airfoils for Large Jet Deflection Angles*, Unpublished Boeing Document D6-6409 TN

27

TABLE 1

PHYSICAL CHARACTERISTICS OF THE SEGMENTED ROTOR

RADIUS ---------------- 4 feet

CHORD -------------- 6 inche.

NUMBER OF BLADES ---------------- 3

ROOT CUTOUT ---------------- 18.9%

SOLIDITY ---------------- .119

TWIST ---------------- 0 degrees

THICKNESS DISTRIBUTION

RADIAL STATION	THICKNESS RATIO t/c
18.9%	21%
50 %	21%
From 50%	Linear Variation
to 100%	From 21% to 15%

APPENDIX 1

TYPICAL HELICOPTER PERFORMANCE CALCULATION

The propulsive force requirements and performance are computed for a typical helicopter with the following characteristics:

fe	18 ft^2
Lift per rotor	18,000 pounds
Rotor Diameter	60 ft.
Altitude	5000 ft.
Tip Speed Ratio	0.60
Advancing Tip Mach No.	0.94

Using the above characteristics the propulsion and lift requirements are:

$X/qd^2\sigma$	.0420
C_T'/σ	.0620

Figure 11 indicates that this flight condition is well within the measured capabilities of the segmented rotor.

NOTES

AERODYNAMIC LOADING OF HIGH SPEED ROTORS

by

JOHN P. RABBOTT, JR.
Assistant Supervisor, Aircraft Advanced Research Section

VINCENT M. PAGLINO
Research Engineer

ABSTRACT

A test of a set of Sikorsky CH-34 rotor blades was conducted in the NASA/Ames Full Scale Wind Tunnel at speeds of 110 to 175 knots. One blade of the set was instrumented to measure differential chordwise pressures at 9 stations from 25 to 99 percent radius. Some test results are presented, two and three dimensional pressure distributions are compared, and a correlation of airload time histories is made, for both uniform and nonuniform inflow assumptions.

INTRODUCTION

The ability to predict the chordwise and spanwise aerodynamic loading on the blades of rotary wing aircraft is essential to achieve a reliable structure and an efficient rotor system. In order to provide full scale experimental data for correlation purposes at speeds in excess of currently available data, tests were conducted on a full scale pressure instrumented Sikorsky CH-34 rotor system at the NASA/Ames full scale wind tunnel, at speeds from 110 to 175 knots. This blade set is the same as that used in the study reported in Reference 1. Analysis of these data, including correlation with theory of both aerodynamic and structural loads, is presented in Reference 2. The purpose of this paper is to present the highlights of those test results which pertain to the aerodynamics of the rotor system, including some brief correlation with theory and with flight test results.

The study reported in Reference 2, upon which this paper is based, was jointly sponsored by the U.S. Army Aviation Materiel Laboratories and Sikorsky Aircraft.

SYMBOLS

c	Blade Chord	Feet
C_n	Section normal force coefficient	——
C_p	Differential pressure coefficient	——
D	Rotor Drag	Pounds
L	Rotor Lift	Pounds
M	Mach Number	——
r	Distance from center of rotation to blade radial station	Feet
R	Blade Radius	Feet
V	Forward Speed	Feet per second or knots
x	Distance from leading edge to blade chordwise station	Feet
α_r	Local blade section angle of attack	Degrees
α_s	Rotor shaft angle of attack	Degrees
μ	Advance Ratio, $V / \Omega R$	——
ψ	Azimuth Angle	Degrees
Ω	Rotor Angular Velocity	Radians per second

2

DESCRIPTION OF TEST FACILITIES AND INSTRUMENTATION

The H-34 rotor system is shown installed in the wind tunnel in Figure 1. This wind tunnel, located at the NASA/Ames Research Center, is of the closed throat, close return type, with a test section 40 feet high and 80 feet wide and a nominal maximum speed capability of 200 knots. Model forces and moments are measured by a six-component mechanical balance located below the tunnel floor. The four-bladed rotor system had a radius of 28 feet, and the blades were of -8 degrees aerodynamic twist with a blade chord of 16.4 inches. Airfoil contour was that of an NACA 0012, except for the tip cap region which was more nearly elliptical. One rotor blade of the set was instrumented with fifty-six electrical pressure gages whose output was recorded simultaneously on magnetic tape. The rotor was controlled from outside the tunnel by means of electrically driven actuator motors which operated the primary hydraulic servos. All data were taken at a rotor tip speed of 650 feet per second.

Figure 2 shows the location of the 56 pressure transducers on the blade. Also shown are the strain gage locations for recording structural loads. The results from this and other instrumentation used during the tests will not be presented here, but are discussed in detail in Reference 2, along with complete data acquisition and reduction techniques. The pressure transducers were located at nine radial stations, with a varying number of pressure taps at each station. The locations were chosen so as to allow for computer integration (Gaussian Method where possible) of the chordwise pressures to obtain the instantaneous blade loading at each span station.

Frequency Response And Measurement Accuracy Of Data System

Analysis of the possible errors in each individual component of the data acquisition and reduction system resulted in an estimated static system amplitude accuracy of 4.1 percent of full scale for all blade pressure measurements. The dynamic response characteristics of the system were such that there was no measurable amplitude distortion up to the tenth harmonic of rotor speed and a maximum of only two percent at the twentieth harmonic. The phase lag of the system versus frequency is shown in Figure 3. Any departure from linearity would indicate a phase distortion of the final waveform, but the nonlinearity of the curve is so small that no correction was applied to the data.

3

DESCRIPTION OF COMPUTATIONAL METHOD

The computational technique used to obtain theoretical results for comparison with these test results is illustrated schematically in Figure 4. The method is based on the aerodynamic approach of Reference 3 but extended to include blade flexibility through the summation of normal modes of vibration and the incorporation of an option for including the influence of the trailing and shed wakes on the rotor loads, using the method of Reference 4 developed by Cornell Aeronautical Laboratory, Inc. The calculations are performed on an IBM 7094 and are initiated by inserting the blade's physical properties and rotor speed into a deck for computing the rotor blade's natural frequencies and mode shapes based on an extension of the Myklestad method for rotating beams (Reference 5). In this investigation, 4 flapwise, 3 chordwise, and 1 torsional mode shapes were used. These results, along with the required flight parameters (forward speed, tip speed, lift, and propulsive force), blade section aerodynamic data, and rotor inflow, are then inserted into the Normal Mode Transient Analysis Program to calculate the blade response. Determination of blade response by the normal mode method is described in References 6 and 7. Briefly, using arbitrary starting values, the transient response of the blade is calculated at finite azimuthal increments until the steady state is reached to within a specified tolerance. If the desired lift and propulsive force and/or blade flapping motions are not achieved an automatic iteration is performed by adjusting rotor inflow and control positions, as indicated in Figure 4. Once convergence is achieved, the rotor blade aerodynamic and structural loads, blade motions, and control positions are printed out.

If the variable inflow option is exercised, the above results are used as input to the Cornell Aeronautical Laboratory variable inflow calculation method of Reference 4. This method represents the rotor wake as a series of discrete shed and trailing vortices. For the present calculations, ten radial segments were used and calculations of inflow were made at 15 degree increments in azimuth, the minimum spacing provided in the method. The wake transport velocity is assumed equal to the vector sum of the mean rotor inflow velocity and the forward speed of the rotor. The variable induced velocity output is then introduced into the Transient Analysis Program and a new blade response determined. This procedure can be repeated but experience has shown that one iteration is adequate. For the correlation conditions of this paper both uniform and nonuniform (variable) inflow were used in the calculations.

After the publication of Reference 2 it was discovered that the variable inflow program of Reference 4 contained two minor computational

4

errors. The effect of correcting these errors will be pointed out in a later section of this paper.

PRESENTATION OF RESULTS

Chordwise Loading

Figure 5 presents typical comparison of measured chordwise load distribution with two-dimensional data for three combinations of spanwise location, Mach number and normal force coefficient, at a forward speed of 175 knots (advance ratio of 0.45). The radial stations and azimuth positions selected coincided closely with data points in Reference 8 at the same Mach number and normal force coefficient, so interpolation would not be necessary. (It was found that care must be exercised when interpolating between data points, since blade surface pressure coefficients are not strictly linear functions of free stream Mach number or angle of attack). It can be observed in this figure and was also observed in other samplings of these data that the full scale rotor pressure distributions are, for the most part, substantially identical to those obtained in the two-dimensional tests of Reference 8.

Figure 6 presents typical examples (complete pressure data are available in Reference 9) of differential blade pressures measured at 175 knots in the full scale tunnel plotted versus chordwise position for 90 degree azimuth increments. Data are shown for 55, 75, 95, 97 and 99 percent radius. (Note that the measurements at 99 percent radius are on the tip cap and therefore not for an NACA 0012 airfoil section.) The load distributions are generally as expected, with the primary exception of the unusual pressure distribution at 95 percent radius and 90 degrees azimuth. (The presence of a similar loading at 97 percent radius can not be determined due to the limited number of pressure gages) These data were particularly carefully checked for validity and no definite explanation for this apparently peculiar behavior is available at this time, but two possibilities are present. First, this distribution may be partly a two-dimensional characteristic. The two-dimensional wind tunnel tests of Reference 8 on a production CH-34 rotor section indicate that at the Mach numbers under consideration (approximately 0.8) similar chordwise loadings may be encountered, but normally at a higher angle of attack. Secondly, the distribution may be influenced by a three-dimensional effect. Examination of the wake trajectory, computed by the method of Reference 4, shows that the tip vortex from the preceding blade is at about 88 percent radius and within one foot of the instrumented blade. If this representation is reasonably accurate there could be a large chordwise variation in inflow

5

due to the returning wake under the rotor. Harmonic analysis of the individual pressure gage output at this station showed a large variation in harmonic content with chordwise location, which would lend support to the latter hypothesis. An excellent discussion of this point is given in Reference 10.

It was found in this investigation that the principle area of two-dimensional and three-dimensional chordwise loading disagreement (if any) is at high Mach numbers (above 0.6). However, there is a good deal of difficulty involved in making valid quantitative comparisons at high Mach number for several reasons. First of all, the high Mach number regions of a rotor are generally regions of very small angle of attack and lift coefficient, so there is the danger of working close to the system accuracy of pressure measurement. Secondly, the pressure distributions, both two- and three-dimensionally, become extremely sensitive to small Mach number and angle of attack changes, so that the requirements on accuracy of Mach number and normal force determination become quite stringent for making valid comparisons of pressure distributions. Another problem is the number and placement of pressure taps required to give an accurate determination of the pressure distribution at high Mach numbers. Examination of the two-dimensional data of Reference 8 has shown that there can be considerable chordwise fluctuation in pressure, also seen in Figure 6 at 0.95 radius, which means that accurate determination of three-dimensional distributions, and therefore particularly center of pressure, may well require considerably more pressure taps than were present during the tests. Investigation of the data of References 8 and 9 is continuing in order to better define these requirements.

Airload Time Histories

Figures 7 and 8 present typical inboard (25 percent radius) and outboard (85 percent radius) time histories of aerodynamic loading for forward speeds of 110, 150, and 175 knots. The rotor in all cases is operating at a tip speed of 650 feet per second, a forward shaft tilt of 5 degrees, a lift of about 8000 pounds, and a propulsive force of about 500 pounds. Complete test conditions are given in Reference 2. Compared are the measured airloads based on the integrated chordwise pressures, and computed airloads based on both uniform and variable inflow assumptions.

At the inboard radial station (Figure 7), the correlation of measured and calculated airloads is seen to be generally good at all speeds. During the advancing part of the cycle, the variable inflow calculation provides an improvement over the uniform inflow by predicting the measured sharp rise in loading at about 20 degrees azimuth. However, as speed increases the variable inflow tends to predict high frequency loading

6

fluctuations on the advancing blade which were not present in the experimental data. It is felt that a more accurate determination of the wake geometry would help to alleviate this discrepancy, as an analysis of the sensitivity of wake location with respect to the rotor blade has shown that small variations in the vertical wake displacement can cause substantial changes in the computed airload's harmonic content. On the retreating portion of the cycle, this blade segment at 25 percent radius passes through the reverse velocity region. At 150 knots the basic variable inflow calculation caused an upflow through the rotor and thus a positive loading in this area as opposed to the negative loading which was measured and also calculated based on uniform inflow. This discrepancy has been found to be caused by two minor errors in the calculation procedure of Reference 4, one involving the sign of the vorticity in reverse flow, and the other involving the use of stall-limited vorticity in the calculation of induced velocity. It was found that correcting these errors affected the calculated airload results only in the reverse flow region. This fact is demonstrated in the airload time history at 175 knots (Figure 7). There was no effect whatever on the calculated structural loads (stresses) as presented in Reference 2. It should be kept in mind of course that the variable inflow theory was originally developed for application at low advance ratio conditions where the reversed flow region is small, and the effects shown here would therefore be small.

Figure 8 shows the airload time histories at the 85 percent radial station for the same three forward speeds. The loading signature is typical of outboard radial stations. Once again the correlation of experiment with both theories is seen to be generally good, with the variable inflow demonstrating a definite improvement over the uniform inflow on the retreating side of the rotor. An interesting phenomenon is the appearance of a sharp loading peak in the experimental data at about 90 degrees azimuth which diminishes in intensity as forward speed is increased. The uniform inflow theory does not indicate this disturbance while the variable inflow theory predicts the disturbance to increase with forward speed. This again suggests a need for more precise determination of the wake geometry.

A trend may be noted on the advancing side in that the degree of measured negative loading is increasing with speed more rapidly than either theory predicts, although variable inflow does tend to improve correlation. This discrepancy at 175 knots becomes more pronounced further outboard, with the measured values approaching an impulsive type loading at 90 and 95 percent radius. The lack of agreement between theory and experiment for this impulsive type loading on the advancing blade at high speed is disturbing to the aerodynamicist, and indicates that substantial additional research is needed to properly understand rotor dynamic airloads.

7

However it should be remembered that the final result of importance to the designer of a structurally reliable rotor system is the ability to predict vibratory blade stresses, and, as has been shown in Reference 2, the rotor blade does not respond substantially to this impulsive type aerodynamic loading as the time duration is short compared to the natural period of the blade lower order flapwise modes of vibration.

Theoretical Angle Of Attack Distribution

Because of the lack of a direct means of measuring blade section angle of attack, it was not possible to make a comparison of measured and computed angle of attack distributions. Therefore Figure 9 was prepared to present a comparison of the theoretical local angle of attack contours for both uniform and nonuniform inflow. The distribution shown corresponds to the 175 knot tunnel condition, but the differences between uniform and nonuniform inflow are typical of the lower speeds as well (depicted in Reference 2).

The primary influence of the inclusion of variable inflow, as calculated by the method of Reference 4, is the substantially greater non-uniformity in computed angles of attack particularly on the retreating side of the disk. Also the angle of attack at the retreating tip is reduced, in this case from 9 to 5 degrees, and the inclusion of variable inflow tends to shift the region of maximum positive angles of attack inboard, notably on the retreating side. There is also a tendency for the variable inflow to decrease the region of negative loading on the advancing side of the disk. Thus it is seen that variable inflow can significantly affect angle of attack, and thus aerodynamic loading, at speeds at least as high as 175 knots.

COMPARISON OF WIND TUNNEL AND FLIGHT TEST DATA

During the test, it was desired to duplicate in the wind tunnel a flight test condition (Flight No. 18 in Reference 1) conducted using this same rotor blade set. The forward speed of 110 knots corresponds to the maximum steady state flight speed of Reference 1. Inadvertently, a greater rotor propulsive force was produced in the tunnel; 2150 pounds versus an estimated flight test value of 1390 pounds. The increased propulsive force, and the -9 degree rather than -7.2 degree shaft angle reported in Reference 1, thus represent a different inflow and loading for the rotors, so these differences should be kept in mind in the following comparison of wind tunnel and flight test data.

Figure 10 presents the averaged aerodynamic loading versus spanwise station for the wind tunnel and flight test data, as well as theoretical

8

calculations based on both uniform and nonuniform inflow assumptions simulating the wind tunnel operating condition. The wind tunnel data appear to be smoother than the flight test data, perhaps reflecting the more easily controlled conditions in the wind tunnel. Both theoretical airload distributions follow the wind tunnel well. The only significant difference in the two calculations is that the variable inflow theory predicts the drop-off in lift towards the blade tip, which the constant inflow assumption precludes. Theoretical calculations based on flight test values of propulsive force have indicated that a higher propulsive force results in a lower average airload at the inboard stations and a higher average airload at the outboard stations. This is in agreement with the characteristics displayed by the wind tunnel and flight test data of Figure 10. The well defined and sharp drop-off in lift from 95 to 99 percent radius is an indication of a very strong tip vortex, which implies that simplifications in the theory may be possible by representing the trailing wake by a tip (and inboard) vortex rather than the ten segments used herein. This would be particularly helpful in reducing the complexity of the problem, and computing time, when considering vortex-vortex interaction in the theory. (See Reference 11 for a discussion of this problem.)

Figure 11 presents a sample comparison of time histories of flight and wind tunnel airloads at comparable radial stations. Discounting the differences in average loading (discussed in connection with Figure 10), the agreement between wind tunnel and flight test data is good. The principle difference in loading signature is noted at 90 percent radius in the region of 120 degrees azimuth, where the flight test data show a sharper drop in lift.

The principle harmonics of the free flight airloads are the first through the fourth. Measured and computed harmonics of the wind tunnel test condition show good agreement with these harmonics (see References 1 and 2). Therefore it appears that the major differences in loading shown in Figure 11 are probably attributable to the difference in operating condition, that is, rotor propulsive force and mean rotor inflow, rather than to differences between wind tunnel and flight testing.

CONCLUSIONS

Analysis of the results of full scale experimental and theoretical rotor airload correlations at speeds from 110 to 175 knots leads to the following principle conclusions:

1.   At several radial stations where direct comparisons could be made, good agreement was obtained between two-dimensional and

9

three-dimensional chordwise airload distributions. However, at the advancing blade tip, where high Mach numbers and rapid loading fluctuations are encountered, there is evidence that a more accurate determination of measured chordwise distribution may be required in order to pinpoint the differences between two- and three-dimensional loading.

2. Correlation of airload time histories with theory was reasonably good with the principle discrepancy occurring at high speed in the region of the advancing blade tip where a much sharper drop-off in lift was measured than predicted — an impulsive type loading. Inclusion of variable inflow in the theory improved airloads correlations on both advancing and retreating blades at speeds as high as 175 knots (advance ratio of 0.45) and evidence was shown that a more precise wake treatment can improve correlation still further.

3. Agreement between flight test and wind tunnel test data was reasonably good, and the major differences could logically be explained by the differences in rotor operating condition.

REFERENCES

1. Scheiman, J., A Tabulation of Helicopter Rotor-Blade Differential Pressures, Stresses, and Motions as Measured in Flight, NASA TMX-952, March 1964.

2. Rabbott, J. P., Jr., Lizak, A. A., Paglino, V. M., A Presentation of Measured and Calculated Full Scale Rotor Blade Aerodynamic and Structural Loads, USAAVLABS Technical Report 66-31, (Sikorsky Engineering Report 58398), In Preparation.

3. Tanner, W. H., Charts For Estimating Rotary Wing Performance In Hover and At High Forward Speeds, NASA CR-114, November 1964. (Sikorsky Engineering Report 50379).

4. Piziali, R. A., and DuWaldt, F. A., A Method For Computing Rotary Wing Airload Distributions In Forward Flight, TREC Technical Report 62-44, July 1962.

5. Myklestad, N. O., Fundamentals of Vibration Analysis, McGraw-Hill Book Company, Inc., New York, 1956.

6. Bisplinghoff, R. L., Ashley, H., and Halfman, R. L.,
    Aeroelasticity, Addison-Wesley Publishing Co., Inc.,
    Cambridge, Mass., 1955.

7. Miller, R. H., Aeroelastic Problems Of VTOL Aircraft,
    Notes for a Special Summer Program on Aeroelasticity,
    Vol. III, Massachusetts Institute of Technology, 1958.

8. Lizak, A. A., Two-Dimensional Wind Tunnel Tests Of An
    H-34 Main Rotor Airfoil Section, TREC Technical Report
    60-53, (Sikorsky Engineering Report 58304), September,
    1960.

9. Rabbott, J. P., Jr., Lizak, A. A., and Paglino, V. M.,
    Tabulated CH-34 Blade Surface Pressures Measured at
    NASA/Ames Full Scale Wind Tunnel, Sikorsky Engineering
    Report 58399, December 1965.

10. Miller, R. H., Unsteady Airloads On Helicopter Rotor
    Blades, Fourth Cierva Memorial Lecture, Presented to
    the Royal Aeronautical Society, London, England,
    October 25, 1963.

11. White, R. P., Jr., VTOL Periodic Aerodynamic Loadings,
    Paper Presented At The Symposium On The Noise and Load-
    ing Actions On Helicopters, V/STOL Aircraft, and Ground
    Effect Machines, August 30 — September 3, 1965.
    Institute of Sound and Vibration Research, University of
   Southampton, England.

11
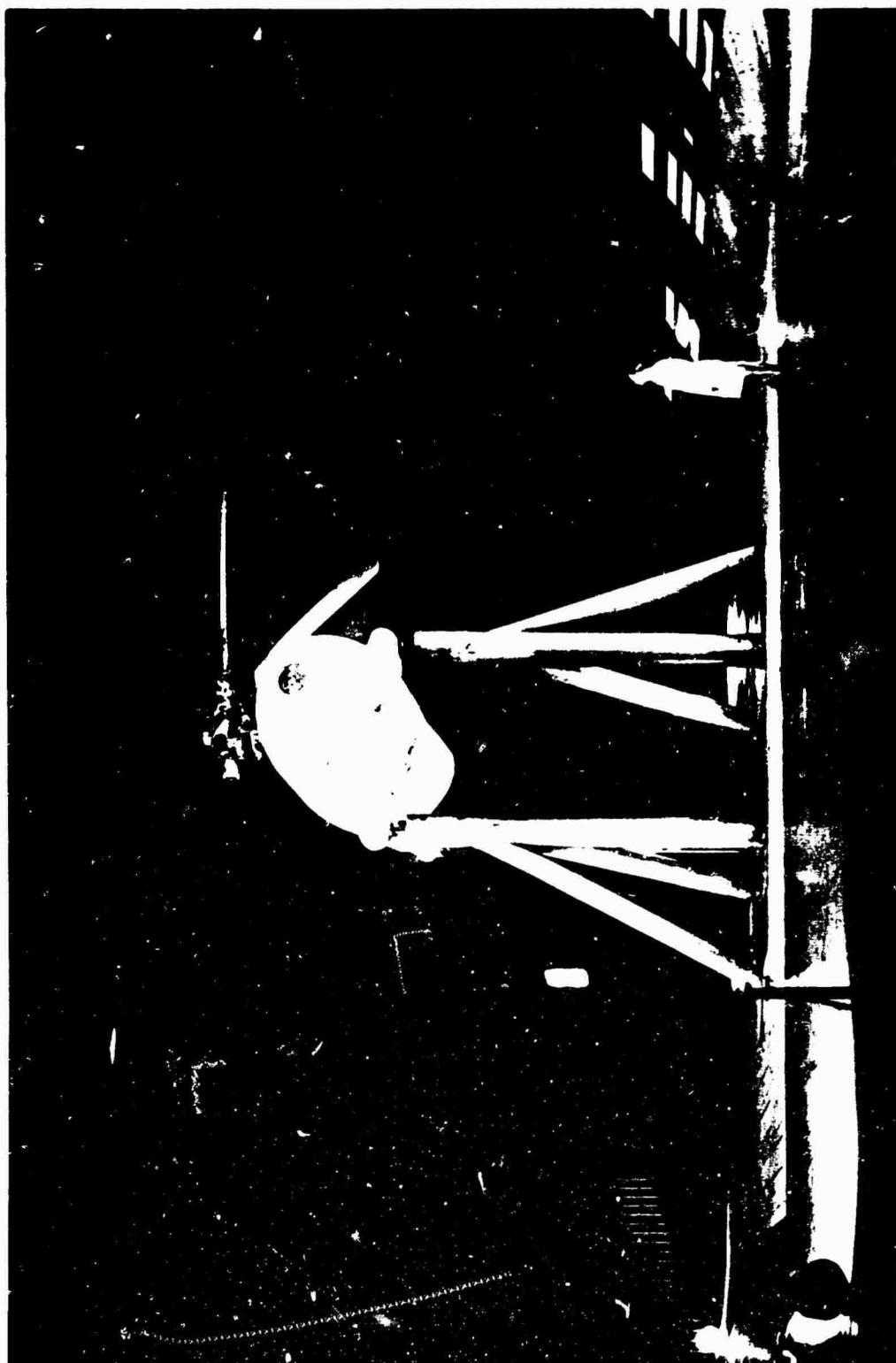
FIGURE 1 SIKORSKY CH-34 ROTOR INSTALLED IN NASA/AMES FULL SCALE WIND TUNNEL

12
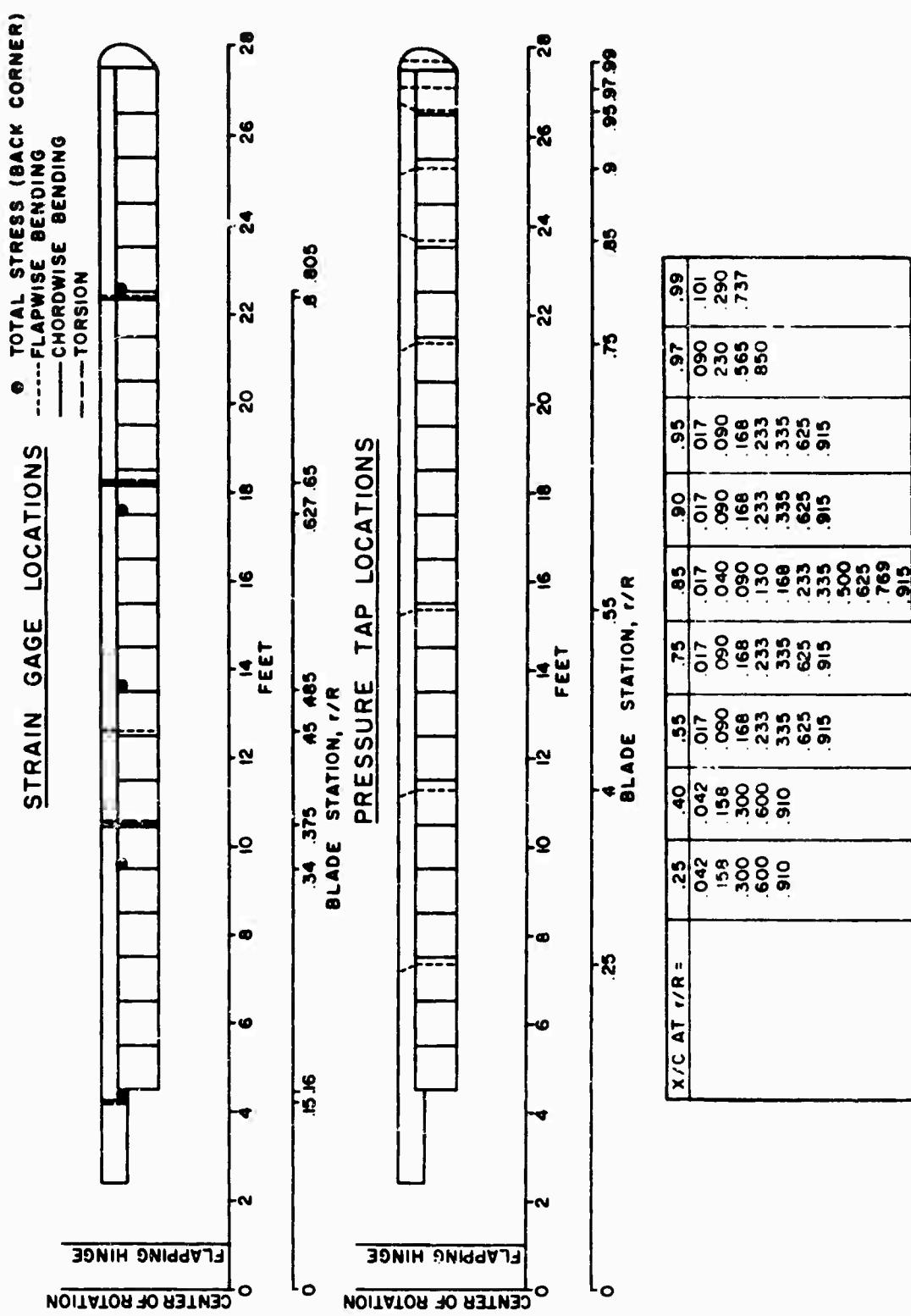
FIGURE 2. LOCATION OF BLADE INSTRUMENTATION

13
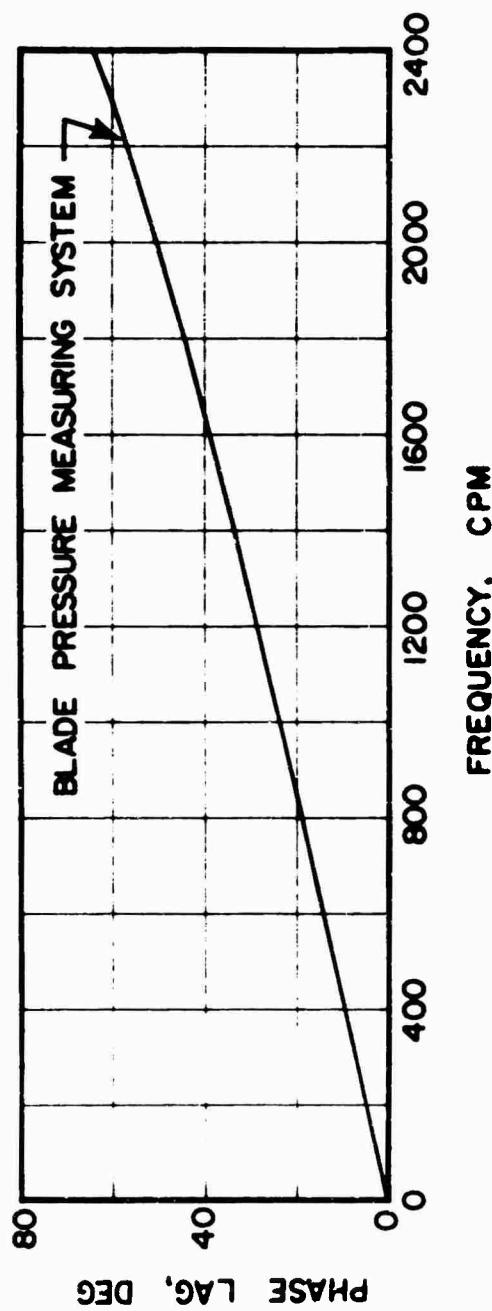
FIGURE 3. DATA SYSTEM PHASE LAG.

14
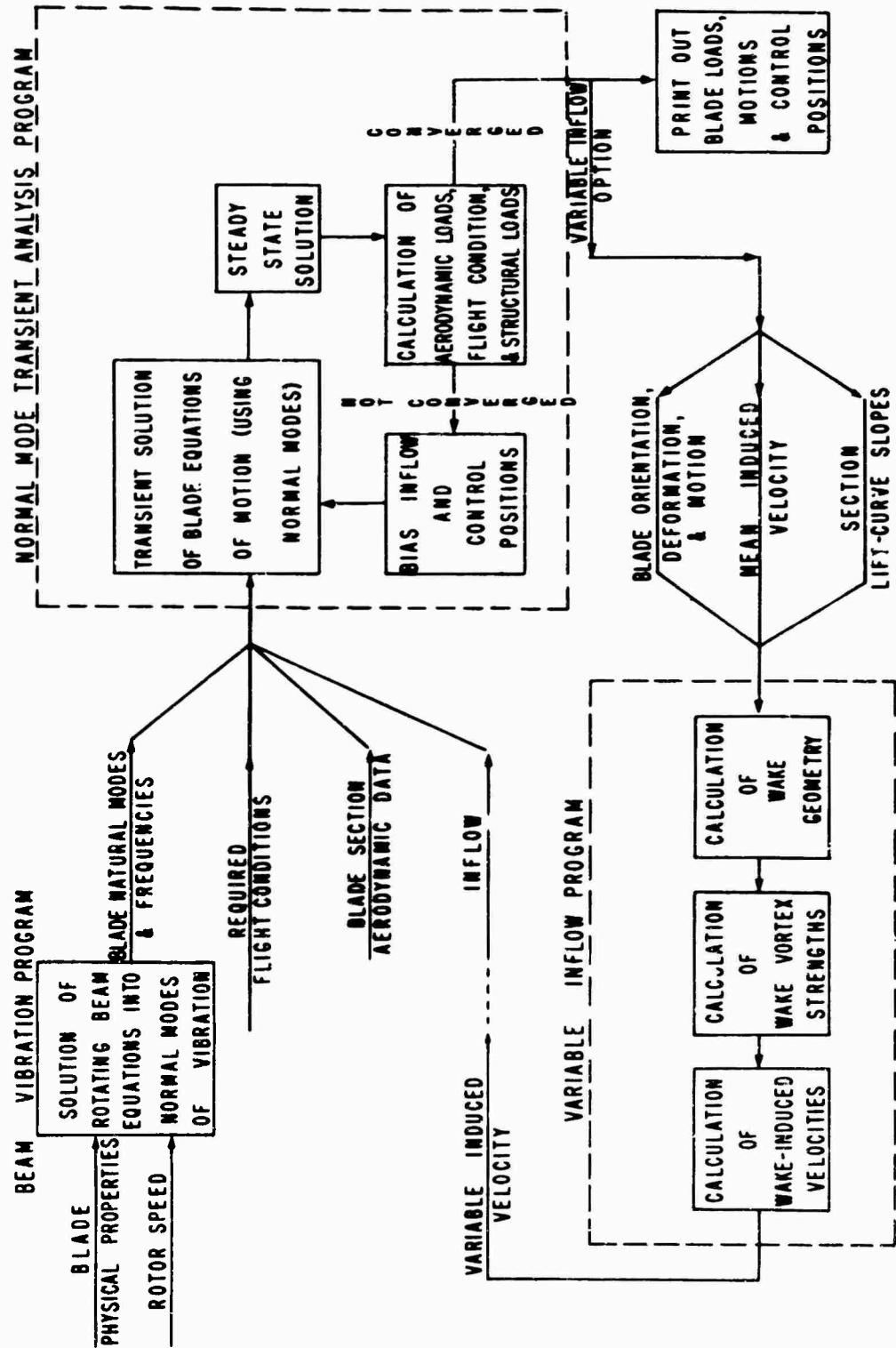
FIGURE 4. COMPUTATIONAL FLOW DIAGRAM.
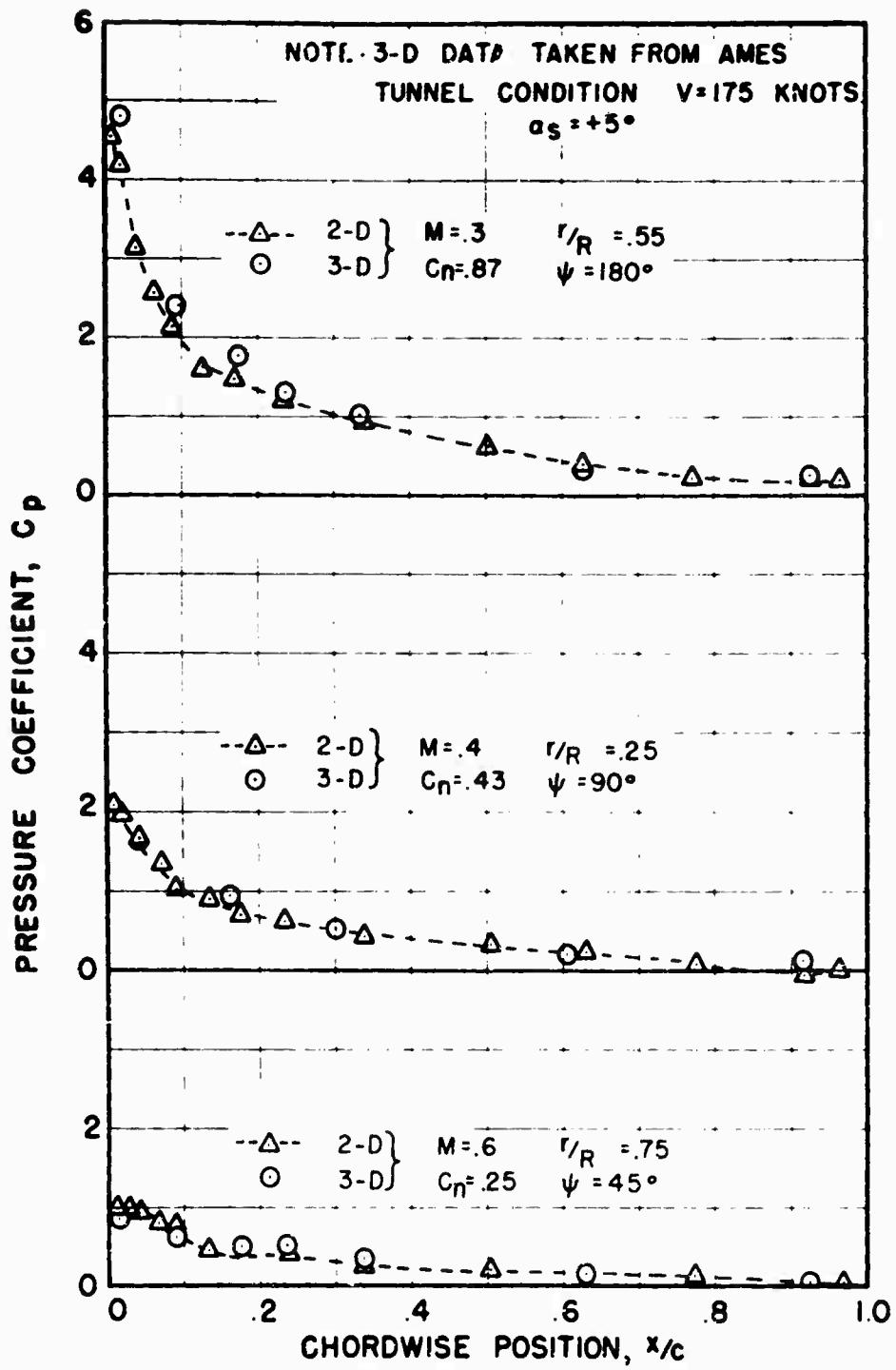
FIGURE 5. COMPARISON OF 2-D AND 3-D CHORDWISE LOADING.

16
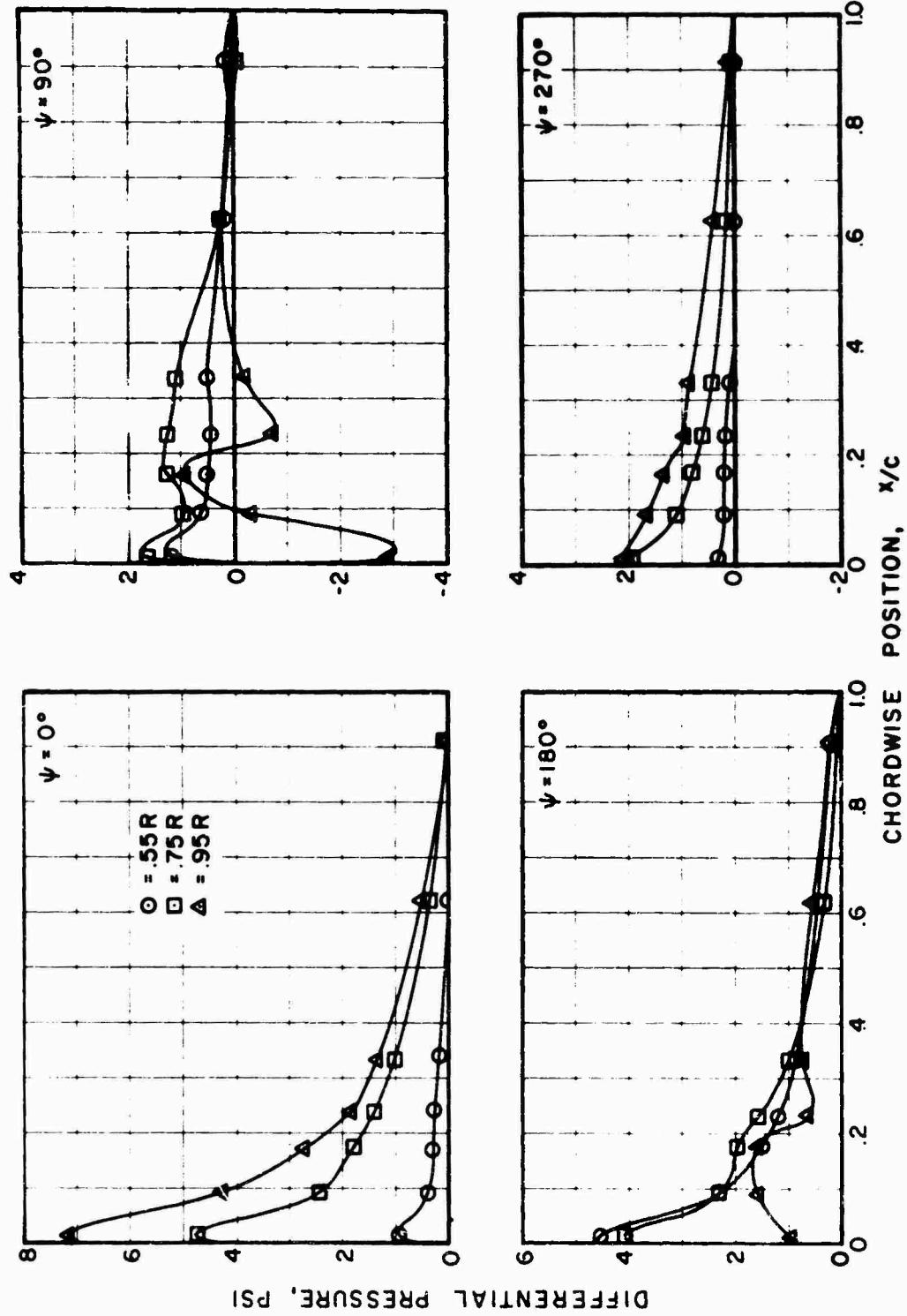
FIGURE 6. SAMPLE CHORDWISE PRESSURE DISTRIBUTIONS.
V=175 KT α_S=-5° L=7100LB D=-250LB $M_{\Omega R}$=0.58
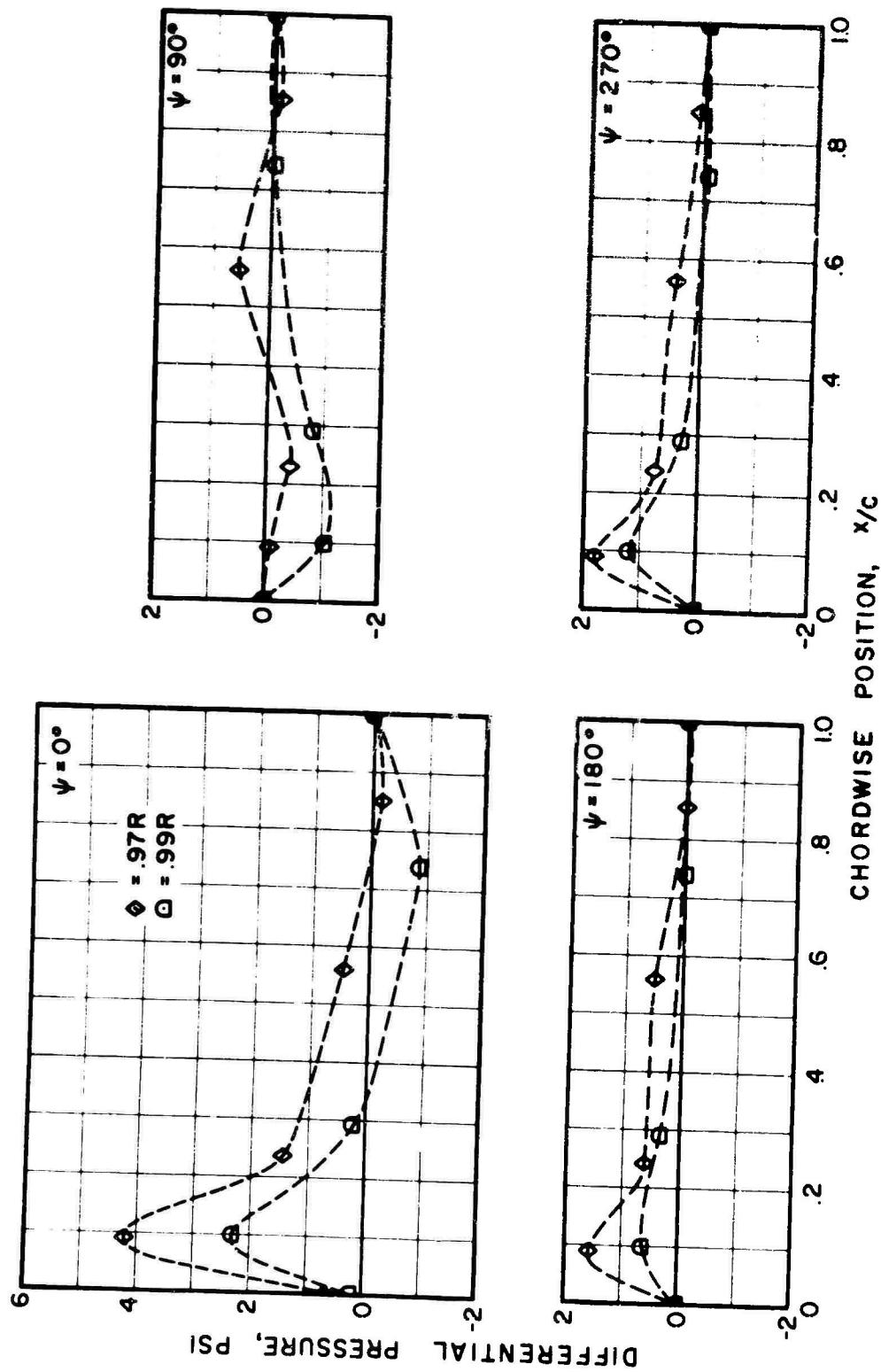
FIGURE 6. CONCLUDED.

18
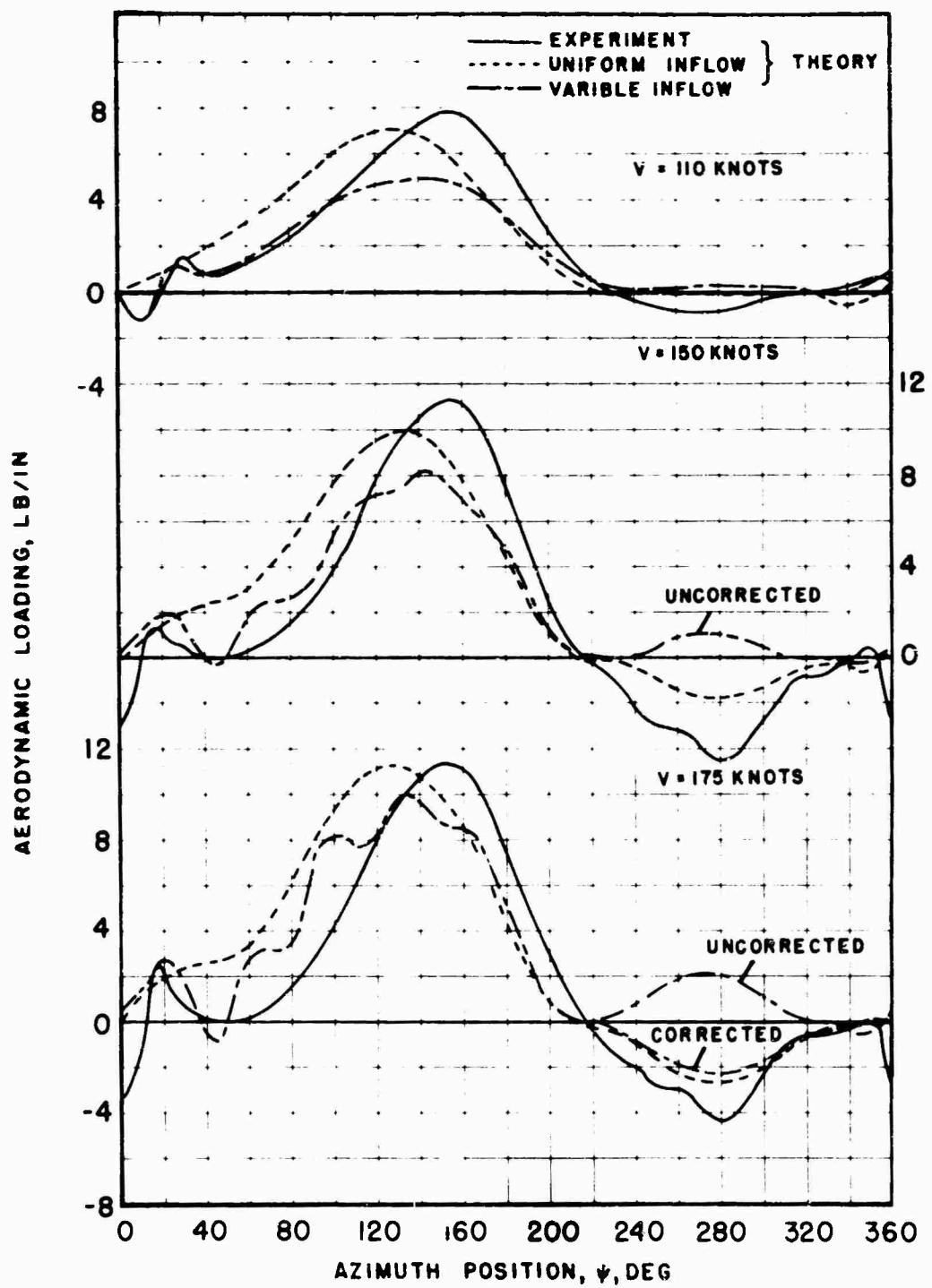
FIGURE 7. TYPICAL INBOARD (25% RADIUS) AIRLOAD TIME HISTORIES AT 3 FORWARD SPEEDS.
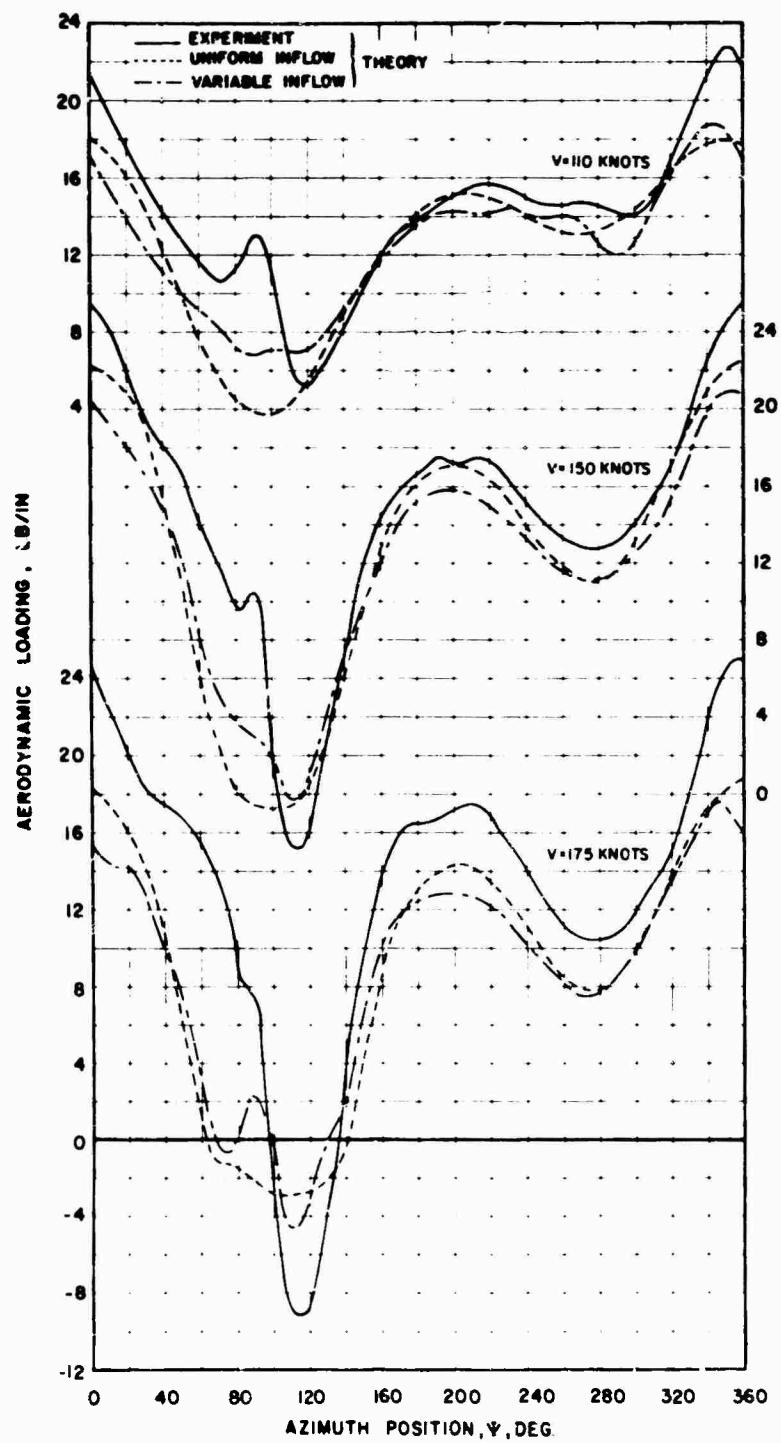
FIGURE 8. TYPICAL OUTBOARD (85% RADIUS) AIRLOAD TIME
HISTORIES AT 3 FORWARD SPEEDS

20

(a) UNIFORM INFLOW (TRIM FLIGHT)

(b) VARIABLE INFLOW (TRIM FLIGHT)
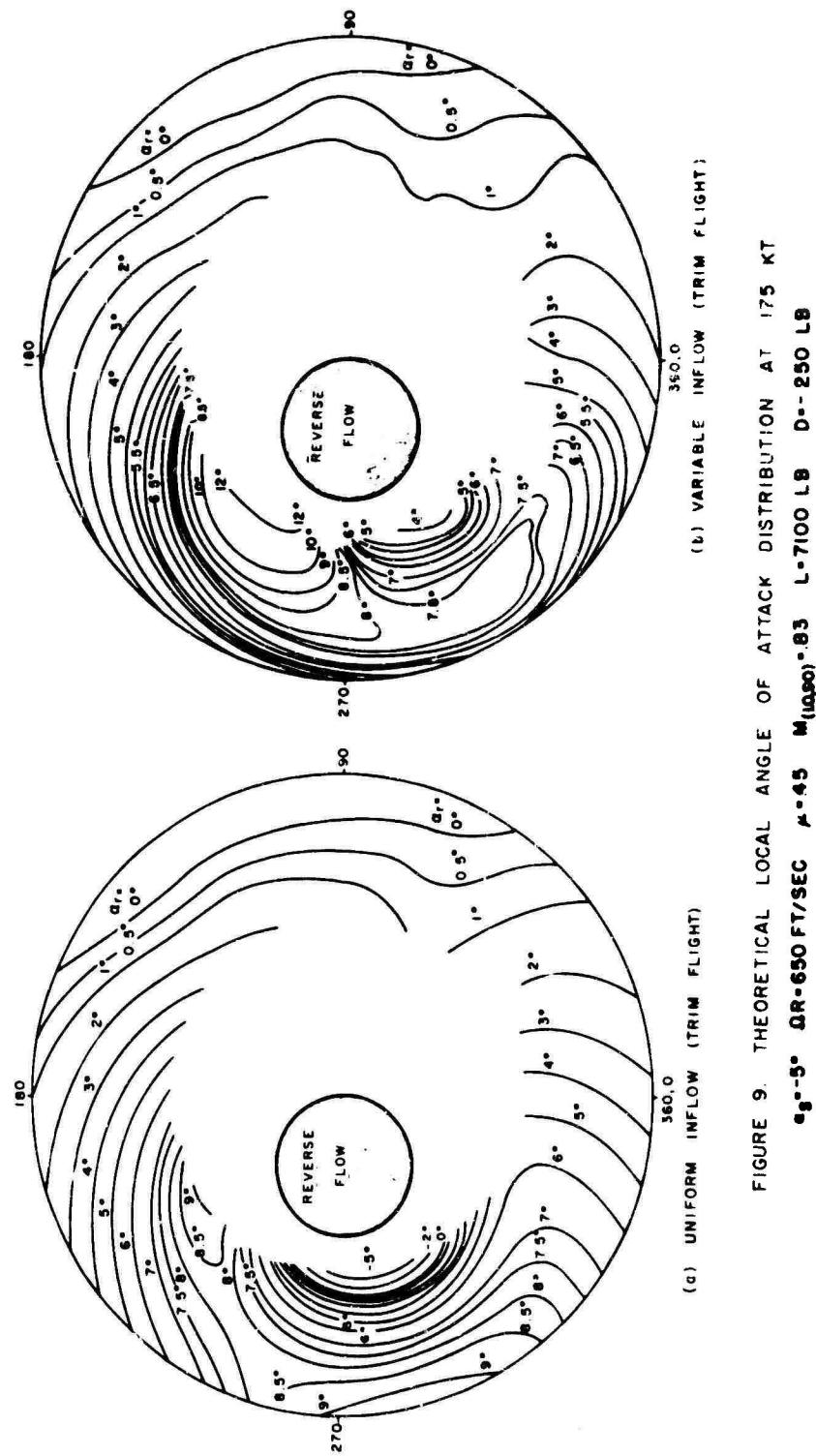
FIGURE 9. THEORETICAL LOCAL ANGLE OF ATTACK DISTRIBUTION AT 175 KT

$a_s = -5°$ $\Omega R = 650$ FT/SEC $\mu = .45$ $M_{(1050)} = .83$ $L = 7100$ LB $D = -250$ LB

21
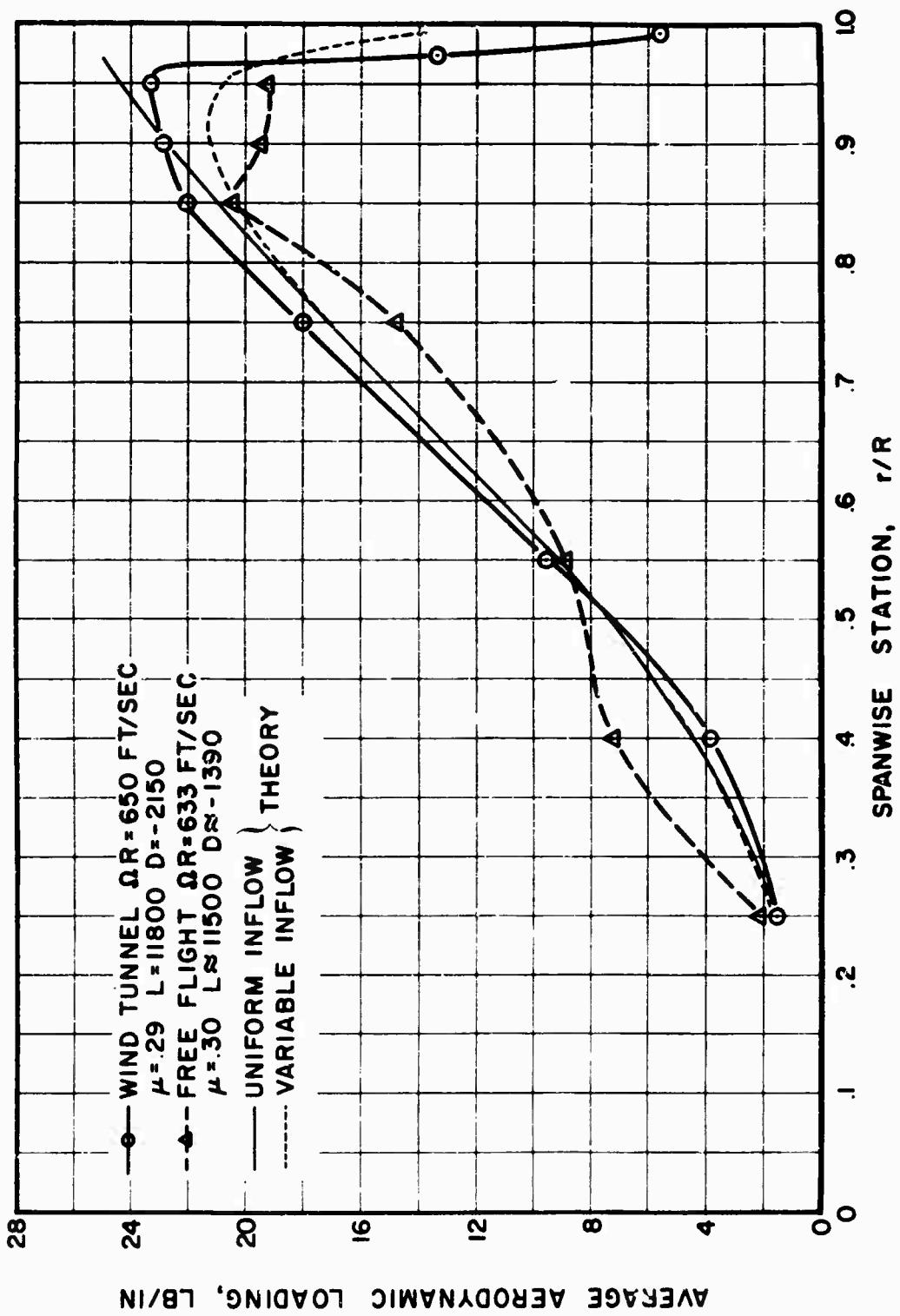
FIGURE 10. COMPARISON OF WIND TUNNEL AND FREE FLIGHT AVERAGE SPANWISE AERODYNAMIC LOADING.

22
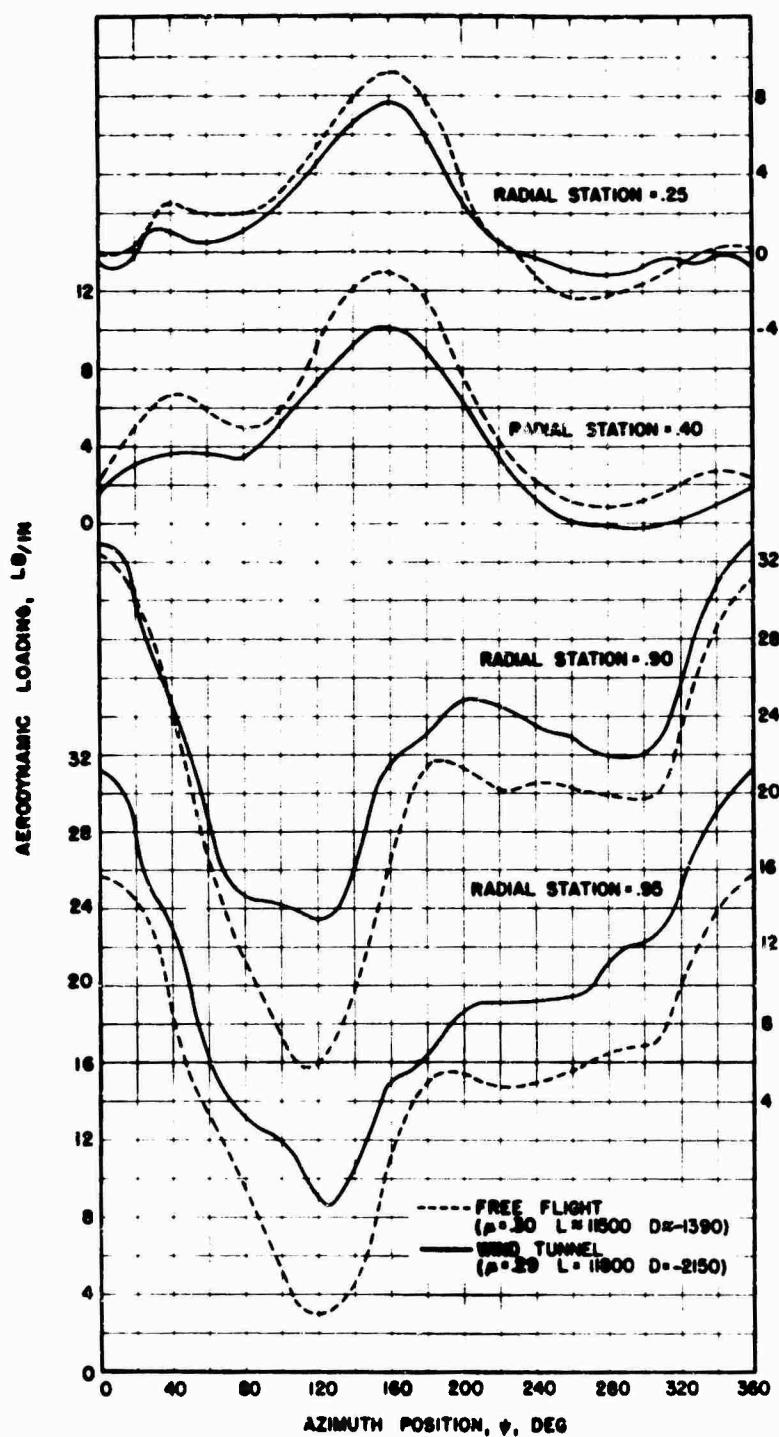
FIGURE II. SAMPLE FREE FLIGHT AND WIND
TUNNEL CORRELATION.

NOTES

PREDICTION OF ROTOR WAKE FLOWS*

by
Peter Crimi
Rochester Applied Science Associates, Inc.
Rochester, New York

SUMMARY

A study was performed with the objective of predicting
the time-varying flow in the vicinity of a helicopter in hovering
or forward flight. An analytical model was formulated which re-
presents the rotor, its wake and the fuselage of the aircraft.
The model for the wake is simplified in a manner consistent with
flow visualization studies by representing the wake as tip vor-
tices emanating from each blade. The wake vortices are assumed
to be free to convect under the influence of the blades, the
fuselage and the wake itself. The fuselage is replaced by a
surface distribution of sources, the strength per unit area
being determined by assuming that the fuselage is subjected to a
uniform steady free stream.

A digital computer program was written which implements
the model developed. Flow calculations were performed which are
found to agree well with measurements of the time average of the
flow in the wake of a two-bladed rotor.   Extensive calculations
were carried out which define the flow in the vicinity of a
UH-1B helicopter for a range of flight conditions from hover to
high-speed cruise. Selected results illustrate the relative im-
portance of various system parameters.

A number of applications of the model in addition to
flow calculations are discussed. For example, means for inves-
tigating the effects of wake distortion on blade loading and
procedures for calculating unsteady loads on the fuselage and/or
auxiliary lifting surfaces are outlined.

INTRODUCTION

A method for accurately predicting the time-varying
flow in the vicinity of a translating or hovering helicopter
would be of considerable value as both an engineering tool and
an aid to research and development. Possible areas of applica-
tion are the determination of harmonic airloads on the blades,
fuselage or auxiliary lifting surfaces, investigation of rotor
transient response and flutter, vibration and fatigue analyses,
and study of downwash impingement and debris entrainment in
ground effect. The method of flow prediction which is reported
here is presently limited to application in only certain of
these areas, but it appears that, with further development, the
scope of its applicability might be considerably broadened.

Direct analysis of the flow in the wake of a rotor for
arbitrary flight conditions is a formidable task, particularly
if fuselage effects are important in the region of interest. The
dependent variables are nonlinear functions of three space vari-
ables, time and each other, with no means available for lineari-
zation. Some results have been obtained previously by retaining
the complex structure of the flow but specifying the wake geome-
try. For example, good agreement with experimental measurements
of blade loading were obtained by calculating the flow at the
rotor plane in this way (Reference 1). The time average of the
induced downwash in certain limited regions was fairly well
approximated using a similar assumption as to wake geometry
(Reference 2).

The objective of this study was to predict the time-
varying flow at an arbitrary point in the wake of a helicopter
rotor. If the wake geometry were assumed known, unacceptably
large errors would result. Instead, the wake structure has been
simplified in a manner consistent with the findings of flow vis-
ualization studies, as will be discussed subsequently. The wake

2

can then be allowed to convect under the influence of the blades, the fuselage and self-induced effects by constructing a numerical analogue with the aid of a digital computer.

In developing the theory, consideration has been limited to aircraft having a single rotor. No restriction has been placed on the number of blades which the rotor may have, however. The aircraft has been assumed to be in steady level flight or hover, out of ground effect, and the forward speed, rotor rotational speed and loading have been assumed to be within the limits of presently operational single-rotor helicopters. Also, in representing the fuselage, the flow has been assumed to be attached and noncirculatory and the fuselage geometry has been somewhat idealized by omitting appendages such as landing skids.

FORMULATION OF THE ANALYTICAL MODEL

It is desired to analytically define the flow in the vicinity of a helicopter in translational or hovering flight out of ground effect. In order that a rational framework for the analytical model may be constructed the essential features of the physical flow should first be outlined.

Generally, there are three primary contributions to the flow at a given point relative to the aircraft. Specifically, the rotor blades, their wake and the fuselage all affect the fluid velocity. These three effects are, of course, interrelated in an extremely complicated and nonlinear manner, but for the purposes of this discussion they can be considered separately.

The rotor blades may be regarded as wings of very high aspect ratio in a harmonically varying stream. While the wake and fuselage do alter the loading on the blades, the total lift at a given azimuth position of the rotor must still be approximately equal to the weight of the aircraft. This implies that the circulation about a given blade must vary approximately sinusoidally with azimuth. The spanwise variation of circulation about a blade is also a function of wake and fuselage effects, and depends on blade twist and planform as well. Results of theoretical computations of harmonic airloads (Reference 1), which agree well with experimentally obtained data, indicate, though, that the spanwise variation of circulation generally does not differ a great deal from an elliptic distribution.

The wake of each blade is generated as a thin sheet of vortical fluid. The vorticity in this sheet has components in the spanwise direction (shed vortices) and in the chordwise direction (trailing vortices). It has been observed from flow visualization studies that this sheet rolls up within a few chord lengths to form a single concentrated vortex trailing from near the tip of the blade (see, for example, Reference 3).

4

While, at least in theory, a vortex should also trail from the vicinity of the root, it appears from the smoke pictures as well as from the results of an analytical treatment of the wake of a hovering rotor (Reference 4) that self-induced effects rapidly carry the root vortices up through the center of the rotor plane where they are dissipated. The tip vortices are quite stable, however, and experience little or no diffusion due to viscous effects for several rotor revolutions.

From the point of view of the fuselage, the flow appears as the superposition of a steady free stream caused by the translation of the aircraft and the periodic flow induced by the rotor and its wake. The contribution of the fuselage to the flow at any point, then, is essentially that due to a body of complicated geometry in unsteady potential flow.

If the fluid is assumed to be inviscid and incompressible, the flow described above has an exact analytical counterpart. The rotor blades could be replaced by doublet sheets, the wake by vortex sheets and the fuselage by a surface distribution of sources. The strengths of these potential singularities would be functions of time and spacial coordinates. The requirement of flow tangency at the blades and the fuselage would provide a pair of nonlinear integral equations for the determination of the strength distributions. The problems involved in the formulation and solution of these equations preclude such an approach. Therefore, three major simplifying assumptions have been utilized in the formulation of the model.

First, the rotor blades have been replaced by line vortices of constant strength spanwise and harmonically varying strength azimuthally. Except in the immediate vicinity of the blades, blade-induced effects should be reasonably well reproduced by such a model. That is, more than one or two chord lengths from a given blade, higher harmonic variations in cir-

5

culation cannot have an appreciable effect on the flow, at least in comparison with fuselage or wake effects. For present purposes, then, blade loading can be regarded as a known quantity.

Second, the wake is represented by individual free vortices, one trailing from the tip of each blade vortex; the strength of each tip vortex varies along its length in accordance with the (known) azimuthal variation of the blade vortex from which it trails. The wake vortices are assigned finite circular cores of rotational fluid (as physical vortices must have), so that the velocity which a vortex induces on itself may be correctly computed. The requirement of constancy of circulation as specified by Kelvin's theorem has not been met. However, as noted previously, the vortex elements needed to fulfill that requirement - shed vortices and trailing root vortices - apparently do not contribute significantly to the flow. For the same reason, the detailed structure of the wake near the blades, where roll-up occurs, and the vortices in the far wake (more than two or three rotor radii downstream of the rotor) have also been omitted.

Lastly, the fuselage is assumed to experience a uniform free stream of constant magnitude and direction. This stream is made up of two components, one being the negative of the velocity of translation of the aircraft, and the other consisting of a time and spacial average of the downwash which would be induced by the rotor and its wake in the absence of the fuselage. At high forward speed, the time and spacial variations of the stream in which the fuselage is immersed are comparatively small and so may be neglected without causing large errors. At low forward speed, the downwash may vary substantially over the fuselage, but the total effect of the fuselage on the flow is generally small compared to rotor and wake effects, so that the error is, presumably, again not appreciable. It is also assumed that the flow about the fuselage is not separated, so consideration must be

6

limited to regions where separation effects are unimportant.

The model for the flow as so simplified can be formulated in a straightforward manner. A coordinate system fixed in the tip-path plane, as shown in Figure 1 for a two-bladed rotor, is utilized. The vector $\underline{V}_f$ in the figure is the free-stream velocity (the negative of the translational velocity of the aircraft), inclined at an angle α_{τ} to the x-axis and parallel to the x-y plane. The angle ψ denotes the aximuth position of the rotor, and $\underline{r}$ is the vector positioning a given point with respect to the origin.

The fluid velocity $\underline{V}$ at a given point located by the vector $\underline{r}_p$ may be expressed in the form

$$\underline{V}(\underline{r}_p) = \frac{-1}{4\pi} \int_{C_V} \frac{\Gamma(t)\,\underline{r}_i \times d\underline{r}}{r_i^3} \quad + \quad \frac{1}{4\pi} \int_{A_f} \frac{\sigma(r)\,\underline{r}_i\,dA_f}{r_i^3} + \underline{V}_f \tag{1}$$

where $\underline{r}_i = \underline{r}_p - \underline{r}$, Γ is the local circulation about a vortex, and σ is the source strength per unit area on the surface replacing the fuselage. The first integral is a line integral taken over all vortices in the flow, which curves are collectively denoted by C_V, and the second is an integral over the surface A_f replacing the fuselage.

The circulation Γ about the blade vortices is known directly in terms of flight parameters. The circulation about a wake vortex at a given point is simply that value assigned to the blade vortex when it was generating that segment of wake. The source strength σ may also be regarded as known insofar as the wake flow calculations are concerned. That distribution is assumed to be such as to produce the flow about a body of known geometry in a uniform free stream, so $\sigma(\underline{r})$ may be determined from a separate calculation.

The only information lacking for the complete specifi-

7
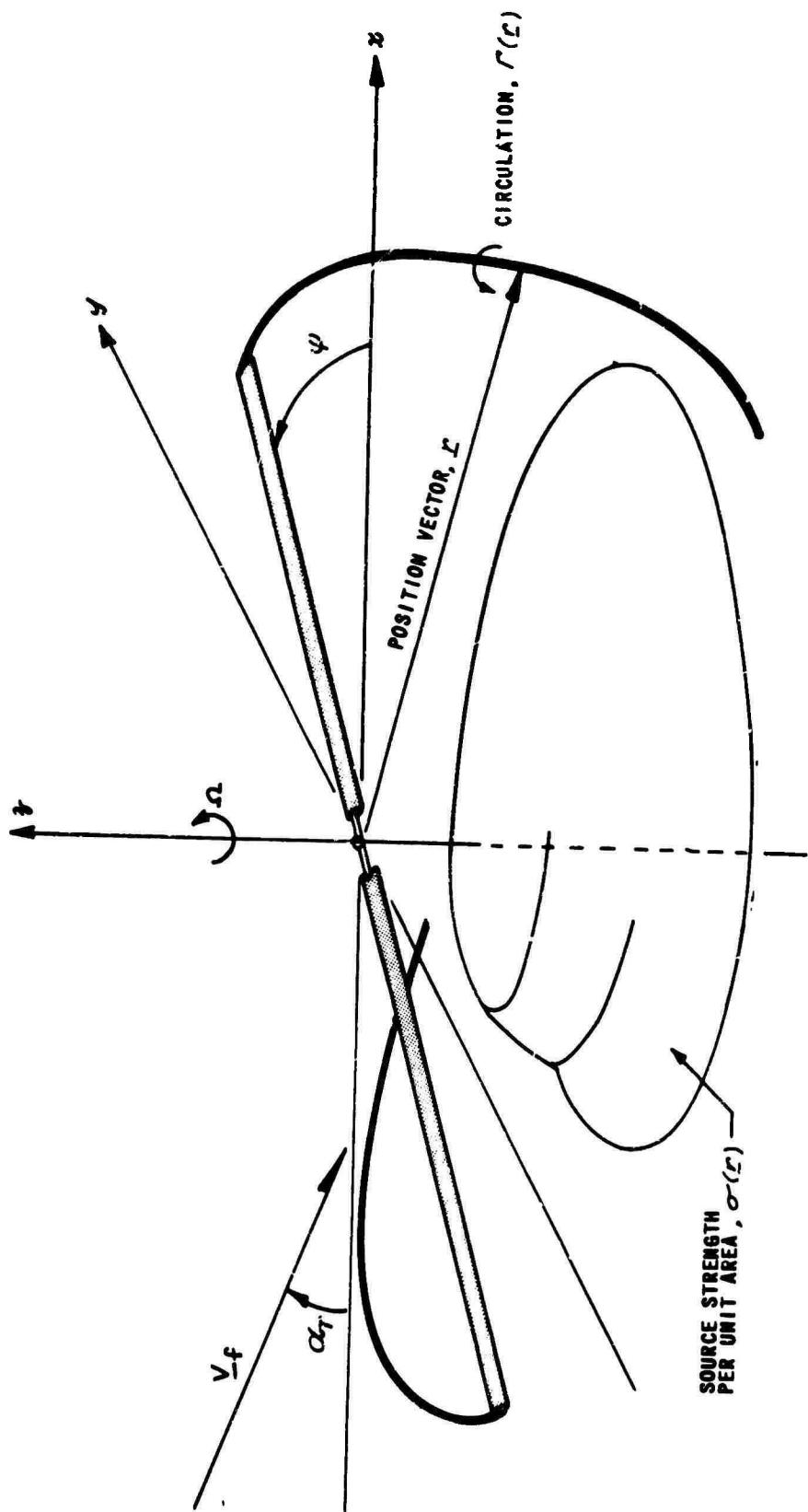
Figure 1 THE COORDINATE SYSTEM

cation of the flow at a given instant, then, is the location of the wake vortices at that instant. The position of a given point on a wake vortex located by the vector $\underline{r}$ is the time integral of the velocity experienced by that fluid particle:

$$\underline{r}(t) = \underline{r}(t_o) + \int_{t_o}^{t} \underline{V}(\underline{r}(\tau)) \, d\tau . \tag{2}$$

Thus, even after simplifying, the flow can only be obtained as the solution of the nonlinear integral equation formed by the substitution of Equation (1) into Equation (2). A direct analytical solution is clearly not feasible, but the problem is amenable to solution by numerical methods using a high-speed digital computer.

IMPLEMENTATION OF THE MODEL

Wake Positioning and Displacement

For purposes of numerical analysis, a series of points $P_1, P_2, \cdots, P_{N_W}$ is marked off on each wake vortex, as shown schematically in Figure 2.


Figure 2 WAKE REFERENCE POINT IDENTIFICATION

The points are placed sufficiently close together so that for purposes of computation of wake-induced velocities, the segment (i) of wake between points P_i and P_{i+1} may be considered as a rectilinear vortex having constant circulation along its length. The wake configuration at any instant is then defined by the locations of these points.

10

Computations are initiated by specifying that each of
the wake vortices lies on a prescribed curve. Generally, this
curve is chosen to be a skewed helix with pitch and skew selected
from simple momentum considerations. The numerical analogues to
Equations (1) and (2) are then performed by first summing the
velocity contributions of all vortex and source elements in the
flow at each reference point (Equation (1)), and then convecting
each point at the computed velocity for a time interval Δt
(Equation (2)). The time interval Δt is chosen to correspond to
a small finite change $\Delta \Psi$ in the azimuth position of the blades:

$$\Delta t = \frac{\Delta \Psi}{\Omega} \tag{3}$$

where Ω is rotor angular speed. Once the new coordinates of each
reference point are computed, the azimuth of the blade vortices
is increased by $\Delta \Psi$ and the velocity computation is performed
again. As the blade vortices are repositioned, a wake vortex
element is added to the flow at the tip of each blade vortex, the
added vortex having a length of approximately $R \Delta \Psi$, where R is
rotor radius. A corresponding element is dropped from the compu-
tations at the downstream end of each wake vortex, so the program
is not encumbered by a wake of ever increasing size. The compu-
tations may be continued indefinitely in this manner, but it has
been found that a periodic wake is eventually established in most
cases, after which there is, of course, no need to perform fur-
ther calculations.

The total number of wake vortices taken into account and
the magnitude of $\Delta \Psi$ determine the accuracy of the flow repre-
sentation at a given point. It has been found that, for a two-
bladed rotor, a value for $\Delta \Psi$ of thirty degrees is sufficiently
small to define the time variations of the flow. The number of
wake elements considered depends on the region of interest and
the forward speed. If the flow beneath the rotor plane is

11

desired, then the wake generated by only a few revolutions of the rotor is needed. It has been found, for example, that with an advance ratio, $\mu = \frac{V_f}{\Omega R}$, of about .25, just two revolutions of wake sufficiently define the flow under the rotor plane. At lower advance ratios, the free stream does not clear the wake from under the rotor as rapidly, so more wake must be retained. With $\mu = .15$, four revolutions of wake are needed, and for hovering, seven or eight revolutions must be retained to compute the flow within about $0.5R$ of the rotor plane.

Computation of Velocity Induced by Wake and Blades

The velocity induced at an arbitrary point P by the vortices representing the wake and blades is simply the sum of the effects of an array of rectilinear vortex segments. If V_{w_i} denotes the velocity induced at P by the element between points P_i and P_{i+1}, it is found from Equation (1) that

$$V_{w_i} = \frac{\Gamma_i}{4\pi h} \left(\cos \theta_1 - \cos \theta_2 \right) \tag{4}$$

where Γ_i is the strength of the element and θ_1, θ_2 and h are defined in Figure 3. The velocity is directed normal to the plane containing P_i, P_{i+1} and P.

The necessity for specifying that the wake vortices have a finite core size is evident from Equation (4). If P is coincident with either P_i or P_{i-1}, the formula for V_{w_i} is indeterminate. When computing wake-induced flow at a given wake reference point, the effect of the two wake elements adjacent to that point must, therefore, be computed by taking core size into account (if a point lies outside the core substance of a vortex, the formula for induced velocity is the same as for a vortex with infinitesimal core size, i.e., Equation (4)). Locally induced velocities depend directly on the curvature of (the centerline of) the vortex at the point in question. An approximation to the

12
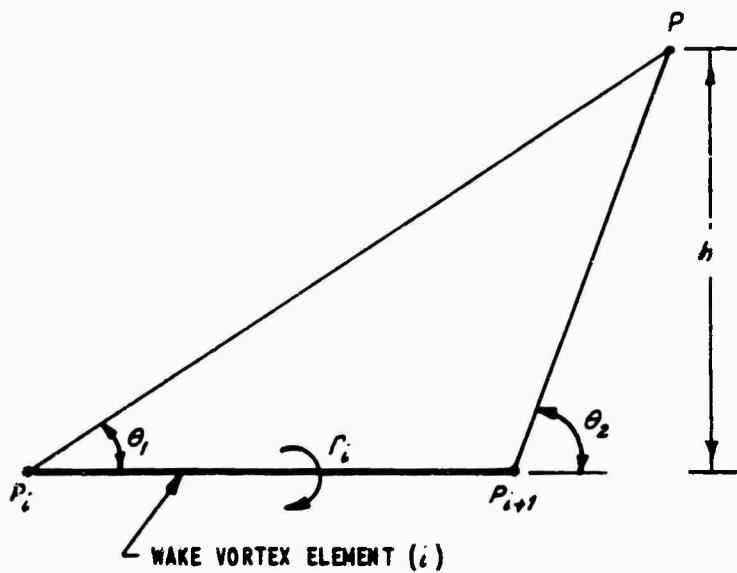
Figure 3 GEOMETRIC RELATIONSHIPS DEFINING THE FLOW INDUCED BY A RECTILINEAR VORTEX ELEMENT

actual curvature is obtained by assuming that the two elements whose effects at point P_i are to be computed lie on the circular arc which passes through points P_{i-1}, P_i and P_{i+1}, as shown in Figure 4. Then it is assumed that the two vortex segments have circular cores of rotational fluid of radii a_{i-1} and a_i, respectively, and that the vorticity within the core is tangent to the arc. The self-induced velocity V_{s_i} at point P_i - i.e., the contributions of the elements adjacent to P_i - may then be written in integral form by summing the effects of circular-arc vortex filaments of differential cross-section. If it is then assumed that the core radii are much less than the radius of curvature R_i, the integrand may be simplified and the

13

integral evaluated. It is then found that

$$V_{s_i} = \frac{1}{8\pi \mathcal{R}} \left\{ \Gamma_{i-1} \left[\ln\left(\frac{8\mathcal{R}}{a_{i-1}} \tan\frac{\phi_{i-1}}{4} \right) + \frac{1}{4} \right] \right.$$

$$\left. + \Gamma_i \left[\ln\left(\frac{8\mathcal{R}}{a_i} \tan\frac{\phi_i}{4} \right) + \frac{1}{4} \right] \right\}$$ (5)

where ϕ_{i-1} and ϕ_i are defined in Figure 4. The self-induced velocity is directed normal to the plane of the arc. The core radius of a given element may be assigned on a rational basis using energy considerations, as discussed later.
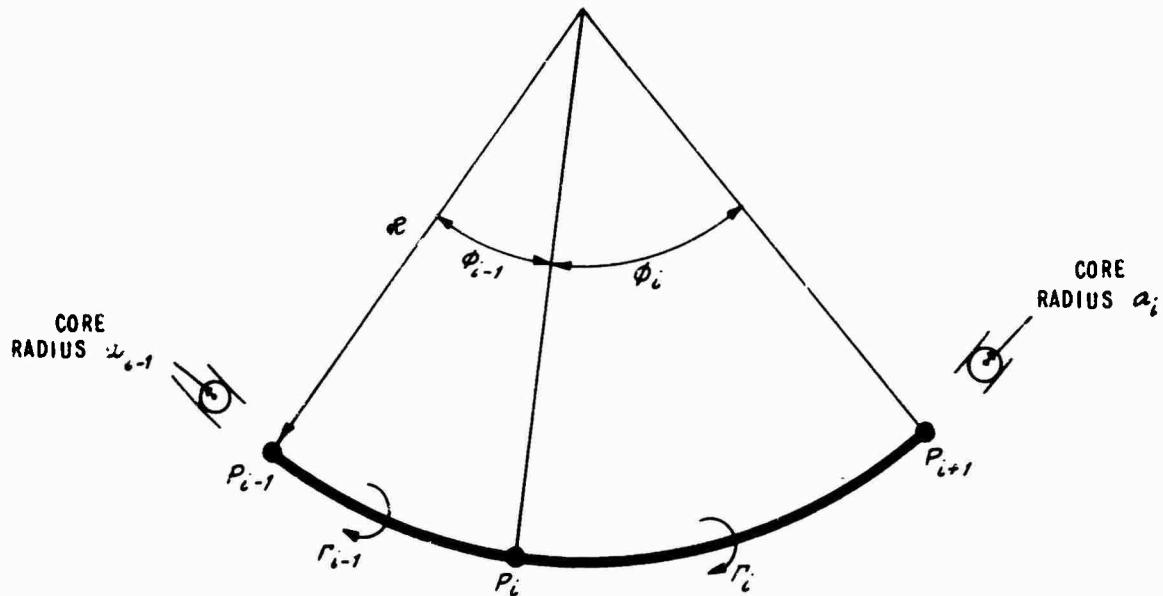

Figure 4 GEOMETRIC RELATIONSHIPS DEFINING THE SELF-INDUCED VELOCITY AT WAKE POINT P_i

14

The Fuselage Representation

As noted previously, the source-strength distribution is
determined for a fuselage in a uniform, steady free stream. Once
this distribution is obtained, the effect of the fuselage is taken
into account in a straightforward manner according to the second
integral in Equation (1).

The computation of the source-strength distribution may
be treated as a separate problem, since the source strength per
unit area σ at a given point $\underline{r}$ may be normalized. That is,
σ may be written in the form

$$\sigma(\underline{r}) = V_{x_\infty} \sigma_x(\underline{r}) + V_{y_\infty} \sigma_y(\underline{r}) + V_{z_\infty} \sigma_z(\underline{r}) \tag{6}$$

where V_{x_∞}, V_{y_∞} and V_{z_∞} are the components of the free stream
experienced by the fuselage, and the normalized strengths σ_x,
σ_y and σ_z are functions only of fuselage geometry. The values
for the free stream velocity components may be obtained by simply
computing the flow in the absence of the fuselage and taking
appropriate averages.

The normalized source strengths are computed according
to the method reported in Reference 5. The fuselage surface is
approximated by an array of quadrilateral elements. The source
strength per unit area on a given quadrilateral is taken to be
constant. Thus, if there are N_f of these elements replacing the
fuselage, there are $3 N_f$ strengths to be determined. The re-
quirement of flow tangency at N_f points (one cn each of the
quadrilaterals) then produces $3 N_f$ linear algebraic equations
for determining the $3 N_f$ unknown strengths. A digital computer
program was coded for determining the source strengths in this
manner.

DETERMINATION OF SYSTEM PARAMETERS

The formulations of the model were nondimensionalized for purposes of coding, with lengths made dimensionless by rotor radius R and velocities by rotor tip speed ΩR. The flight conditions of the aircraft being represented relate to the computer program through the following dimensionless parameters: advance ratio $\mu = \frac{V_f}{\Omega R}$, nondimensionalized blade vortex circulation $\Gamma_b / (\Omega R^2)$, tip-path plane angle α_r and the ratio of wake-vortex core radius to rotor radius, $\frac{a}{R}$. The quantities which determine μ are, of course, generally available. Specification of the other parameters is accomplished in the manner discussed below.

Blade Vortex Strength, $\Gamma_b (\psi)$

The circulation about a rotor blade at a given azimuth position ψ is actually varying in the radial direction (more or less elliptically). It was felt, though, that a sufficient approximation to blade-induced effects would be obtained by making the circulation constant spanwise and of a magnitude equal to the maximum attained on the actual blade. It might be supposed that blade-induced effects would then be somewhat exaggerated, but comparisons of computed and measured flows indicate that the error so introduced is not large enough to be discernable.

If the circulation is assumed to vary elliptically in the spanwise direction, the maximum circulation Γ_m about a blade is given by (neglecting root effects and making small-angle approximations where appropriate),

$$\Gamma_m = \frac{8 L_\beta (\psi)}{\pi \rho \Omega R^2 (1 + \mu \sin \psi)^2}$$

$$\approx \frac{8 L_\beta (\psi)(1 - 2\mu \sin \psi)}{\pi \rho \Omega R^2}$$

16

where L_B is the total lift acting on the blade and ρ is the air density. Then, assuming that the total lift acting on the rotor is constant and equal to the gross weight W of the aircraft, it follows that

$$\frac{\Gamma_m}{\Omega R^2} = 2\pi \lambda \left(1 - 2\mu \sin \psi\right) \tag{7}$$

where λ is a blade loading parameter, defined by

$$\lambda = \frac{4W}{\pi^2 N_B \, \rho \, \Omega^2 \, R^4}$$

with N_B denoting the number of blades on the rotor.

Inclination of the Tip-Path-Plane, α_T

The tip-path-plane angle is a complicated function of flight conditions, rotor dynamics and blade cyclic and collective pitch settings. Various methods are available for computing this angle (see, for example, Reference 6), but their use requires iterative or graphical procedures and the values of parameters which are generally not well defined.

Reasonable values for α_T have been obtained without resorting to elaborate methods by using the formula

$$\alpha_T = \frac{2\,C_{0_f}}{\pi N_B} \frac{\mu^2}{\lambda} \tag{8}$$

where C_{0_f} is the fuselage drag coefficient, defined as the ratio of fuselage drag to $\frac{\pi}{2} \rho V_f^2 R^2$. Equation (8) was obtained by neglecting rotor in-plane drag and fuselage lift. The angle α_T, if assumed small, must then be simply the ratio of fuselage drag to rotor thrust (aircraft weight). Values for α_T obtained from Equation (8) were found to be within 20 to 30 per-

17

cent of measured values for a UH-1A helicopter (from Reference 7) using a value for C_{D_f} of .014 (Reference 8).

Wake-Vortex Core Radius, a

The nondimensionalized core radius of each vortex element must be specified as it is generated by a blade vortex. This core size should correspond to that of the tip vortex formed in the physical flow when the wake rolls up.

In order to obtain an estimate of the core size, three major simplifying assumptions have been made. First, all vorticity in the flow except that contained in the wake under analysis has been neglected. This may be rigorously justified as an adjunct to the development which follows, but the calculations are somewhat lengthy and so have been omitted. The justification uses the fact that some distance from the wake the flow before and after roll-up is effectively the same. Second, it is assumed that the wake may be considered as though it were generated by a wing of the same geometry as the blade in steady translational flight. That is, the tip and root vortices of a rotor blade are assumed to have the same core size as the tip vortices generated by a wing of the same aspect ratio in steady translational flight, having the same loading as the blade had when it generated the segment of wake being analyzed. Third, it is assumed that the roll-up of the wake of a wing in steady translational flight can be treated as an unsteady two-dimensional problem rather than a steady three-dimensional one. The only justification (other than intuitive argument) for the latter two assumptions is that they do yield results which appear to be realistic.

Consider, then, a wing of large aspect ratio in steady translational flight, as shown in Figure 5. If Γ denotes the circulation about the wing, then at some position X in the wake upstream of the point where roll-up begins (View A-A,

18
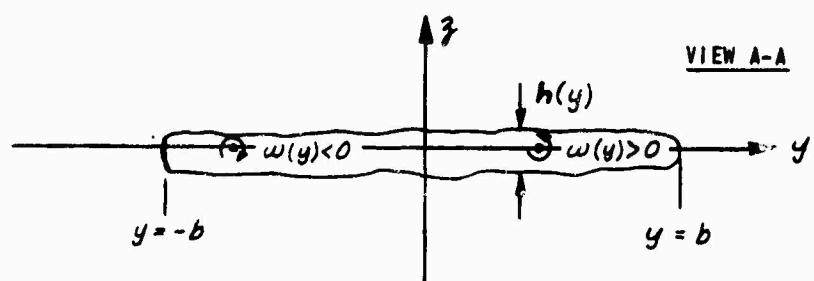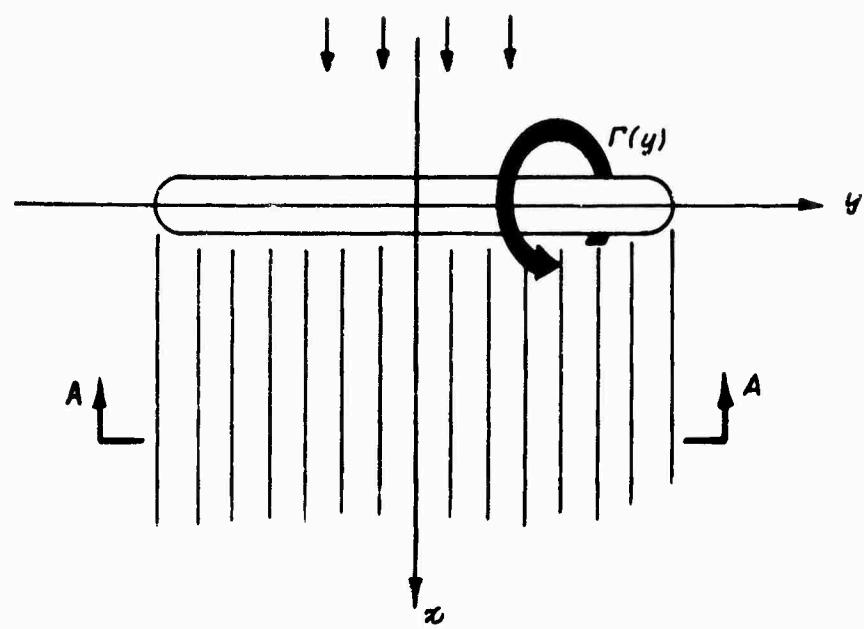
Figure 5 REPRESENTATION OF THE WAKE BEFORE ROLL-UP

Figure 5), the circulation per unit length $\gamma(y)$ is given by

$$\gamma(y) = -\frac{d\Gamma}{dy} = \omega h \tag{9}$$

where $\omega(y)$ is the magnitude of the vorticity in the wake and $h(y)$ is the thickness of the wake sheet (see Figure 5). Given the loading on the wing - i.e., on the rotor blade at some azimuth - $\gamma(y)$ may then be specified through Equation (9). Note that $\gamma = 0$ at some point, say y_o, where Γ is a maximum. Also, since $\Gamma(-b) = \Gamma(b) = 0$, $-b$ corresponding to blade root and b to blade tip, it follows that

$$-\int_{-b}^{y_o} \gamma(y) dy = \int_{y_o}^{b} \gamma(y) dy = \Gamma_m$$

where Γ_m denotes the maximum value of $\Gamma(y)$. Replacing variation in x in the wake by variation in time in a plane parallel to the $y \cdot 3$ plane and fixed in the wake, the sheet of vorticity would be observed to roll up into a pair of vortices whose cores consist of the rotational fluid which was contained in the sheet.

This process will be assumed, in what follows, to be two-dimensional. That is, the flow in the wake-fixed plane is taken to be the same as though the wake were extended to positive and negative infinity in the x-direction, and that in each plane parallel to that plane the flows are identical; or taken still another way, it is assumed that derivatives with respect to x are small in comparison to changes in y or 3 insofar as roll-up is concerned.

If the cores of the vortices formed by the roll-up are assumed to be of circular section and of approximately uniform vorticity, and if it is further assumed that ω is constant in

20

the sheet before roll-up (except at y_o, where it changes sign), it follows that the core radii of the two vortices will be equal. Further, because the moment of impulse of the flow is conserved, the vortices locate on the y-axis with their respective positions $y = y_L$ and $y = y_R$ given by

$$y_L = \frac{1}{(-\Gamma_m)} \int_{-b}^{y_o} y\, \Gamma'(y)\, dy$$

$$y_R = \frac{1}{\Gamma_m} \int_{y_o}^{b} y\, \Gamma'(y)\, dy \quad .$$

(10)

The situation after roll-up is as shown in Figure 6.
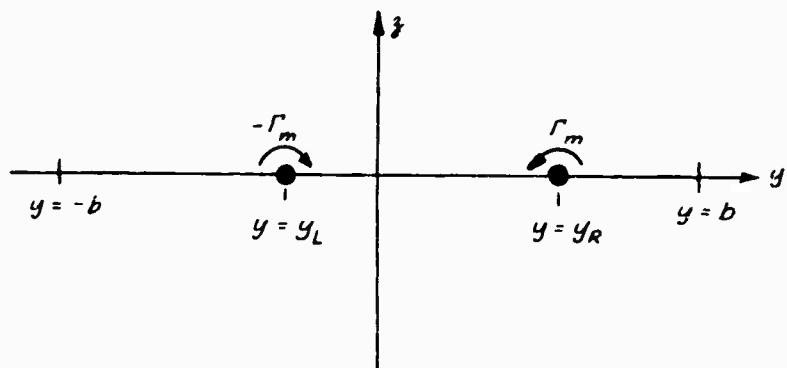
Figure 6   REPRESENTATION OF THE WAKE AFTER ROLL-UP

21

If viscous effects are neglected, the kinetic energy of the flow per unit depth, T , must be conserved. By deriving expressions for T for before and after roll-up and equating them, a relationship for core radius a may be obtained.

From Reference 9, T is given, in general, by

$$T = -\frac{\rho}{2} \iint \omega \, \Psi \, dy \, dz \tag{11}$$

where

$$\Psi(y,z) = \frac{1}{2\pi} \iint \omega \, \ln \left[\frac{(y-\eta)^2 + (z-\zeta)^2}{b^2} \right]^{\frac{1}{2}} d\eta \, d\zeta \, .$$

The integrals are taken over the entire area where ω is not zero. If γ/h is substituted for ω in Equation (11) and h is assumed to be much less than b , the integrands may be simplified and the integrals evaluated. It is then found that, in the limit of vanishing sheet thickness, T before roll-up is given by

$$T = -\frac{\rho}{4\pi} \int_{-b}^{b} \int_{-b}^{b} \gamma(y) \, \gamma(\eta) \, \ln \left| \frac{y-\eta}{b} \right| dy \, d\eta \tag{12}$$

Similarly, it is found that after roll-up,

$$T = \frac{\rho \, \Gamma_m^2}{2\pi} \left[\ln \left(\frac{y_R - y_L}{a} \right) + \frac{1}{4} \right] \tag{13}$$

so that the core radius a is determined from

$$\ln \left(\frac{y_R - y_L}{a} \right) = -\frac{1}{2} \int_{-b}^{b} \int_{-b}^{b} \frac{\gamma(y) \, \gamma(\eta)}{\Gamma_m^2} \, \ln \left| \frac{y-\eta}{b} \right| dy \, d\eta - \frac{1}{8} \, . \tag{14}$$

22

The result of Equation (14) may be put in a form more directly related to blade circulation as follows. Let Γ be expanded in a Fourier series, according to

$$\frac{\Gamma(\theta)}{\Gamma_m} = \frac{2}{\pi} \sum_{k=1}^{\infty} a_k \sin k\theta \tag{15}$$

where $\cos\theta = \frac{y}{b}$. Then

$$\gamma(\theta) = \frac{1}{b \sin\theta} \frac{d\Gamma}{d\theta}$$

$$= \frac{2\Gamma_m}{\pi b \sin\theta} \sum_{k=1}^{\infty} k a_k \cos k\theta$$

Also, it is found from Equations (10) and (15) that

$$\frac{y_R - y_L}{b} = \frac{1}{b \Gamma_m} \int_{-b}^{b} y \, \gamma(y) dy$$

$$= a_1 \; .$$

If γ and $y_R - y_L$ are then substituted in Equation (14) and the integrations performed, it is found that

$$\frac{a}{R} = \frac{a_1}{2} \left(1 - \frac{r_0}{R}\right) e^{-\left[\sum\limits_{k=1}^{\infty} k a_k^2 - \frac{1}{4}\right]} \tag{16}$$

where r_0 is the radial distance from the axis of revolution to the blade root.

Some numerical computations were performed, utilizing Equation (16), to determine the order of magnitude of core size predicted by this method and to provide an indication of the

23

amount by which the core size varies with azimuth and forward speed. Data for the computations were generated by a blade-loads program that Cornell Aeronautical Laboratory developed for the U. S. Army Aviation Materiel Laboratories (these results are generally in good agreement with experimentally obtained loadings). Three flight conditions were considered: (1) a UH-1A rotor at 105 kt. forward speed, (2) a UH-1A rotor at 30 kt. forward speed, and (3) a 5-foot-diameter experimental rotor in hovering flight. The ratio of rotor radius to vortex core radius was calculated for four azimuth positions of the blades in each case, using a 12-point harmonic analysis of circulation distribution. The results of the computations are tabulated below.

Flight Condition	Ratio of Rotor Radius to Core Radius			
	$\psi = 0$	$\psi = 90°$	$\psi = 180°$	$\psi = 270°$
105 kt. - UH-1A	24.0	13.3	17.5	21.0
30 kt. - UH-1A	18.7	15.0	14.4	24.1
Hover - 5 Ft.Rotor	21.9	21.9	21.9	21.9

This method of predicting vortex core radius appears to provide a reasonable order of magnitude for that quantity - from about 4.0 to 7.5 percent of rotor radius. Most notable is the lack of any substantial variation in core radius either with forward speed or azimuth position. The variations obtained may be considered small since a change of 20 or 30 percent in core radius produces a much smaller change in self-induced velocity, with the latter varying as the logarithm of the former.

It was, therefore, possible to incorporate a major simplification in the digital computer program, by assigning a representative value of .05 to the ratio of core radius to rotor

radius, independent of azimuth position or flight conditions. It
was verified that this simplification does not cause an appreciable
error.

RESULTS OF COMPUTATIONS

General Remarks

Wake flow calculations were carried out in two phases.
The program was first operated with the fuselage representation
omitted. The sensitivity of the wake model to various parameters
and the general character of the solutions were investigated, and
a comparison of computed flow with experimental measurements was
made. Once it was determined that the model was both operation-
ally practical and constituted a valid representation of the flow,
extensive calculations were performed which incorporated the fuse-
lage representation. The latter results correspond to a UH-1B
helicopter at five different forward speeds ranging from hover to
high-speed cruise. Before discussing the details of the results
obtained, though, the following remarks concerning the qualitative
nature of the flows computed should be made.

There was some concern during the formulation as to the
numerical and/or physical stability of the model; i.e., it was
questioned whether the approximations made in integration or
possibly the nature of vortical flows themselves would allow a
periodic flow to be established. It was found, however, that the
model generally does produce a periodic flow, even though the
initial, or starting, wake configuration may differ greatly from
the periodically verying wake geometry.   There was some evidence
of nonperiodic behavior at very low advance ratios, however,
which appears to be attributable to an inherent instability in
free-vortex flows. At an advance ratio below about .07, wake-
induced effects are comparable with the magnitude of the free

25

stream, so the individual vortices then interact to a great extent. It results that, for very low advance ratios, an increasingly nonperiodic flow is evident in proceeding down the wake, starting from about two to three revolutions of wake below the rotor. The wake geometry and the flow is periodic above this point (which is about half a rotor radius below the rotor plane, for moderate loading). Halving the interval of integration or adding wake elements does not noticeably alter this situation.

The general character of the wake geometries obtained is illustrated in Figure 7. The tip vortices for a two-bladed rotor are shown drawn in perspective projection for the case of $\mu = .14$, $\lambda = .00236$, $\alpha_T = 2.3$ degrees and $\Delta\psi = 15$ degrees. A periodic flow was obtained for this case. The individual wake elements were projected as straight lines between the wake reference points. Both the initial wake configuration and the configuration at $\psi = 0$ after periodicity was established are shown so that the extent of the wake-induced distortion may be seen. The large vertical displacements two to three rotor radii downstream (which are somewhat exaggerated by the perspective) might in part be attributable to the size of the integration increment taken, and so are not necessarily representative of the flow in the far wake. The concentration of vortices at the lateral extremes of the wake, giving the appearance of the wake behind a conventional wing, is clearly evident in the figure.

Comparisons with Experimental Measurements

In order to properly assess the model of the rotor, it was decided to compare computed and measured flows. Satisfactory quantitative data pertaining to instantaneous fluid velocities could not be located. A rather extensive wind tunnel program was carried out by NACA, however, to measure average velocities in the wake of a two-bladed teetering rotor at moderate to high

26

DISTORTED WAKE

SKEW-HELICAL WAKE CONFIGURATION
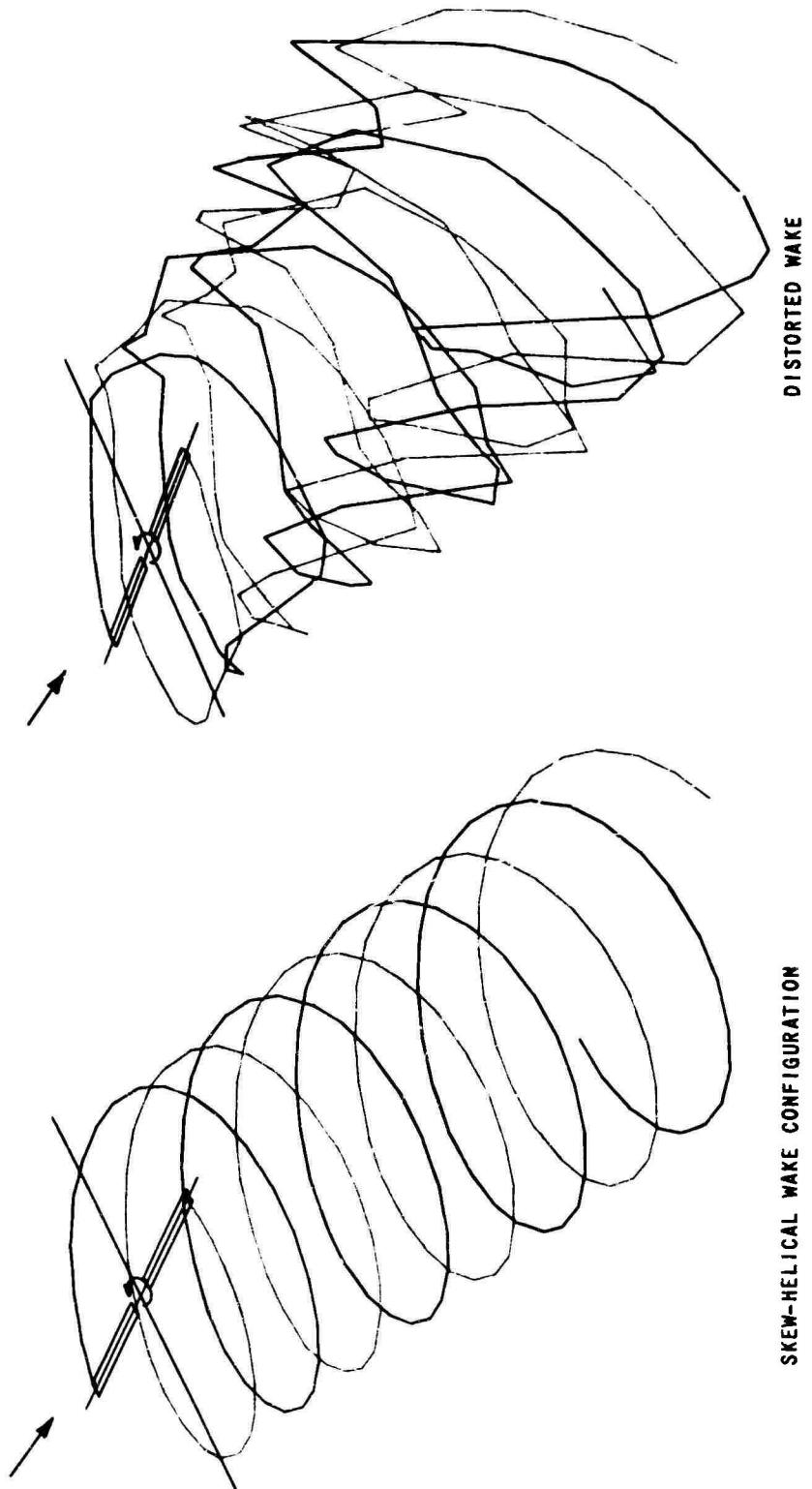
Figure 7 COMPARISON OF INITIAL WAKE GEOMETRY WITH THE CONFIGURATION AFTER PERIODICITY
IS ESTABLISHED FOR μ = 0.14, λ = 0.00236, AND α_T = 2.3 DEGREES

advance ratios. The results of the program are presented in Reference 10. The data are presented in Reference 10 as plots of $\frac{\bar{v}}{v_o}$ as a function of the three spacial coordinates, where $\bar{v}$ is the time average of the induced downwash (i.e., with the free stream component subtracted off) normal to the tip-path-plane, and v_c is the value for that quantity as predicted by simple momentum theory. For moderate to high advance ratio, $v_c = \Omega R C_T / (2\mu)$ where C_r is rotor thrust coefficient. It was estimated by the authors of that report that the error accumulated in measuring $\bar{v}/v_o$ was less than about ± 0.1 at the moderate advance ratios.

A comparison was made of the average of computed velocities with these measurements for one of the test flight conditions. For the case chosen, the advance ratio μ was 0.14, the thrust coefficient C_T was .00371, where C_T is defined as the ratio of rotor thrust to $\pi \rho \Omega^2 R^4$, and the inclination of the tip-path-plane α_T was 2.3 degrees. Comparisons of computed and measured results are shown plotted in Figures 8, 9 and 10. The data is plotted for the coordinate system of Figure 1, with the coordinates nondimensionalized by rotor radius.

Figures 8 and 9 show the variation of $\bar{v}/v_c$ with y for values of X of 0 and 0.5 respectively, with each figure showing the variation at both $\jmath = -0.07$ and $\jmath = -0.2$. The computed and measured values are seen to agree fairly well for these values of X . It should be noted that this agreement is obtained even though the instantaneous computed values of the downwash vary a great deal from the mean. The extent of the variation is illustrated in Figure 10. In this figure, the ratio of the induced downwash v to v_o is plotted against blade azimuth ψ for $\chi = 0.5$, and $y = 0.5$ for both $\jmath = -0.07$ and $\jmath = -0.2$. The computed and measured mean values are also indicated on the plots.

28
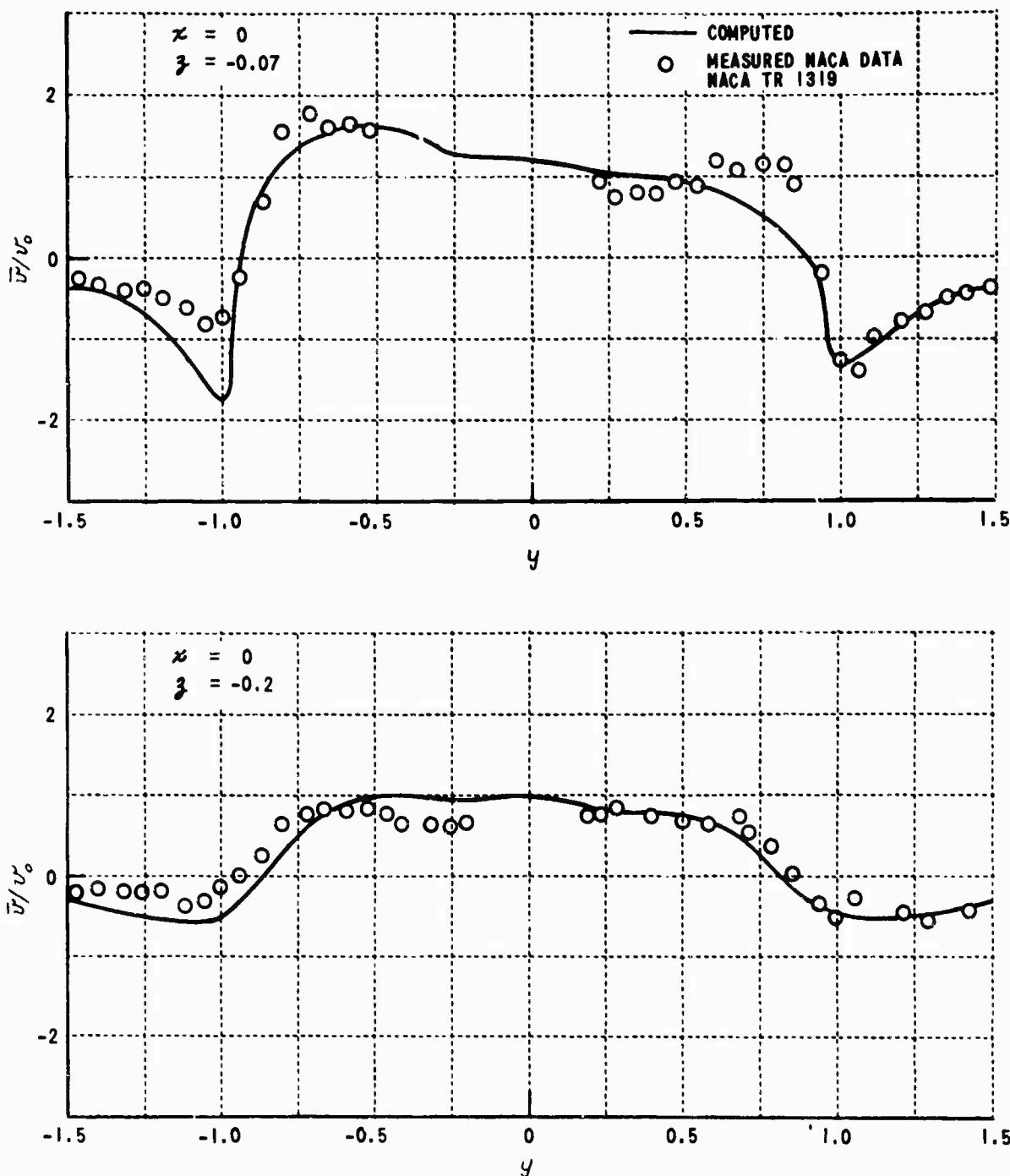
Figure 8   COMPARISON OF COMPUTED AND MEASURED INDUCED DOWNWASH
BELOW THE ROTOR PLANE, $\mu = 0.14$, $C_T = 0.00371$, $x = 0$

29
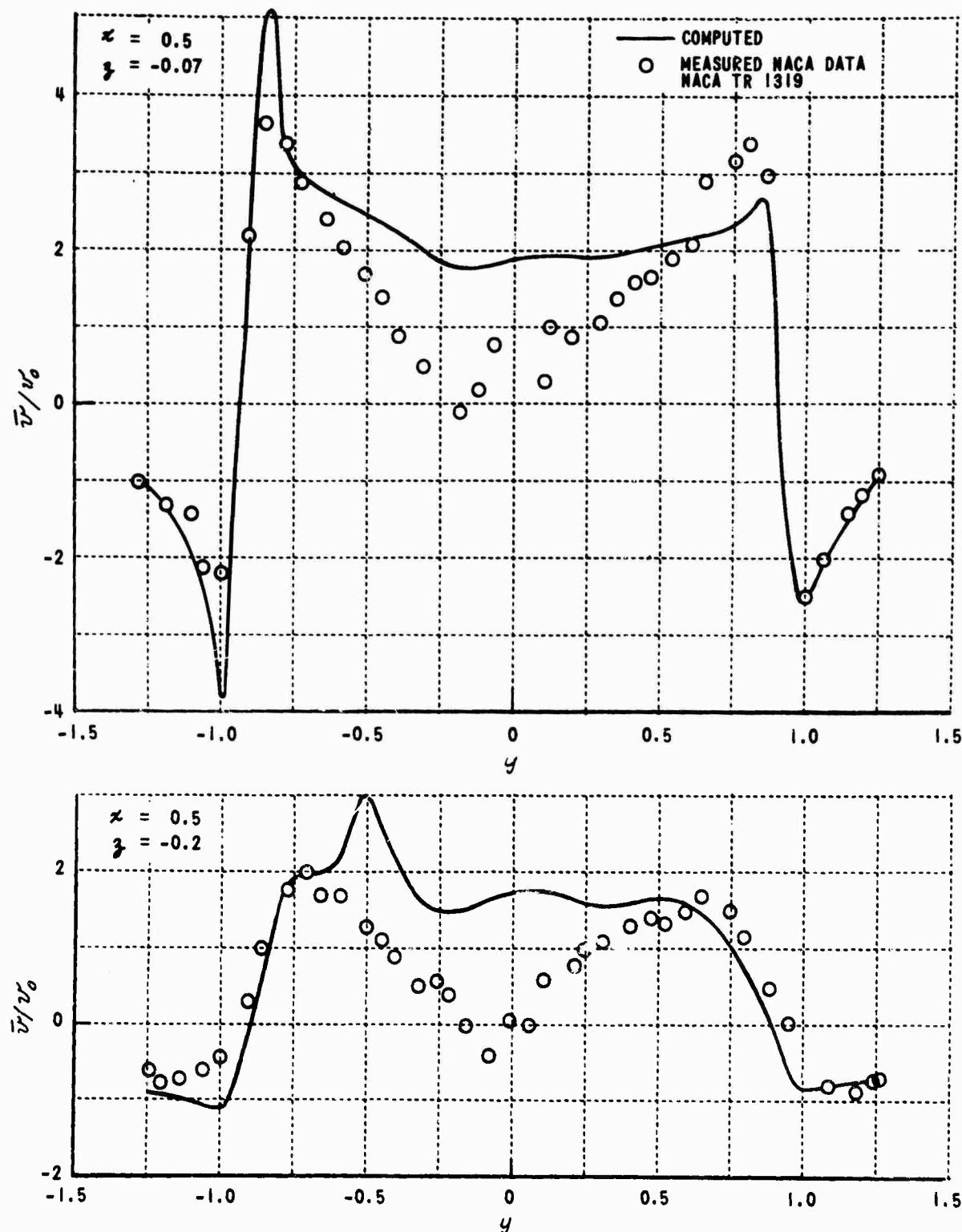
Figure 9   COMPARISON OF COMPUTED AND MEASURED INDUCED DOWNWASH
BELOW THE ROTOR PLANE, μ = 0.14, C_T = 0.00371 , x = 0.5

30
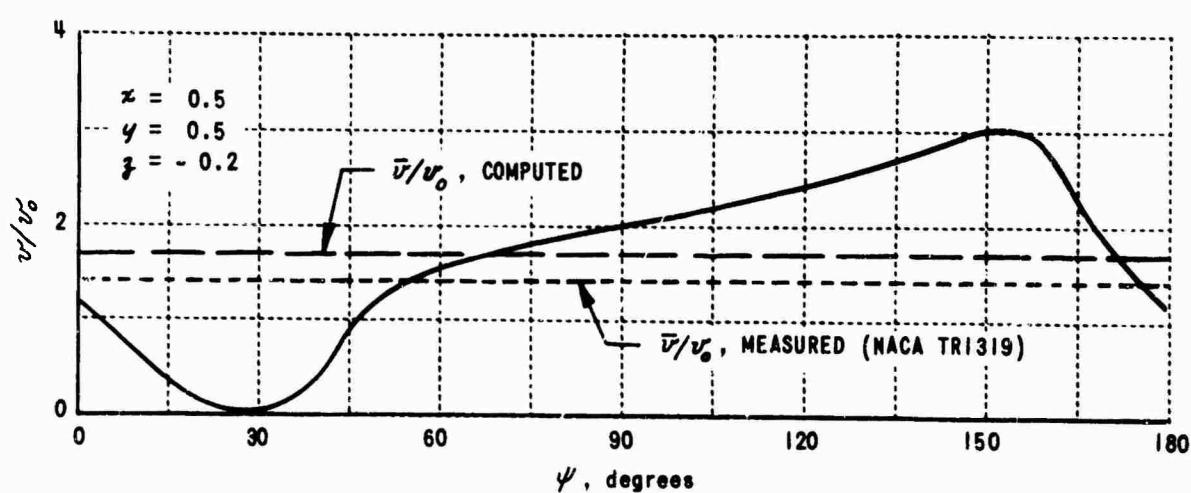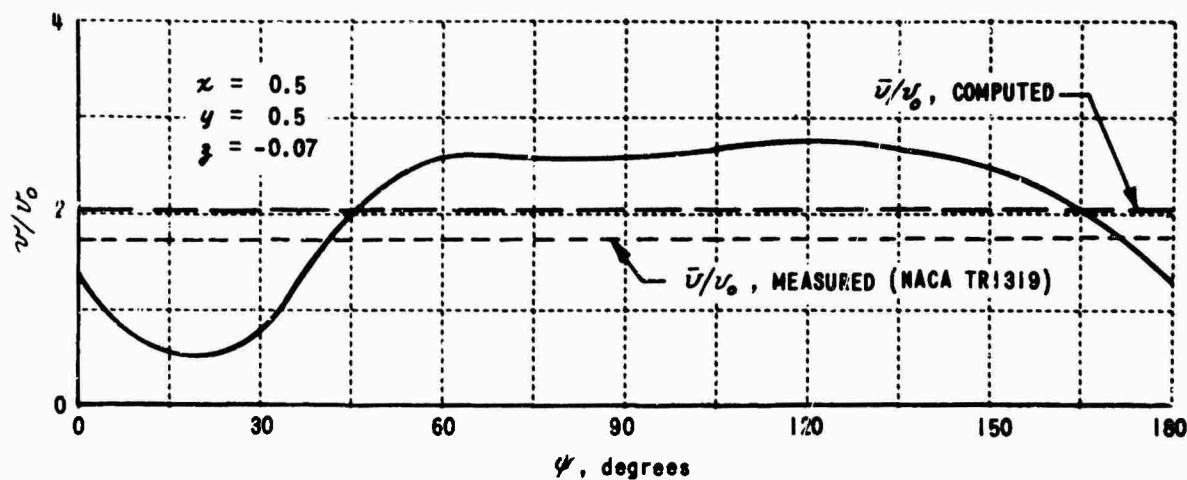
Figure 10 COMPUTED VARIATION OVER ONE PERIOD OF THE INDUCED DOWNWASH
AT TWO POINTS BELOW THE ROTOR PLANE

31

Rather poor agreement was obtained downstream of the rotor hub in the vicinity of the x-y plane, as may be seen in Figure 9. The lack of agreement may be due in part to the effects of the structure supporting the test rotor. These effects were not discussed by the experimenters in their report. Omission from the analytical model of the inboard wake structure may also contribute to the discrepancy, since this portion of the wake would be expected to produce an upwash near the x-y plane.

Flow Calculations for a UH-1B Helicopter

Extensive calculations were performed to determine the flow in the vicinity of a UH-1B helicopter. The aircraft was assumed to have a gross weight of 5675 pounds (about two thirds of maximum gross weight) and a rotor speed of 31.4 radians per second, giving a value for the blade loading parameter, λ , of .00209. A total of five cases were treated, corresponding to forward speeds from 0 to 110 knots. The values of the important parameters for these cases are tabulated below.

Advance Ratio μ	Tip-Path-Plane Angle α_r, degrees	Number of Revolutions of Wake per Blade
0	0	7
.0732	.655	5
.1465	2.62	4
.220	5.91	3
.269	8.84	2

In all cases, $\Delta \Psi$ = 30 degrees, and of course, N_B = 2. The fuselage was represented by a total of 192 source-sheet elements. The somewhat simplified geometry used for the surface replacing the fuselage is depicted in plan and elevation in Figure 11. The coordinate system in Figure 11, and the one used

32
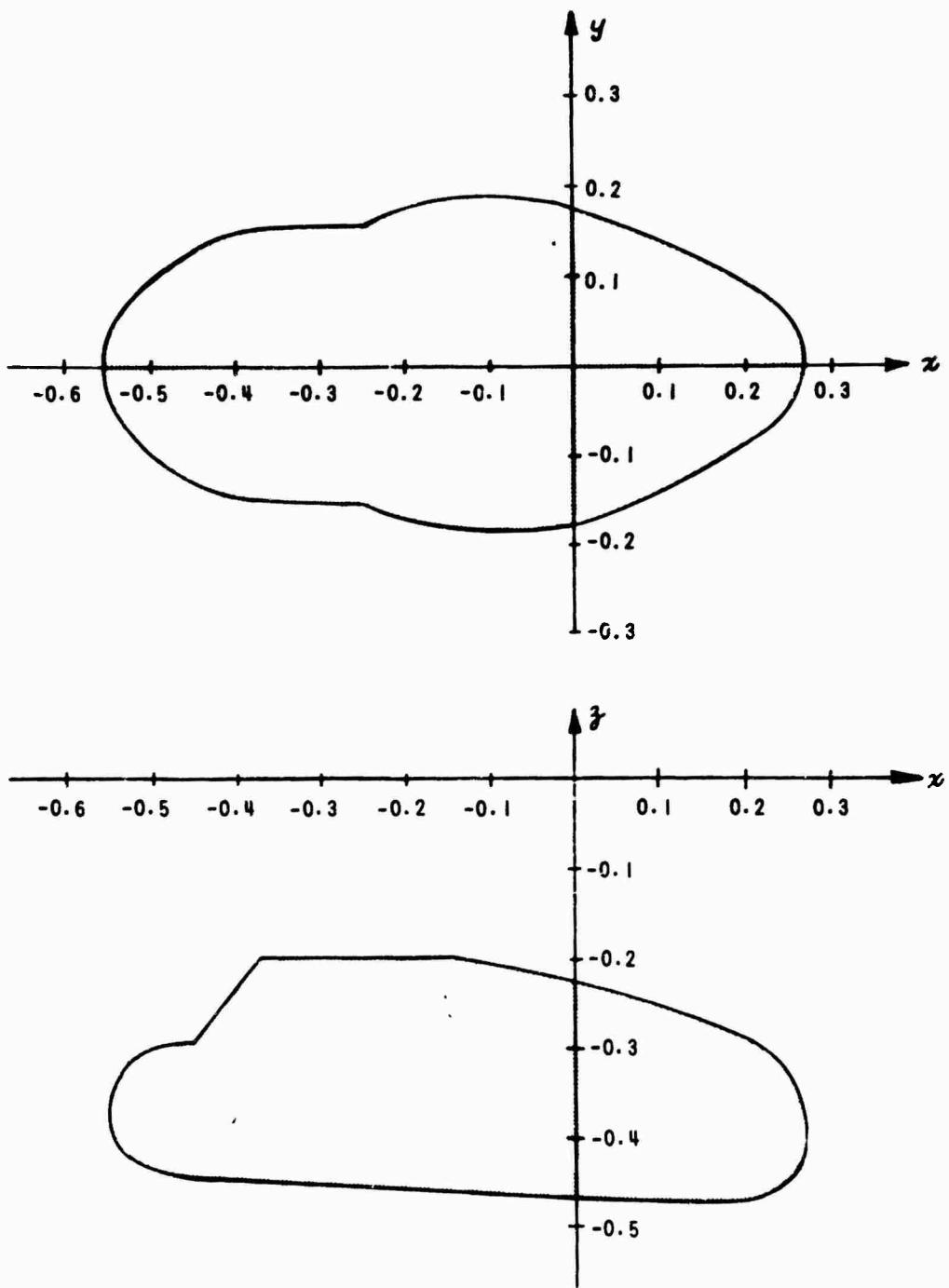
Figure 11 FUSELAGE REPRESENTATION USED IN FLOW
CALCULATIONS FOR A UH-IB HELICOPTER

33

for the plots of flows following Figure 11, is that of Figure 1, nondimensionalized by rotor radius.

Flow calculations were performed within the volume external to the fuselage and having the limits

$$-1.1 \leq x \leq -0.1$$

$$-0.45 \leq y \leq +0.45$$

$$-0.45 \leq \mathfrak{z} \leq -0.15$$

In all five cases, a periodic flow was established within this volume.

Selected results of the computations are presented in Figures 12 through 16 as plots against x of the dimensionless velocity components V_x, V_y and $V_\mathfrak{z}$, which relate to their dimensional counterparts by a factor $\lambda \Omega R$, for $y = .3$ and $\mathfrak{z} = -.25$. The time averages over one period of V_x, V_y and $V_\mathfrak{z}$ are also plotted, these averages being denoted by $\bar{V}_x$, $\bar{V}_y$ and $\bar{V}_\mathfrak{z}$, respectively. A complete presentation of the results may be found in Reference 11.

As may be seen from the figures, increasing μ has the effect of reducing the relative amount of unsteadiness in the flow. At advance ratios of 0.1465 and above, the flow is primarily due to the interactions of the fuselage and the free stream.

The spacial variation of the flow displays a marked difference in character at $\mu = 0$ (Figure 12) from the variation at the non-zero advance ratios. The downwash rises sharply aft of about $x = -.8$ in the hovering case. The region of large downwash may readily be identified as lying within the wake envelope, which has contracted to about $\left[(.8)^2+(.3)^2\right]^{\frac{1}{2}} = .85$ of a rotor radius at $\mathfrak{z} = -.25$.

34
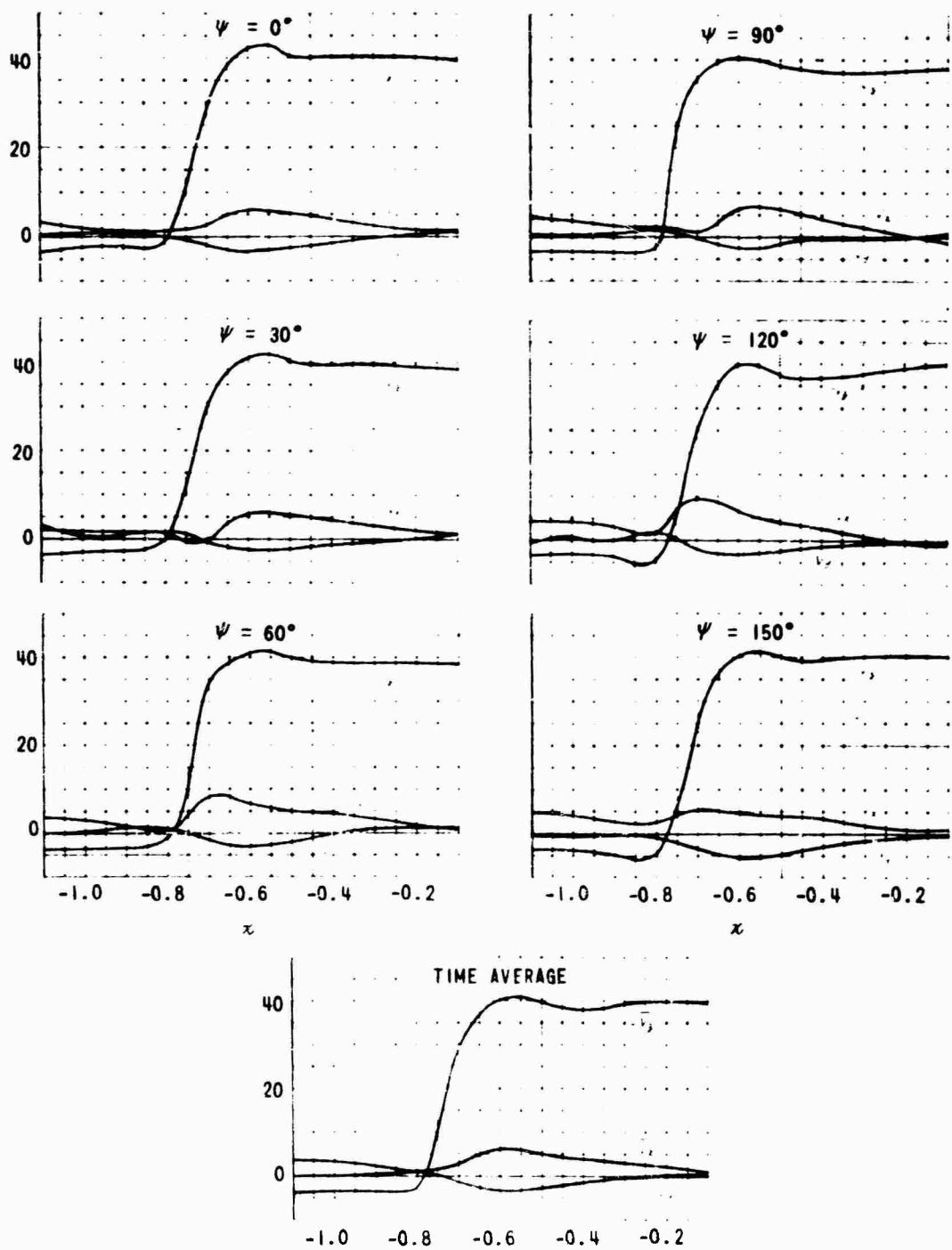
Figure 12 VARIATION OF VELOCITY COMPONENTS WITH x
FOR $y = 0.3$, $z = -0.25$ AND $\mu = 0$
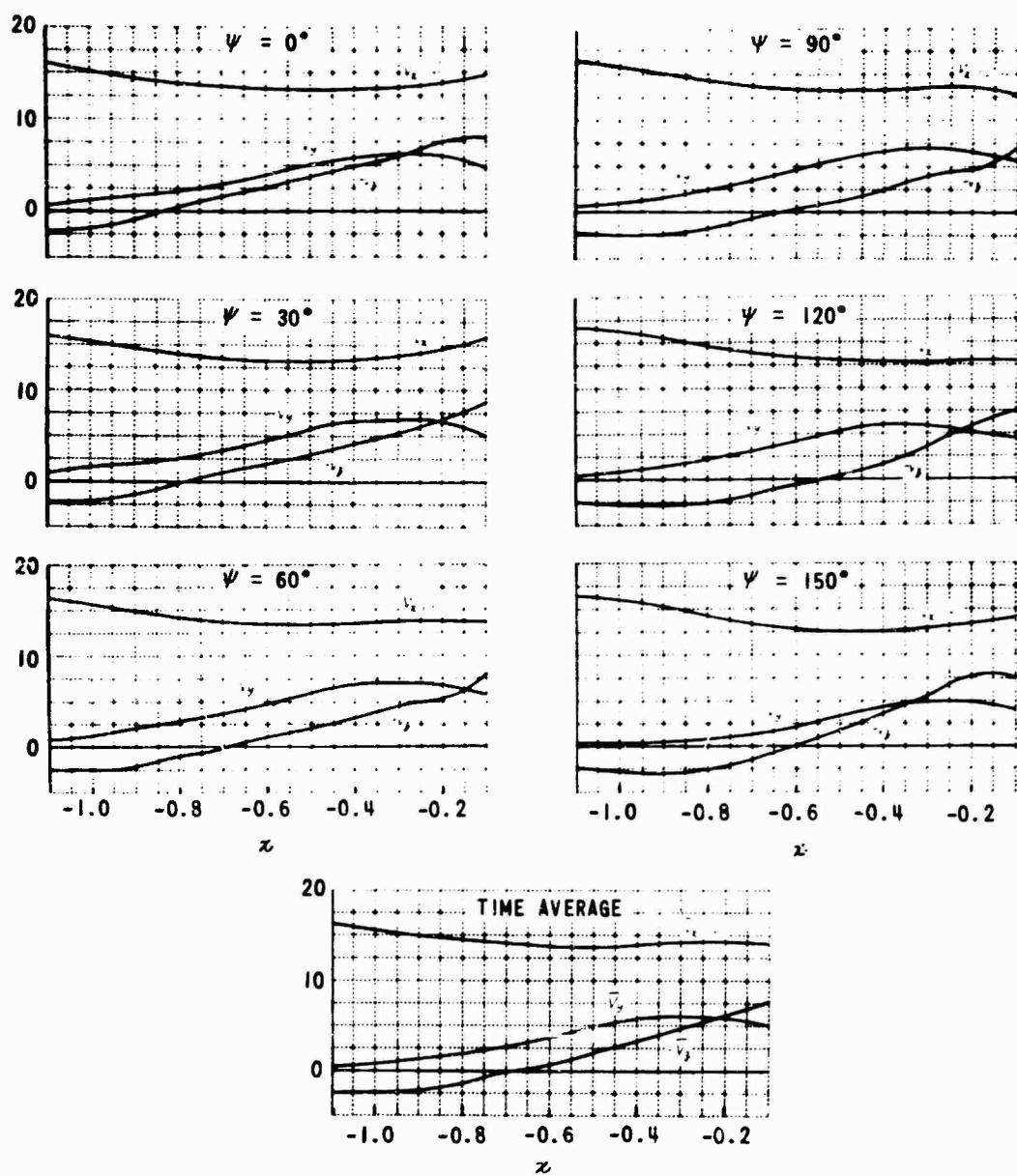
Figure 13 VARIATION OF VELOCITY COMPONENTS WITH x
FOR $y = 0.3$, $z = -0.25$ AND $\mu = 0.0732$
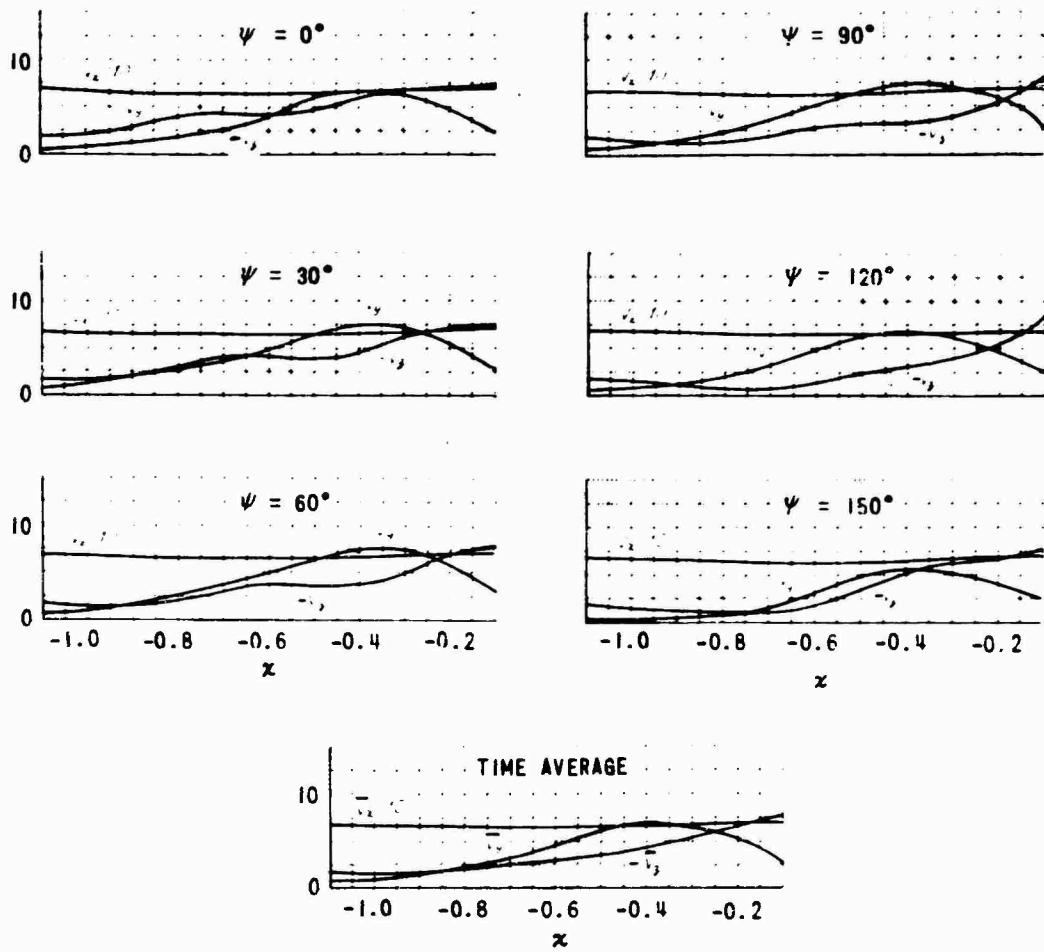
Figure 14 VARIATION OF VELOCITY COMPONENTS WITH x
FOR $y = 0.3$, $z = -0.25$ AND $\mu = 0.1465$

37
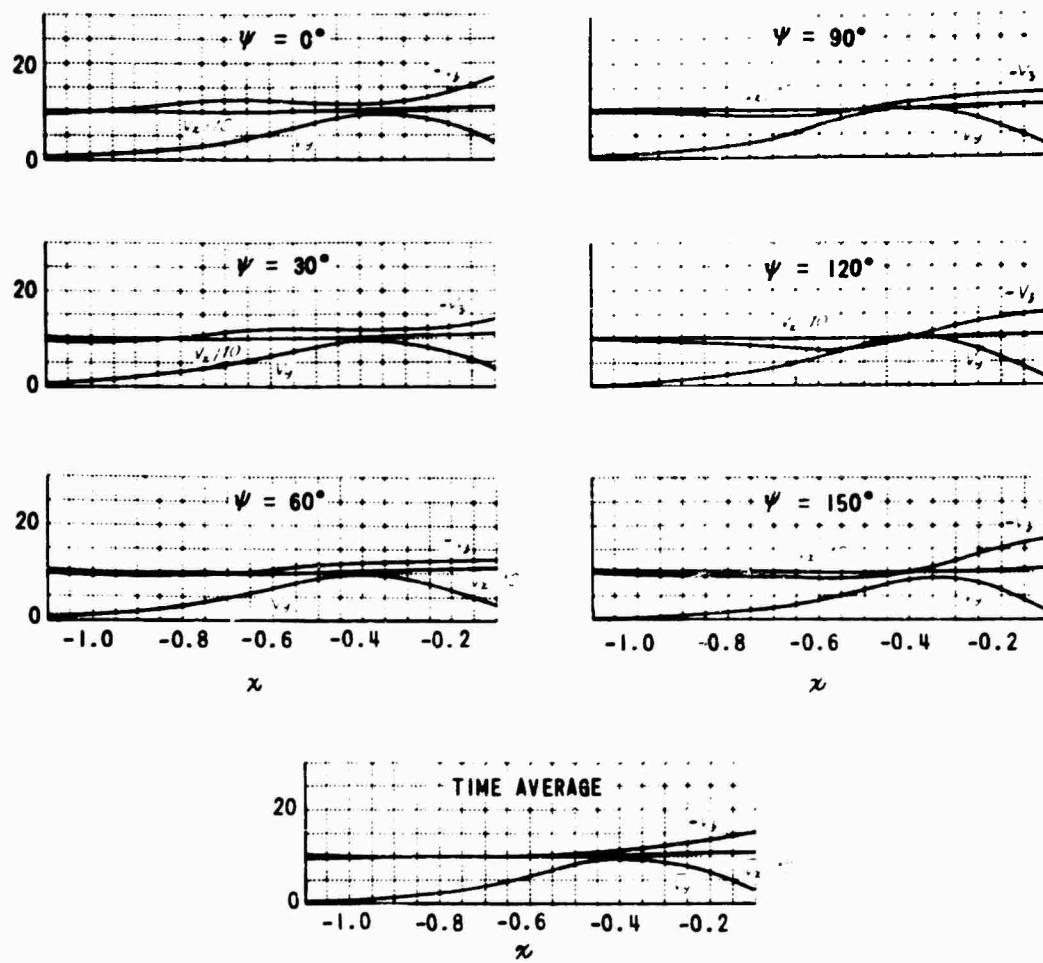
Figure 15 VARIATION OF VELOCITY COMPONENTS WITH x
FOR $y = 0.3$, $z = -0.25$ AND $\mu = 0.220$
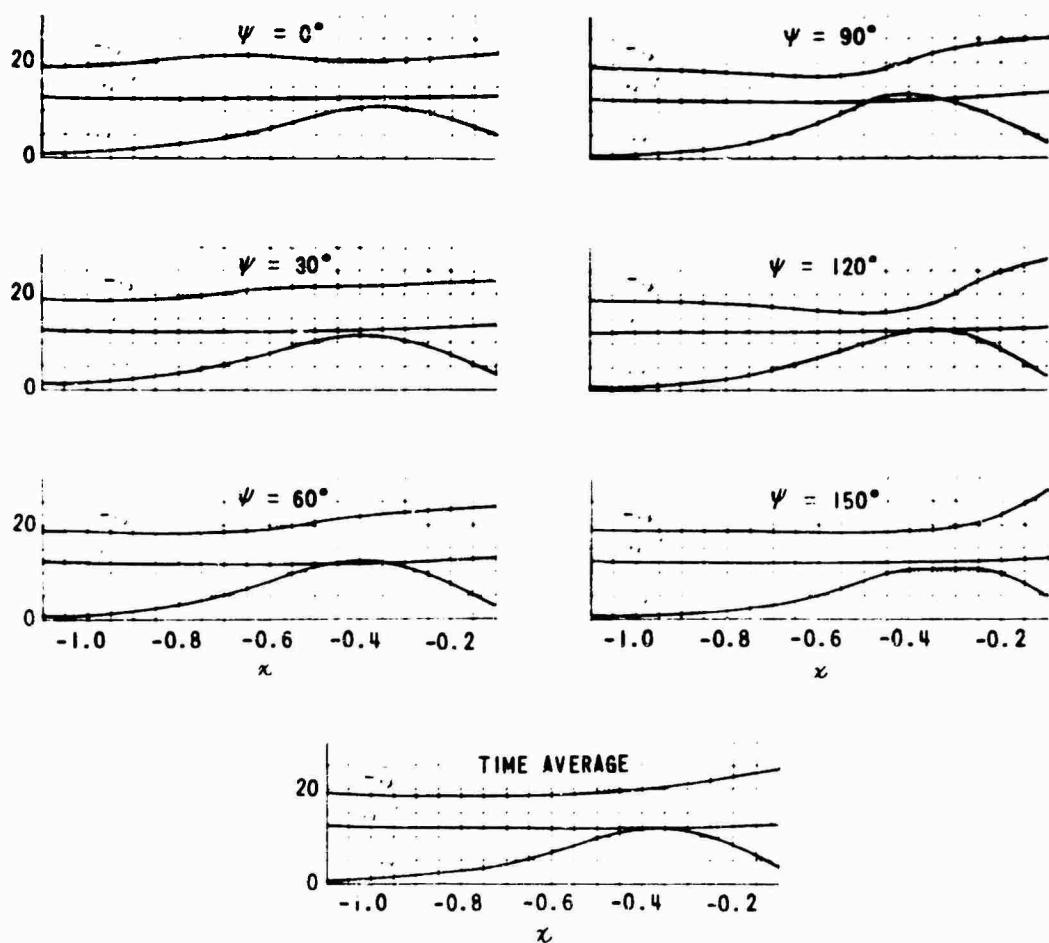
Figure 16 VARIATION OF VELOCITY COMPONENTS WITH x
FOR $y = 0.3$, $z = -0.25$ AND $\mu = 0.269$

39

POSSIBLE APPLICATIONS OF THE MODEL DEVELOPED

The model of a rotor wake which has been developed should have a number of applications in addition to flow calculations. For example, the effects of wake distortion on blade loading could be determined by modifying an existing blade-loads computer program, such as the one described in Reference 1, to accept arbitrary wake geometries. The locations of the wake elements at each azimuth position, as determined from the wake-flow program, would form the inputs needed to account for wake distortion.

Refinements of the fuselage representation would allow calculations of unsteady loads acting on the fuselage. Specifically, an exact numerical analogue of the flow could be constructed. That is, at each azimuth position of the blade vortices, the strengths of the fuselage source strengths could be recomputed so that the flow at each fuselage element is tangent to the surface; the fuselage boundary condition would then be satisfied exactly (within the limits of the digital analogue itself) both spacially and in time. Instantaneous pressures at arbitrary points on the fuselage could then be routinely calculated.

In a similar manner, unsteady interference effects on an auxiliary lifting surface could be determined by representing the surface as a distribution of bound vortices. The vortex strengths needed to satisfy the correct boundary conditions at each instant could be computed and pressures then evaluated.

40

REFERENCES

1. Piziali, R. A. and DuWaldt, F. A., "A Method for Computing Rotary Wing Airload Distribution in Forward Flight," Cornell Aeronautical Laboratory Report BB-1495-S-1, TCREC TR 62-44, November 1962.

2. Castles, W. and DeLeeuw, J., "The Normal Component of the Induced Velocity in the Vicinity of a Lifting Rotor and Some Examples of Its Application," NACA TR 1184, 1954.

3. Fradenburgh, E. A., "Flow Field Measurements for a Hovering Rotor Near the Ground," Paper presented at AHS 5th Annual Western Forum, Los Angeles, California, September 25-26, 1958.

4. Brady, W. G., and Crimi, P., "Representation of Propeller Wakes by Systems of Finite Core Vortices," Cornell Aeronautical Laboratory Report BB-1665-S-2, February 1965.

5. Hess, J., and Smith, A., "Calculations of Nonlifting Potential Flow About Arbitrary Three-Dimensional Bodies," J.Ship Research, Vol. 8, No. 2, September 1964.

6. Payne, P. R., Helicopter Dynamics and Aerodynamics, Mac-Millan, New York, 1959.

7. Burpo, F., and Lynn, R., "Measurement of Dynamic Air Loads on a Full-Scale Semirigid Rotor," TCREC TR 62-42, December, 1962.

8. McCloud, J., and Biggers, J., "Full-Scale Wind-Tunnel Tests
    of a Medium-Weight Utility Helicopter at Forward Speeds,"
    NASA TN D-1887, May 1963.

9. Lamb, H., Hydrodynamics, Sixth Edition, Dover, New York,
    1945.

10. Heyson, H., and Katzoff, S., "Induced Velocities Near a
    Lifting Rotor With Nonuniform Disk Loading," NACA TR 1319,
    1957.

11. Crimi, P., "Theoretical Prediction of the Flow in the Wake
    of a Helicopter Rotor, Part 1 - Development of Theory and
    Results of Computations," CAL Report No. BB-1994-S-1,
    September 1965.

NOTES

SUMMARY

The results of some flow visualisation experiments on the trailing vortices from a model rotor blade are presented. It is found that, at low tip-speed ratios, trailing vortices close to the leading edge of the disc first pass up through the disc before entering the main f   field. At the rear of the disc the vortices maintain a regular pattern relative to each other. The vortices are fully rolled up in about 60° of azimuth movement of the blade.

Measurements with a hot-wire anemometer show that the vortex core is about one-tenth of a blade chord in diameter, which is consistent with a laminar core state. Outside the core the velocity field is irrotational.

Some observations have been made of a trailing vortex as it approaches the support pylon. The vortex at first follows the pylon contours and remains a tightly-rolled core, but it ultimately leaves the pylon surface and its structure breaks down, rather like the vortices from the leading edges of a delta wing.

THE MOVEMENT, STRUCTURE AND BREAKDOWN

OF TRAILING VORTICES FROM A ROTOR BLADE

by

I.A. Simons, R.E. Pacifico, J.P. Jones

Department of Aeronautics & Astronautics,

Institute of Sound & Vibration Research,

University of Southampton,

England.

INTRODUCTION

The advances[1,2] which have taken place in the calculation of rotor blade loadings now indicate that our greatest lack of knowledge is of the geometry and dynamics of the near wake. We have clear evidence[3] that the tip vortices do not follow the skewed helix which the tips themselves trace out in space. In fact the distortion may be such that tip vortices and blades come close together, if not into actual contact, at certain azimuth positions. When this occurs, very marked changes take place in the true loading[1], and big differences between the results of experiment and of a theory which omits wake distortion are to be expected.

A further problem in the calculation of blade airloads is that the mathematical models used are themselves open to criticism because they

assume that the trailing vortex sheet rapidly rolls up into vortex filaments. At any appreciable distance (greater than a chords length, say) from a vortex this cannot be a significant objection, but for smaller distances it is obviously necessary to have a better idea of the induced flow field. Thus Simons[4] has shown that there can be large reductions in the predicted peak loadings on a blade if a Rankine, rather than a point, vortex is assumed. It also seems likely that the wake distortion itself will depend upon the vortex velocity field, particularly as much of the distortion originates at the points where vortex filaments pass over each other.

Our principal aim, therefore, was to obtain more data on the structure of the trailing vortex from a rotor blade. Unfortunately this is not very easy to do since carrying a probe around with the blade is likely to interfere with the flow and, on the evidence[5,6] available, the vortex is not fully rolled-up until at least one-half a blade radius from the tip. At that distance, of course, the wake distortion will certainly move the vortex and the problem then is to find it. Thus our first task was to locate the trailing vortices in space, in the hope that we might then be able to study their structure in some way, and our first experiments were exercises in vortex flow visualisation.

This, of course, has been done before by several people, but most extensively by M. Tararine[3]. Tararine in fact demonstrated the distortion caused, at the sides and the rear of the disc, by the mutual interference of successive trailing vortices. Sufficiently far downstream the trailing

2

vortices have all moved so that they lie, almost as a vortex sheet, in a
curved surface. Along the edges of the disc there is, at moderately low
tip-speed ratios, a large upwash which keeps the trailing vortices almost
in the plane of the disc. Numerical calculations of this type of
distortion have been described by White[7] and Scully[8]. But elementary
considerations suggest that there ought also to be, at low tip-speed ratios
at any rate, substantial wake distortion close to the leading edge of the
disc. Any trailing vortex from a blade creates an upwash outside itself;
therefore, as the vortices move aft relative to the disc, those at the front
create an upwash field which extends for some way over the disc until the
vortex filaments are too far below to have significant influence.

This sort of distortion was envisaged by Miller[9] and has been
demonstrated numerically by Scully[8]. Ham[10] made some measurements of the
instantaneous pressures on a blade in the $= 180^{\circ}$ position, and found very
sharp pressure peaks which would be consistent with the presence of a vortex
close to the blade. But the only direct evidence of its existence has been
given by Gray[11], who measured the vortex positions of a rotor in ground
effect by trailing smoke from a blade tip. Gray shows the paths of a tip
vortex for various values of tip-speed ratio and these clearly indicate that
the vortex remains above the plane of the disc for a short distance before
descending into the general downwash field. However, he gives no photo-
graphs for he was not directly interested in this phenomenon and he does in
fact report that the flow is very unsteady in certain circumstances.
Therefore, since this is a low tip-speed ratio phenomenon and our large wind

3

tunnel limits rotor experiments to these flight regimes, it was felt that to try to reveal this particular wake deformation would give an extra purpose to the flow visualisation programme.

The material presented in this paper falls into three parts. The first, which is summarised in a film, is concerned with the flow near the leading and trailing edges of a rotor disc. The second follows naturally, since the results for the flow at the rear of the disc made it comparatively easy to get some idea of trailing vortex structure simply by placing a hot-wire at the appropriate position in the flow. The third part, which deals with some aspects of vortex flow in the vicinity of a body, was not originally planned, but came as a pleasant surprise, particularly in view of the other interests of the University in vortex flows.

APPARATUS AND PROCEDURE

The experiments were carried out on a 9' diameter, two-hinged-blade model rotor of 4 inches chord in the 15' x 12' working section of the low-speed wind tunnel in the University of Southampton. A general view of the rig is shown in Fig. 1. The maximum tunnel speed in this section is such that with a reasonable rotational speed, tip-speed ratios greater than 0.25 cannot be achieved, but this was not too restrictive. The smoke generator was of a normal commercial type in which oil is allowed to come into contact with a heated plate and the resulting smoke is forced through a nozzle under pressure from a carbon dioxide storage bottle.

To reveal the effect of blade position or flow structure and vortex growth the following procedure was used. The region of flow under

4

examination was illuminated by a flash triggered by the shutter of a movie camera, and the rotor was arranged to turn at a speed such that the blade passage frequency was very slightly higher than the camera shutter speed. Thus the impression received by the film was of <u>one</u> blade advancing very slowly around the disc. For this technique to be convincing the blades must be properly in track, otherwise the image is apparently that of a single blade which is oscillating as it rotates. As always in flow visualisation the principle problem was to get sufficient light into the right place and then to find a convenient spot for the camera. Broadly speaking the illumination of the smoke has to be perpendicular to the viewing plane. Thus in the film sequences and still shots to be described the smoke, camera and light-source were all placed with the primary aim of getting good pictures.

The hot-wire anemometer which was used to study the vortex velocity field was kindly loaned to us by Dr. P.O.A.L. Davies. It is of the standard constant current variety with a wire about $\frac{1}{8}$ inch long and 5 microns in diameter supported between 30 s.w.g. prongs. A feature of the equipment is that the wire output is linearised before presentation so that a direct reading of velocity is possible.

RESULTS

Rotor Flow Visualisation

The results obtained are presented as a movie at the end of the lecture, but is worthwhile to consider a few features which are best brought out by stills.

5

Fig. 2 shows a sequence for a case where the tip-speed ratio is 0.04, the collective pitch is 8° and the shaft axis is tilted forward at an angle of 8°. Smoke is injected in a narrow vertical region at an azimuth angle of 180°. In the first frame of Fig. 2 the blade is about 45° from the smoke, but has not yet passed through it. In the final frame the blade is about 30° of azimuth beyond the smoke. Thus the first visible vortex in the first frame is trailing from the blade which passed through the smoke somewhat less than one-half a revolution earlier. The second clear vortex, i.e. closest to the pylon, is the trailing vortex from the blade which is again approaching the smoke.

Several points are worthy of note. First of all there is a very strong upwash ahead of the disc in this flight condition. Secondly while two of the vortices have a very clear cut "eye", the smoke in the remaining (earlier) turns is diffused. Finally, when the blade is in the vicinity of the plane of the smoke, the trailing vortex from the preceding blade is above the plane of the disc, whilst the trailing vortex from the blade in the picture is below the disc. In these pictures the camera is slightly below the disc plane at $\psi = 180^{\circ}$. However, still pictures taken in the plane, definitely show the vortex to be above the blade. Thus the trajectory of the cross-section of a vortex at $\psi = 180^{\circ}$ is an arc at first directed upwards and then downwards, much in the same manner as calculated by Ham[10]. The vortex is above the disc plane for a time which is about that required for one-half a revolution of the rotor. This is in agreement with Gray's results[11]. Another point of agreement with Gray is shown in the difficulty

6

which is experienced in obtaining a clear "eye" for more than a very few turns of the wake. This phenomenon is discussed in greater detail below (Sec. 4). The sequence of frames when the blade has passed through the smoke allows us to form some idea of the time required for a trailing vortex sheet to fully roll up. It is clear from the last frame that rolling-up is not quite complete but the process does seem to have stopped in the first frame when the blade has turned about another quarter of a revolution. We may conclude, therefore, that the rolling-up process is complete in about the time taken to travel one blade radius. In terms of the blade chord, this is in general agreement with the distances which have been found for the completion of the rolling-up process behind straight wings[5,6].

The same kind of arguments which predict the distortion at the front of the disc indicate that at the rear the vortices should maintain their distances and distribution. This is confirmed in Fig. 3 which shows the cross-sections through the trailing vortex system in the vertical plane $\psi = 0^\circ$. As would be expected, these cross-sections are spaced farther apart than the corresponding cross-sections at the leading edge of the disc and, generally speaking, the central "eye" is more persistent. The arrangement of vortices at the trailing edge of the disc is so regular that the results for only one case are indicated in the film. A diagram of the relative vortex core positions at the front and rear of the disc, for a range of tip-speed ratios, is given in Fig. 4. It is clear, from a comparison of the positions of corresponding cross-sections, that considerable vertical distortion is taking place, but the investigations do not show whether a vortex may actually come into contact with a blade. From the photographs it seems obvious that

7

this must happen but it is, of course, possible for the vortices to distort laterally, so that they cross the disc plane outside the disc. Some indication that this may occur has been given by Scully[8]. Also the exact time spent above the disc is a crucial factor, but the results certainly suggest that blades and vortices must pass very close.

In a flight condition corresponding closely to that of Figs. 2 and 3, Gray[11] observed a large vertical oscillation of the vortex at the leading of the disc. No such oscillation was present in our tests. To convey some idea of the general steadiness of the flow it should perhaps be stressed that these pictures are not the outcome of high-speed photography, but are essentially a succession of stills taken very slightly more than one-half a revolution apart.

The Velocity Field of a Vortex

The very regular nature of the flow at the trailing edge of the disc offers a convenient method of measuring the structure of, and distribution of velocity around, a vortex. If a hot-wire anemometer can be placed along the line of travel of the eyes of the vortices, then a characteristic signature will be produced each time a vortex passes over the wire. Provided that the mean convection speed is small compared with induced velocity, the anemometer output should be a very good indication of the distribution of velocity within a vortex. Also, by placing the hot-wire at different points on the wake spirals, it is possible to get some idea of the development and growth of a vortex with time.

The hot wire was placed, in the plane $\psi = 0^o$, with its length

8

parallel to the vortex axis, so that it was most sensitive to velocities in
the plane of the induced velocity field. Coarse adjustments to the position
were made by eye, using smoke as a guide to the line of convection. Very
fine adjustments to the position of the wire relative to the vortices were
made by making very small changes to the tunnel speed.

Typical records of the anemometer output are shown in Figs. 5, 6.
These are for a vortex which is somewhat less than one revolution old.
Because a hot-wire is a rectifier its output is always positive whatever the
magnitude and direction of the velocity. Thus if the centre of a vortex
passes over the wire, the indicated velocity rises, from the mean value, to
a maximum and then falls very rapidly back to the mean value, only to rise
again to the peak followed by a reduction back to the mean value. The
occurrence of a steep-sided trough in the record is a good indication that
the centre of the vortex is actually passing over the wire.

The records show that for a mean convection speed of about 12 ft./
sec. the peak velocity is about 45 ft./sec. They also show the existence of
a core of finite dimensions. The precise dimensions of this core were not
easily determined, partly because of its small size, and partly because the
flow within the core appears to be unsteady. In addition there were some
very small, comparatively long period, fluctuations in the paths of the
vortices, so that only a small fraction of the total number of traces could
be used for analysis. (This particular unsteadiness is attributed to the
influence of the wake of the pylon). Nevertheless it was possible to obtain
sufficient data to get an approximate idea of the vortex size and the results

9

are summed up in Fig. 7. For the limited number of tests done no effect of wake age or blade Reynolds number was detectable within the overall scatter. The average vortex core diameter is slightly less than 10% of the blade chord and a comparison between the rate of growth with . and Lamb's[12] theoretical solution for the decay of a viscous point vortex suggests that the core is laminar. There is thus some conflict of experimental evidence, for the hot-wire anemometer records clearly show the existence of high frequency fluctuations within the core. But some guide to what is really happening may be contained in the traces themselves.

In Fig. 6 the vortices are moving from left to right relative to the wire, and it will be observed that generally the leading edge of the core trace is much smoother than the trailing edge. This suggest that the recorded turbulence may be due to the interference of the probe itself with the flow within the core.

These results have implications for both theory and for model testing. For if the cores of full-size vortices are really of the same proportions, then, in calculation, it should be sufficient to represent them by point vortices. But if the cores of full-size trailing vortices are really turbulent, rather than laminar, then the effective kinematic viscosity within them could easily be fifty times greater, and the core diameter would then be of the order of a blade chord. There is some evidence from Spreiter and Sacks[6] that vortices may indeed be of these dimensions. We must also conclude that higher harmonic loadings measured in model tests may not be fully representative of full-scale, unless steps are taken to ensure that the

10

vortex cores are turbulent and remain so.

Outside the core our measurements indicate that the flow is virtually irrotational. Superimposed upon the record in Fig. 5 is a curve representing the induced velocity field due to a pair of point vortices situated at the core centres, and chosen in strength so as to give the correct induced velocity at a small distance from the centre. The fit is very good. Thus the classical Rankine vortex, consisting of a "solid" core embedded in an irrotational flow, is a suitable model for blade tip vortices.

THE BREAKDOWN OF TRAILING VORTICES

The above account represents the limit of what it was possible to plan on the basis of some preliminary flow visualisation experiments. The results have an intrinsic interest for they do give confidence in certain applications of theory but, as always, they pose more questions than they answer. It is hoped to be able to provide more answers at another time and suitable experiments are now being planned.

In the course of our investigations another phenomenon was revealed, and we would like to devote some time to this because it may be important to V/STOL design, and because it has a wider application in fluid mechanics.

The vortices in Figs. 8, 9, 10 were revealed by emitting smoke from a fixed nozzle, with the rotor and the tunnel fan turning at low speed. Under these conditions some of the smoke is trapped in the boundary layer of the blade and is carried round with it. As the blade moves away from the injection point the trapped smoke passes into the trailing vortex. Since its velocity is very small most of the smoke enters the core and very clear

11

flow patterns are obtained until the supply of smoke is exhausted. A disadvantage of this technique is that the smoke trail is non-uniform. Close to the injection point there is an excess of smoke and the picture is consequently diffuse. This excess does, however, disperse rapidly. Typical examples are given in Fig. 8 which shows trailing vortices leaving the blade tips and advancing towards the pylon.

The subsequent behaviour is best revealed by a camera mounted on the foot of the pylon. As the vortex approaches the pylon it deforms, since that part closest to the leading edge is slowed down. The limit of this deformation is shown in the third plate of Fig. 9 when the vortex appears to be wrapped around the nose of the pylon. There is in fact some accompanying distortion in a vertical direction so that the vortex core also runs down the nose of the pylon. A little while later the clear cut core has begun to break up, as plate (iv) shows, from both ends. The flow in the pylon boundary layer becomes more diffuse, but the core itself begins to spiral in a helix, whose pitch is of the order of a core diameter, plate (vi). As the vortex moves across the pylon this spiralling, or "unwinding", of the vortex propagates outwards towards a similar spiral which is moving inwards from the edge of the vortex. Thus, within a very short distance, the vortex structure has changed from a tightly-rolled core to a diffuse, swirling flow. Some further idea of the changes which have been brought about is given by Figs. 10, 11. Fig. 10 shows a cross-section of the moving vortex- obtained by illuminating a darkened tunnel with only a slit of light - as it passes the pylon. The white line is simply a marker showing the pylon leading edge.

12

The first cross-section is almost circular, and a definite, but more diffuse, core can still be observed in the third cross-section, but the next picture shows the structure to have become without form. Fig. 11 shows how the velocity, measured with a hot-wire anemometer, varies in a vortex core just ahead of the pylon and within a vortex which has broken down. Although the second trace shows the existence of a periodic disturbance, no clear structure is evident.

This phenomenon is reminiscent of the breakdown which occurs in the leading edge vortices formed above narrow delta wings. Fig. 12, which is due to Krishnamoorthy[13], shows how this breakdown develops, on a very slowly oscillating wing from a spiral whose pitch is of the order of a core diameter, into a diffuse turbulent "bubble". The exact mechanism of the breakdown has not yet been properly established although a number of theories have been suggested. But it is known that when a vortex breaks down there is a sharp rise in the intensity of the pressure fluctuations on the surface beneath the breakdown. Thus if, as seems likely from these tests, breakdown occurs when a trailing vortex passes over a fuselage, there could be high noise and vibration levels within the fuselage. Another point of interest to helicopter designers is that a vortex which has broken down in this way will not have a very peaky induced velocity field. Therefore, it might be expected that the interference with following blades, e.g. in a tandem rotor, will be much reduced.

A further possibility is that trailing vortices can break down without necessarily coming into contact with a solid body. This is certainly

13

true of leading edge vortices, although the presence of an obstacle does tend to precipitate breakdown[14]. In this connection it is interesting to note that Gray[11] also observed a sudden change in core structure, with the disturbance propagating away from the leading edge of the disc in both directions along the vortex filament. Gray explains that this is the reason why a clear-cut structure is not visible beyond the third turn.

Therefore, since we have observed the same difficulty at the leading edge of the disc, it is likely that vortex breakdown occurs somewhere along the vortex. But it is not easy to argue that this breakdown is spontaneous, since the clear-cut structure does persist at the rear of the disc. It is necessary, therefore, to postulate some interference with a vortex which has broken down, and this could very well be due, at the front but not at the rear, to a blade passing through, or very close to, a vortex. Some support for this is contained in Fig. 9, for there is evidence to suggest that the breakdown propagating inwards towards the pylon originated at about 270° azimuth. In this region the wake distortion sweeps the vortices up and flow visualisation shows that they lie very close to the blade tips.

CONCLUSIONS. FURTHER DEVELOPMENTS

Visualisation of the flow through a model rotor by means of smoke has shown that, at low tip-speed ratios, the trailing vortices at the leading edge of the disc first pass up through the rotor, and then move down with the general downwash field. At the rear of the disc, the vortices move faster than the mean downwash but maintain their relative positions approximately on a straight line. There is, therefore, considerable vertical distortion of the first few turns of the helical wake in a fore-and-aft plane. The

14

trailing vortices can be regarded as fully rolled-up by the time the blade tip has travelled about one blade radius.

It is our intention to extend this work to rotors with more blades and to examine different azimuth stations. It is also hoped that the technique can be developed to deal with tandem rotors.

Measurements, on a model scale, with a hot-wire anemometer have shown that the vortex core is less than about one tenth of a blade chord in diameter, and that the flow field outside the core is essentially irrotational. If this result carries over to full-scale, then the concept of vortex filaments should be quite adequate for use in mathematical models for blade loading calculations. This conclusion will, however, have to be checked further, since the vortex core size indicates that the flow within it is laminar. The next hot-wire anemometer measurements will, therefore, be made with the blade tip regions roughened to try to establish turbulent flow. It is thought that this may lead to substantial increases in the core size.

Finally, it has been shown that a trailing vortex undergoes a complete change in structure after only part of it has been in contact with a solid body. The reason for this is not known, although there are strong similarities with the vortex breakdown phenomenon.

In general we conclude that much more needs to be done to establish the validity, or range of application to full-scale, of model rotor tests. This is particularly true of the boundary layer state and, although it is not immediately obvious from the presentation, there have been indications of appreciable tunnel wall effects. But tests on a rotor may have something

15

tc offer to the general field of fluid dynamics research. Hot-wire measure-
ments made at various points in the trailing vortex of a blade provide a
convenient way, than measurements behind a fixed wing, of examining the
development of a vortex with time. It may also be possible to carry out
more easily controlled investigations into vortex breakdown.

References.

1. R.A. PIZIALI   Method for Solution of the Aeroelastic Response
Problem for Rotating Wings.
Proceedings of the Symposium on the Noise and
Loading Actions on Helicopters, V/STOL Aircraft
and Ground Effect Machines.
University of Southampton, England. Sept. 1965.

2. R.H. MILLER   Rotor Blade Harmonic Airloading.
A.I.A.A. Journal Vol. 2. No. 7. July, 1964,
pp. 1254-1269.

3. S. TARARINE   Experimental and Theoretical Study of Local
Induced Velocities Over a Rotor Disc.
Proceedings CAL/TRECOM Symposium on Dynamic
Loads Problems Associated with Helicopters and
V/STOL Aircraft. Vol. 1. June, 1963.

4. I.A. SIMONS   Blade/Vortex Interaction on Helicopter Rotors in
Forward Flight.
University of Southampton I.S.A.V. 127 Jly '65
To be published in the Journal of Sound &
Vibration.

5. N.A.V. PIERCY   Aerodynamics. English Universities Press 2nd
Edition 1947.

6. J.R. SPREITER   The Rolling-up of the Trailing Vortex Sheet and
   A.H. SACKS   its Effect on the Downwash Behind Wings.
J.Ae.Sci. 18, 1, 21-32. 1951.

7. R.P. WHITE Jnr.   VTOL Periodic Aerodynamic Loadings.
Proceedings of the Symposium on the Noise and
Loading Actions on Helicopters, V/STOL Aircraft
and Ground Effect Machines.
University of Southampton, England. Sept. 1965.

8. M. SCULLY   M.I.T. Bachelors Thesis 1964.
Paper presented at the Symposium on the Noise
and Loading Actions on Helicopters, V/STOL
Aircraft and Ground Effect Machines.
University of Southampton, England. Sept. 1965.

9. R.H. MILLER   Unsteady Air Loads on Helicopter Rotor Blades.
Fourth Cierva Memorial Lecture to the Royal
Aeronautical Society, October, 1963. Journal
R.Ae.Soc. 68, 640, April, 1964 pp. 217-229.

17

10. N.D. HAM

An Experimental Investigation of the Effect of a
Non-Rigid Wake on Rotor Blade Airloads in
Transition Flight.
Proceedings CAL/TRECOM Symposium on Dynamics
Loads Problems Associated with Helicopters and
V/STOL Aircraft. Vol. 1. June, 1963.

11. R.B. GRAY

Experimental Smoke and Electromagnetic Analog
Study of Induced Flow Field about a Model Rotor
in Steady Flight within Ground Effect.
N.A.S.A. Tech. Note D-458 August, 1960.

12. H. LAMB

Hydrodynamics. Cambridge University Press
1932. 6th Edition.

13. V. KRISHNAMOORTHY

Vortex Breakdown and Measurements of Pressure
Fluctuations over Slender Wings.
Southampton University Ph.D thesis 1966.

14. B.J. ELLE

An Investigation of low speed of the flow near
the apex of thin delta wings with sharp leading
edges. A.R.C. R. & M. 3176. 1958.

FIG. 1.   General view of rig.

19

FIG. 2. Movement & Growth of Vortices at leading edge of disc. Rotor speed 240 r.p.m. Collective pitch 8°. Shaft inclination 9°. Tip-speed ratio 0.04.

20

FIG. 2 contd. Movement & Growth of Vortices at leading edge of disc.

21
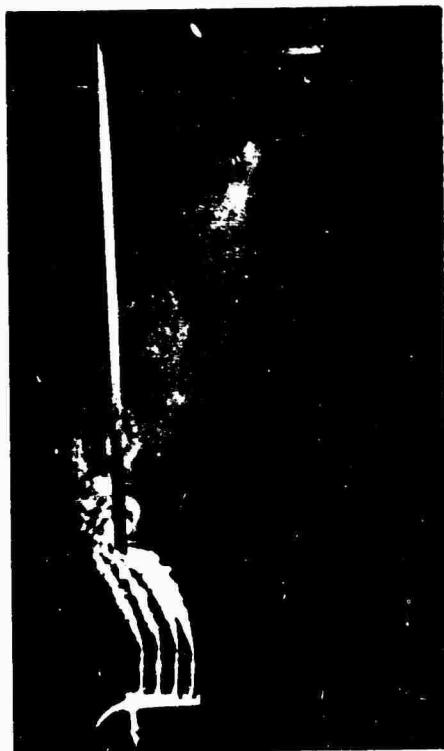
FIG. 3. Movement & Growth of Vortices at rear of disc. Rotor r.p.m. 240. Collective pitch 8°. Shaft inclination 8°. Tip-speed ratio 0.04
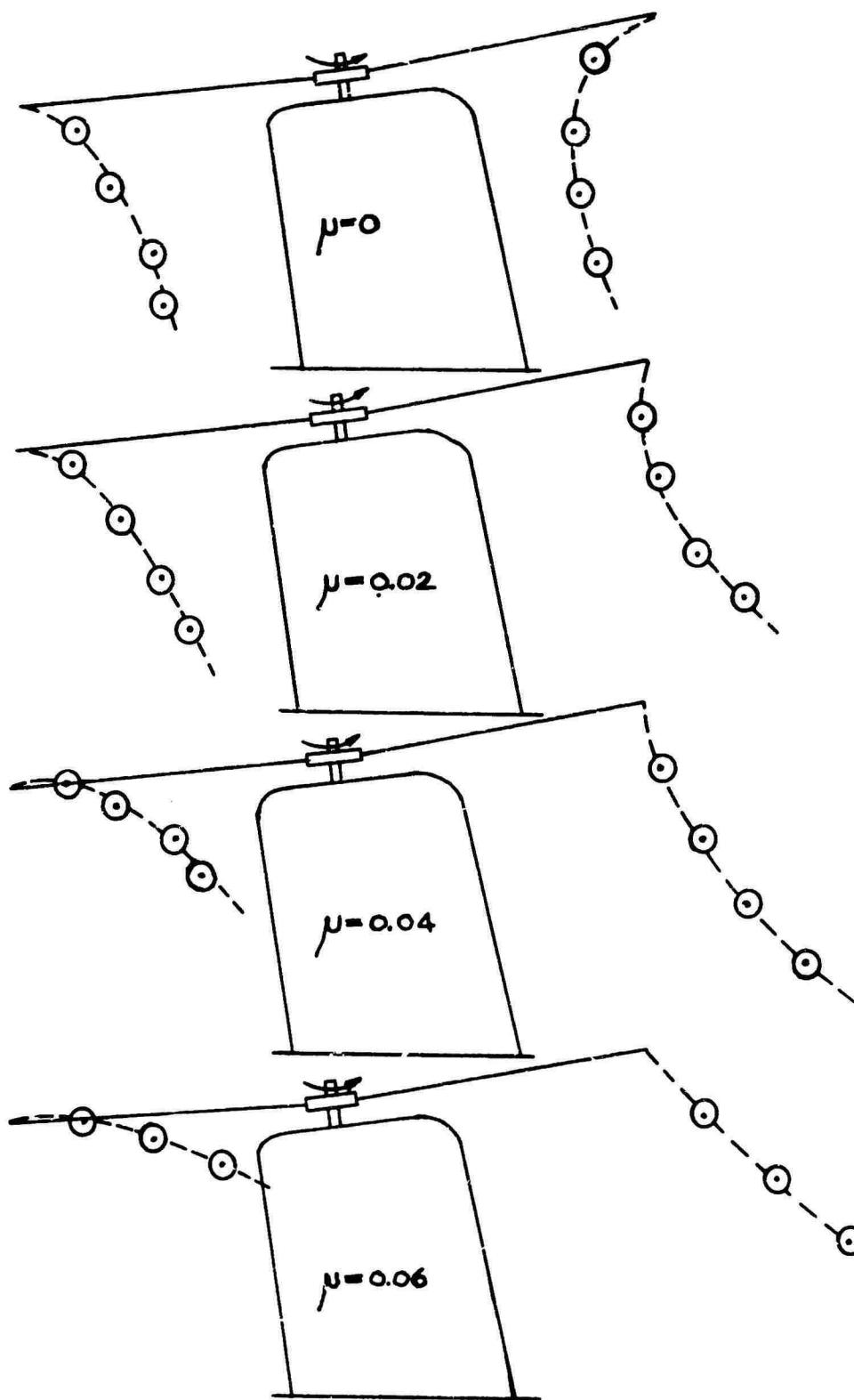
FIG. 4. Vortex paths in the fore-and-aft plane. Rotor speed 240 r.p.m. Collective pitch 8°. Shaft inclination 8°. Note: Ground plane is 6 ft. below rotor hub, and is not shown on the diagram.

23

35 FT/SEC.

30

25

20

15

10

5

0

MEASURED VELOCITY DISTRIBUTION

THEORETICAL POTENTIAL FLOW SOLUTION

$$V = \sqrt{\left(\frac{k}{2\pi r}\right)^2 + V_m^2}$$

VELOCITY OF CONVECTION OF VORTICES — V_m.

TIMING MARKERS AT 0.01 SECOND INTERVALS.
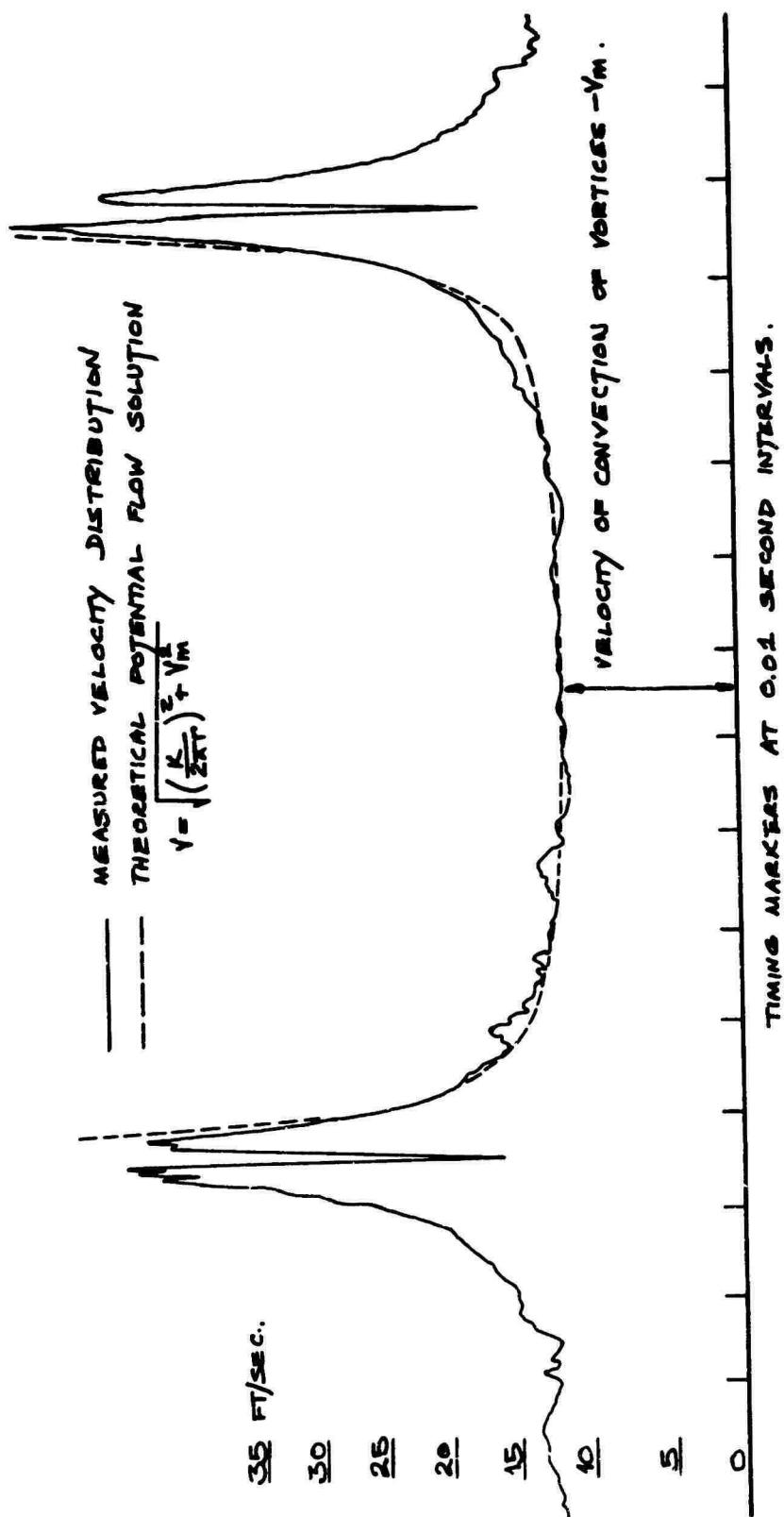
FIG. 5. Hot-wire anemometer record. Wake age ± 300° of azimuth. Rotor speed 300 r.p.m. Collective pitch 8°. Shaft inclination 8°. Tip-speed ratio 0.04. Note: The vortices are moving from left to right relative to the hot-wire probe.

24
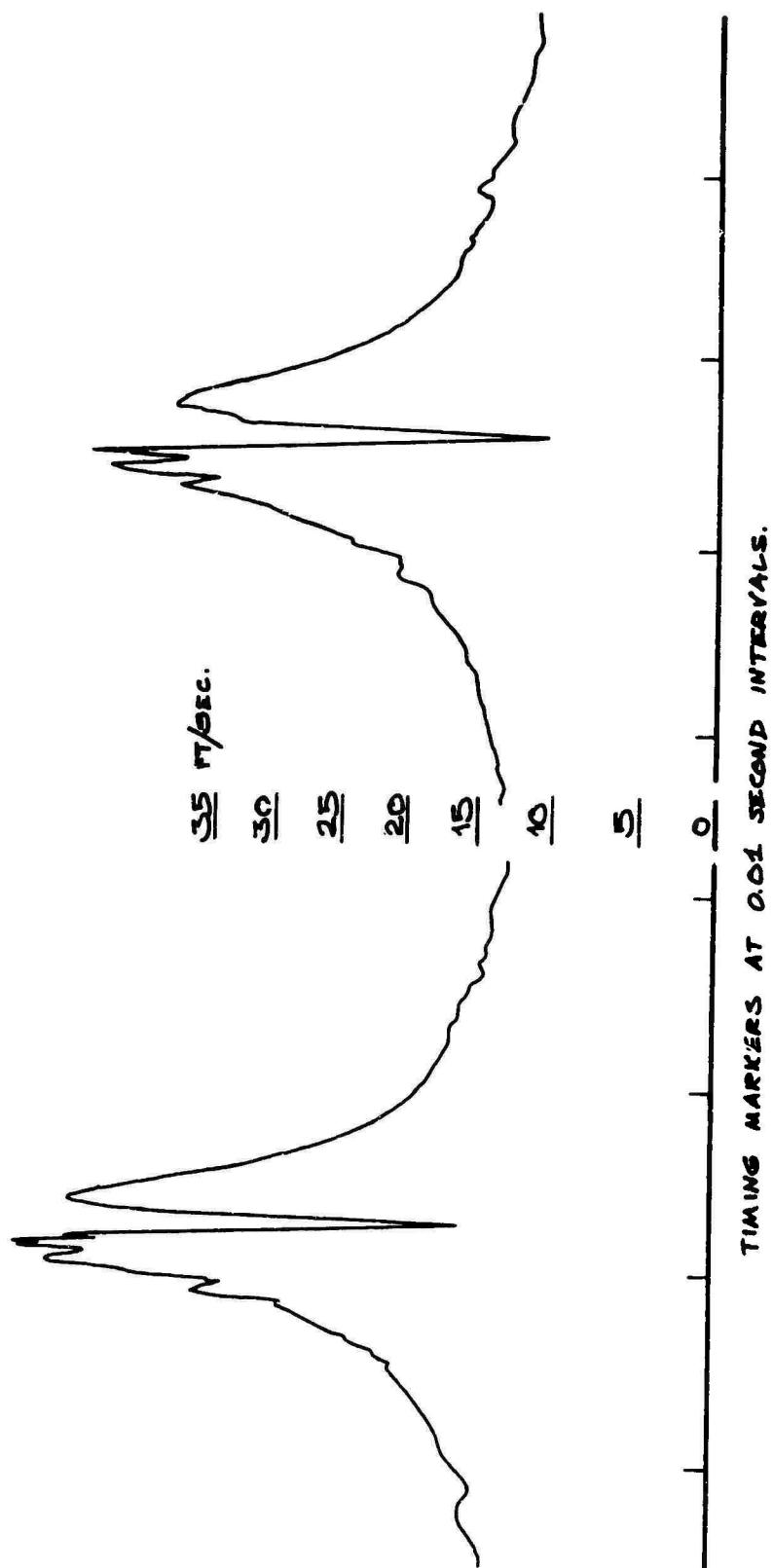
FIG. 6. Sample records from hot-wire anemometer. Wake age ± 300° of azimuth. Rotor conditions as for Fig. 5.
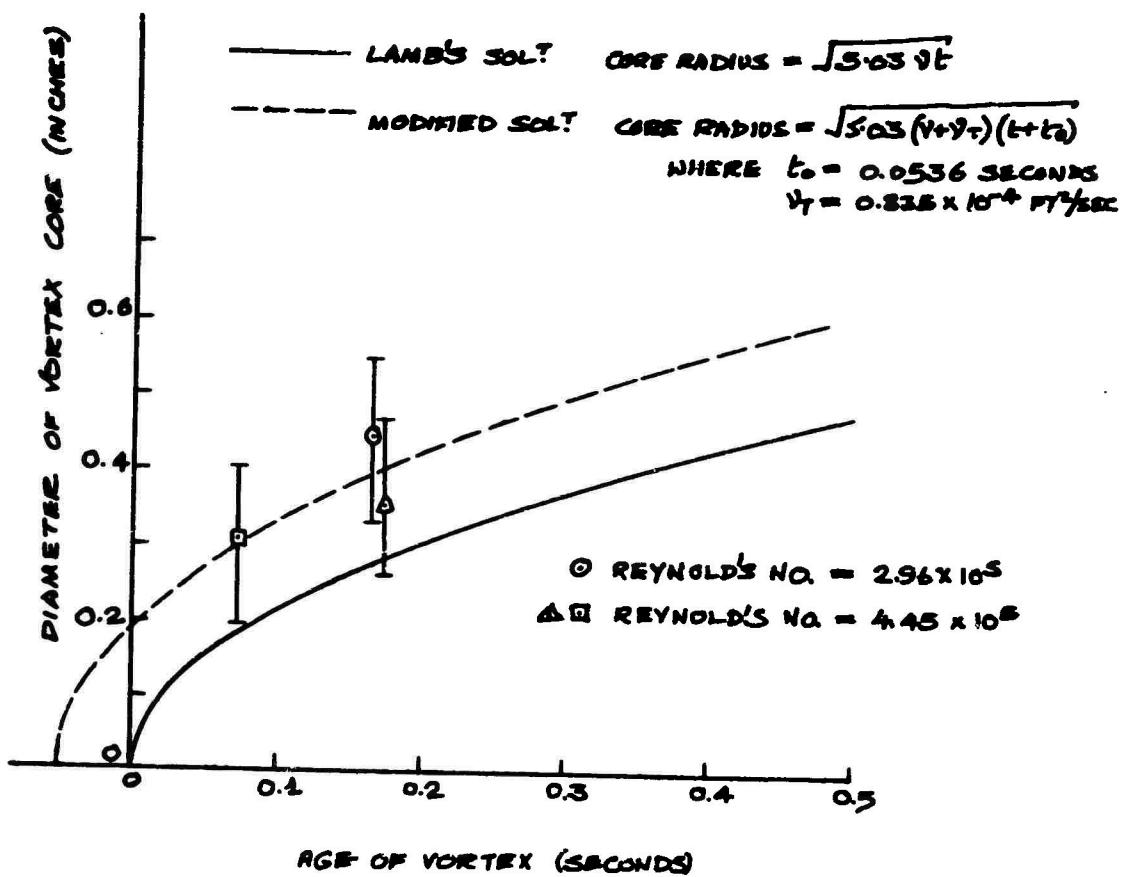
FIG. 7. A comparison of core size with theoretical prediction.

FIG. 8. Movement of Trailing Vortices towards the pylon.
Rotor speed 60 r.p.m. Wind speed 2.75 ft./sec.
Collective pitch 8°. Shaft inclination 8°.
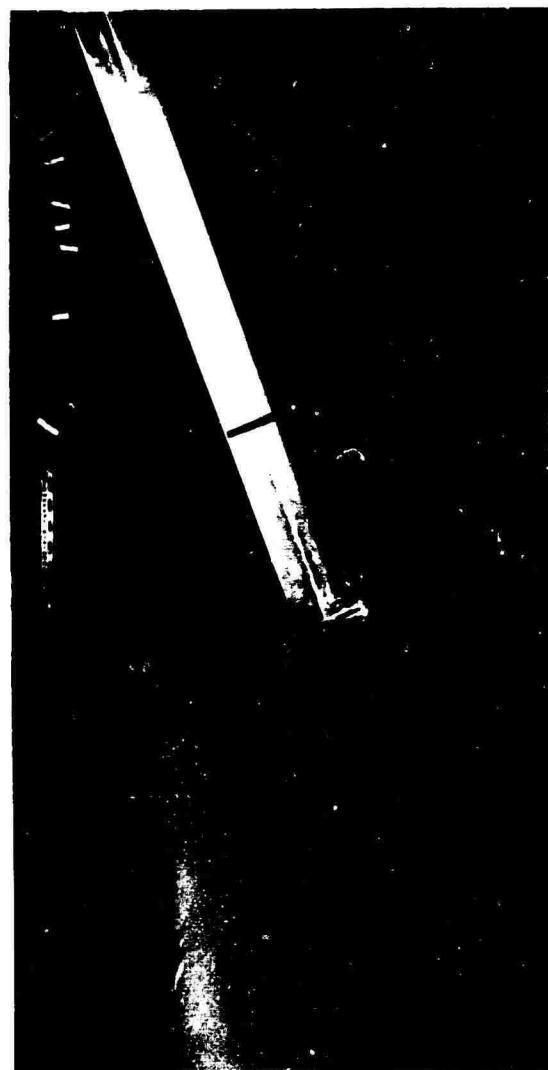
FIG. 9. Vortex/pylon interference. Rotor conditions as tor Fig. 8.
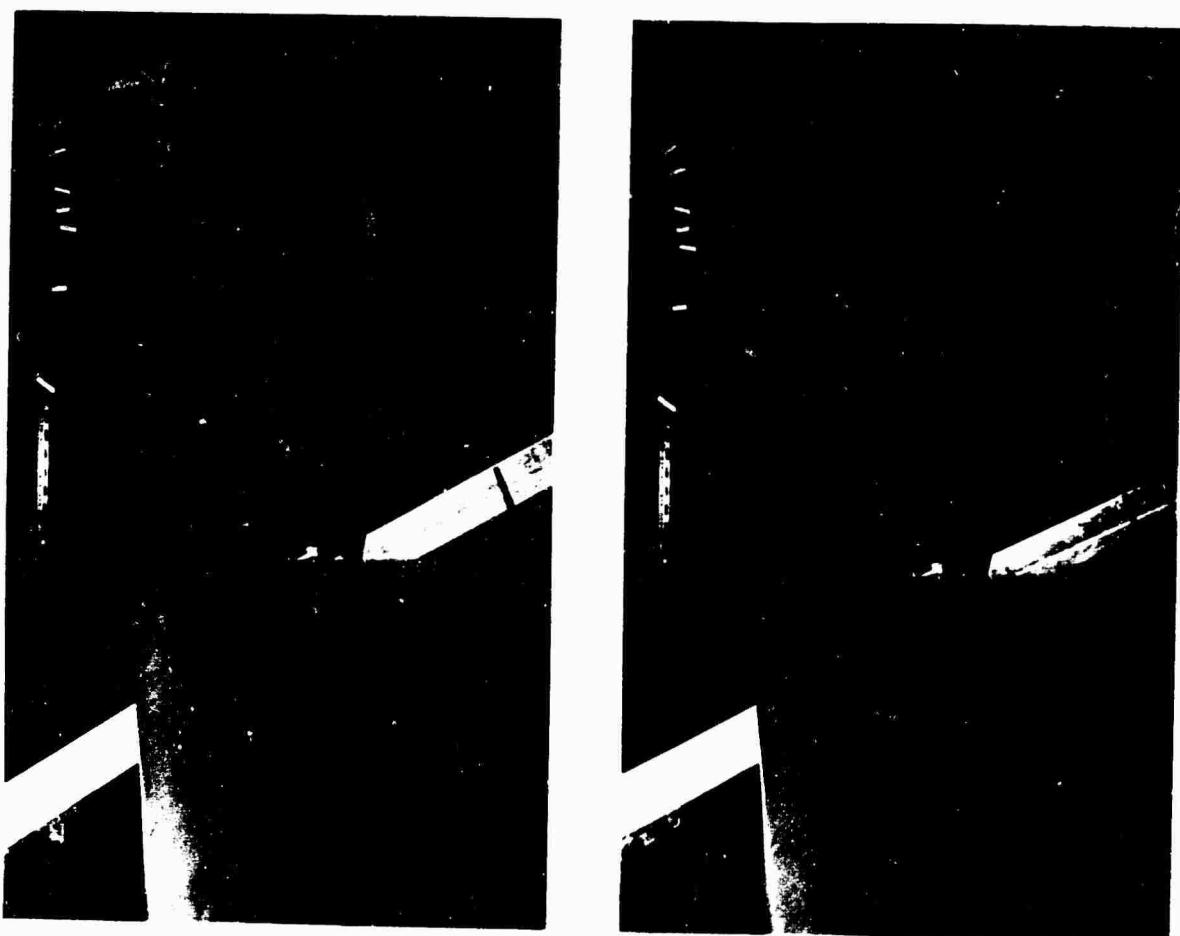
FIG. 9. contd. Vortex/pylon interference.

FIG. 9. contd. Vortex/pylon interference.

30

FIG. 9. contd. Vortex/pylon interference.

31
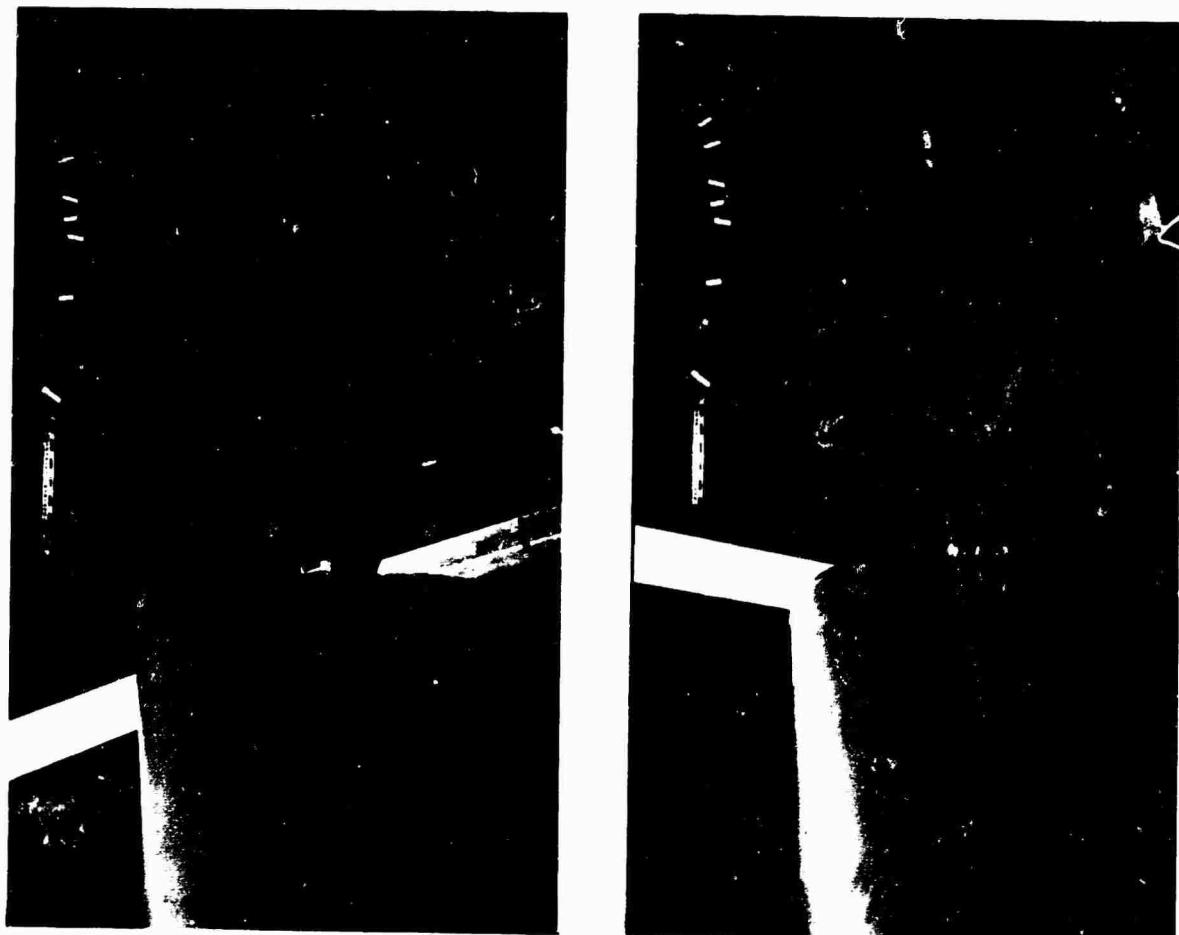
FIG. 10. Cross-section of vortex in vicinity of pylon. Conditions as for Fig. 8.
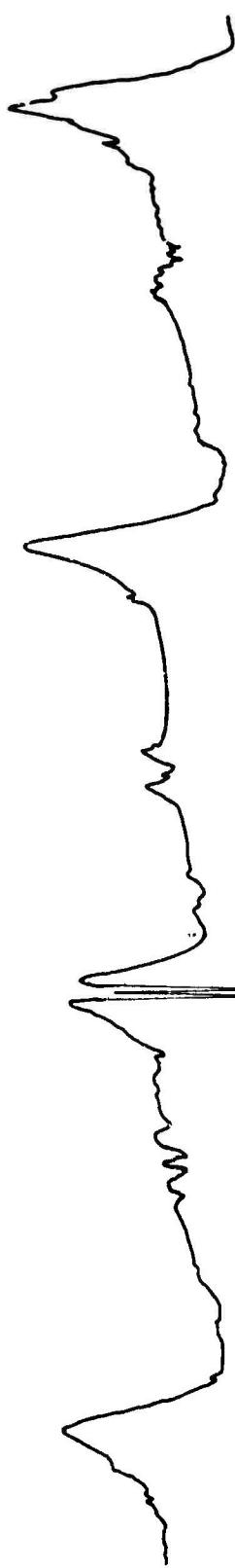
'UNBROKEN' VORTEX ABOUT 12" IN FRONT OF PYLON NOSE.

TIMING MARKERS AT 0.1 SECOND INTERVALS.
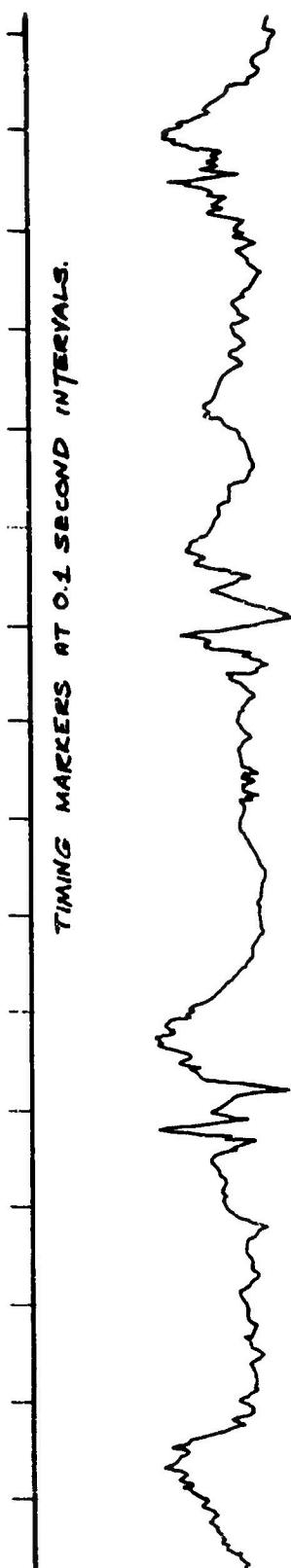
'BROKEN DOWN' VORTEX ABOUT 30" BEHIND PYLON NOSE.
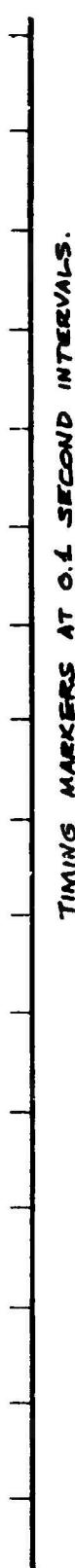
TIMING MARKERS AT 0.1 SECOND INTERVALS.

FIG. 11. Hot-wire Anemometer records in the vortex close to the pylon. Conditions as for Fig. 8.
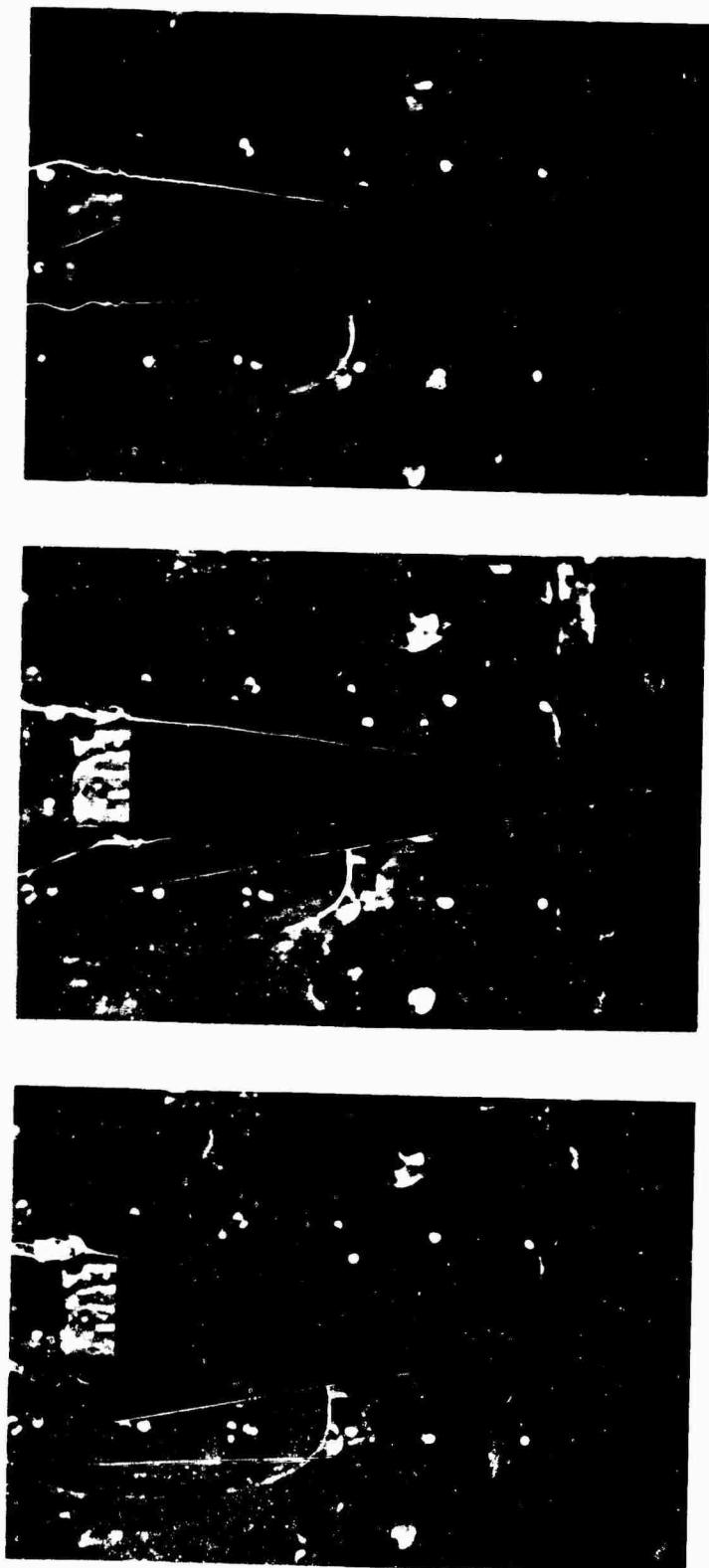
FIG. 12. Development of breakdown in a leading edge vortex.

I.A. SIMONS

Graduated from Southampton University in 1963 with a B.Sc. (Eng) degree in Aeronautical Engineering. From 1963 to the present has continued at the University on helicopter rotor aerodynamics research under Dr. J.P. Jones. The main interests have been in the induced velocity aspects of rotors.

Later this year will be joining Bölkow G.M.B.H. in Munich as a Development Engineer in their helicopter division.

R.E. PACIFICO

After three years national service in the Royal Air Force joined Canadian Marconi Corporation in Montreal, installing and supervising the maintenance of electronic equipment. Returning to England in 1957 studied electronic measurement at Southampton College of Technology. Joined the University in 1959 in the electronics section of the Department of Aeronautics and Astronautics. For the past four years has been engaged on instrumentation associated with the helicopter research programme. This has included design and development of small pressure transducers.

J.P. JONES

Graduated from University College Southampton in 1952 with a University of London B.Sc. (Eng). Research student, working on rotor blade wake flutter and behaviour in forward flight 1952-1954. Lecturer in Aerodynamics, University of Southampton 1954-1959. Research interests in rotor aerodynamics and in the flow over highly swept wings. Senior Lecturer 1959-1961. Westland Reader 1961 to date.

In 1955 received a Summer Scholarship to M.I.T. where worked with R.H. Miller. In 1964 appointed Visiting Associate Professor at M.I.T. Papers on rotor aerodynamics and dynamics, vortex flows and stability, and on analogue and hybrid computation.